AAAS

Science

3 JULY 2025

MOLECULAR GLUE

Computational mining expands the target space for induced-proximity drugs **pp. 32 & 45**

ASU Science

PRIZE FOR TRANSFORMATIONAL IMPACT

Apply now to the Arizona State University and *Science* Prize for Transformational Impact!

Arizona State University and *Science* have partnered to create the **ASU–*Science* Prize for Transformational Impact**. This prize recognizes transformational research that uses innovative methods and approaches to identify problems and develop solutions with impacts on policy and decision-making.

The grand prize winner will receive a prize of **US$30,000** and their prize-winning essay will be published in *Science* online and print. A runner-up will receive **US$10,000** and have their essay published in *Science* online.

APPLY BY **AUGUST 15, 2025**

www. Science.org/ASU

CONTENTS

3 JULY 2025 | VOLUME 389 | ISSUE 6755

18

Thabile Sithole, who has HIV, says now-canceled U.S. aid helped Eswatini stem mother-to-child transmission. Her son is uninfected.

PHOTO: OUPA NKOSI

EDITORIAL

NEWS

FEATURES

COMMENTARY

LETTERS

POLICY FORUM

PERSPECTIVES

BOOKS ET AL.

Gut check for preventive care: Bringing next-generation microbiome analytics to the clinic

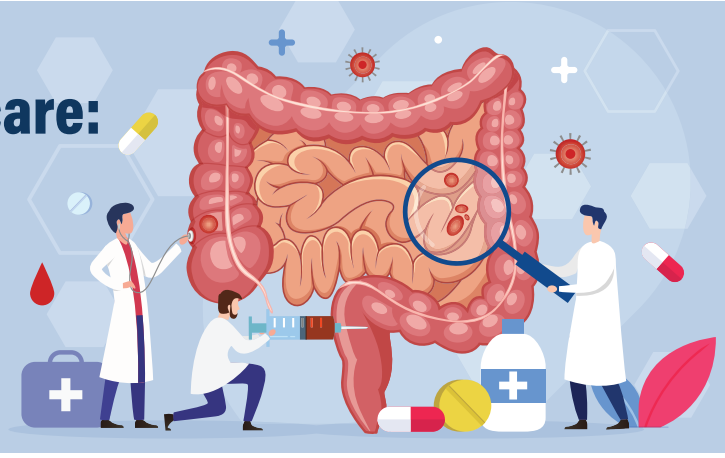

Kohey Kitao, CEO of Noster shares his insights on the future of gut-based health diagnostics.

Gut health is increasingly seen as a cornerstone of overall well-being—and Noster Inc. is at the forefront of transforming how we monitor it. Through advanced metabolome and microbiota analysis, the Kyoto-based biotech company is developing tools to detect disease risk early and personalize health care decisions. The Science custom publishing team sat down with CEO Kohey Kitao to learn how Noster's technologies are reshaping the concept of the modern health check.

Why focus on the gut for health screening and diagnostics?

The gut is one of the most metabolically active organs in the body. It not only reflects diet and lifestyle but also produces key metabolites that regulate immunity, metabolism, and even mood. Our goal is to capture and analyze these molecular signatures—what we call the "inner bio-signals"—to enable early, individualized risk assessments for chronic diseases like diabetes, obesity, and cardiovascular conditions.

What services does Noster provide to monitor gut health?

We provide comprehensive gut microbiome and metabolome analysis using liquid chromatography–mass spectrometry (LC-MS) and next-generation sequencing (16S rRNA and whole-genome). Already adopted in research and clinical settings—including executive health screenings at the Keio University Center for Preventive Medicine—our platform delivers unique, personalized reports co-developed with clinicians to support early detection and tailored health insights.

Does metabolome analysis improve traditional health assessments?

Traditional health checks rely on clinical lab markers that often reflect late-stage changes. Our technology identifies subtle shifts in gut-derived metabolites—such as short-chain fatty acids or HYA (10-hydroxy-cis-12-octadecenoic acid), a compound we discovered at Noster—long before conventional symptoms or lab results appear. HYA, for instance, promotes the release of GLP-1, a hormone that regulates appetite and glucose metabolism. Monitoring its level offers an opportunity to take earlier action than was possible before to prevent chronic disease.

Can you describe how these gut checkups work in a real-world setting?

Kohey Kitao, CEO of Noster

Absolutely. In a typical health-check procedure, participants submit stool samples as part of their health screening. We analyze the microbiota and metabolome, generate a comprehensive gut health report, and provide actionable insights. Based on their metabolic profile, individuals receive personalized nutrition and lifestyle guidance, potentially preventing disease before it starts.

Does this approach benefit the broader health care system?

Early detection translates directly to cost savings and better outcomes. Our tests are non-invasive, scalable, and highly predictive. By incorporating molecular gut data into standard wellness programs, we reduce unnecessary procedures and enable physicians to target care more precisely. This is a model of preventive, personalized, and sustainable health care.

What's ahead for Noster?

We're expanding clinical collaborations and working to make gut-based diagnostics a routine part of annual health evaluations worldwide. We're also growing our proprietary biomarker library and refining automated reporting tools to make our platform even more accessible to clinics, researchers, and insurers.

Final thoughts?

We're entering an era in which gut data can empower people to take control of their health. At Noster, we're proud to lead this transformation—turning complex science into practical tools that help people enjoy healthier lives.

Learn more about Noster's microbiome healthcare analytics technologies: www.noster.inc/services

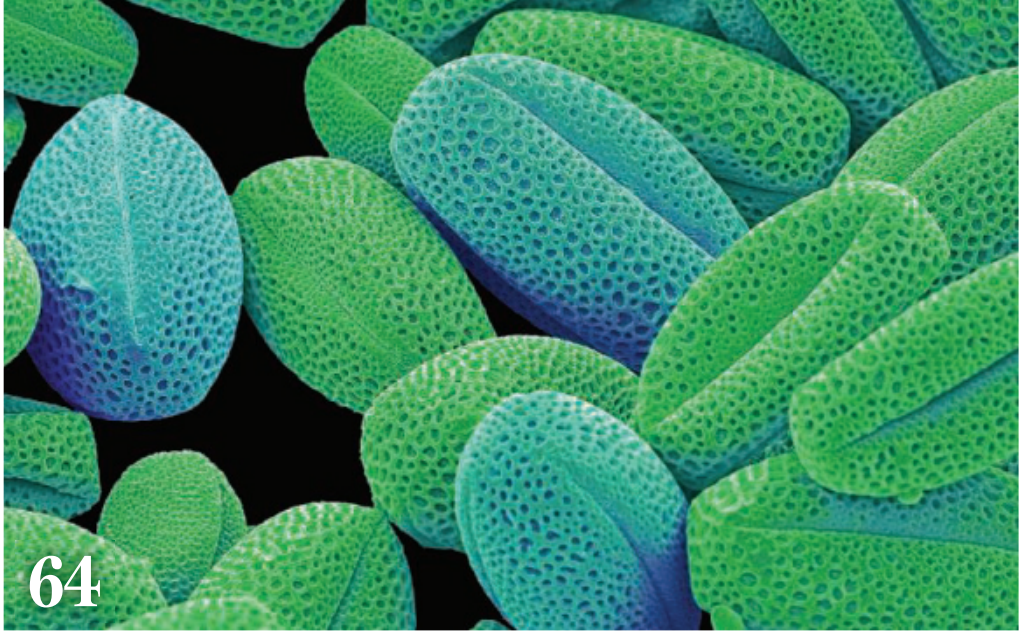

IMAGE: STEVE GSCHMEISSNER/SCIENCE SOURCE

PRIZE ESSAY

REVIEWS

REVIEW SUMMARY

RESEARCH

HIGHLIGHTS

RESEARCH SUMMARIES

RESEARCH ARTICLES

ON THE COVER

This illustration shows the interface of the kinase NEK7 (light blue) and the E3 ubiquitin ligase substrate receptor cereblon (teal). The interaction is facilitated by the small molecule MRT-3486 (orange). This molecular glue compound creates new features at the surface of cereblon that permit formation of the complex with NEK7, thus promoting ubiquitination and degradation of this protein. See pages 32 and 45. Credit: A. Fisher/*Science*

ON THE PODCAST

Losing years of progress against HIV, and farming plastic on Mars

WORKING LIFE

***Science* serves as a forum for discussion of important issues related to the advancement of science by publishing material on which a consensus has been reached as well as including the presentation of minority or conflicting points of view. Accordingly, all articles published in *Science*—including editorials, news, commentary, and book reviews—are signed and reflect the individual views of the authors and not official points of view adopted by AAAS or the institutions with which the authors are affiliated.** *Science* (ISSN 0036-8075) is published weekly on Thursday, except last week in December, by the American Association for the Advancement of Science, 1200 New York Avenue, NW, Washington, DC 20005. Periodicals mail postage (publication No. 484460) paid at Washington, DC, and additional mailing offices. Domestic individual membership, including subscription (12 months): $165 ($74 allocated to subscription). Domestic institutional subscription (51 issues): $2865; Foreign postage extra: Air assist delivery: $135. First class, airmail, student, and emeritus rates on request. Canadian rates with GST available upon request, GST #125488122. Publications Mail Agreement Number 1069624. **Printed in the U.S.A. Change of address:** Allow 4 weeks, giving old and new addresses and 8-digit account number. **Postmaster:** Send change of address to AAAS, P.O. Box 96178, Washington, DC 20090–6178. **Single-copy sales:** $15 each plus shipping and handling available from backissues.science.org; bulk rate on request. **Authorization to reproduce** material for internal or personal use under circumstances not falling within the fair use provisions of the Copyright Act can be obtained through the Copyright Clearance Center (CCC), www.copyright.com. The identification code for *Science* is 0036-8075. *Science* is indexed in the *Reader's Guide to Periodical Literature* and in several specialized indexes.

Science AAAS

EDITOR-IN-CHIEF **Holden Thorp**, hthorp@aaas.org

EXECUTIVE EDITOR Valda Vinson

EDITORS, RESEARCH Sacha Vignieri, Jake S. Yeston **EDITOR, COMMENTARY** Lisa D. Chong

DEPUTY EXECUTIVE EDITOR Lauren Kmec

DEPUTY EDITORS Stella M. Hurtley (UK), Phillip D. Szuromi **SENIOR EDITORS** Caroline Ash (UK), Michael A. Funk, Angela Hessler, Di Jiang, Priscilla N. Kelly, Marc S. Lavine (Canada), Sarah Lempriere (UK), Mattia Maroso, Yevgeniya Nusinovich, Ian S. Osborne (UK), L. Bryan Ray, H. Jesse Smith, Keith T. Smith (UK), Jelena Stajic, Peter Stern (UK), Yury V. Suleymanov, Valerie B. Thompson, Brad Wible **ASSOCIATE EDITORS** Jack Huang, Sumin Jin, Bianca Lopez, Sarah Ross (UK), Madeleine Seale (UK), Corinne Simonti, Ekeoma Uzogara **SENIOR LETTERS EDITOR** Jennifer Sills **NEWSLETTER EDITOR** Christie Wilcox **NEWSLETTER INTERN** Jasmin Galvan **RESEARCH & DATA ANALYST** Jessica L. Slater **LEAD CONTENT PRODUCTION EDITORS** Chris Filiatreau, Harry Jach Sr. **CONTENT PRODUCTION EDITOR** Amelia Beyna **CONTENT PRODUCTION EDITORS** Anne Abraham, Robert French, Julia Haber-Katris, Nida Masiulis, Abigail Shashikanth, Suzanne M. White **SENIOR PROGRAM ASSOCIATE** Maryrose Madrid **EDITORIAL MANAGER** Joi S. Granger **EDITORIAL ASSOCIATES** Aneera Dobbins, Lisa Johnson, Jerry Richardson, Anita Wynn **SENIOR EDITORIAL COORDINATORS** Alexander Kief, Ronmel Navas, Isabel Schnaidt, Alice Whaley (UK), Brian White **EDITORIAL COORDINATORS** Samuel Bates, Clair Goodhead (UK), Kat Kirkman **ADMINISTRATIVE COORDINATOR** Karalee P. Rogers **ASI DIRECTOR, OPERATIONS** Janet Clements (UK) **ASI OFFICE MANAGER** Carly Hayward (UK) **ASI SR. OFFICE ADMINISTRATORS** Simon Brignell (UK), Jessica Waldock (UK) **COMMUNICATIONS DIRECTOR** Meagan Phelan **DEPUTY DIRECTOR** Matthew Wright **SENIOR WRITERS** Walter Beckwith, Joseph Cariz, Abigail Eisenstadt **WRITER** Mahathi Ramaswamy **SENIOR COMMUNICATIONS ASSOCIATES** Zachary Graber, Sarah Woods **COMMUNICATIONS ASSOCIATES** Kiara Brooks, Haley Riley, Mackenzie Williams

NEWS EDITOR Tim Appenzeller

NEWS MANAGING EDITOR John Travis **INTERNATIONAL EDITOR** David Malakoff **DEPUTY NEWS EDITORS** Rachel Bernstein, Shraddha Chakradhar, Martin Enserink, David Grimm, Eric Hand, Michael Price, Kelly Servick, Matt Warren (Europe) **SENIOR CORRESPONDENTS** Daniel Clery (UK), Jon Cohen, Jeffrey Mervis **ASSOCIATE EDITORS** Jeffrey Brainard, Michael Greshko, Katie Langin **NEWS REPORTERS** Adrian Cho, Jennifer Couzin-Frankel, Phie Jacobs, Jocelyn Kaiser, Rodrigo Pérez Ortega (Mexico City), Robert F. Service, Erik Stokstad, Paul Voosen, Meredith Wadman **CONSULTING EDITOR** Elizabeth Culotta **CONTRIBUTING CORRESPONDENTS** Vaishnavi Chandrashekhar, Dan Charles, Warren Cornwall, Andrew Curry (Berlin), Ann Gibbons, Sam Kean, Kai Kupferschmidt (Berlin), Andrew Lawler, Mitch Leslie, Virginia Morell, Dennis Normile (Tokyo), Cathleen O'Grady, Elisabeth Pain (Careers), Charles Piller, Sara Reardon, Richard Stone (Senior Asia Correspondent), Gretchen Vogel (Berlin), Lizzie Wade (Mexico City) **INTERN** Alexa Robles-Gil **COPY EDITORS** Julia Cole (Senior Copy Editor), Hannah Knighton, Cyra Master (Copy Chief) **ADMINISTRATIVE SUPPORT** Meagan Weiland

CREATIVE DIRECTOR Beth Rakouskas

DESIGN MANAGING EDITOR Chrystal Smith **GRAPHICS MANAGING EDITOR** Chris Bickel **PHOTOGRAPHY MANAGING EDITOR** Emily Petersen **MULTIMEDIA MANAGING PRODUCER** Kevin McLean **DIGITAL DIRECTOR** Kara Estelle-Powers **DESIGN EDITOR** Marcy Atarod **DESIGNER** Noelle Jessup **SENIOR SCIENTIFIC ILLUSTRATOR** Noelle Burgess **SCIENTIFIC ILLUSTRATORS** Austin Fisher, Kellie Holoski, Ashley Mastin **SENIOR GRAPHICS EDITOR** Monica Hersher **GRAPHICS EDITOR** Veronica Penney **SENIOR PHOTO EDITOR** Charles Borst **PHOTO EDITOR** Elizabeth Billman **SENIOR PODCAST PRODUCER** Sarah Crespi **SENIOR VIDEO PRODUCER** Meagan Cantwell **SOCIAL MEDIA STRATEGIST** Jessica Hubbard **SOCIAL MEDIA PRODUCER** Sabrina Jenkins **WEB DESIGNER** Jennie Pajerowski

CHIEF EXECUTIVE OFFICER AND EXECUTIVE PUBLISHER

Sudip Parikh

PUBLISHER, SCIENCE FAMILY OF JOURNALS Bill Moran

DIRECTOR, BUSINESS OPERATIONS & ANALYSIS Eric Knott **MANAGER, BUSINESS OPERATIONS** Jessica Tierney **SENIOR MANAGER, BUSINESS ANALYSIS** Cory Lipman **BUSINESS ANALYSTS** Kurt Ennis, Maggie Clark, Isacco Fusi **BUSINESS OPERATIONS ADMINISTRATOR** Taylor Fisher **DIGITAL SPECIALIST** Marissa Zuckerman **SENIOR PRODUCTION MANAGER** Jason Hillman **SENIOR MANAGER, PUBLISHING AND CONTENT SYSTEMS** Marcus Spiegler **CONTENT OPERATIONS MANAGER** Rebecca Doshi **PUBLISHING PLATFORM MANAGER** Jessica Loayza **PUBLISHING SYSTEMS SPECIALIST, PROJECT COORDINATOR** Jacob Hedrick **SENIOR PRODUCTION SPECIALIST** Kristin Wowk **PRODUCTION SPECIALISTS** Kelsey Cartelli, Audrey Diggs **SPECIAL PROJECTS ASSOCIATE** Shantel Agnew

MARKETING DIRECTOR Sharice Collins **ASSOCIATE DIRECTOR, MARKETING** Justin Sawyers **GLOBAL MARKETING MANAGER** Allison Pritchard **ASSOCIATE DIRECTOR, MARKETING SYSTEMS & STRATEGY** Aimee Aponte **SENIOR MARKETING MANAGER** Shawana Arnold **MARKETING MANAGER** Ashley Evans **MARKETING ASSOCIATES** Hugues Beaulieu, Ashley Hylton, Lorena Chirinos Rodriguez, Jenna Voris **MARKETING ASSISTANT** Courtney Ford **SENIOR DESIGNER** Kim Huynh

DIRECTOR AND SENIOR EDITOR, CUSTOM PUBLISHING Erika Gebel Berg **ADVERTISING PRODUCTION OPERATIONS MANAGER** Deborah Tompkins **DESIGNER, CUSTOM PUBLISHING** Jeremy Huntsinger **SENIOR TRAFFIC ASSOCIATE** Christine Hall

DIRECTOR, PRODUCT MANAGEMENT Kris Bishop **PRODUCT DEVELOPMENT MANAGER** Scott Chernoff **ASSOCIATE DIRECTOR, PUBLISHING INTELLIGENCE** Rasmus Andersen **SR. PRODUCT ASSOCIATE** Robert Koepke **PRODUCT ASSOCIATES** Caroline Breul, Anne Mason

ASSOCIATE DIRECTOR, INSTITUTIONAL LICENSING MARKETING Kess Knight **ASSOCIATE DIRECTOR, INSTITUTIONAL LICENSING SALES** Ryan Rexroth **INSTITUTIONAL LICENSING MANAGER** Nazim Mohammedi, Claudia Paulsen-Young **SENIOR MANAGER, INSTITUTIONAL LICENSING OPERATIONS** Judy Lillibridge **MANAGER, RENEWAL & RETENTION** Lana Guz **SYSTEMS & OPERATIONS ANALYST** Ben Teincuff **FULFILLMENT ANALYST** Aminta Reyes

ASSOCIATE DIRECTOR, INTERNATIONAL Roger Goncalves **ASSOCIATE DIRECTOR, US ADVERTISING** Stephanie O'Connor **US MID WEST, MID ATLANTIC AND SOUTH EAST SALES MANAGER** Chris Hoag **DIRECTOR, OUTREACH AND STRATEGIC PARTNERSHIPS, ASIA** Shoupeng Liu **SALES REP, ROW** Sarah Lelarge **SALES ADMIN ASSISTANT, ROW** Victoria Glasbey **DIRECTOR OF GLOBAL COLLABORATION AND ACADEMIC PUBLISHING RELATIONS, ASIA** Xiaoying Chu **ASSOCIATE DIRECTOR, INTERNATIONAL COLLABORATION** Grace Yao **SALES MANAGER** Danny Zhao **MARKETING MANAGER** Kilo Lan **ASCA CORPORATION, JAPAN** Rie Rambelli (Tokyo), Miyuki Tani (Osaka)

DIRECTOR, COPYRIGHT, LICENSING AND SPECIAL PROJECTS Emilie David **RIGHTS AND PERMISSIONS ASSOCIATE** Elizabeth Sandler **LICENSING ASSOCIATE** Virginia Warren **RIGHTS AND LICENSING COORDINATOR** Dana James **CONTRACT SUPPORT SPECIALIST** Michael Wheeler

EDITORIAL
science_editors@aaas.org

NEWS
science_news@aaas.org

INFORMATION FOR AUTHORS
science.org/authors/
science-information-authors

REPRINTS AND PERMISSIONS
science.org/help/
reprints-and-permissions

MULTIMEDIA CONTACTS
SciencePodcast@aaas.org
ScienceVideo@aaas.org

MEDIA CONTACTS
scipak@aaas.org

PRODUCT ADVERTISING & CUSTOM PUBLISHING
advertising.science.org
science_advertising@aaas.org

CLASSIFIED ADVERTISING
advertising.science.org/
science-careers
advertise@sciencecareers.org

JOB POSTING CUSTOMER SERVICE
employers.sciencecareers.org
support@sciencecareers.org

MEMBERSHIP AND INDIVIDUAL SUBSCRIPTIONS
science.org/subscriptions

MEMBER BENEFITS
aaas.org/membership/
benefits

INSTITUTIONAL SALES AND SITE LICENSES
science.org/librarian

Sound policy demands sound science

Michael Kratsios

For more than a decade, prominent scientists across disciplines and institutions in the United States have expressed concerns about the quality of the nation's science and, in the best scientific tradition, called for self-correction. That is why the fiercely negative reaction of some members of the scientific establishment to last month's Restoring Gold Standard Science executive order from President Trump comes as a surprise to some. The order, after all, aims to address these long-standing concerns about the impact, conduct, and public trust of science. As the just-released White House guidance memorandum for federal research agencies on implementing Gold Standard Science makes clear, the intent of this action is to bring the nation's research enterprise into alignment with the high standards that the scientific community has long set for itself.

In a 2014 *Science* editorial, Marcia McNutt, then serving as editor-in-chief of this publication, highlighted ongoing replication issues and reiterated the foundational importance of transparency and reproducibility for the conduct of science. In 2015, the Center for Open Science introduced its Transparency and Openness Promotion Guidelines, helping scientific institutions and journals hold themselves to higher standards. In 2019, the National Academies of Sciences, Engineering, and Medicine published a report on the same topic, titled "Reproducibility and Replicability in Science," with recommendations to the scientific community. These conversations continue today.

The executive order calls for a commitment to ensuring that taxpayer-funded science is reproducible, transparent, and falsifiable; subject to unbiased peer review; clear about errors and uncertainties; skeptical of assumptions; collaborative and interdisciplinary; accepting of negative results as positive outcomes; and free from conflicts of interest. To be sure, these have been the aims of the scientific enterprise all along, but few can deny that there have been lapses.

Nevertheless, since President Trump signed the Gold Standard Science order, the outcry from part of the scientific community reframes this action as an extreme and divisive step. Although some critics grudgingly admit the principles that make up Gold Standard Science are uncontroversial and commendable, they have framed this effort as co-opting or weaponizing the language of open science. Indeed, a recent news article in *Science* called attention to researchers shrugging their shoulders about "overstated" problems in reproducibility, publication bias, transparency, and more. This reactionary attitude is counterproductive and reflects the danger of allowing politicization to creep into the nation's scientific enterprise; scientists dismissing Gold Standard Science appear to be more concerned with their preferred policy outcomes than with the procedures that reinforce scientific rigor and excellence.

This week's memorandum further instructs each research agency to develop minimally burdensome metrics, evaluation mechanisms, and personnel training for incorporating the principles of Gold Standard Science into its work. Occasional reports to the Office of Science and Technology Policy will ensure accountability and provide opportunities to examine and refine processes for continual improvement.

What exists at the public's largesse exists for the public's benefit. In a self-governing republic, it is the responsibility of those appointed to represent the people to help direct and coordinate the taxpayer-supported research enterprise in the national interest. Essential to that task is preserving both the freedom of science from partisan politics and democratic government from the excessive influence of the scientific establishment. How scientific inquiry and findings should shape policy-making is itself a prudential, political judgment. But science and politics need not be in conflict. Ensuring that the science used in decisions conforms to the highest standards of research integrity makes these judgments themselves transparent and scientific, and represents a sincere effort to uphold America's scientific enterprise within the constraints of political reality and with due respect for the public.

...science and politics need not be in conflict.

The federal agencies that are subject to the Gold Standard Science order are only one part of the research ecosystem. Ideally, this effort will set an example for the rest of the research enterprise to do the same, especially the nation's universities, scientific professional societies, and publishers of the scientific literature as they continue their own efforts to improve the quality of research.

The loudest voices in this ongoing conversation may never be convinced, but rather than dismiss Gold Standard Science, the scientific community has the opportunity to take this government-led effort at self-reform and review how it too can support the highest standards of scientific integrity. □

Michael Kratsios is director of the White House Office of Science and Technology Policy, Washington, DC, USA. director@ostp.eop.gov

Published online 24 June 2025; 10.1126/science.adz9562

Sluggishness and defensiveness helped enable an executive order on research integrity

H. Holden Thorp

In the last few weeks, *Science* has published commentary condemning and supporting the Restoring Gold Standard Science executive order from the Trump administration that purports to strengthen research integrity in the United States through greater government oversight. The scientific community has largely reacted negatively to the directive, fearing that the way oversight by political appointees is specified in the order will lead to interference in the curiosity-driven process of science. This distress is understandable given the administration's abrupt and arbitrary actions to cut research funding and curtail or even stop the participation of foreign students in research. The United States has been a global leader in science because of high levels of funding, less government interference, and participation of the best talent from around the world. These aspects appear to be in danger, and it is logical to suspect that the executive order is another mechanism for weakening the scientific enterprise.

The administration's view, as articulated on this page by Michael Kratsios, director of the White House Office of Science and Technology Policy, is that the struggles that parts of the scientific community have with research integrity justify this action. The so-called "replication crisis," which began mostly in psychology studies that were statistically underpowered, has created the impression that unreliable research is widespread and not reproducible. The steady stream of papers with problematic images revealed by sleuths has been interpreted as a sign that large numbers of life sciences papers are questionable. And the concentration of many of these errors in Alzheimer's disease research, where the stakes are high and the investigators are prominent, has created a perfect target for political attack.

The scientific community needs to face up to the extent to which its own actions have fed this perspective. Although science is driven by data, politics and public opinion are shaped by anecdotes and storytelling. Thus, pointing out that many of these incidents are the result of a small number of actors does nothing to change the political narrative. The sluggishness of journals and institutions to respond to problems in research integrity is also fodder for criticism. But more important, the defensiveness of investigators and institutions in responding to problems severely heightens the suspicion. Rather than filing lawsuits and hiding behind carefully crafted statements, the scientific community should be engaging in a conversation about problems and potential solutions.

The reaction of the Alzheimer's research community to problems with papers on amyloid proteins is a case in point. Investigations of numerous studies across multiple laboratories raised substantial doubt about their validity. The reaction of amyloid researchers largely has been to characterize the situations as "rare fraudulent research," rather than owning the fact that in the public eye, these incidents are persuasive and easily used for political attacks. In another case, a prominent neuroscientist went to great lengths to show that he personally "did not engage in any fraud or falsification of scientific data," even though the problematic papers came from the lab that he ran. This appears to the public as an effort to absolve himself and blame junior members of his group. Indeed, Kratsios seized on this incident in a recent public statement.

It is possible to support science and hold it accountable at the same time.

A remedy for this situation is for the scientific enterprise to reaffirm its values and hold its members to them, irrespective of actions from a government entity in the United States or elsewhere. Scientific papers should be carefully written not to extend beyond what the evidence supports; adequate amounts of supporting data should be available to researchers who want to repeat analyses and experiments; corrections and retractions to the scientific record should be posted quickly and collaboratively; safeguarding trainees should be prioritized over powerful actors in the system; and sleuths and journalists who turn up problems in research should be recognized as improving science rather than vilified. Although most of the scientific enterprise does live up to these values, the community itself should be the one to hold transgressors accountable without provocation from the federal government. Only then will the message that the vast majority of findings are correct be taken by skeptics as genuine.

It is possible to support science and hold it accountable at the same time. The adherence to a false choice that only one or the other is possible has made it easier for anecdotally driven attacks to succeed politically and for reforms to be externally imposed. It is within the collective control of the scientific enterprise to change the response and the perception. □

H. Holden Thorp is Editor-in-Chief of the *Science* journals. hthorp@aaas.org

Published online 24 June 2025; 10.1126/science.adz9553

INFECTIOUS DISEASES

One-shot flu drug may beat vaccines

In a large study, one injection of a long-lasting treatment protected people for an entire influenza season

JON COHEN

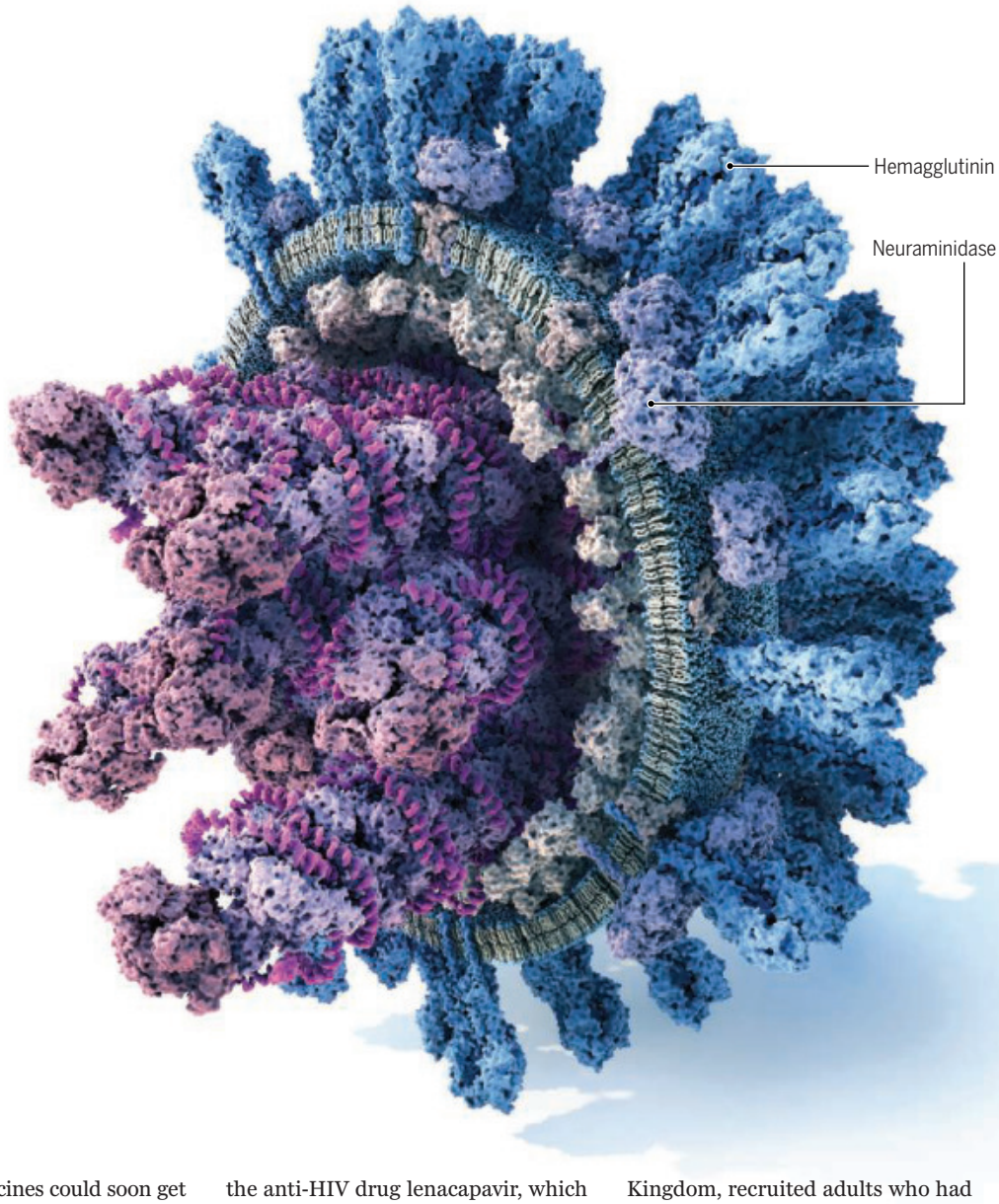

CD388 inhibits neuraminidase, one of two key proteins on the surface of the influenza virus, seen in a cutaway model.

IMAGE: C. BICKEL/*SCIENCE*

Influenza vaccines could soon get some serious competition—or assistance. A new clinical trial shows a single shot of a long-lasting flu drug may protect people for an entire season, and it might do so more effectively than vaccines.

In a study that enrolled 5000 healthy adults before the flu season started and followed them until after it ended, the highest dose of the drug provided 76.1% protection from disease, compared with a placebo shot, its developer, Cidara Therapeutics, reported in a press release and on an investor call on 23 June.

"This is one of the most exciting recent advances for influenza prevention," says Kathleen Neuzil, a veteran influenza vaccine researcher recently forced out of her job as head of the Fogarty International Center at the National Institutes of Health by President Donald Trump's administration. The drug's promise echoes that of the anti-HIV drug lenacapavir, which protects people from infection for 6 months and on 18 June won approval from the Food and Drug Administration as a so-called pre-exposure prophylactic.

Called CD388, the flu shot contains a reformulated version of zanamivir, a flu drug also known as Relenza that GSK brought to market in 1999 and is approved to both treat and prevent disease. Zanamivir, which must be inhaled daily, targets neuraminidase, an enzyme made by the virus that frees newly made virions from the surface of infected cells. To create a longer lasting version, Cidara developed a chemical variant of the drug and attached several copies of it to a piece of an antibody called the Fc fragment, which is engineered to resist being broken down by the human body.

The study, which took place in the United States and the United Kingdom, recruited adults who had not received the influenza vaccine. They were given one of three different doses of CD388 or a placebo shot under the skin between September and December 2024. Over the next 24 weeks, the researchers tallied the number of participants who had respiratory symptoms, such as coughing and a fever, and a confirmed test for the influenza virus.

All three doses provided what Cidara's chief medical officer, Nicole Davarpanah, described as "highly statistically significant protection," although the lowest had only 57.7% efficacy and the middle dose 61.3%. No serious side effects occurred at any dose.

Seasonal influenza vaccines, which are given either by injection or as a nasal spray, are designed to protect against at least three of the seasonal strains that circulate each winter. Their effectiveness at preventing

disease depends heavily on how well they match the flu strains going around in the human population but averages only about 40% because mutations in flu viruses often allow them to dodge immune responses.

In contrast, CD388 is effective against a wide variety of strains, a study in mice published by Cidara researchers the 17 March issue of *Nature Microbiology* shows. The drug attacks a region of neuraminidase that cannot easily change without compromising viral fitness. But Neuzil cautions that although resistance to neuraminidase inhibitors is rare in flu viruses, it does occur, and Cidara's press release did not address the issue. "This would be important to follow," she says.

Epidemiologist Arnold Monto of the University of Michigan School of Public Health says he anticipated Cidara's positive results, based on a study he helped conduct more than 25 years ago. In 1999, Monto and his co-workers reported in *JAMA* that inhaling zanamivir every day during the flu season offered 84% protection. The finding went nowhere because most people don't want to take a daily drug to prevent the flu, Monto says. But a single injection may attract a large market. "This strategy is very attractive in many ways," he says.

Monto adds that much will depend on the drug's future price, which the company did not want to discuss. "Flu vaccines are very cheap," he notes. And several research groups are working to develop "universal" flu vaccines that work against virtually all strains and pack more punch than existing ones.

Other drugs to prevent influenza are also in the works, including one being made by Cerberus Therapeutics that delivers zanamivir via "nanobodies"—tiny antibodies derived from camels that are relatively easy to produce in massive quantities—says immunologist and Cerberus Co-Founder Hidde Ploegh. Although he calls CD388 a "valuable approach" and the new data "compelling," Ploegh believes Cerberus will have an advantage because its drug is squirted up the nose. "If you think of ease of distribution, compliance, and acceptance, then I think any approach that avoids needles is preferable," he says. Then again, Cerberus has yet to reach human studies.

Cidara plans to launch large-scale efficacy trials of CD388 in the Southern Hemisphere's flu season, which starts in early 2026. Those studies will allow participants to also get vaccinated against flu, if they want; the two interventions combined could offer even better protection. The trial will focus on people with compromised immune systems or chronic conditions that make them particularly vulnerable to severe influenza. "If the inhibitor can be manufactured at a large scale at a reasonable price, it could be very helpful as a prophylaxis for high-risk people," says flu research Adolfo García-Sastre of the Icahn School of Medicine at Mount Sinai. "It's a very interesting technology." □

TRUMP TRACKER

NIH WILL RESTORE GRANTS The National Institutes of Health (NIH) is moving to reinstate hundreds of grants that a federal judge ruled had been canceled illegally by President Donald Trump's administration. Since January, NIH has canceled more than 2000 grants in response to Trump's executive orders banning federal funds for topics such as diversity, equity, and inclusion and transgender health, leading to various court challenges. After a Massachusetts district judge last month ruled in favor of plaintiffs in two of those lawsuits, covering about 900 terminated awards, senior NIH official Michelle Bulls on 25 June told staff that many of those grants "must be reinstated, as soon as practicable." NIH had paused new cancellations the previous day. However, the agency continued to screen grants for the forbidden topics. —Jocelyn Kaiser

VACCINE PRESERVATIVE PULLED A U.S. panel last week recommended removing the preservative thimerosal from influenza vaccines. It has been shown to be safe, but vaccine opponents claim it causes neurological damage. Last week's meeting of the Advisory Committee on Immunization Practices (ACIP), which recommends what vaccines people in the U.S. should receive and when, influencing insurance coverage, was the first since Health and Human Services Secretary Robert F. Kennedy Jr. fired all 17 members last month and handpicked seven replacements, including several vaccine opponents. ACIP chair Martin Kulldorff, a biostatistician, also opened last week's meeting with a vow to examine the cumulative impact of the entire early-life vaccination schedule. The panel did recommend a new antibody—clesrovimab, by Merck—for babies to prevent respiratory syncytial virus infections, the most common cause of infant hospitalization. —Meredith Wadman

***NATURE* JOURNALS AXED** The Trump administration has ended several U.S. science agencies' subscriptions to Springer Nature journals, including the prestigious *Nature* titles. The move, which will end easy access to the journals for thousands of agency staff scientists, follows recent accusations by administration officials that many academic journals are biased. The for-profit, publicly traded Springer Nature is one of the world's largest scientific publishers, producing more than 3000 journal titles. The cuts, first reported last week by *Axios*, include subscriptions by the Departments of Agriculture and Energy, according to a government spending database, and perhaps the NIH as well. —Jeffrey Brainard

THEY SAID IT

Having folks speak up is contagious.

U.S. Environmental Protection Agency attorney Nicole Cantello, one of 278 agency employees who signed a 30 June "Declaration of Dissent" accusing EPA officials of politicizing the agency and undermining its mission

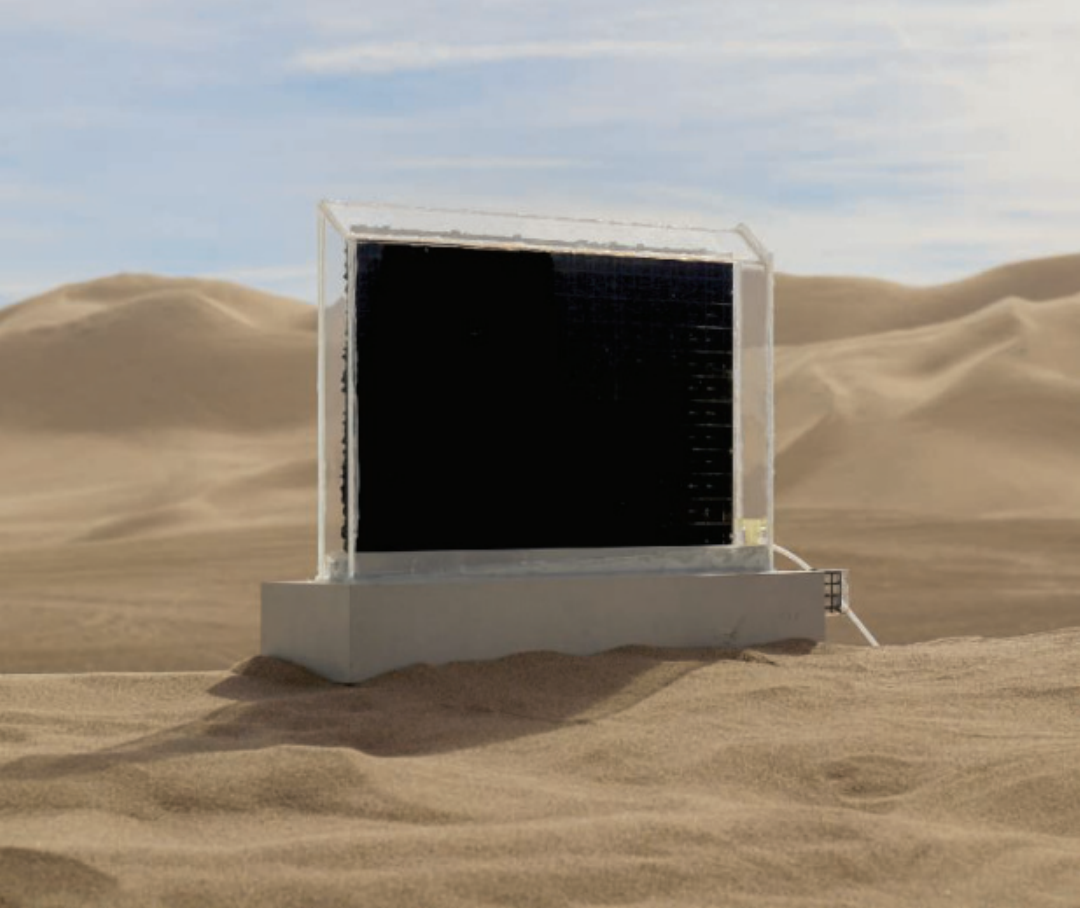

MATERIALS SCIENCE

Devices pull water out of thin air

Absorbent materials get cheaper and more efficient **ROBERT F. SERVICE**

A device built at the Massachusetts Institute of Technology harvests water in Death Valley, California, using the Sun's heat.

More than 2 billion people worldwide lack access to clean drinking water, with global warming and competing demands from farms and industry expected to worsen shortages. But the skies may soon provide relief, not in the form of rain but humidity, sucked out of the air by "atmospheric water harvesters." The devices have existed for decades but typically are too expensive, energy-hungry, or unproductive to be practical.

Now, however, two classes of materials called hydrogels and metal-organic frameworks have touched off what Evelyn Wang, a mechanical engineer at the Massachusetts Institute of Technology (MIT), calls "an explosion of efforts related to atmospheric water harvesting."

So far, none of the devices can compete with established approaches to augment water supplies, such as desalinating seawater. But some applications—cooling data centers and slaking the thirst of soldiers on the move—could support higher costs until the technology scales up, says Samer Taha, CEO of Atoco, a California-based startup. "There are many applications where atmospheric water harvesting can help."

Water capture technology may date back to the Inca who, living on the desert coast of South America, are thought to have collected morning dew on mesh nets, feeding it into cisterns. More recently, companies have deployed devices that use air-conditioners to cool air below the dew point, causing water vapor to condense, or water-absorbing desiccant materials such as salts, which are then heated to release the liquid. But both approaches require lots of energy, raising costs and limiting their reach.

The trick is to find a material that captures lots of water but readily frees it, too. Hydrogels—soft, porous networks of polymer fibers often impregnated with salts—seem to fit the bill. In a June report in *Nature Water*, Xuanhe Zhao, a mechanical engineer at MIT, and his colleagues describe a water harvester that, thanks to a novel hydrogel, requires no external energy input at all.

The team sandwiched the hydrogel, which contains lithium-chloride salt, between two glass sheets. At night, water vapor enters the gel and is trapped by the salts. During the day, sunlight heats the gel, evaporating the water. The vapor condenses on the glass panels, forming droplets that trickle down and are captured. So far the results are modest: Prototypes can produce up to 1.2 liters of water per kilogram of hydrogel per day in the dry desert air of Death Valley, California.

Other researchers are using modest amounts of energy and dirt-cheap materials to harvest much more water. For example, in a February report in *Advanced Materials*, Guihua Yu, a chemist at the University of Texas at Austin, and his colleagues describe a promising hydrogel made by altering cellulose, chitosan, and starch—complex carbohydrates common in agricultural and food waste. The biomaterials have a dense structure that limits the amount of water they can store, and they tend to hold onto much of what they snag, even when heated.

So Yu's team modified its hydrogel with chemical compounds known as zwitterionic groups that repel one another, stretching open the carbohydrates and making them more porous. Then the researchers added other compounds that cause the hydrogel to shrink when heat is applied, helping to squeeze trapped water out. Together, these changes enabled a prototype device to harvest up to 14 liters of water per kilogram of hydrogel daily. For now, getting the water out still requires raising temperatures to 60°C with an electric heater. However, Yaxuan Zhao, a graduate student in Yu's lab, says the low cost of the biomaterials means the device could be deployed along with solar panels in off-grid communities and emergency relief efforts.

Jeremy Cho, a mechanical engineer at the University of Nevada, Las Vegas, and his colleagues believe dividing a water capture device into two layers can help keep energy costs down. They use a hydrogel membrane containing salts that attract water vapor. Once concentrated, the water is pulled farther into a salty liquid desiccant layer for storage. The process empties the pores in the hydrogel, freeing it up

PHOTO: MASSACHUSETTS INSTITUTE OF TECHNOLOGY

to capture more water. Releasing the water from the desiccant takes only a modest amount of heat. "It's a lot easier to heat a liquid than a solid," Cho says, which raises efficiency. According to a October 2024 report in the *Proceedings of the National Academy of Sciences*, the setup could collect nearly 17 liters of water per day for each kilogram of absorbing material in humid environments, and a still respectable 5.5 liters in a Las Vegas-type arid environment.

Some of the most productive devices rely on a different kind of material: metal organic frameworks (MOFs). These porous atomic scaffolds have channels and pockets that can be designed to attract and store specific molecules—in this case water. Although MOFs tend to hold less water than hydrogels, they can capture and release it more quickly, allowing them to go through dozens of such cycles in the time it takes hydrogels to go through one.

The key is to tailor them with alternating chemical groups that attract and repel water, says University of California, Berkeley chemist Omar Yaghi. In 2023 he and his colleagues reported an aluminum-based MOF that was cheap to make in bulk and that could wring water from desert air. In preliminary, unpublished tests, Yaghi says, prototype devices using a tweaked version of his team's MOF can produce 200 liters of water per kilogram per day with only small amounts of added heat.

Yaghi has licensed the technology to Atoco, which is exploring using it to generate water to cool data centers, harnessing their waste heat to speed the cycling. Atoco plans to open pilot scale facilities in Texas and Arizona next year to test scaled-up versions, Taha says.

Despite all of these emerging solutions, "there is still room for improvement," says Cody Friesen, an atmospheric water harvesting pioneer at Arizona State University. Today, he notes, desalination plants can convert large amounts of seawater to drinking water at a cost of less than 1 cent per liter. Water harvesting devices are orders of magnitude more expensive and nowhere near as prolific. With the community still sorting through various materials options and device designs, "We are not all singing out of the same hymn book," he says.

But Friesen's own company, Source Global, is an encouraging example. It has installed water-producing "hydropanels," which use a proprietary desiccant, at more than 450 sites worldwide, mostly in remote, off-grid locations. And Friesen believes costs will drop as manufacturing is scaled up, much as has happened with solar panels and batteries.

"Atmospheric water harvesting will eventually be the lowest cost delivered potable water on the planet," he predicts. □

IN FOCUS

Mountain mammals aren't super-sniffers

Mountain goats and other mammals that dwell at high elevations have diminished olfactory systems relative to their low-elevation relatives, researchers reported last week in *Current Biology*. The surprising finding suggests smell is not as important for survival in mountains' cold, dry, thin air—which doesn't carry scent well and can cause nasal congestion—so these animals have evolved to invest resources in developing other senses. Mammals living above 1000 meters have about 23% fewer genes coding for nasal receptors and an 18% smaller olfactory bulb on average compared with those that live closer to sea level, the researchers found. The higher the animal lived, the more extreme the difference. —Annika Inampudi

PHOTO: BRAD MITCHELL/ALAMY STOCK PHOTO

IN OTHER NEWS

PANDEMIC ORIGIN THEORIES DISMISSED

A scientific committee convened by the World Health Organization (WHO) has firmly rejected two minority views about how the COVID-19 pandemic began, but could not resolve what actually did spark it, the panel announced last week. The report from the 27-member Scientific Advisory Group for Origins of Novel Pathogens, representing 24 countries, found no compelling evidence that scientists created the virus responsible for the pandemic, and it dismissed theories, widely promoted by China, that imported frozen fish introduced it to that country. There still is not enough hard evidence to say whether the origin was a natural spillover from infected animals or a leak from a laboratory, the group says. But, like a previous assessment by a different WHO panel, it leaned toward a natural origin. The new report—which relied on published scientific papers, intelligence agency assessments, government reports, and interviews with scientists and journalists—faults the governments of the United States and Germany for not sharing more information from their intelligence communities. But it reserves its strongest criticism for China, which it said did not supply requested data. –Jon Cohen

PHOTO: VICTOIRE DOUNIAMA/*THE NEW YORK TIMES* VIA REDUX

GLOBAL HEALTH

Scattershot vaccination fails to slow mpox spread in Congo

Limited vaccine doses weren't used strategically, WHO finds **JON COHEN**

The country hardest hit by mpox, the Democratic Republic of the Congo (DRC), has had only a trickle of vaccine doses to fight the outbreak across a geographically vast territory that is home to 100 million people. A new analysis by researchers at the World Health Organization (WHO) shows it was also hampered by a scattershot use of that limited vaccine supply.

"I call it the confetti strategy: You distribute a little bit everywhere," says Ana Maria Henao-Restrepo, a WHO vaccine specialist who led the analysis. "The possibility of having an impact is diminished substantially." She has presented the findings at recent WHO meetings and shared the slides with *Science*. Although the country has managed to vaccinate more than 700,000 people since October 2024, the WHO analysis suggests it has made little difference.

Misaki Wayengera, a geneticist in neighboring Uganda, which is battling its first ever outbreak of the debilitating disease, says he "loves" this analysis. "It gives us the first really intensive, scientifically well-designed assessment of the impact of an mpox vaccination program in Africa," says Wayengera, who advises his government's health ministry about epidemics.

The DRC had the world's first documented case of mpox in 1976, and for decades it had sporadic outbreaks that died out within months and did not reach beyond remote areas. But in 2024, a novel strain of the monkeypox virus that causes the disease spread rapidly through the eastern part of the country, jumping borders to Uganda and other neighbors. That June, the country approved the use of an mpox vaccine, but it would take another 5 months for doses donated from abroad to arrive.

Supplies were always tight, and an mpox plan for Africa issued in September 2024 by WHO and the Africa Centres for Disease Control and Prevention said the first doses should go to populations at highest risk, which mainly meant contacts of known cases. This strategy creates a "ring" of immunity around each case to prevent spread of the virus. Ring vaccination was key to the success of the global vaccine campaign that eradicated smallpox nearly 50 years ago. Wayengera agreed that African countries battling mpox should use the same strategy, as he argued in a commentary pub-

A resident of the eastern Democratic Republic of the Congo gets an mpox vaccine in November 2024.

lished in the December 2024 issue of *The Lancet Global Health*.

But the DRC and other African countries have limited ability to do the surveillance needed to confirm cases and identify their contacts—critical components of a ring vaccination campaign. Mpox symptoms are easy to confuse with chickenpox, and in much of the DRC, confirming an mpox case "is almost impossible for us because there are provinces that do not have laboratories," says Nanou Yanga, who helps lead the vaccination efforts for the DRC's health ministry. The country also lacks the funds needed to quickly geolocate cases, she adds, which helps guide where to offer vaccination. The incursion of a rebel group into cities and towns in the eastern DRC has added an extra burden in the region, leading many mpox treatment centers to close and large populations to relocate.

To assess the impact of the DRC's vaccination efforts, the WHO scientists, working with the DRC ministry of health, looked at the city of Kinshasa, which has a population of 17 million and by early March had distributed about 500,000 vaccine doses. The researchers geolocated all of the confirmed cases in the city for 2 months after the vaccination campaign took place. They saw cases decline in some areas and increase in others, regardless of which had received vaccines. "You cannot really see any patterns or trends," Henao-Restrepo says.

One reason the vaccine appears to have had little effect is that transmission in Kinshasa—which at first was largely driven by sex workers and their clients—peaked in August 2024, long before the vaccine became available. By the time it arrived, there was likely a "buildup of natural immunity in the highest-risk populations," says Olivier le Polain, a disease modeler who heads an epidemiology and analytics division at WHO and worked on the analysis.

Ring vaccination campaigns must closely follow the epidemiology of an outbreak, says Henao-Restrepo, who has helped the DRC conduct successful ring vaccination efforts against Ebola outbreaks. "The best approach is to focus on areas where the transmission is still going up," she says. "You have to have the love and the dedication to look at the detailed data if you really want to beat the virus."

Henao-Restrepo acknowledges the challenges of tracking mpox cases. But she says vaccination campaigns must try to be more aggressive in reaching contacts of those infected. "We have to be faster with the vaccination and more targeted to ensure that we really change the trajectory of the outbreak," she says. (New funding recently in from Gavi, the Vaccine Alliance, is now shoring up case tracking, Yanga says.)

Wayengera agrees that moving quickly is key. Genetic analyses show that the Uganda outbreak traces to a novel monkeypox variant that surfaced in September 2023 in Kamituga, a mining town in the eastern DRC. "It took almost a year for us to really begin to think about getting vaccine to DRC," he says. "By the time we got in, transmission had already exploded. If we had acted in Kamituga area just at [the] time of onset of this outbreak, we would have put out the fire."

Uganda's own vaccination campaign, launched in January, has had some success containing spread among sex workers and their clients, Wayengera says. But despite the more than 100,000 doses of vaccine donated to the country, the outbreak is far from over. Like the DRC, Uganda has struggled to trace contacts and conduct ring vaccination. "Sex workers don't keep records of what they do, and if you ask who at end of the day were your contacts, it's very difficult to map this out," he says. The virus, as in the eastern DRC, has also spread widely through nonsexual contact—which is more difficult to track—affecting many children.

If African countries can intensify surveillance and obtain more doses of vaccine, Wayengera is confident that ring vaccination combined with campaigns that have a broader reach can have a major impact against mpox's spread. "I don't think the opportunity is lost," he says. "Do we have the resources to widen the net beyond the epicenters of the disease outbreaks? These are the issues we are trying to fight with here." □

SEISMOLOGY

Glacial melt due to global warming is triggering earthquakes

Study provides first solid link between climate change and increased earthquake hazard

PAUL VOOSEN

Climate change is worsening many natural hazards, including droughts, heat waves, and storm surges. Now, a new one has joined the list: earthquakes. Researchers have found that as global warming accelerates melting of mountaintop glaciers, the meltwater, percolating underground, increases the risk of damaging earthquakes.

The evidence comes from beneath Grandes Jorasses, a glacier-clad peak in the Alps that is part of the Mont Blanc massif, home to Western Europe's tallest mountains. Precise seismic records show a heat wave in 2015 kicked off a surge of small earthquakes under the mountain. Although the tremors themselves were not damaging, the chances of large earthquakes are known to rise with the frequency of small ones. "It increases the hazard dramatically," says Toni Kraft, a seismologist at ETH Zürich and co-author of the new study, published this month in *Earth and Planetary Science Letters*.

Scientists have known for decades that water, pressurized by the weight of kilometers of rock overhead, plays a key role in triggering earthquakes. When water gets squeezed into the pore spaces of rocks, the added pressure can counteract forces that keep faults clamped shut, leading to slip. In eastern Taiwan, for example, movement along a fault—one that ruptured in a magnitude 6.8 earthquake in 2003—is thought to vary seasonally with rainfall. The same mechanism is at play in the clusters of earthquakes sometimes triggered by natural gas fracking, wastewater storage, and advanced geothermal energy projects, which all inject pressurized water deep underground.

Global warming can also release water into the ground as it melts mountain glaciers. The process had not been convincingly tied to earthquakes, but the new work makes a good case, says Kwanghee Kim, a seismologist at Pusan National University. "It provides multiple lines of evidence that the geosphere is responding to climate change."

In the Mont Blanc region, existing records already displayed a clear seasonal trend: Small

tremors tend to rise in late summer, after meltwater from glaciers penetrates the rocks, and decrease again in early spring. But Kraft and his colleagues wanted to zoom in on the seismic record to see whether climate change was also driving a trend. "The goal is to have as unbiased a view of seismicity as possible," Kraft says. He and his colleagues found it in records from the closest high-quality seismometer, installed in 2006 some 13 kilometers south of the mountain. It had captured more than 12,000 earthquakes previously overlooked because they were so small.

The catalog showed a clear jump in earthquake magnitude and frequency starting in 2015, after a severe heat wave melted the high alpine ice, says Verena Simon, a seismologist at ETH Zürich and the study's lead author.

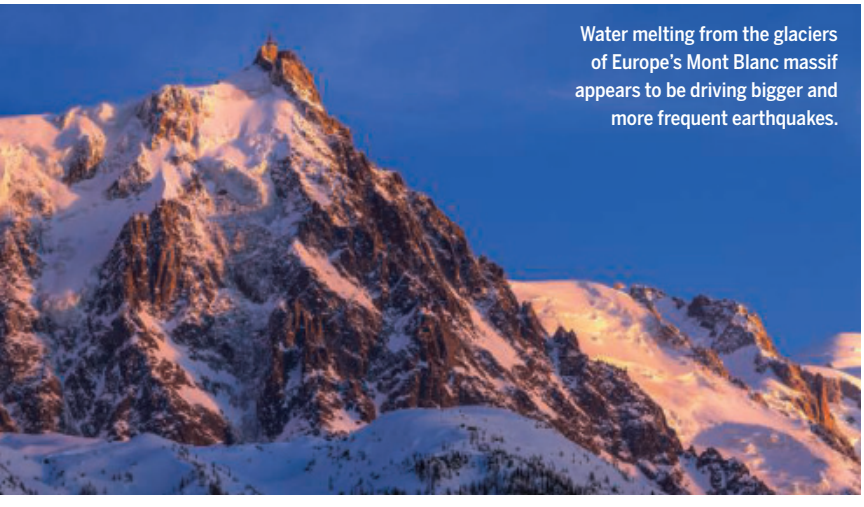

Water melting from the glaciers of Europe's Mont Blanc massif appears to be driving bigger and more frequent earthquakes.

The team then looked at weather records for other years. It found that stronger heat waves seemed to lead to bigger jumps in seismicity—albeit with a delay of a year for shallow earthquakes, and 2 years for quakes as deep as 7 kilometers. "We assume the system must have reached a triggering point," Simon says, as meltwater found pathways through the mountains and primed more faults to rupture.

The famed 11-kilometer-long Mont Blanc tunnel had already shown how easily water can flow through the interior of Grandes Jorasses and its neighbors. Tunnel construction in the early 1960s was hampered by torrents of water. The water was fresh, lacking the minerals it would contain if it was percolating more slowly through the mountains. The excavation also revealed numerous faults, created by the collision of tectonic plates that formed the Alps, that could be conduits ferrying water down to earthquake source zones.

When combined with the researchers' seismic data and broader models of Alpine melt, the evidence adds up to a "remarkably clear picture," says William Ellsworth, a seismologist at Stanford University. Pressurized water quickly percolates to faults that are often on the verge of slipping—and sometimes pushes them over the edge. "Essentially everywhere, the Earth is in a relatively critical state," Ellsworth says.

Additional years of data or studies that show a similar uptick elsewhere in the Alps would bolster the climate connection, says Philippe Vernant, a geodynamicist at the University of Montpellier. The seismic patterns of the Alps are tricky, he says, and other factors could be at play. For example, he says, the surge of earthquakes might represent a delayed response to the excavation of the Mont Blanc tunnel and the shift it caused in the plumbing of the mountains.

The climate-driven quakes are unlikely to threaten the tunnel or any nearby towns, Kraft says. Overall, the Alps are thought to be capable of earthquakes as big as magnitude 6, and most infrastructure is built to withstand such a quake. But other ranges including the Himalayas can experience much larger earthquakes—and are home to many melting glaciers. If this same dynamic is playing out beyond the Alps, Kraft says, scientists and communities need to start to take it into account. It seems the world's shrinking glaciers won't go quietly. □

ARCHAEOLOGY

Wooden tools point to ancient taste for plants

Discovery in China also suggests Asian hominins crafted in wood rather than stone **ANDREW CURRY**

Proponents of the "paleo diet" like to imagine the deep past as an all-meat barbecue buffet. And thus far, the kinds of tools dating to the dawn of humanity—countless stone blades and choppers, along with a few wooden spears and throwing sticks—seemed to support the idea of a prehistoric diet heavy on mammoth steaks.

Wooden tools from a site in China, reported this week in *Science* (p. 78), emphasize that ancient hominins ate their veggies, too. The 300,000-year-old implements are digging sticks, carved from branches and tree roots using stone blades. The pointy, hand-size implements were probably used to harvest carbohydrate-rich tubers and roots from the soft ground of a prehistoric lakeshore. "It's the first time we've found such an old site with evidence of hominins exploiting an underground food resource," says Bo Li, a geochronologist at the University of Wollongong and co-author of the new research. "This group of hominins knew what plants were edible or not, and were specifically looking for these plants with wooden tools."

Their sophisticated workmanship also suggests that although stone tools are scarce at sites in East Asia, early hominins there were no less skilled in toolmaking than contemporaries in Europe, the authors say. They were simply working in another, more perishable medium. "Having a site like this is amazing," says Annemieke Milks, an archaeologist at the University of Reading who was not part of the new study. The tools "are a window into the sophistication of technology in the organic realm we don't really see."

The site, called Gantangqing, was discovered in the 1980s near Kunming, China. As archaeologists dug deep into what was once the shore of a prehistoric lake, they found thousands of pieces of wood in a space just a few meters square, preserved for millennia by wet underground conditions. Judging from animal bones found at the site, meat was probably on the menu occasionally. But the rest of the menu was colorful, nutritious, and largely vegetarian. Along with the tools, researchers uncovered ample plant remains, including hazelnuts, pine nuts, grapes, and kiwis. In the lake and along its muddy shore, early hominins would also have been able to pluck and eat the leaves and seeds of water lilies

PHOTO: FRANCOIS ROUX/ALAMY

Hand-size digging sticks from a ancient lakeshore served for harvesting edible roots.

and dig up water chestnuts and other edible roots and rhizomes.

Initial attempts to date the wood were inconclusive. They were too old for radiocarbon dating, which ceases to be useful after about 50,000 years. By 2018, new dating methods for dating sediments and other nearby material showed the wood was about 300,000 years old. Besides being the earliest confirmed digging sticks, the tools are the oldest organic implements found in Asia. "They are a first in this part of the world," says Michelle Langley, an archaeologist at Griffith University who was not part of the research team.

That put them in the middle of a pivotal moment, known as the Middle Stone Age. "It's a very special period in terms of the Paleolithic globally," Li says. In Africa and Europe, Neanderthals and the ancestors of modern humans were making significant advances in toolmaking, crafting small cutting blades along with more complex stone choppers and axes.

Yet Middle Stone Age sites in Asia looked different. Stone tools there remained relatively simple or were missing entirely. Some archaeologists explained the contrast as a lack of sophistication on the part of Asian hominins, who many suspect belonged to another species of early human called *Homo erectus,* or to the Denisovans, closely related to Neanderthals. Others proposed an alternative explanation, sometimes referred to as the bamboo hypothesis: Perhaps ancestral humans in Asia were using organic materials, such as bamboo and wood, to make tools that often disappeared from the archaeological record when they decomposed. Gantangqing might be one of the vanishingly few exceptions. "These tools do support the idea that there could be a complex repertoire of organic technologies which are 'archaeologically invisible,'" Langley says.

At Gantangqing the closest sources of workable stone were more than 5 kilometers away. "The presence of wooden artifacts at the site is likely the result of the strategic choice to replace the functions of stone tools with wooden tools," says Xing Gao, an archaeologist at the Chinese Academy of Science's Institute of Vertebrate Paleontology and Paleoanthropology and a co-author of the new paper.

The landscape at Gantangqing might help explain why its inhabitants harvested plants rather than pursuing game like their contemporaries in Europe. Evidence from the site suggests hominins there lived in subtropical forests rather than open grassland, possibly offering a greater abundance and variety of edible vegetation. "Habitats were quite varied through time and across space," says Amanda Henry, an archaeologist at Leiden University. "We should not expect hominins to have eaten the same foods everywhere."

Archaeologists, however, say the site is additional evidence that hominins everywhere probably ate more plants than was thought. "Our narratives about past diets focus really heavily on stories about hunting and meat-eating," Henry says. "It's nice to get more and more archaeological data to push back against the 'man the hunter' narrative." □

BY THE NUMBERS

In a departure from historical trends, the National Science Foundation (NSF) tilted heavily toward computer science—and ignored the life sciences—in selecting its latest round of graduate research fellows. Two former directors of the prestigious program did the analysis. The 500 awardees, announced last month, were selected from a pool of 3000 students given honorable mention status in the first round of fellowship decisions, announced in April. —Jeffrey Mervis

Percent of honorable mention recipients awarded NSF graduate research fellowships in June

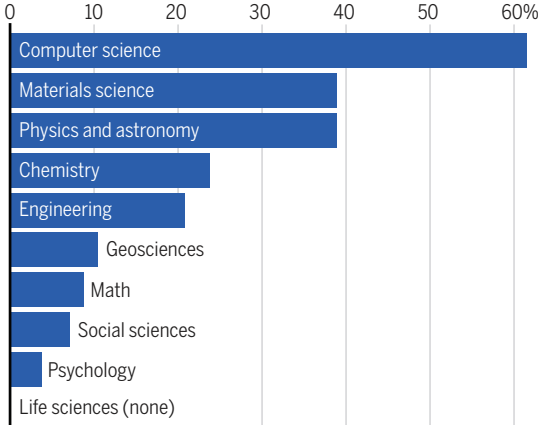

CREDITS: (PHOTO) BO LI; (GRAPHIC) M. HERSHER/*SCIENCE*; (DATA) GISELE MULLER-PARKER AND SUSAN BRENNAN

FEATURES

LEFT BEHIND

Siyabonga Nyawo, a 16-year-old in Eswatini, stopped taking his HIV medication after a U.S.-funded program that transported him to a clinic once a month ended.

GRAPHIC: V. PENNEY/*SCIENCE*

In Lesotho and Eswatini, U.S. budget cuts threaten to wipe out years of progress against HIV

JON COHEN
Photography by **OUPA NKOSI**

On 14 May, Temalangeni Dlamini, 20, traveled 10 kilometers from her rural home in southern Eswatini to the Matsanjeni Health Centre for the first checkup of her pregnancy, which was already 8 months along. Dlamini was hoping to give birth at the clinic, and this required an evaluation beforehand. The procedure included an HIV test, and to her surprise, Dlamini was positive. The doctor immediately put her on antiretroviral (ARV) treatment, which would also protect her child from infection.

The small, low-slung brick clinic has long received assistance from the U.S. President's Emergency Plan for AIDS Relief (PEPFAR), which paid for nurses, outreach workers, cellphones, and internet access, and provided transport for staff to make home visits. But in January, President Donald Trump's administration began dismantling PEPFAR's main funder, the U.S. Agency for International Development (USAID), and scrapping thousands of grants and contracts.

For Dlamini's family, the cuts hit home. In the past, the health center would have sent staff to her house after her diagnosis to test her two children and other relatives living nearby for HIV. If needed, everyone who tested positive would receive transport to the clinic, where they would receive treatment and then viral testing to make sure they were taking the drugs and had not developed resistance. This type of intensive follow-up is especially crucial for children, who depend on adults to take their medicines, and, if the virus is unchecked, become sick and die more quickly. Teens, being teens, often have difficulty taking daily pills.

On their own Eswatini and Lesotho, small countries in southern Africa, have the highest percentage of adults living with HIV in the world. Aid from the U.S. government has helped them rein in their epidemics, but cuts in those assistance programs now threaten the gains.

This story is part of a series about the impacts of U.S. funding cuts on global health, supported by the Pulitzer Center.

Now, the clinic could no longer afford the visit to Dlamini's home. Gcebile Shongwe, a testing counselor at the clinic who had made many such trips, says she initially could not believe that PEPFAR's support had ended. "I was so distressed," she said. "I was shattered."

Eswatini, a small landlocked country that borders South Africa and Mozambique, has long had the unfortunate distinction of having the world's highest percentage of adults living with HIV. Second is Lesotho, another small nation 500 kilometers to the south that's entirely surrounded by South Africa. But over the past 20 years, PEPFAR's support has helped both sharply reduce new infections as well as illness in those living with the virus. Now, many fear they will become sad examples of the damage caused by the Trump administration's sudden disruption of HIV/AIDS funding.

Both governments already pay for a large percentage of the drugs that have helped drive the progress and have pledged more help. But neither country is likely to make up for the tens of millions of dollars in support they appear to have lost. "We're at the cusp of achieving epidemic control," says Christopher Makwindi, who heads the Elizabeth Glaser Pediatric AIDS Foundation (EGPAF) office in Eswatini and has worked on the program there for 14 years. "I feel there's going to be a reversal of all the gains."

Science spent a week in mid-May traveling around Eswatini and Lesotho, meeting with PEPFAR "implementing partners" such as EGPAF and with health care providers, government officials, peer counselors, lab workers, and affected communities. In both countries, HIV control efforts are in free fall, and lives are at risk.

Makwindi says the termination of funding "was a shock" that baffles him to this day. He takes a generous view of the U.S. motivation: "I still believe that someone didn't do due diligence and just terminated us." Nuha Ceesay, Eswatini country director for the Joint United Nations Programme on HIV/AIDS (UNAIDS), has a harsher assessment. What the Trump administration has done is akin to saying, "I am going to unplug this life support machine from you," he says. "It is up to you to find an alternative, and whether you perish or not, that's not my business."

SINCE ITS LAUNCH by then-President George W. Bush in 2003, PEPFAR has invested more than $120 billion in helping more than 50 countries. The program estimates it has started 21 million people on anti-HIV drugs and saved 26 million lives. It has also supported giving drugs to prevent infections—so-called pre-exposure prophylaxis (PrEP)—for 2.5 million people. Many supporters say it was a powerful "soft diplomacy" tool, and until Trump took over in January, PEPFAR enjoyed strong bipartisan backing, including from former Senator Marco Rubio (R–FL), now secretary of state and acting USAID chief.

Eswatini and Lesotho, with populations of 1.2 million and 2.3 million, respectively, are prime examples of the program's impact. HIV prevalence in both countries peaked in 2015, when 31% of adults in Eswatini and 25% of those in Lesotho were infected, according to estimates from UNAIDS. Eswatini had 12,000 newly infected children and adults that year, Lesotho 14,000. Steadily ramping up treatment and prevention helped bring down adult prevalence to 25.1% in Eswatini in 2023, the latest year for which data are available, and 18.5% in Lesotho. In both countries new infections fell by roughly two-thirds, and AIDS-related deaths have been cut in half since 2010.

UNAIDS has a global goal to end the AIDS epidemic "as a public health threat" by 2030 that it summarizes as "95-95-95." It means 95% of people living with HIV know their status, 95% of those people are on ARVs, and 95% of that group has undetectable viral levels in their blood. Because undetectable people do not transmit the virus to others, reaching those numbers will help staunch the HIV epidemic. In 2021, Eswatini was one of the first countries in the world to reach the targets, and last year, it was at 95-98-95. Lesotho is now at 97-97-99. But both faced formidable challenges even before the aid cutoff.

A national survey of households in Eswatini in 2021 by ICAP, a global health group based at Columbia University, in collaboration with government researchers found that women over age 15 had nearly seven times the rate of new infections as men, in part because young women frequently have older male partners who are already infected. By the age of 49, half of all men and women in the country were living with HIV. The percentage of people taking ARVs who fully suppressed their virus was far lower in younger age groups, likely because they didn't consistently take their medication. In girls and women between ages 15 and 24, the number was only 76%,

Donor breakdown

Many low- and middle-income countries rely heavily on donors to fight HIV/AIDS. The U.S. government has long been the largest contributor by far, but that assistance will steeply decline if President Donald Trump's 2026 budget is approved. Six other countries together account for 23% of funding. Some of them plan cuts as well.

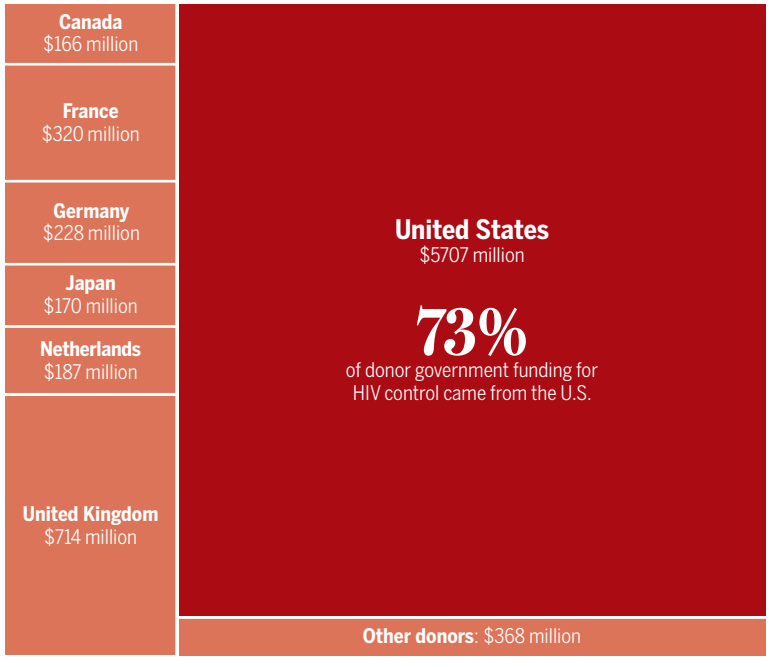

In 2023, donor governments contributed approximately **$8 billion** for HIV treatment and prevention initiatives.

CREDITS: (GRAPHIC) V. PENNEY/*SCIENCE*; (DATA) KAISER FAMILY FOUNDATION, *DONOR GOVERNMENT FUNDING FOR HIV IN LOW- AND MIDDLE-INCOME COUNTRIES IN 2023*

Pregnant women wait to see a nurse at the health clinic in Nazareth, a corn-growing region in Lesotho. Staff cuts have driven up waiting times to at least 4 hours and the clinic no longer tests pregnant people or their babies for HIV. "We are going to have exposed infants, a lot of them, because we are not doing anything for the expectant mothers," says Pasane Mazeboyane Matekane, the head nurse.

Lucille Goodness Mamba was close to dying from AIDS in 2006 and lost three children, she thinks because they, too, were infected. But thanks to treatment Mamba, 42, is doing well today and has given birth to a daughter who is HIV-free, which she attributes to the U.S. President's Emergency Plan for AIDS Relief. U.S. aid cuts ended her counselor job at the Matsanjeni Health Centre, but she has been temporarily rehired by an emergency government program and continues to help people with HIV stick with their treatment. Her future is in limbo.

Mookho Pasane (right), 29, has been on antiretroviral drugs since 2018 and this is her fourth baby born HIV-negative. But because breastfeeding can transmit the virus, the 9-month-old is getting another test at the Thamae Health Centre in Maseru, Lesotho. Makarabo Pamahapi (left), 45, who is administering it, is living with HIV herself and is a low-paid "lay counselor." Three better trained and more highly paid staffers at the clinic who were supported by a Columbia University program have lost their jobs because of U.S. government cuts. "The job is a lot of work, and it takes a lot of time," Pamahapi says.

and in men between ages 25 and 34 just 63%.

The same survey in Lesotho found similar patterns. Lesotho also attracts many migrant women to work in textile and apparel manufacturing; among those factory workers, HIV prevalence levels rise above 40%. UNAIDS estimates that if the U.S. government ends all funding for PEPFAR-supported treatment and prevention programs, the world will see 6.6 million preventable new infections and 4.2 million preventable AIDS-related deaths by 2029. There's no breakout of the impact on Eswatini and Lesotho, but they will surely be disproportionately affected.

Reversal of fortune

HIV-related deaths in countries supported by the President's Emergency Plan for AIDS Relief (PEPFAR) have plummeted over the past 15 years. Cuts in control efforts already announced by donors will cause the number to rise again, a model suggests. The 30% reduction of PEPFAR's budget proposed by President Donald Trump's administration, combined with other funding cuts, could increase deaths between 50% and 250%. The data include reported and projected deaths in 26 PEPFAR-funded countries.

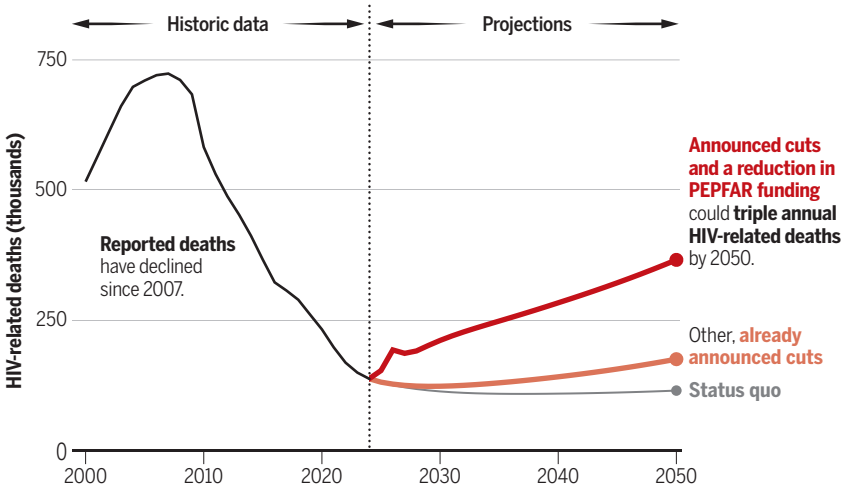

OVER THE YEARS, Eswatini and Lesotho each have received just shy of $1 billion from PEPFAR, including about $70 million in 2024. Roughly 60% of that money has come through USAID. The remainder is disbursed by the U.S. Centers for Disease Control and Prevention (CDC) and the Department of Defense, both of which are slated to continue to support some programs in Lesotho and Eswatini through September.

Just how much U.S. money is still flowing into the countries is not entirely clear. But since the cuts began on 29 January, their impacts have been unmistakable. Staff supported by the groups providing the aid—including EGPAF, ICAP, and the Baylor Foundation—had to stop their work immediately, then were given 3-week waivers because the programs were deemed to do "lifesaving" work. A few weeks later, the flow of money was shut off for good. Why the waivers didn't last was never made clear.

Soon, problems in both countries began to cascade. Fleets of SUVs with PEPFAR logos sat idle in parking lots. Implementing partners laid off most staff and no longer had funds to pay for health care workers at clinics and hospitals, leaving many unemployed and scrambling to support their own families. The governments have rehired some people, but staff shortages are the norm. ARVs remain available but getting them has become increasingly complicated. Outreach workers have cut back on contacting patients who do not show up to refill their medications.

Plans to apply a recent research breakthrough in PrEP are in peril as well. Although studies have clearly demonstrated that taking anti-HIV pills each day can prevent infection, trials of PrEP in teenage girls and young women in sub-Saharan Africa have failed to show a benefit. For complex social and cultural reasons that discourage them from taking a pill—stigma about being promiscuous, partners who resent being distrusted—daily PrEP has failed to work for them. A new injectable PrEP drug called lenacapavir that lasts for 6 months—which *Science* deemed the Breakthrough of the Year in 2024—won approval by the U.S. Food and Drug Administration on 18 June. In December 2024, PEPFAR, in conjunction with the Global Fund to Fight AIDS, Tuberculosis, and Malaria, pledged to provide 2 million doses of injectable lenacapavir over the next 3 years. Now, that pledge has a question mark.

PEPFAR began as an emergency program—a stopgap to prevent millions from dying. Most recipient countries were expected to transition to paying all costs by 2030. Officials in Eswatini and Lesotho have pledged to devote more of their own funding and to find less expensive ways to replace PEPFAR's often gold-plated programs. What shocked them was how abruptly the United States abandoned them—by "feeding USAID into the woodchipper," in the words of Elon Musk, who as head of Trump's cost-cutting efforts led the agency's dismantling. "We are grossly disappointed," says Tapiwa Tarumbiswa, who heads the HIV/AIDS program for the Lesotho Ministry of Health. "We feel left alone, like sort your own problem."

Trump added insult to injury in his 4 March speech to a joint session of the U.S. Congress, when he said Lesotho was "a country nobody has ever heard of" and made the false claim it received $8 million in U.S. funding to "promote LGBTQI+."

Tarumbiswa says he "totally understands" that the Trump administration wants his country to take care of its own people, but Lesotho needs more time. The radical policy shift, he says, "is a huge turnaround from what we know the U.S. government to be."

Lesotho's health minister, Selibe Mochoboroane, would have preferred a "proper transition" as well but says aid recipients have to accept that new administrations change policies. "It is a wake-up call," Mochoboroane says. "As African leaders, we need to live within our means."

It's too soon to see sharp increases in new infections, disease, and death from HIV/AIDS. But that is the likely result, health workers say. Many people are already going untested and untreated. Some on treatment have stopped taking their ARVs, and the number of "expert clients"—

CREDITS: (GRAPHIC) V. PENNEY/*SCIENCE*; (DATA) TEN BRINK, DEBRA *ET AL.*, *THE LANCET HIV*, 12:5, E346-E354 (2025)

Gcebile Shongwe (top right), a health worker, came to Temalangeni Dlamini's house in Eswatini to test her children and others living at the homestead for HIV after Dlamini, 8 months pregnant, tested postive. Test strips showed all eight children were negative.

people living with HIV whom PEPFAR funded to counsel their peers—has steeply declined. Short-staffed clinics are expecting to see more burnout and more patients walking away because it takes too long to receive care and treatment. Prevention services are set to dwindle.

Because efforts to collect and analyze data from clinics are also faltering, the impact may be difficult to see. "We may never know unless somebody else funds that assessment at some point," says Lephosa Likobe, a clinician in Lesotho's capital, Maseru, who works for EGPAF, which continues to receive some PEPFAR funding through CDC.

"Now we don't even wait until Sunday to pray," says Simon Morebotsane, another EGPAF doctor.

In the midst of the gloom, Dlamini's family, at least, enjoyed some good news. The day after she learned she was infected, *Science* offered to transport Shongwe, the clinic worker, the 10 kilometers to the homestead where Dlamini and some of her relatives live in wattle houses. Shongwe tested eight children, pricking their fingers and putting drops of blood on paper strips.

All eight tested negative. □

CHILDREN AT RISK

More from this series on how U.S. foreign aid cuts threaten child health around the world: https://scim.ag/USAID

COMMENTARY

LETTERS

NEXTGEN VOICES

Supporting scientists who study and work abroad

We gave young scientists this prompt: **When pursuing science education or work abroad, what is the biggest challenge you face? What one change would help scientists from your country or region overcome this challenge?** Read a selection of the responses here. Follow NextGen Voices on social media with hashtag #NextGenSci. **—Jennifer Sills**

Combat biases

Even when fluent in the local language, students with accents face hidden biases that limit participation, affect performance, and lead to impostor syndrome. Accent diversity should be normalized through bias mitigation workshops and a culture of inclusive listening.

Tanmoy Chakraborty Department of Electrical Engineering, Indian Institute of Technology, Delhi, New Delhi, India. Email: tanchak@iitd.ac.in

The traditional mindset in many Arab cultures views women as servants within the home and criticizes the idea of a self-reliant woman studying or working in a foreign country. Universities, religious leaders, media outlets, and government institutions should work to dislodge these deep-rooted cultural barriers by providing workshops, awareness campaigns, and testimonials by successful women who have studied abroad.

Hager Khaled Mekkawy Faculty of Biotechnology, Misr University for Science and Technology, Cairo, Egypt. Email: hager.kh.m@gmail.com

As a South African who has spent time in France, I've found that the greatest challenge in pursuing science abroad is the systemic devaluation of African knowledge systems, institutions, and scholarly voices. This marginalization manifests in unequal access to research funding, limited representation in authorship and editorial boards, and visa regimes that treat African scholars as security risks rather than intellectual equals. To overcome these inequities, African institutions should partner with leading international institutions to establish Africa-based research hubs that offer dual-degree programs and collaborative research governance. African scientists should not just be participants in science but also co-creators of knowledge agendas.

Karen Jacqueline Cloete UNESCO-University of South Africa (UNISA) Africa Chair in Nanosciences and Nanotechnology Laboratories, College of Graduate Studies, UNISA, Pretoria, South Africa. Email: kabouterclоete@gmail.com

Build communities

In India's collectivist culture—rich in community support, shared living, and accessible help—I never felt isolated. Adapting to the UK, where people mask emotions, was difficult. Encouraging the Indian diaspora to stay connected to their cultural roots and to actively support new arrivals would accelerate cultural adjustment.

ILLUSTRATION: ROBERT NUEBECKER

Mentorship programs, community gatherings, and peer networks would also provide emotional support and build community.

Ranjeet Singh Mahla Kennedy Institute of Rheumatology, Oxford, UK. Email: ranjeet.mahla@kennedy.ox.ac.uk

In the early years of my PhD in Belgium, I often moved silently between my lab and dorm. As the first woman from my Chinese village to study abroad, I faced language barriers, cultural differences, and a deep sense of isolation. To combat the loneliness, I invited other international students to go hiking with me. On the trail, we talked, laughed, and shared our stories, creating a support system. Institutions should facilitate and fund communities and social activities led by international students. Human connection and mutual understanding sustain science beyond the lab.

Dandan Peng Department of Mechanical Engineering, KU Leuven, Leuven, Vlaams-Brabant, Belgium. Email: dandan.peng@polyu.edu.hk

When I left Chile to work in Canada, I realized that immigrants must keep their jobs to maintain their immigration status, which makes them vulnerable to abuse. Institutions should encourage immigrant scientists to unionize to protect their status as workers. By building communities, young international scientists can highlight the issues they face and tackle them together.

Arturo Perez Department of Psychology, University of Alberta, Edmonton, AB, Canada. Email: aiperez@ualberta.ca

Provide care for caregivers

In the US, I had to balance work and raising a young child. I struggled to develop friendships and find dependable childcare, and I felt isolated from my family in Algeria. Support for parents working abroad should include childcare expenses, access to vetted caregivers, and flexible working hours.

Nora Rouabah Department of English Language and Literature, Batna 2 University, Batna, Algeria. Email: n.rouabeh@univ-batna2.dz

In India, caring for elders is expected, and living abroad can feel like abandonment. Tight work schedules have prevented me from leaving Belgium to visit family, even in emergencies, and visa barriers prevent family from visiting me. Replacement options for teaching in emergency situations, extensions for grant deadlines, and guidance on eldercare visas are small yet meaningful steps that universities could take to support international scholars.

Joseph Flavian Gomes Institute of Economic and Social Research (IRES)/Louvain Institute of Data Analysis and Modeling, UCLouvain, Louvain-la-Neuve, Belgium. Email: joseph.gomes@uclouvain.be

Invest in underresourced regions

When I left Greece for the UK, I was expected to show up with lab portfolios, summer internship experiences, and prestigious mentors, resources only available in academic environments far more privileged than mine. Top institutions should invest in scientists of all backgrounds by expanding programs that offer structured mentorships between researchers at higher- and lower-resource institutions.

Fotini Drallou University of Nicosia Medical School, Engomi, Nicosia, Cyprus. Email: fdrallou@gmail.com

When applying for a PhD in the US, I was asked to provide a list of my publications in specialized fields, an impractical requirement given the lack of specialized laboratory facilities and funding in Sudan. To commit to inclusion and diversity, institutions should modify admission requirements to allocate PhD positions for students from underrepresented countries. US and European institutions could create pre-PhD exchange programs with the applicants' home countries and then assess applicants based on critical thinking, problem-solving, and analysis skills instead of on publications.

Tyseer Abdalrahman Department of Human Physiology, Nile University, East Nile Locality, Khartoum State, Sudan. Email: tyseerabdalrahman@gmail.com

Applications often assume access to strong mentorship, fluent academic English, and financial stability, none of which is guaranteed in Brazil. Inclusive fellowships for underrepresented international researchers would reduce structural inequalities by prioritizing academic potential over institutional prestige, offering mentorship support, and covering essential costs such as relocation and visa fees.

Julio Santos Laboratory of Experimental Neurology, University of Southern Santa Catarina, Criciuma, Santa Catarina, Brazil. Email: drjuliosantosc@gmail.com

Consider communication styles

When I lived in Germany, I faced challenges navigating direct communication and negotiation styles despite being fluent in English. Germany's direct, task-focused culture contrasts with India's hierarchical, context-driven norms. Academic training programs should incorporate AI-driven tools that simulate real negotiation scenarios, offering a judgment-free space to practice requests for equipment, time, raises, or coauthorship and to practice reacting to blunt refusals to requests.

Vini Tiwari Department of Cellular and Molecular Medicine, University of California, San Diego, San Diego, CA, USA. Email: v3tiwari@health.ucsd.edu

In China, modesty was a strength; in the US, confidence is expected. Institutions can account for cultural norms by incorporating written reflections and online discussions into assignments instead of relying solely on verbal participation. In meetings, an online feedback option can provide a low-pressure way to voice ideas.

Teng-Jui Lin Department of Chemical and Biomolecular Engineering, University of California, Berkeley, Berkeley, CA, USA. Email: tengjuilin@berkeley.edu

In China, introductions often require formal channels, whereas in the US, networking depends on proactive outreach and self-promotion. This cultural gap can hinder collaboration opportunities, access to grants, and career advancement. Institutions can cultivate self-promotion skills through training and cross-cultural competency courses.

Shihao He Department of Neurosurgery, Peking Union Medical College Hospital, Beijing, China. Email: heshihaoo@outlook.com

In the Czech Republic, disagreeing with senior researchers is considered disrespectful. In Israel and the US, quietly deferring to authority figures can be seen as a lack of initiative or ability. Short-term programs such as summer schools or internships could help. Seeing how different cultures approach open dialogue, self-promotion, and science could expose scientists to these unwritten rules early in their careers.

Jan Kadlec Department of Brain Sciences, Weizmann Institute of Science, Rehovot, Israel. Email: jan.kadlec@weizmann.ac.il

Streamline visa requirements

I am in Ireland, but because I am from Türkiye, I have to spend extra time and money on visa applications before considering academic networking opportunities in other EU countries. Visa waivers or short-term and easy options for scientists traveling between accredited institutions would decrease the inequality, attract more talent, and serve as a reminder that scientific progress is a global endeavor.

Fatma Betul Dincaslan School of Pharmacy, University College Cork, Cork, Ireland. Email: fdincaslan@ucc.ie

Because of the war in Ukraine, traveling abroad, as I did to Latvia, for scientific reasons has become a challenge. There are no direct flights from Ukraine, border crossings can take days, and men of conscription age face legal restrictions on leaving the country, even for short academic visits. A dedicated, transparent mechanism for fast-tracking short-term academic travel permits would allow Ukrainian scientists to stay connected with the global scientific community. International institutions can show support by issuing formal invitations and advocating for flexible travel arrangements for Ukrainian scholars.

Yana Suchikova Research Department, Berdyansk State Pedagogical University, Zaporizhzhia, Ukraine. Email: yanasuchikova@gmail.com

While in the US for a China-US joint PhD program focusing on the optimization of power systems, I experienced prolonged visa uncertainty and months of security checks. I was reluctant to leave the country, fearing I may not be able to return, and the extended separation from my family was difficult. Institutions should establish formal agreements with the US government to ensure that international researchers with valid visas, especially those in sensitive fields, can reenter the country without reapplying. Universities could maintain a list of eligible researchers and provide documentation affirming their status.

Zelong Lu College of Electrical Engineering, Zhejiang University, Hangzhou, Zhejiang Province, China. Email: zelonglu@zju.edu.cn

Standardize academic requirements

Thai universities often charge international students two to three times the local tuition, yet their degrees are widely dismissed in China, where only top-ranked global universities are seen as academically credible. To protect international students, universities must ensure transparent, fair pricing and demonstrate real teaching and research quality. China should evaluate Thai universities based on academic merit rather than rankings, and government bodies, public agencies, and major employers should take the lead in ending discrimination against legitimate but lower-ranked institutions.

JiaHao Shi College of Public Health Sciences, Chulalongkorn University, Bangkok, Thailand. Email: jiahao.cason.shi@outlook.com

Because my Indian educational qualifications did not seamlessly translate to Australian institutions, I needed extra credentials. The benchmarks for research quality, publication norms, and expected level of independent contribution also differed. Indian universities should adapt course content, assessment techniques, and research criteria to meet international benchmarks.

Ankita Gupta Institute of Environment & Sustainable Development, Banaras Hindu University, Varanasi, Uttar Pradesh, India. Email: ankita.iesd@bhu.ac.in

Offer career services

Faculty hiring at Brazilian public universities involves public exams with standardized evaluation criteria, whereas countries such as the US have substantially different application procedures, required materials, and academic benchmarks. University-led seminars with alumni who have successfully built careers abroad could help scientists, both those hoping to build long-term careers internationally and especially those planning to return to Brazil with stronger skills, wider networks, and familiarity with international funding opportunities.

Andressa Monteiro Venturini Department of Environmental Science, American University, Washington, DC, USA. Email: aventurini@american.edu

I had the opportunity to travel from Egypt to the UK, Denmark, Poland, and Spain to pursue a postgraduate degree. However, after graduation, I returned home without the career prospects or financial stability that I had anticipated, a challenge many international students face. Students often return home after graduation because they cannot afford work permit expenses. Host institutions should acknowledge this struggle and help students navigate their options after graduation, including the search for jobs in their home countries. Career offices could leverage international alumni networks to prepare students for success when they return home.

Hagar Abousidara Akadeemy, Cairo, Egypt. Email: hagerabousidara@gmail.com

Increase financial support

Because of Egypt's severe currency depreciation, the fees for standardized English language tests (US $160 to 200) can equate to 2 months' salary. To help applicants, universities should partner with nongovernmental organizations and donors to provide free English exams for students from developing countries.

Alaa Mostafa Department of Sociology and Philosophy, Faculty of Education, Alexandria, Alexandria Governorate, Egypt. Email: alaamos2017@yahoo.com

Studying abroad comes with expenses such as accommodation, travel, and visa fees. However, financial support and fellowships are often restricted. During my studies, I was excluded from most academic fellowships and awards in Hungary, my home country, because I was studying abroad. Yet many financial support and fellowship opportunities at my host universities in Germany, Singapore, and Israel were limited to citizens. Academic institutions should promote equal opportunities for all students or create dedicated scholarships for international students.

Anna Uzonyi Department of Molecular Genetics, Weizmann Institute of Science, Rehovot, Israel. Email: anna.uzonyi@weizmann.ac.il

Establish research partnerships

In Iraq, universities must hire researchers with local credentials, whereas my host institution in the US prioritizes merit-based research. This mismatch in standards discourages diaspora scientists from returning to Iraq. Instead, Iraqi universities should foster knowledge exchange, build trust, and bypass government bureaucracy by establishing diaspora offices to match expatriate researchers with home-institution counterparts, co-design projects, and host virtual seminars.

Ali Saber Department of Immunology, University of Pennsylvania, Philadelphia, PA, USA. Email: alisaber@sas.upenn.edu

Because Russia is cut off from much of the world, Chinese students who obtain Russian doctoral degrees have trouble finding jobs at home. Fortunately, China and Russia have funded a number of joint research projects, and this collaboration could facilitate study-abroad programs and increase opportunities for students returning to China.

Yan Ge College of Resources and Environment, Northeast Agricultural University, Heilongjiang Province, China. Email: amy_geyan@163.com

In Angola, I encountered systemic barriers that are common across sub-Saharan Africa: insufficient research infrastructure, minimal funding, and fragile postgraduate systems. Regional research networks between Brazil and sub-Saharan African nations would strengthen local research capacity through mentorship, shared resources, and Global South cooperation. These initiatives could support proposal development, coauthored publications, and academic exchange, particularly among Portuguese-speaking countries.

Howard Lopes Ribeiro Jr. Center for Research and Drug Development, Federal University of Ceará, Fortaleza and Ceará, Brazil. Email: howard@ufc.br

10.1126/science.aea0626

POLICY FORUM

BIOSECURITY

The consequences of letting avian influenza run rampant in US poultry

The approach proposed by a high-ranking US government official would be dangerous and unethical

Erin M. Sorrell[1], Michelle Kromm[2], Gigi Gronvall[1], Andrew Pekosz[3], and Meghan F. Davis[1]

As of 20 May, the US Department of Agriculture (USDA) has confirmed highly pathogenic avian influenza (HPAI) in more than 173.1 million birds since the outbreak began in January 2022. The secretary of the US Department of Health and Human Services, Robert Kennedy Jr., has suggested allowing the unmitigated spread of HPAI in turkeys and chickens to identify surviving birds—a sentiment supported by Brooke Rollins, secretary of the USDA, which, along with state-level departments of agriculture, has jurisdiction over animal disease outbreaks (*1*). This approach would be dangerous and unethical. Allowing a highly lethal, rapidly evolving, and contagious virus to run a natural course of infection in poultry would lead to unnecessary suffering of poultry and put other susceptible animals on and near affected farms at risk. It would prolong exposure for farmworkers, which could increase viral adaptation and transmission risks for poultry, other peridomestic animals, and humans.

There is no evidence that this virus will slow down; Brazil reported its first cases in commercial poultry on 16 May (*2*). Although a drop in US case reporting is expected this summer as the virus moves southward with migratory birds, the US should be prepared for a surge this fall as birds return. To date, the USDA estimates that roughly 70% of H5 cases on commercial poultry farms have been linked to wild bird introductions, not farm-to-farm transmission (*3*). This is evidence that biosecurity measures (limiting visitors, avoiding mixing species, and implementing infection prevention and control measures), along with rapid culling, have been largely successful at both containing the virus on positive farms and excluding it from neighboring facilities. Yet Kennedy was quoted as saying that farmers "should consider maybe the possibility of letting it run through the flock so that we can identify the birds, and preserve the birds, that are immune to it" (*1*). Such a "let-it-spread" strategy may identify small numbers of poultry infected by H5 influenza virus that do not develop severe disease for unknown reasons; however, these birds could serve as a new long-term reservoir for the virus. Recent interest in bringing ostriches that may or may not have been exposed to H5 on a positive farm in Canada to the US seems to reinforce the idea that the administration has an ongoing interest in animals that come from let-it-spread situations.

CHALLENGES

Containment strategies

The threat that H5 influenza viruses pose to domestic poultry is not new; introduction of the virus can decimate a commercial facility or backyard flock in days. Over the past decade, regulatory agencies and poultry companies have prepared for and responded to HPAI using scientifically validated protocols for outbreak response and containment (quarantine of farms and culling of flocks). However, the current circulating viruses, which belong to clade 2.3.4.4b, are unlike any predecessors: They are more prevalent; spread by multiple transmission pathways; and have been found in multiple hosts, including dairy cows, wild mammals, companion animals, and humans. Although it is not possible to fully predict future virus behavior, evidence suggests that there should be more (not less) worry about lapses in containment compared with prior experience given how frequently multiple genotypes in the clade have spilled over into diverse species (from marine mammals to rodents) and have shown the potential to establish mammal-to-mammal transmission chains. When a virus is given opportunity to freely infect a host, it often evolves to be a more efficient pathogen in that species. Therefore, selecting for resistant birds in the manner proposed by Secretary Kennedy may also increase the chances of H5 evolving to be a better pathogen in poultry.

Rapid culling of positive flocks is central to containment of the virus on a farm because poultry infected with H5 shed a tremendous amount of virus. If effective controls designed to mitigate the quantity of viral shedding and known transmission pathways are removed, the exposure risk for other animals and humans on site and on neighboring farms will increase, and the opportunity for H5 to evolve to be a more effective poultry pathogen increases. The more exposed hosts of any species, the more opportunity there is for H5 adaptation and for the development of variants better suited for replication in new hosts to find a foothold. The worst-case scenario is that those mutations support more-efficient transmission between mammalian species, including humans, expanding the host range and geography of H5.

The lone survivors

In addition to the increased adaptation risks, any surviving birds would not have economic value as breeding stock because crossing a commercial bird with another commercial bird that survived H5 would lead to unknown health, welfare, and economic traits. The poultry industry has long harnessed genetic selection, using multiple genetic lines to identify beneficial traits that underpin the reliability and affordability of the food supply. Poultry that produce the meat and eggs that are consumed are the result of four to five generations of genetic selection—a refined process that builds on itself over years of investment and research. This process has increased feed efficiency and has driven more sustainable animal protein production. It is unknown whether these traits, which are critical to maintain, would be compatible with H5 resistance (*4*). Further, even if it were possible to estimate the percentage of poultry that survive H5 infection (something that has not been permitted in the US since the control strategy was established), protection against this current circulating clade does not ensure resistance to infection with other avian influenza viruses, such as recently detected H7N9 (*5*). Narrowing this genetic pool down, which is what would happen under the let-it-spread approach, would lead to less genetic diversity compared with our current commercial poultry population. Although research on genetic modification or selective breeding could identify traits that confer resistance to the currently circulating virus (*6*), developing a genetic supply chain and population with those traits takes multiple years, giving the virus ample time to mutate and overcome resistance traits.

Turkeys are highly susceptible to avian influenza, and high stocking density contributes to rapid transmission within flocks once the virus is introduced.

PHOTO: M. DAVIS

The animal-human interface

In 1997, the first human cases of H5 were reported in Hong Kong, leading to 18 total cases and six deaths (*7*). As of January 2025, the World Health Organization has documented 964 cases (466 deaths) in 24 countries. The US reported its first confirmed human case of H5 in April 2022; since then, 70 additional cases have been reported. Of these, 27 (26 since April 2024) were associated with exposure to infected poultry, and the most severe cases have been from avian-to-human spillover events. To date, humans have served as dead-end hosts for H5; however, the threat of these viruses acquiring the necessary mutations to support efficient human-to-human transmission has been the focus of much speculation, preparedness planning, policy debate, and research.

Research has provided clues on key molecular markers for efficient influenza replication and/or transmission in mammalian animal models and human cell lines (*8*). However, the mechanisms by which avian influenza viruses of various subtypes adapt to become more humanlike are not fixed in the number or order of specific mutations (or reassortment events). There are insufficient data to accurately predict risk factors for host adaptation (*9*). However, it has been observed that the more virus circulating, the more opportunity exists for adaptation. Although the US Centers for Disease Control and Prevention ranks the current threat of H5 infection in the general population as low risk, it is important to note that the 71 cases (one death) in the US likely underestimate the case count given the known probable and asymptomatic cases (*5*). Of these, 68 were reported in agricultural workers interacting with sick or dead animals, which each represent direct transmission from animals to humans. Although one worker has been hospitalized, most human cases have been mild. This may shift with the emergent genotype D1 variants, which have been associated with more-severe infections. Outside of the workers already exposed, the remainder of the US population (and the global community) is susceptible to this virus. A pandemic—particularly one that simultaneously affects the food system—can damage local and global economies and social structures.

CONSEQUENCES

Multiple species at risk

Uncontrolled spread leads to greater loss of life for a variety of animal species and contributes unnecessary risk for human exposure. Infected poultry facilities serve as H5 factories, producing large amounts of virus through respiratory secretions and fecal material and creating a risk for transmission to other poultry, farmworkers, and peridomestic species (*10*). It is unclear how this let-it-spread approach would be implemented in US poultry farms.

Biosecurity can mitigate transmission risk up to a certain amount of environmental viral load, but it is a piece of the puzzle, not a standalone mitigation strategy. When the risk reduction impact of culling is eliminated, biosecurity alone cannot be expected to be enough to protect neighboring farms. It is not financially feasible to enhance farm biosecurity to the point of reducing disease spread; barns are built to raise animals not to provide the same biosafety levels required of high-containment laboratories. Previous outbreak management has shown that uncontrolled viral replication in poultry can overwhelm risk mitigation strategies; this is why culling an entire farm is a critical aspect of disease mitigation for high-consequence human and animal pathogens (*11*). We believe that three key questions must be addressed if the US government takes a let-it-spread approach: How would it affect our disease reporting structures, associated disease reporting incentives, and other control measures in poultry but also in the broader livestock community? How would other at-risk populations, such as nearby poultry farms, companion animals, and poultry farmworkers, be protected while the virus works through a flock? How would feed be safely delivered to infected flocks and animal waste be managed without exacerbating transmission risks?

Disrupted food systems

When poultry are left to succumb to infection and the virus spreads, more protein ends up composting in the ground (deceased poultry) or simply is not produced (no chickens to produce eggs). The rampant spread of H5 could further destabilize access to affordable and

sustainable domestic protein sources. Poultry and eggs are a major source of affordable protein for most Americans, outpacing red meat and pork. The combination of available stores of frozen chicken and a less-affected domestic broiler flock means that chicken meat prices have been relatively stable thus far. By contrast, many states have faced egg shortages, limiting availability, raising prices (increases of more than 50% from last year), and in some cases leading to rationing. How will implementing the let-it-spread approach support the USDA goal of lowering and stabilizing egg prices?

Restrictions on trade

Prior documented H5 HPAI outbreaks in the US occurred in 1983, 2004, and 2014 to 2015 (*8*, *12*). The 2014–2015 outbreak, the largest outbreak in US history before 2022, led to a loss of more than 50 million birds (roughly a third of this outbreak), with an estimated economic impact of $1.0 billion to $3.3 billion (*13*). It accounted for losses of 12% of the egg-laying population and 8% of turkeys grown for meat—numbers that pale in comparison with what the industry faces now. This event resulted in trade restrictions on US poultry exports, distorted markets, and exacerbated economic losses (*14*).

The National Poultry Improvement Plan is a voluntary federal-state-industry mechanism for surveillance and control of certain high-consequence poultry diseases. It identifies states, flocks, hatcheries, dealers, and slaughter plants that meet certain disease control standards specified in its various programs. As a result, customers (including international ones) can buy products from source flocks that tested clean of certain diseases or produced under disease prevention conditions. If a let-it-spread approach is adopted, how will our international trading partners react, and what impacts will their reactions have on US trade markets?

Uncertainty, especially in rural communities

US poultry production has a competitive global advantage owing to domestic feed resources, primarily soybean meal and corn. If there are fewer chickens because of a let-it-spread approach, there is lower demand for feed—potentially disrupting a variety of supply chains. Rural communities are also often hit hardest during HPAI outbreaks; they experience immediate impacts to affected farms and downstream impacts to processing plants, feed mills, and packaging and shipping companies. It is unclear how the approach for uncontrolled spread will support the survival of rural communities and businesses. What will the direct and indirect economic impacts of product and market loss be on poultry producers, crop farmers, animal feed producers, and other supporting supply chain participants?

In addition, without containment measures in place, how do we account for the prolonged and unnecessary distress of infected birds and for the mental and financial health effects for farmers who must continue to operate their farms as their flocks suffer and succumb to a devastating disease?

STEPS TOWARD COURSE CORRECTION

The USDA recently granted conditional approval to Zoetis for their H5 poultry vaccine (*15*). Vaccination, although currently not part of the containment strategy for H5 in poultry, could complement depopulation strategies that target culling only to H5-positive barns on an affected facility—should epidemiologic evidence support this approach (specifically if studies demonstrate that barns are independent of each other in terms of disease transmission). Additionally, one critical gap that has been repeatedly ignored is the inclusion and involvement of poultry producers, industry members, and veterinarians in policy decisions that affect animal health and welfare, financial sustainability, and food security. A One Health approach must first be chosen, which includes assessing animal, food, and human health risks as well as economic stability before policies are promoted—and surely before they are adopted. One Health strategies prioritize coordination of surveillance, data sharing, and intersectoral communication, including with industry partners, experts, and the public; however, such briefings with national-level stakeholders and other parties interested in following the H5 outbreak—often held on a regular basis and before any major US government announcements (e.g., by the USDA, Centers for Disease Control and Prevention, and Food and Drug Administration)—have not been held since mid-January 2025. A let-it-spread strategy would challenge surveillance efforts that allow linkage of poultry reporting and virus characterization to human cases, wastewater surveillance, dairy bulk milk testing, and wild bird monitoring. These efforts are essential warning systems for clinicians, veterinarians, and state authorities. The US is not prepared for uncontrolled spread of H5 in avian species—let alone in mammalian or human hosts. It is not just poultry being put at risk. One must consider the proximity and density of livestock production in the US—let alone endangered or ecologically important wild bird species (such as the bald eagle).

If this policy is enacted, it will need to be rolled back in favor of collaborative, on-the-ground, and real-time implementation science. Building on the available knowledge for spillover risk and enhanced biosecurity at farms (poultry and dairy) is critical. New, science-based approaches must be considered while maintaining the implementation of scientifically validated procedures. Instead of letting it spread, which may dampen requirements or compliance with detection and reporting, we recommend enhancing case detection, reporting, and response to H5—not just to safeguard human health and address poultry welfare but for the safety of companion animal, livestock, and ecosystem health as well. □

REFERENCES AND NOTES

1. A. Mandavilli, "Kennedy's Alarming Prescription for Bird Flu on Poultry Farms," *New York Times*, 18 March 2025; https://www.nytimes.com/2025/03/18/health/kennedy-bird-flu.html.
2. "Brazil confirms its first bird flu outbreak in a commercial poultry farm," *Associated Press*, 16 May 2025; https://apnews.com/article/brazil-bird-flu-outbreak-commercial-poultry-857151a8155775941f8fa563d88a9ce2.
3. USDA, Animal and Plant Health Inspection Service (APHIS), "2022–2023 Highly Pathogenic Avian Influenza Outbreak: Summary of Depopulation Methods and the Impact on Lateral Spread" (2023); https://www.aphis.usda.gov/sites/default/files/hpai-2022-2023-summary-depop-analysis.pdf.
4. Otto's Farms, "The Evolution of Broiler Chickens: From Wild Fowl to Modern Poultry" (2024); https://ottosfarms.com/the-evolution-of-broiler-chickens-from-wild-fowl/.
5. USDA, APHIS, "APHIS Confirms H7N9 Highly Pathogenic Avian Influenza (HPAI) in a U.S. Flock" (2025); https://www.aphis.usda.gov/news/program-update/aphis-confirms-h7n9-highly-pathogenic-avian-influenza-hpai-us-flock.
6. A. Idoko-Akoh *et al*., *Nat. Commun.* **14**, 6136 (2023).
7. K. Y. Yuen *et al*., *Lancet* **351**, 467 (1998).
8. F. Krammer, E. Hermann, A. L. Rasmussen, *J. Virol.* **99**, e0220924 (2025).
9. M. Imai *et al*., *Virus Res.* **178**, 15 (2013).
10. A. Nagy, L. Černíková, K. Sedlák, bioRxiv 10.1101/2025.02.12.637829 (2025).
11. USDA, APHIS, Veterinary Services, "Epidemiologic and Other Analyses of HPAI-Affected Poultry Flocks: July 15, 2015 Report" (2015); https://www.aphis.usda.gov/media/document/301/file.
12. J. L. Greene, "Update on the Highly-Pathogenic Avian Influenza Outbreak of 2014-2015" (Congressional Research Service, 2015); https://www.congress.gov/crs-product/R44114.
13. S. E. Ramos, M. MacLachlan, A. Melton, "Impacts of the 2014-2015 Highly Pathogenic Avian Influenza Outbreak on the U.S. Poultry Sector" (USDA, Economic Research Service, LDPM-282-02, 2017); https://www.ers.usda.gov/publications/pub-details?pubid=86281.
14. B. Tuck, "Impact of poultry and egg production losses and poultry processing losses due to the avian influenza" (University of Minnesota Extension, 2015); https://extension.umn.edu/community-research/impact-poultry-and-egg-production-losses-and-poultry-processing-losses-due-avian.
15. *Nat. Biotechnol.* **43**, 461 (2025).

ACKNOWLEDGMENTS

The views expressed in this Policy Forum represent the opinions of the authors alone.

10.1126/science.adx8639

[1]Department of Environmental Health and Engineering, Bloomberg School of Public Health, Johns Hopkins University, Baltimore, MD, USA. [2]Food Forward LLC, Minneapolis, MN, USA. [3]Department of Molecular Microbiology and Immunology, Bloomberg School of Public Health, Johns Hopkins University, Baltimore, MD, USA. Email: esorrell@jhu.edu

NEUROSCIENCE

Sequenced evidence

Transcriptome analyses identify neural progenitor cells in the adult human hippocampus

Margaux Quiniou[1,2] and **Sebastian Jessberger**[1,2,3]

Challenging the long-held dogma that the generation of neurons ends in mammals early after birth, pioneering papers in the 1960s suggested that new neurons are born in the rodent brain throughout life. These adult-born neurons were detected in several regions, including the hippocampus, which is important for learning, memory, and mood control and is impaired in diseases such as Alzheimer's disease. From this emerged a decades-long controversy, with numerous studies providing evidence for—or against—the lifelong activity of neural progenitor cells (NPCs) as a source of newborn neurons in the human hippocampus. On page 58 of this issue, Dumitru *et al.* (*1*) report the use of single-nucleus RNA sequencing (snRNA-seq) and spatial transcriptomics to identify cells with transcriptional signatures of NPCs and newborn neurons in the human hippocampus from childhood to old age. Together with previous work (*2*–*4*), the findings indicate that neurogenesis persists throughout life in the human hippocampus.

The level of variability that is intrinsic to adult human neurogenesis remains largely unknown.

For decades, neurons in the mammalian brain, including the human brain, were considered to be exclusively generated during embryonic and early postnatal development—that is, the adult brain is not permissive for NPC proliferation and the subsequent birth of new neurons. Thus, from the very first studies that suggested that neurogenesis does not end with early postnatal development but rather continues throughout life in select mammalian brain areas (*5*), the findings were met with substantial skepticism (*6*). Over time, experimental accessibility to the mouse and rat brain provided overwhelming evidence for the presence of lifelong neurogenesis in the rodent hippocampus—for example, based on genetic lineage tracing, thymidine analog labeling, and eventually direct observation of dividing progenitors and their neuronally differentiating daughter cells by use of in vivo imaging of the living mouse hippocampus (intravital imaging) (*7*). Further, numerous studies showed that neurons born in the adult rodent hippocampus are important for certain aspects of cognition and hippocampus-dependent mood control (*7*). Yet the field remained divided on the question of whether neurogenesis also occurs in the human hippocampus throughout adulthood (*6*, *8*).

Initial evidence that neurogenesis persists in the human hippocampus was based on thymidine analog labeling (bromodeoxyuridine) (*3*). Sample sizes were limited, and the data obtained were associated with thymidine analog labeling concerns, which are now largely refuted. Other techniques to measure neurogenesis in human hippocampi were added by using, for example, antibodies that label cycling progenitor cells or newborn immature neurons. The use of such categorical markers assumed that neurogenesis in humans displays the well-characterized marker sets detected in rodent hippocampal neurogenesis. However, the evolutionary distance between rodent and human brains may account for species-specific differences. In addition, variable postmortem fixation times, unclear specificity of markers, and the possible effects of the developmental stage (such as childhood versus adulthood) of marker profiles complicated their interpretation. Whereas some groups found clear evidence of neurogenesis throughout life, others could not detect newborn neurons beyond childhood (*9*–*11*).

The advent of transcriptomic methods promised to settle the case. But it turned out to be not so simple: The expectation that grouping cells by gene expression pattern would result in clearly segregated clusters of cells that could be unambiguously labeled as NPCs or immature neurons was met with setbacks (*12*). This is not necessarily surprising; even in the rodent brain, many studies failed to identify clear clusters of NPCs because these cells show substantial transcriptomic similarity to glial cells, such as astrocytes. This is despite the irrefutable proof of the presence of neurogenic stem cells in rodents obtained, for example, with intravital imaging (*13*). Further, it is reasonable to speculate that transcriptomic signatures and/or temporal dynamics across the differentiation trajectory from NPCs to newborn neurons may be distinct between rodents and humans. For example, cortical neurons in the mouse brain need a few weeks to fully mature, whereas they need years (if not decades) to do so in the human cortex, indicating diverse developmental timescales across species (referred to as neoteny) (*14*). Thus, more sophisticated tools were needed to study human adult neurogenesis: Machine learning–based approaches were used to define signatures of human immature neurons from the fetal hippocampus, which ultimately helped to show their presence in the adult human hippocampus (*4*). Such signatures were also identifiable in previously published datasets that had been initially interpreted in the opposite direction—that is, taken as evidence for the "absence" of immature neurons (*4*). However, proliferating NPCs remained difficult to isolate because of their natural sparsity and the similarity of their RNA signatures to those of other cell types.

Dumitru *et al.* used several approaches to identify NPCs and immature neurons within the adult hippocampus. They sequenced more than 100,000 cells isolated postmortem from the hippocampal tissue of humans spanning ages 0 to 5 years, thus representing a childhood cohort. Using snRNA-seq, both NPCs and immature neurons were readily identified. Next, to detect the same cell types in adult brains, hippocampi from individuals ranging from 13 to 78 years of age similarly underwent snRNA-seq, although some samples were previously enriched for proliferating cells (a key feature of NPCs and performed by cell sorting for the Ki67 marker). A machine learning algorithm that had been trained on the childhood dataset then identified cells of the neurogenic lineage according to their defined RNA signatures. The authors

thus showed the presence of NPCs and immature neurons in the human hippocampus across the life span. They additionally performed spatial transcriptomics with single-cell resolution using adult hippocampal tissue and identified the whole neurogenic lineage in adult humans, from proliferating NPCs to differentiating newborn neurons.

Some individuals (5 out of the 14 adults >20 years of age) that were analyzed by Dumitru *et al.* did not show evidence of lifelong neurogenesis. However, it is unclear whether this is due to technical variability or is of biological relevance. The level of variability that is intrinsic to adult human neurogenesis remains largely unknown. Previous work in mouse models and in humans indicates that neurogenesis in the adult hippocampus is disrupted in certain brain diseases, including Alzheimer's disease. However, more data are required to establish whether neurogenesis is involved in the pathogenesis of human disease and represents a potential future therapeutic target (*7*, *11*, *15*). Reductions in costs and technical improvements are expected to enable higher-throughput transcriptomic analyses of human brain tissue, and the work by Dumitru *et al.* will help the field to establish positive (and negative exclusion) consensus RNA profiles to quantify NPCs and newborn neurons in human hippocampal samples. Furthermore, spatial multiplexed protein analyses with single-cell resolution and unbiased proteomics analyses of human brain samples will provide additional datasets in the future.

The study by Dumitru *et al.* adds an important puzzle piece to the understanding of neurogenesis in adults by using unbiased transcriptomics to identify NPCs in the adult human hippocampus, providing evidence that the whole neurogenic process, from dividing NPCs to newborn neurons, persists into old age in humans. The findings bring the field one step closer to finding the truth regarding the lifelong birth of new neurons in the human hippocampus and will enable future studies to investigate how lifelong neurogenesis in humans contributes to brain function and plasticity in health and disease. □

REFERENCES AND NOTES

1. I. Dumitru *et al.*, *Science* **389**, 58 (2025).
2. K. L. Spalding *et al.*, *Cell* **153**, 1219 (2013).
3. P. S. Eriksson *et al.*, *Nat. Med.* **4**, 1313 (1998).
4. Y. Zhou *et al.*, *Nature* **607**, 527 (2022).
5. J. Altman, G. D. Das, *J. Comp. Neurol.* **124**, 319 (1965).
6. G. Kempermann *et al.*, *Cell Stem Cell* **23**, 25 (2018).
7. A. Denoth-Lippuner, S. Jessberger, *Nat. Rev. Neurosci.* **22**, 223 (2021).
8. M. F. Paredes *et al.*, *Cell Stem Cell* **23**, 780 (2018).
9. S. F. Sorrells *et al.*, *Nature* **555**, 377 (2018).
10. E. P. Moreno-Jiménez *et al.*, *Nat. Med.* **25**, 554 (2019).
11. M. Boldrini *et al.*, *Cell Stem Cell* **22**, 589 (2018).
12. D. Franjic *et al.*, *Neuron* **110**, 452 (2022).
13. G. A. Pilz *et al.*, *Science* **359**, 658 (2018).
14. P. Vanderhaeghen, F. Polleux, *Nat. Rev. Neurosci.* **24**, 213 (2023).
15. J. Terreros-Roncal *et al.*, *Science* **374**, 1106 (2021).

ACKNOWLEDGMENTS

M.Q. acknowledges support from a Boehringer Ingelheim Fonds (BIF) PhD Fellowship.

10.1126/science.ady8328

[1]Laboratory of Neural Plasticity, Faculties of Medicine and Science, Brain Research Institute, University of Zurich, Zurich, Switzerland. [2]Neuroscience Center Zurich, University of Zurich and ETH Zurich, Zurich, Switzerland. [3]University Research Priority Program (URPP), Adaptive Brain Circuits in Development and Learning (AdaBD), University of Zurich, Zurich, Switzerland. Email: jessberger@hifo.uzh.ch

MOLECULAR BIOLOGY

A tighter grip on gene expression

A previously unknown cofactor function stabilizes transcription factor binding across the genome

Filip Nemčko[1] and **Alexander Stark**[1,2]

Cells rely on precise gene regulation to produce specific proteins exactly when needed. Central to this are enhancers and promoters, DNA sequences that dictate the location, timing, and intensity of gene expression. According to the established model, these sequences are interpreted by transcription factors bearing domains that bind to specific sites within enhancers and promoters. Once bound, transcription factors recruit cofactors that transmit regulatory signals to the machinery responsible for RNA synthesis. These cofactors remodel chromatin, mediate protein interactions, or perform other tasks that regulate gene expression (*1*). However, this model seems to have missed an important and conceptually distinct function. On page 43 of this issue, Bianchi *et al.* (*2*) report a previously unidentified regulator that acts as a molecular "grip" to stabilize transcription factors at DNA binding sites across the human genome.

Bianchi *et al.* undertook a systematic reanalysis of 35 large-scale mutagenesis screens, covering diverse biological processes. The authors found that two proteins, selenophosphate synthetase 1 (SEPHS1) and glutamine-rich protein 1 (QRICH1), displayed remarkably similar phenotypic responses across the 35 screens, despite their apparently unrelated cellular functions. SEPHS1 has a key role in selenium metabolism and redox homeostasis, whereas QRICH1 has been implicated in regulating transcription as part of the endoplasmic reticulum stress response (*3*, *4*), protein misfolding, and cell death. However, independent gene perturbations across 1178 cell lines from the cancer dependency map (DepMap) project (*5*) and human genetic data further reinforced the two proteins' connection. For example, mutations in SEPHS1 cause symptoms that closely resemble Ververi-Brady syndrome, a condition linked to mutations in QRICH1, which suggests that both proteins are involved in the same biological pathway (*6*, *7*). In agreement with these observations, Bianchi *et al.* determined (through immunoprecipitation from cell extracts) a physical association between QRICH1 and SEPHS1.

Investigating the cellular role of the QRICH1-SEPHS1 complex, Bianchi *et al.* identified a direct involvement in regulating gene transcription. Genetically engineered cultured cells lacking either SEPHS1 or QRICH1 displayed dysregulation of the same genes, demonstrating that the two proteins operate as a single regulatory unit. Chromatin immunoprecipitation followed by sequencing (ChIP-seq) revealed that the complex occupies more than 14,000 genomic sites, despite the absence of intrinsic DNA-binding capability. Instead, Bianchi *et al.* report that the complex is recruited to chromatin by zinc-finger (ZNF) transcription factors, leading the authors to name it Zincore (Zinc finger coregulator). This family of transcription factors uses zinc ions to stabilize their structure, enabling them to bind DNA. Bianchi *et al.* identified Zincore interactions with ZNF protein 91 (ZFP91), ZNF652, ZNF526, and PR/SET domain 15 (PRDM15), which together account for 12% of all Zincore binding sites. Among these, ZFP91 was shown to bind to the CTTTAAR motif, a conserved sequence found in promoters that previously had no identified binding partner—a so-called "orphan" motif (*8*).

Bianchi *et al.* further used cryo–electron microscopy to determine the structure of the complex bound to ZFP91 and its DNA-binding motif. The authors discovered a distinctive regulatory mechanism in which Zincore "grips" and stabilizes ZNF proteins on to DNA, enhancing tran-

scription factor binding. The structure depicts Zincore as a tetrameric assembly—a dimer of SEPHS1 molecules bound to two QRICH1 monomers. Within this assembly, SEPHS1 directly anchors to the ZNFs of ZFP91, which are themselves wrapped around the DNA. SEPHS1 uses an "arginine-clamp" to secure ZFP91 to DNA by constraining its ZNFs in their DNA-bound conformation. Mutating clamp residues arginine at position 371 (R371) or R330 diminished the DNA binding and transcriptional activity of ZFP91. Notably, mutations in R371 are also found in patients with a neurodevelopmental syndrome, implicating a loss of Zincore's grip in disease. The "stabilizing grip" mechanism is a newly identified mode of cofactor function and transcriptional regulation. Rather than directly modulating gene expression through activating or repressing cues, Zincore stabilizes the binding of transcription factors to target DNA sites. This suggests that many DNA binding domains might not be sufficient to stably interact with DNA in an autonomous fashion, as assumed by the established model. Indeed, in the absence of Zincore, ZFP91 binding to chromatin was markedly reduced in cultured cells, confirming that stabilization by Zincore translates to more persistent DNA occupancy by the transcription factor.

Structural analysis revealed that Zincore binds ZFP91 in a protein sequence–independent manner, primarily targeting the backbone of the ZNF domains rather than specific amino acid side chains. Computational simulations corroborated this observation, suggesting that the arginine clamp can dock onto diverse ZNF domains that bear a conserved structure involving two cysteine and two histidine residues (C2H2), with each C2H2 ZNF domain contacted by SEPHS1. Given that nearly half of all human transcription factors are C2H2 ZNF transcription factors (*9*), and that approximately 88% of its genomic binding sites remain to be accounted for, Zincore appears to have a globally important function as a cofactor for many C2H2 ZNF transcription factors.

The findings of Bianchi *et al*. raise the question of whether other transcription factors partner with Zincore and the rules that govern these interactions. Another question is whether Zincore only regulates transcription factors with activating functions or if it is also required for repressors and insulators, potentially fine-tuning their distinct regulatory roles. Many ZNF transcription factors—for example, repressors such as Krüppel-associated box (KRAB) factors and insulators such as CCCTC-binding factor (CTCF)—have functions distinct from transcriptional activation. Furthermore, although QRICH1 is associated with gene activation (*3*), the depletion of either Zincore subunit leads to both up- and down-regulation of gene expression. And despite its widespread expression and requirement for mouse embryonic development, Zincore is not broadly essential in all cells, and human syndromes associated with Zincore dysfunction predominantly manifest with neuronal specificity. More broadly, why has evolution equipped the ZNF transcription factor family with a dedicated stabilizer? There could be molecular grips or analogous stabilizing mechanisms for other transcription factor families yet to be discovered. □

REFERENCES AND NOTES

1. F. Reiter, S. Wienerroither, A. Stark, *Curr. Opin. Genet. Dev.* **43**, 73 (2017).
2. D. Bianchi *et al*., *Science* **389**, 43 (2025).
3. K. You *et al*., *Science* **371**, eabb6896 (2021).
4. F. Oudouhou *et al*., *Biochemistry* **56**, 2261 (2017).
5. A. Tsherniak *et al*., *Cell* **170**, 564 (2017).
6. A. Ververi *et al*., *Clin. Genet.* **93**, 286 (2018).
7. S. V. Mullegama *et al*., *Am. J. Hum. Genet.* **111**, 778 (2024).
8. X. Xie *et al*., *Nature* **434**, 338 (2005).
9. S. A. Lambert *et al*., *Cell* **172**, 650 (2018).

ACKNOWLEDGMENTS

A.S. acknowledges support from Boehringer Ingelheim GmbH, the Austrian Research Promotion Agency, and the Austrian Science Fund.

10.1126/science.adz2519

[1]Research Institute of Molecular Pathology (IMP), Vienna BioCenter (VBC), Vienna, Austria.
[2]Medical University of Vienna, Vienna BioCenter (VBC), Vienna, Austria. Email: stark@starklab.org

STRUCTURAL BIOLOGY

Expanding the reach of molecular glue degraders

An epitope-centric screening approach widens the neosubstrate landscape for targeted protein degradation

Marcus D. Hartmann[1,2]

Molecular glue degraders (MGDs) are an emerging modality for targeting proteins intractable by classical small-molecule drugs, such as transcription factors relevant in cancer. They catalytically deplete unwanted proteins by reprogramming E3 ubiquitin ligases—remodeling their substrate recognition interfaces to redirect them from endogenous substrates to MGD-induced "neosubstrates," which are then tagged for proteasomal degradation (*1*, *2*). Despite substantial progress, MGD discovery remains heavily reliant on empirical screening, with most efforts focused on proteins that share a specific β-hairpin motif that is recognized by the ubiquitin ligase substrate receptor cereblon (CRBN) in the presence of bound MGD (*2*, *3*). On page 45 of this issue, Petzold *et al.* report the identification and validation of degrons beyond this canonical β-hairpin that can be exploited by MGDs (*4*). Several of the identified targets are of therapeutic interest, and the findings hold promise for enabling a more rational and targeted approach for MGD development.

MGDs are typically derived from thalidomide and bind to CRBN's C-terminal thalidomide-binding domain, also known as the CULT domain (*5*). This domain, in concert with the N-terminal LON domain, mediates substrate and neosubstrate recognition by binding natural degron motifs or small-molecule ligands, such as MGDs (*6*–*8*). The shared binding moiety of known natural degrons and MGDs is a cyclic imide ring, accommodated in a tryptophan-lined pocket within the CULT domain. In known natural degrons, this moiety is positioned at the C terminus of the substrate protein, with the preceding residues adopting a helical conformation, poised to form backbone interactions with three CULT hotspot residues: asparagine at position 351 (Asn^{351}), histidine at position 357 (His^{357}), and tryptophan at position 400 (Trp^{400}) (*8*). In canonical neosubstrate recruitment, these interactions are mimicked by the MGD protruding from the same binding pocket, in cooperation with a β-hairpin motif in the neosubstrate that engages the MGD-modulated CULT surface. This β-hairpin, known as the G-loop, is defined by a conserved glycine in a fixed position, which enables the same hydrogen-bonding pattern with the three CULT hotspot residues as in natural degrons (*9*). MGDs are chemically tailored to complement specific G-loop properties on target neosubstrates. However, the major limitation of this approach lies in the requirement for an accessible β-hairpin G-loop motif and in the difficulty of achieving selectivity between multiple potential targets with similar degrons.

Petzold *et al.* combined computational mining with experimental screening and validation to systematically expand the CRBN neosubstrate landscape, broadening their scope across three stages. They began by searching experimental and pre-

Achieving targeted protein degradation

MGDs bind to and remodel the substrate-recognition interface of the ubiquitin ligase substrate receptor CRBN to direct it from endogenous substrates to specific "neosubstrates." On binding to CRBN, the substrate is tagged with a ubiquitin chain and subsequently degraded by the proteasome, enabling MGDs to achieve targeted protein degradation.

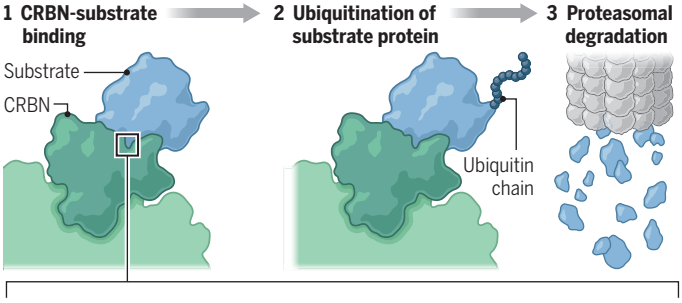

Natural substrate binding
Known natural CRBN substrates have an imide ring at their C terminus, which enters a pocket in CRBN. The preceding residues adopt a helical conformation that interacts with CRBN hotspot residues Asn^{351}, His^{357}, and Trp^{400}.

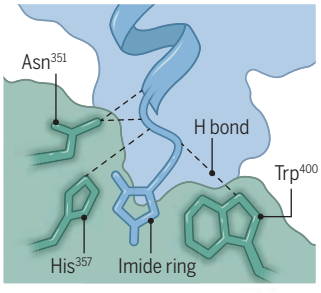

Canonical β-hairpin G-loop
The cyclic imide ring of the MGD enters the binding pocket; the rest of the MGD protrudes, and, together with a β-hairpin motif on the neosubstrate, it mimics the binding of the natural substrate to the hotspot residues.

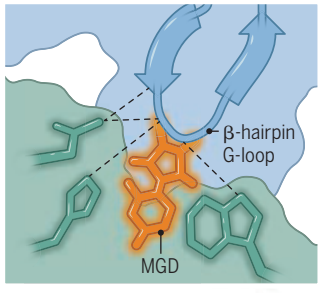

Helical G-loop
Neosubstrates that lack the β-hairpin motif but have a minimal G-loop at the C terminus of an α helix can work with an MGD to form the canonical interactions with the hotspot residues.

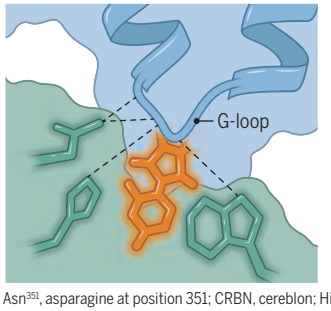

Surface mimicry
Neosubstrates that lack a G-loop motif but contain an epitope that mimics the topology and electrostatics of the canonical G-loop can bind to CRBN through the MGD and hotspot residues.

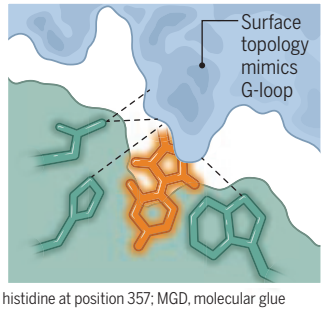

Asn^{351}, asparagine at position 351; CRBN, cereblon; His^{357}, histidine at position 357; MGD, molecular glue degrader; Trp^{400}, tryptophan at position 400.

GRAPHIC: A. FISHER/*SCIENCE*

dicted protein structures for β-hairpin G-loop motifs resembling those in known neosubstrates. This initial screen yielded more than 1400 candidate proteins, many of which were validated as "glueable"—i.e., recruitable to CRBN by MGD—and degradable in MGD assays. These included not only established neosubstrates, such as C_2H_2 zinc finger transcription factors (*3*), but also previously unrecognized β-hairpin G-loop targets such as NEK7—a protein kinase implicated in autoinflammatory diseases (*10*). A crystal structure revealed that the NEK7 G-loop is recognized in a similar fashion to that of the known neosubstrate casein kinase 1α (CK1α) yet induces a partially open CRBN conformation. This challenges the prevailing assumption that a closed conformation—where the LON and CULT domains are docked—is required for productive neosubstrate engagement and ubiquitination (*6*).

Next, to discover G-loop motifs beyond the β-hairpin structure, Petzold *et al.* rescreened their structure database with a minimal degron query covering only the tip of the canonical G-loop. This search identified about 200 additional proteins with a minimal G-loop motif embedded at the C terminus of an α helix. Among these was the FKBP-rapamycin binding (FRB) domain of the mammalian target of rapamycin (mTOR) protein (*11*), which was subsequently validated as a glueable neosubstrate in proximity-based assays. A crystal structure showed that this helical G-loop binds CRBN in a mode closely resembling that of β-hairpin G-loops while also reproducing both the helical geometry and the characteristic hydrogen-bonding network with hotspot residues Asn^{351}, His^{357}, and Trp^{400} seen in natural degrons (*9*).

In the last stage of the study, Petzold *et al.* moved beyond recognizable G-loop degrons entirely. Instead, they used surface-matching algorithms to discover degron-like epitopes that mimic the topology and electrostatics of canonical G-loops, regardless of sequence or secondary structure. Applying this approach to a panel of therapeutically relevant proteins lacking G-loop motifs, they identified a candidate epitope within an SRC homology 3 (SH3) domain of VAV1—a guanine-nucleotide exchange factor implicated in autoimmune and inflammatory diseases (*12*). MGD-inducible CRBN binding and degradation were experimentally validated, and a crystal structure revealed that the epitope engages CRBN through hydrogen bonds to the three CULT hotspot residues (see the figure). Notably, unlike classical G-loops, two of these interactions are mediated by side chains rather than backbone atoms—demonstrating a previously unknown mode of degron mimicry based entirely on surface complementarity.

With these manifold findings, the study of Petzold *et al.* substantially expands the understanding of CRBN substrate recruitment. The discovery of helical degrons demonstrates that CRBN can accommodate a broader range of structural motifs than previously assumed, highlighting how MGD-recruited G-loop neosubstrates generally mimic natural substrate binding (*9*). Notably, the observation that surface complementarity—rather than conserved sequence or structure—is sufficient to mediate neosubstrate engagement might enable the design of MGDs with true epitope-level specificity, potentially overcoming long-standing challenges in substrate selectivity among targets that share a common degron motif (*13*). Moreover, as observed for canonical G-loop neosubstrates and further substantiated by Petzold *et al.*, CRBN binding can involve additional surface patches on both the CULT and LON domains (*14*). Together with the finding that productive binding does not require a fully closed CRBN conformation—as shown for NEK7—this suggests that MGDs could exploit the intrinsic flexibility of the LON-CULT interface to enable cooperatively stabilized modes of neosubstrate engagement. It will be exciting to see which of the study's conceptual advances translate into future MGD development and how they might enable the rational and selective targeting of previously inaccessible proteins. □

REFERENCES AND NOTES

1. S. L. Schreiber, *Cell Chem. Biol.* **31**, 1050 (2024).
2. H. Yoon, J. C. Rutter, Y.-D. Li, B. L. Ebert, *J. Clin. Invest.* **134**, e175265 (2024).
3. Q. L. Sievers *et al.*, *Science* **362**, eaat0572 (2018).
4. G. Petzold *et al.*, *Science* **389**, eadt6736 (2025).
5. A. N. Lupas, H. Zhu, M. Korycinski, *PLOS Comput. Biol.* **11**, e1004023 (2015).
6. E. R. Watson *et al.*, *Science* **378**, 549 (2022).
7. S. Ichikawa *et al.*, *Nature* **610**, 775 (2022).
8. C. Heim *et al.*, *Biochem. Biophys. Res. Commun.* **637**, 66 (2022).
9. C. Heim *et al.*, *Biochem. Biophys. Res. Commun.* **646**, 30 (2023).
10. Y. He, M. Y. Zeng, D. Yang, B. Motro, G. Núñez, *Nature* **530**, 354 (2016).
11. J. Choi, J. Chen, S. L. Schreiber, J. Clardy, *Science* **273**, 239 (1996).
12. M. F. Neurath, L. J. Berg, *Trends Immunol.* **45**, 580 (2024).
13. A. Mullard, *Nat. Rev. Drug Discov.* **23**, 799 (2024).
14. V. Oleinikovas *et al.*, *Annu. Rev. Pharmacol. Toxicol.* **64**, 291 (2024).

10.1126/science.ady4446

[1]Department of Protein Evolution, Max Planck Institute for Biology, Tübingen, Germany. [2]Interfaculty Institute of Biochemistry, University of Tübingen, Tübingen, Germany. Email: marcus.hartmann@tuebingen.mpg.de

QUANTUM COMPUTING

Shrinking quantum randomization

Randomness in quantum computing is realized in a few layers of quantum gates

Naoki Yamamoto and **Kaito Wada**

When rolling a dice, each of the six faces appears randomly with equal probability. This simple phenomenon of randomness plays a key role in many technologies such as cryptography (*1*), complex physical simulations (*2*), and magnetic resonance imaging (*3*). In classical computer science, randomized algorithms can perform more efficient computation with less memory use compared to algorithms that follow deterministic paths (*4*). Randomness also has an important technological role in quantum computing, but generating this requires a large number of operations. On page 92 of this issue, Schuster *et al.* (*5*) report a quantum circuit (an abstract sequence of actions for computation) that achieves randomness with an exponentially reduced number of operations. This lowers the engineering barrier for achieving fast and efficient quantum computing in various applications.

In the absence of noise, the evolution of states in quantum mechanics is mathematically represented by a unitary matrix (a complex square matrix). The size of this matrix increases in powers of two (2^n by 2^n; n is number) with the number of qubits—quantum bits that are analogous to bits (0 or 1) in classical computing. For current quantum devices that function with more than 100 qubits, the matrix becomes enormously large (*6*). Although classical computers cannot efficiently process such a large unitary matrix, quantum computers can. In addition, distribution of information in a quantum system can occur extremely fast because of the many degrees of freedom, which adds another level of complexity—and power—to quantum computing (*7*).

...transforming classical randomized algorithms into quantum systems opens new and efficient algorithms for quantum computing.

As in classical computing, randomized algorithms are useful in various applications such as quantum cryptography (*8*) and quantum simulation (*9*). A large random circuit can execute a complex sequence of tasks, which a classical computer cannot efficiently solve (*10*). A random quantum circuit can choose an arbitrarily unitary matrix—which acts as a collection of logical gates—independently of their distribution within a quantum system. However, it takes an exponentially large number of operations to construct a fully random quantum circuit. Alternatively, the concept of approximate random quantum circuit applies a sequence of quantum gates (unitary matrix) randomly without requiring an exponential number of operations (*11*). Conventional belief is that the number of quantum gates (depth of a circuit) in an approximate random circuit generally increases linearly with the number of qubits. Although this approach is effective for computing a small number of qubits, a deep circuit with many layers of sequence is needed when the qubit number increases.

Schuster *et al.* built approximate random quantum circuits with a reduced circuit depth of a logarithm of the number of qubits. This not only exponentially decreases the size of an approximate random circuit but also brings down the complexity of randomized quantum information processing. The authors patched individual operations in a so-called brick wall structure. Each "brick" represents a small random circuit. Stacking two layers of bricks closely resembles a fully random circuit at a substantially shallow depth. Unitary matrices corresponding to this shallow circuit became indistinguishable, which often requires many layers of quantum gates using existing approaches. Schuster *et al.* demonstrated the generation of pseudo-random unitary matrices for a broad range of circuit geometry with a depth equal to a polynomial in a logarithm of n qubits.

The method of Schuster *et al.* can potentially improve the efficiency of almost all quantum technologies that rely on random quantum circuits. For example, similar to how random measurements improved magnetic resonance imaging, classical shadow (*12*)—a protocol for estimating a quantum state without a full description of the state—is now possible with the shallow random quantum circuit. This technique could also be used to extract fundamental quantum physical properties such as phase of matter and strongly correlated phenomena. Beyond technology applications, transforming classical randomized algorithms into quantum systems opens new and efficient algorithms for quantum computing. Rapid randomization of many-qubit quantum systems, which is a key requirement for a large-scale randomized quantum algorithm, is achieved by the shallow random quantum circuit.

The findings of Schuster *et al.* offer profound perspective in quantum physics. What is the fundamental limit on physically observable properties? Perhaps, some properties are imperceptible because, as suggested by Schuster *et al.*, inherent random circuits within the nature of physical phenomena hide quantum information exponentially fast. This calls to mind the Heisenberg uncertainty principle, which fundamentally limits the amount of information that can be obtained in quantum mechanics. Techniques such as "squeezing" have been developed to manipulate the Heisenberg uncertainty principle (*13*) by changing the distribution of uncertainty within a system (reducing uncertainty in one quantum property while increasing the uncertainty in another). Although this can increase the precision of a measurement, it cannot break the fundamental limits of quantum mechanics. Would it be ever possible to extract the hidden quantum information? A time-reversal quantum operation that can rewind a system to its previous state (*14*) is one such candidate, and a shallow random circuit could contribute to demonstrating this. □

REFERENCES AND NOTES

1. M. Blum, S. Micali, *SIAM J. Comput.* **13**, 850 (1984).
2. K. Binder, D. W. Heermann, *Monte Carlo Simulation in Statistical Physics* (Springer, 2010).
3. M. Lustig, D. Donoho, J. M. Pauly, *Magn. Reson. Med.* **58**, 1182 (2007).
4. R. Motwani, P. Raghavan, *Randomized Algorithms* (Cambridge Univ. Press, 1995).
5. T. Schuster, J. Haferkamp, H.-Y. Huang, *Science* **389**, 92 (2025).
6. A. Miessen, D. J. Egger, I. Tavernelli, G. Mazzola, *PRX Quantum* **5**, 040320 (2024).
7. Z. Li *et al.*, *Science* **380**, 1381 (2023).
8. N. Gisin, G. Ribordy, W. Tittel, H. Zbinden, *Rev. Mod. Phys.* **74**, 145 (2002).
9. L. K. Joshi *et al.*, *Phys. Rev. X* **12**, 011018 (2022).
10. F. Arute *et al.*, *Nature* **574**, 505 (2019).
11. J. Emerson, Y. S. Weinstein, M. Saraceno, S. Lloyd, D. G. Cory, *Science* **302**, 2098 (2003).
12. H.-Y. Huang, R. Kueng, J. Preskill, *Nat. Phys.* **16**, 1050 (2020).
13. M. Fox, *Quantum Optics: An Introduction* (Oxford Univ. Press, 2006).
14. M. Gärttner *et al.*, *Nat. Phys.* **13**, 781 (2017).

10.1126/science.adz0147

Department of Applied Physics and Physico-Informatics, Keio University, Yokohama, Japan.
Email: yamamoto@appi.keio.ac.jp

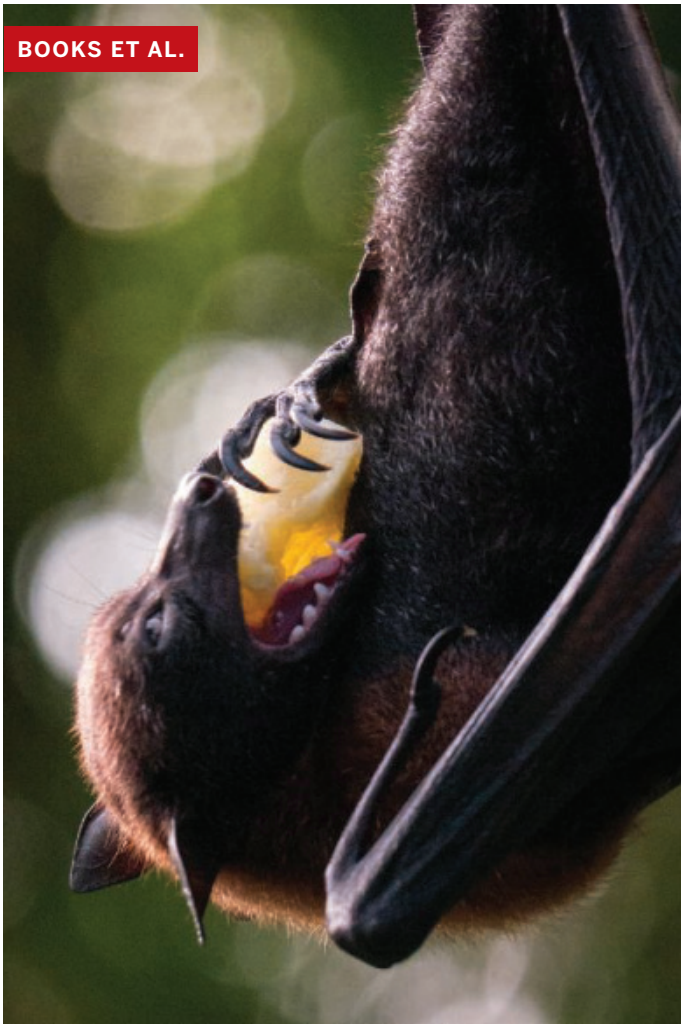

PHOTO: METTE SIG VIA SHUTTERSTOCK

Studying freely moving bats has yielded new findings about the brain.

NEUROSCIENCE

The brain in motion

Behaviors are features, not bugs, in our quest to understand neural processes

Alison M. Bell

Nachum Ulanovsky
MIT Press, 2025.
302 pp.

NATURAL NEUROSCIENCE | From flamboyant courtship displays to massive feats of migration, examples of captivating animal behavior are easy to find. It is therefore sobering to realize that, until recently, much of our understanding of how the brain generates behavior has been limited to studies of head-fixed, immobilized, and often anesthetized animals. This limitation explains why it has been easy for ecological and evolutionary researchers like me to avoid reading the neuroscience literature, and it illustrates the substantial divide between proximate (how?) and ultimate (why?) approaches to the study of animal behavior.

In his new book *Natural Neuroscience*, Nachum Ulanovsky argues that this is all about to change. We are in the midst of a major shift in the way that the neurobiology of behavior can be studied, he maintains, thanks to technologies that are now allowing neural activity to be measured and manipulated in freely moving, freely behaving animals. But according to Ulanovsky, it is not just technological limitations that have thus far rendered neuroscience paradigms so unnatural—it is also a Cartesian legacy of reductionism that has deep conceptual and philosophical roots.

The tradition of viewing brains as machinelike and a strong emphasis on experimental control to reduce "noise" still dominate the field. Ulanovsky makes the case that relying exclusively on a reductionist approach poses problems and that allowing animals to move and participate during experimentation is worth the trouble.

Drawing on his own studies of navigation in bats, a paradigmatically mysterious critter (*1*), Ulanovsky provides example after example of how incorporating more natural behavior into studies reveals new insights. When he and his colleagues allowed bats to move in space, for example, they found cells that specified space and direction. When they allowed bats to interact with other bats, they found social place cells in the hippocampus that represented the position of other individuals. "In other words, every time we made a step toward more naturalistic behaviors, we discovered surprising new findings about the brain."

So just how "natural" does "natural neuroscience" have to be? Throughout the book, Ulanovsky is conciliatory, arguing that adding any element of nature, even if only incremental, is an improvement.

The prevailing reductionist approach in sensory neuroscience aims to control and/or eliminate behavior and then passively present subjects with sensory stimuli. This has been necessary for technical reasons but has also been justified on the grounds that uncontrolled behavior and movement are sources of noise. But in chapter 5—my favorite of the book—Ulanovsky writes that "almost all sensory information from the world passes through the behavior step (i.e., active-sensing behaviors) to reach the brain. Natural behaviors are a fundamental aspect of these sensory-acquisition systems…we must allow the subject to do what these exquisite systems have evolved for—to acquire sensory information actively."

Part of why this message resonated with me is that scientists working at higher levels of biological organization are also starting to appreciate that active behaviors—such as habitat selection, migration, and niche construction—can affect ecological and evolutionary processes by influencing the environments and hence the selection pressures that animals experience. It seems we are all independently converging on the idea that behavior is important for processes at both lower and higher levels of organization.

That being said, the ecologist in me wanted the book to unpack the notion of "natural" a little more. How do we practice "natural neuroscience" when nature is, itself, variable and changing—now more so than ever? And how have neural mechanisms evolved to cope with environments that vary in space and time? I was also surprised to see that the book did not mention genomic technologies, such as single-cell and spatial transcriptomics, that are also enabling more natural neuroscientific methods by providing a common currency for comparing across cell types, behavioral states, brain regions, and species—thereby avoiding some of the problems of homology that have plagued comparative neuroscience in the past.

At the end of the day, this book is an invitation for rapprochement between mechanistic and evolutionary approaches to the study of animal behavior. Ideally, it will not only inspire neuroscientists to make their studies more "natural" but also encourage behavioral ecologists to tackle the neural basis of fascinating behaviors. □

REFERENCES AND NOTES

1. T. Nagel, *Philos. Rev.* **83**, 435 (1974).

10.1126/science.adz0453

The reviewer is at the Department of Evolution, Ecology, and Behavior and the Carl R. Woese Institute for Genomic Biology, University of Illinois, Urbana-Champaign, Urbana, IL, USA. Email: alisonmb@illinois.edu

BIOLOGY

Rejecting genetic essentialism

Scientists must dispel the myths about human difference that lead to bias and systemic oppression, argues a geneticist **Santiago J. Molina**

Shoumita Dasgupta
University of California Press, 2025. 286 pp.

WHERE BIOLOGY ENDS AND BIAS BEGINS | Ongoing policy decisions and discourse from US President Donald Trump and his administration suggest the full-fledged return of long-discredited eugenicist ideas about how to optimize the human race (*1*). Such a return relies on the crystallization of essentialist views of various axes of human difference, including gender, race, sexuality, and disability. Those who express these views frequently distort and invent scientific claims to naturalize essentialist views, which, in turn, resonate with cultural movements that aim to reify traditional gender roles and further divide racial and ethnic groups. Although the return of this unscientific approach to human difference is perhaps unsurprising in a society that was itself founded on genocide and slavery, the persistence of bigotry and hatred represents a major challenge for contemporary cognitive and social scientists.

...the persistence of bigotry and hatred represents a major challenge for contemporary cognitive and social scientists.

Geneticist Shoumita Dasgupta's thorough explanation of the science of psychological bias and human genetics in *Where Biology Ends and Bias Begins* offers a starting point for an updated overview of research in these fields that sheds light on the history of essentialism and what to do about it. The key strength of this important book is that it incorporates an account of the science of human difference writ large, including not only race and ethnicity but also disability, gender, reproduction, and sexuality. It also provides an organized overview of the history and state of this research to intentionally dispel any confusion about what is and is not "biologically real."

In the first part of the book, Dasgupta illustrates the scientific and political significance of different bodies of knowledge around human difference with concrete examples. In the second part, she adds additional historical context to situate this research in a broader conceptual frame. In parts three and four, Dasgupta presents issues of contemporary relevance for debates around genetic essentialism, including inequalities in access to genetic medicine, race-based medicine, and genome editing. Throughout the book, she pushes the reader to consider what actions scientists and physicians can take to effectively counter the language of essentialism and contribute to a more equitable society.

In part because of the book's ambitious scope, the interconnecting narrative between the chapters is sometimes lost. This criticism should not dissuade potential readers from picking up the book but does leave open questions. For example, while the book urges readers to consider how the science of genomics and human genetics dispels genetic essentialist thinking, Dasgupta's driving concerns about the reproduction of implicit and explicit bias fall to the wayside. What is the relationship between the ideology of essentialism and implicit bias, a reader might wonder, and how can the science of genetics and genomics be more effectively communicated to audiences outside of the classroom that have little to no interest in the perspectives of experts? If bias is indeed the culprit behind the promulgation of harmful policies that target marginalized communities, medical racism and inequity, and conservative infringement on women's bodily autonomy, how does an updated overview of scientific research address such biases?

As Dasgupta recognizes, providing new information does not effectively change individuals' biases. To combat this impasse, the final chapter of the book and the afterword provide helpful pedagogical and conversational strategies to better communicate research findings. Here, she asks the reader to consider two questions to counter the misuse of scientific evidence and the spread of bias: In what spheres and spaces do I have privilege or influence, and how can I leverage my privilege and influence for good? These prompts serve as valuable starting points for scientists to develop a more reflexive and proactive approach to antiracism and should be foundational for students in the life sciences.

The narrative and political limitations of the book are in part because it does not sufficiently name the ideological and institutional movements that give heft to bias: patriarchy, racial capitalism, settler-colonialism, and white supremacy. Although Dasgupta seems keenly aware of the importance of addressing such systemic forces, holding sharply that "racism, sexism, homophobia, transphobia, disability bias, and many other forms of discrimination exist explicitly in society, and in these cases, the hierarchies of power are not a bug of the system but a feature for those who create them," these forces rarely appear in the text. In her opinion, wrongly held beliefs must be first debunked before addressing structural modes of oppression. Perhaps such a strategy would have been effective if the book incorporated more lessons from the social sciences, which were largely and disappointingly absent. Readers seeking to include social scientific perspectives on this topic might also consult Troy Duster's *Backdoor to Eugenics*, Anne Fausto-Sterling's *Sex/Gender: Biology in a Social World*, and Dorothy Roberts's *Fatal Invention*. □

REFERENCES AND NOTES

1. G. L. Wojcik, *Nature* **641**, 37 (2025).

10.1126/science.adu5497

The reviewer is at the Department of Sociology, Northwestern University, Evanston, IL, USA. Email: santiagojmolina@northwestern.edu

PRIZE ESSAY

MICROBIOME

The vaccine we all wear

Skin microbiota can be engineered into topical vaccines

Djenet Bousbaine

When a pathogen infects a host, a cascade of defense mechanisms is unleashed, with the goal of clearing the pathogen. Many foundational principles in immunology are derived from the study of these responses. By contrast, immunity to our microbiome is more enigmatic. This peaceful community of microbes colonizes a human body to provide essential support to its host. Despite such benefits, the immune system responds strongly to microbial colonists. Why would our immune system dedicate a large fraction of its resources to beneficial microbes?

Research over the past 15 years has taught us that, akin to the responses to pathogens, immunity to commensal microbes can be similarly antigen specific (*1*, *2*) and involve commensal-specific cells that circulate systemically (*3*). Furthermore, the identity of the microbe defines the tone and response elicited (*4*). However, in sharp contrast to the immunity to pathogens, these responses occur through an intact barrier and without inflammation. Why would the immune system create such sophisticated responses in the absence of a threat? My colleagues and I hypothesized that the host monitors and builds immunity against commensals preemptively to protect against inevitable exposure through a barrier breach, such as a cut on the skin.

To approach this question (*5*), we focused on the immune response elicited by commensal skin microbes, in particular the prevalent bacteria *Staphylococcus epidermidis*. Colonization with *S. epidermidis* generates antigen-specific T cells that participate in wound healing (*6*). By contrast, very little is known about the B cell response to skin microbes. In light of the important role that B cells play in skin pathologies (*7*) and the impact of the microbiota on antibody responses at other anatomical locations (*8*), we wondered about the role of skin microbiota in B cell responses.

Two observations suggested that skin commensals could induce B cell responses: the presence of microbes coated with antibodies in human skin swabs (*9*) and the discovery that B cells reside in healthy skin and not just in diseased states, as previously believed (*10*). We began by testing whether colonization of mice with *S. epidermidis* led to an antibody response. We applied bacterial cultures to the heads of mice by gently rubbing their skin with a swab. These colonized mice had impressive systemic B cell responses and harbored high titers of class-switched circulating anti–*S. epidermidis* antibodies. We also observed similarly high antibody titers against native skin commensal microbes in nonhuman primates and humans, which suggested that this response is conserved (see the figure).

Next, we sought to identify the molecular targets of the antibody response. Our collaborators in the Belkaid laboratory demonstrated that antigen sampling was mediated by Langerhans cells through intact skin (*11*). However, like most commensal-derived antigens, the identity of *S. epidermidis* antigens remained unknown. We used a series of cell surface mutants combined with bioinformatics to identify the cell wall–attached accumulation-associated protein (Aap) as a predominant antigen. The main epitope in Aap, like some T cell antigens identified in the intestine (*12*, *13*), is highly conserved and present across Gram-positive bacteria. This finding suggests that B cells in the skin, like intestinal T cells, may recognize broadly shared commensal antigens. Such a mechanism could expand the range of commensals that the immune system can recognize at once.

Can this response be harnessed for therapeutic benefit? If immunity to commensals is indeed induced preemptively, one might imagine redirecting this response against pathogens as a new form of vaccination. We previously showed that such an approach could yield potent antitumor responses by redirecting the T cell response elicited by *S. epidermidis* (*3*). Because Aap is the dominant B cell antigen, we reasoned that it must already contain the optimal structure, localization, and accessibility for B cell vaccination. Thus, we inserted a new antigen directly into Aap. Notably, colonization with *S. epidermidis* expressing a fusion of Aap with a nontoxic fragment of tetanus toxin generated potent serum antibody responses that protected against a lethal challenge with the toxin, in line with a model in which the immune system responds preemptively against the microbiome (see the figure).

We wondered whether this strategy would also be compatible with the complex antigens found in modern vaccines. Although bacterial antigens, such as tetanus toxin fragment, can be expressed in *S. epidermidis*, viral or tumor immunogens are generally difficult to produce in bacteria. To circumvent this challenge, we reasoned that instead of producing the antigens in bacteria, immunogens could be purified from another source (e.g., mammalian cell culture) and attached directly to the surface of *S. epidermidis*. To achieve this goal,

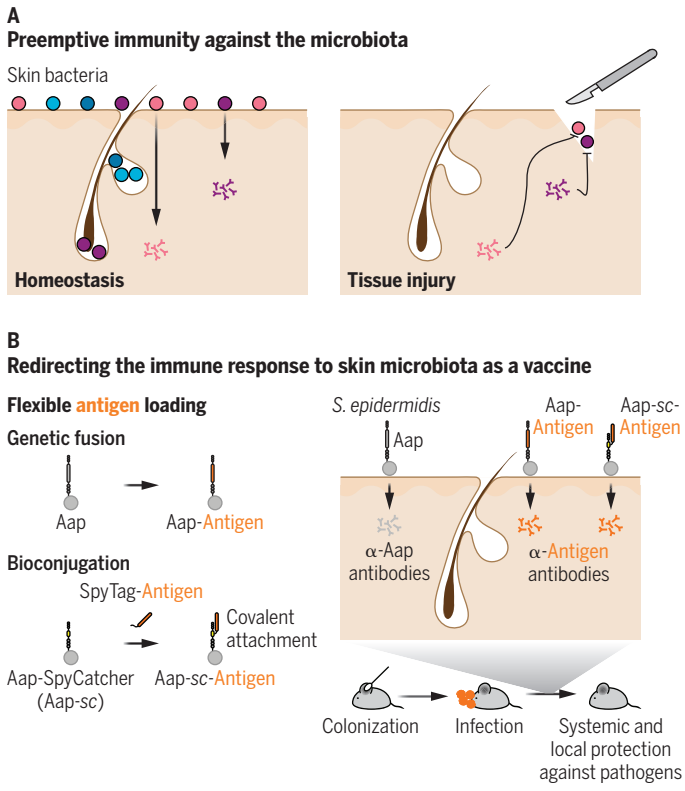

Preemptive immunity against the microbiota provides a previously unrealized route of vaccination. (A) Physiologic colonization with skin commensal microbes, such as *Staphylococcus epidermidis*, leads to a preemptive systemic and local B cell response poised to protect the host in case of barrier breach—e.g., after a skin cut. **(B)** Accumulation-associated protein (Aap) is the predominant antigen found on the surface of *S. epidermidis*. The response to this antigen can be redirected by fusing an antigen, such as a nontoxic fragment of the tetanus toxin, to Aap. For antigens that are more complex and difficult to express in bacteria, the immunogen can be purified (e.g., from mammalian cells) and covalently conjugated to *S. epidermidis* using the SpyCatcher system. Topical application of such engineered strains of *S. epidermidis* leads to robust systemic and local protection.

GRAPHIC: ADAPTED FROM (5) AND ERIN CHEN BY A. MASTIN/*SCIENCE*

we equipped *S. epidermidis* with a variant of Aap fused to SpyCatcher (*14*); this enabled any exogenously purified SpyTagged protein to be covalently attached to the surface of *S. epidermidis* without affecting its viability or colonization efficiency. Mice were then colonized with *S. epidermidis* conjugated to a purified tetanus toxin fragment, which delivered a "pulse" of antigen rather than sustained production from the bacteria. These mice were protected against a lethal challenge with tetanus toxin, even after the number of colonizations was markedly reduced. Perhaps even more notable, this strategy generated local immunity in their pulmonary mucosa, which is challenging to induce with traditional immunization but is crucial for protection against respiratory pathogens. Thus, by simply applying engineered microbes on the skin, we showed that commensal-specific B cell responses could be redirected into powerful systemic and mucosal immunization. Despite living peacefully with our microbiome, our immune system is constantly monitoring commensals. Understanding and harnessing this immunity opens the door to the development of needle-free vaccination strategies.

Pathogens have taught us essential lessons about immunology, yet much remains to be discovered. Our work shows how noninflammatory interactions between commensal microbes and the immune system can have a profound effect on systemic and local immunity. As elegantly posited by Janeway, progress in immunology "will require a rediscovery of microbiology by immunologists" [(*15*), p. 4486]. Perhaps the answers lie within the study of the lion's share of immune responses, which are not directed against pathogens but rather against a universe of commensal microbiota. □

REFERENCES AND NOTES

1. E. Ansaldo *et al.*, *Science* **364**, 1179 (2019).
2. J. N. Chai *et al.*, *Sci. Immunol.* **2**, eaal5068 (2017).
3. Y. E. Chen *et al.*, *Science* **380**, 203 (2023).
4. Y. Yang *et al.*, *Nature* **510**, 152 (2014).
5. D. Bousbaine *et al.*, *Nature* **638**, 1054 (2025).
6. J. L. Linehan *et al.*, *Cell* **172**, 784 (2018).
7. G. F. Debes, S. E. McGettigan, *J. Immunol.* **202**, 1659 (2019).
8. S. Hapfelmeier *et al.*, *Science* **328**, 1705 (2010).
9. D. Metze, A. Kersten, W. Jurecka, W. Gebhart, *J. Invest. Dermatol.* **96**, 439 (1991).
10. R. P. Wilson *et al.*, *J. Invest. Dermatol.* **139**, 2477 (2019).
11. I. Gribonika *et al.*, *Nature* **638**, 1043 (2025).
12. D. Bousbaine *et al.*, *Science* **377**, 660 (2022).
13. K. Nagashima *et al.*, *Nature* **621**, 162 (2023).
14. B. Zakeri *et al.*, *Proc. Natl. Acad. Sci. U.S.A.* **109**, E690 (2012).
15. C. A. Janeway Jr., *J. Immunol.* **191**, 4475 (2013).

ACKNOWLEDGMENTS

I am in debt to my postdoctoral mentor, M. Fischbach, who has been a constant source of inspiration and support throughout the years. I also would like to thank my co-mentors, C. Barnes and Y. Belkaid, for their guidance as well as the past and present members of the Fischbach laboratory, in particular those who made this work possible. This project was supported by postdoctoral fellowships from the Swiss National Science Foundation and a K99/R00 transition award from the US National Institutes of Health.

10.1126/science.adz0485

Department of Bioengineering, Stanford University, Stanford, CA, USA.
Email: djenetb@stanford.edu

GRAND PRIZE WINNER

Djenet Bousbaine received an undergraduate degree and master's degree from the Swiss Federal Institute of Technology (EPFL) and a PhD from the Massachusetts Institute of Technology. She is currently a postdoctoral fellow at Stanford University in the laboratory of Michael Fischbach. Her research combines bacterial genetics, immunology, and biochemistry to probe the molecular interactions between the microbiome and the immune system and leverages new mechanistic insights to develop noninvasive approaches to induce targeted immune responses. Her recent work uncovered B cell responses to skin microbiota, which she used to engineer a skin bacterium into a previously unexplored modality of topical vaccines.
www.science.org/doi/10.1126/science.adz0485

FINALISTS

Ayele Argaw-Denboba received an undergraduate degree from Addis Ababa University and a PhD from the University of Rome Tor Vergata. After completing his postdoctoral fellowship at the European Molecular Biology Laboratory, he started his laboratory at the Max Planck Institute of Immunobiology and Epigenetics in Freiburg, Germany, in 2023. His research investigates gut microbiome–epigenome interactions in mammals.
www.science.org/doi/10.1126/science.adz0492

Mohammad Arifuzzaman received an undergraduate degree from the University of Dhaka and a PhD from Duke University. After completing his postdoctoral fellowship at Weill Cornell Medicine, he started his laboratory in the Department of Medicine at Weill Cornell Medicine in 2024. His research focuses on diet–gut microbiota interactions and their effect on immunity and metabolism.
www.science.org/doi/10.1126/science.adz0502

NOSTER | Science
MICROBIOME
PRIZE

PHOTOS: (TOP TO BOTTOM) CONOR MCCLUNE; SARAH KEMPFF/CIBSS; COURTESY OF MOHAMMAD ARIFUZZAMAN

REVIEW SUMMARY

FERROELECTRICS

Ferroelectric materials toward next-generation electromechanical technologies

Fei Li*, Bo Wang, Xiangyu Gao, Dragan Damjanovic, Long-Qing Chen, Shujun Zhang

Full article and list of author affiliations: https://doi.org/10.1126/science.adn4926

BACKGROUND: Ferroelectrics are widely recognized for their exceptional functional properties, particularly piezoelectricity, which enables the efficient conversion of electrical energy into mechanical energy and vice versa. This ability has positioned ferroelectric materials at the forefront of numerous modern technologies. During the past 100 years, a wide array of ferroelectric materials with excellent piezoelectric properties have been developed, including lead zirconate titanate ceramics, lead-free ceramics, scandium-doped aluminum nitride thin films, polyvinylidene fluoride–based ferroelectric polymers, and relaxor ferroelectric crystals. These innovations have expanded the scope of advanced ferroelectric applications and provided greater flexibility in device design. They have also notably benefited numerous piezoelectric devices. Their functions in cell phones, for example, are many and include piezoelectric cooling fans that cool integrated circuit chips and maintain device performance. Ultrasonic transducers, which have facilitated advancements in critical areas such as medical imaging, where high-resolution ultrasound is essential, are another example. Nonetheless, there remains a pressing need for ferroelectric materials with even better performance to address the challenges posed by emerging technologies. For example, to facilitate the application of piezoelectric fans and motors, piezoelectric ceramics with even higher piezoelectric coefficients are required for reducing the driving voltage and energy consumption.

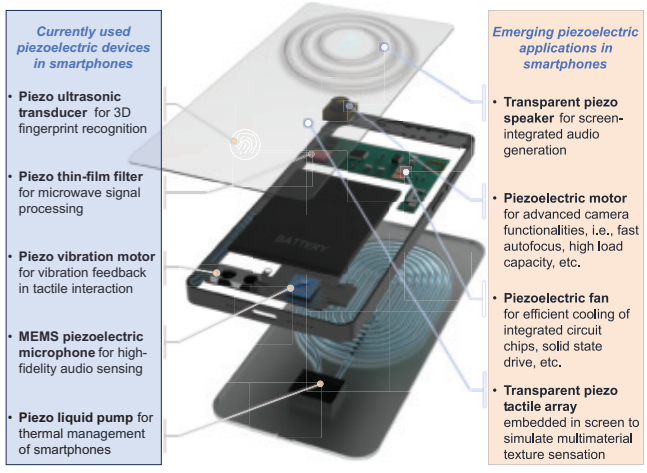

Currently used and emerging piezoelectric devices in the field of 3C (computer, communication, and consumer electronics). The smartphone is used as an example of a typical consumer electronic product to illustrate the diversity of piezoelectric applications. MEMS, microelectromechanical system.

ADVANCES: The primary approach to achieving high piezoelectricity in ferroelectrics has focused on inducing instability in the orientation of spontaneous polarization, which involves flattening the free-energy profile that connects various stable and metastable polar states, as described in phenomenological theory. Numerous theoretical and experimental studies have demonstrated that such a flat free-energy profile can be achieved through the design of a compositionally driven ferroelectric phase boundary, particularly a morphotropic phase boundary. This strategy has gained popularity in the wake of the development of the phase diagram for lead zirconate titanate solid solution. Recently, researchers have identified approaches to further tailor the free-energy profile by carefully arranging long-range ferroelectric domains and introducing local structural heterogeneity at the nanoscale. These innovations have led to the highest piezoelectricity recently observed in rare-earth element–doped relaxor ferroelectric crystals. Alternative strategies for achieving even higher piezoelectricity are being actively explored, including engineering the grain orientation in ceramics, facilitating ion redistribution under electric fields, and incorporating the flexoelectric effect at the nanoscale. These diverse strategies, when combined, hold great promise for pushing the boundaries of piezoelectricity in ferroelectrics and expanding their applicability in advanced technologies.

OUTLOOK: New high-performance ferroelectric materials have emerged, such as ferroelectric ceramics with a piezoelectric coefficient >2000 pC N^{-1} (4 to 10 times higher than currently used materials) and ferroelectric crystals simultaneously possessing high piezoelectricity and high light transparency. These materials hold immense potential in consumer and health care electronics, playing a crucial role in next-generation integrated circuit chip cooling devices, adaptive zoom systems, and wearable, implantable, and self-powered medical diagnostic devices.

Looking ahead, research is increasingly focused on developing lead-free or biodegradable ferroelectrics to address environmental concerns. In parallel, environmentally friendly manufacturing techniques, such as low-temperature sintering, aerosol deposition, and bioinspired methodologies, are being explored to reduce energy consumption and carbon emissions, aligning with global sustainability and carbon neutrality goals. Additionally, textured ferroelectric ceramics have emerged as a promising alternative to crystal counterparts, offering good piezoelectric properties along with the robust mechanical strength of ceramics, while reducing overall costs.

In the search for new materials, advances in computational methods, such as first-principles calculations and phase-field simulations, along with progress in material characterization technologies, such as in situ high-resolution atomic-scale imaging, are enabling more accurate predictions of material behavior and properties. These developments are undoubtedly accelerating the progress of high-performance ferroelectrics. □

*Corresponding author. Email: ful5@xjtu.edu.cn Cite this article as F. Li *et al.*, *Science* **389**, eadn4926 (2025). DOI: 10.1126/science.adn4926

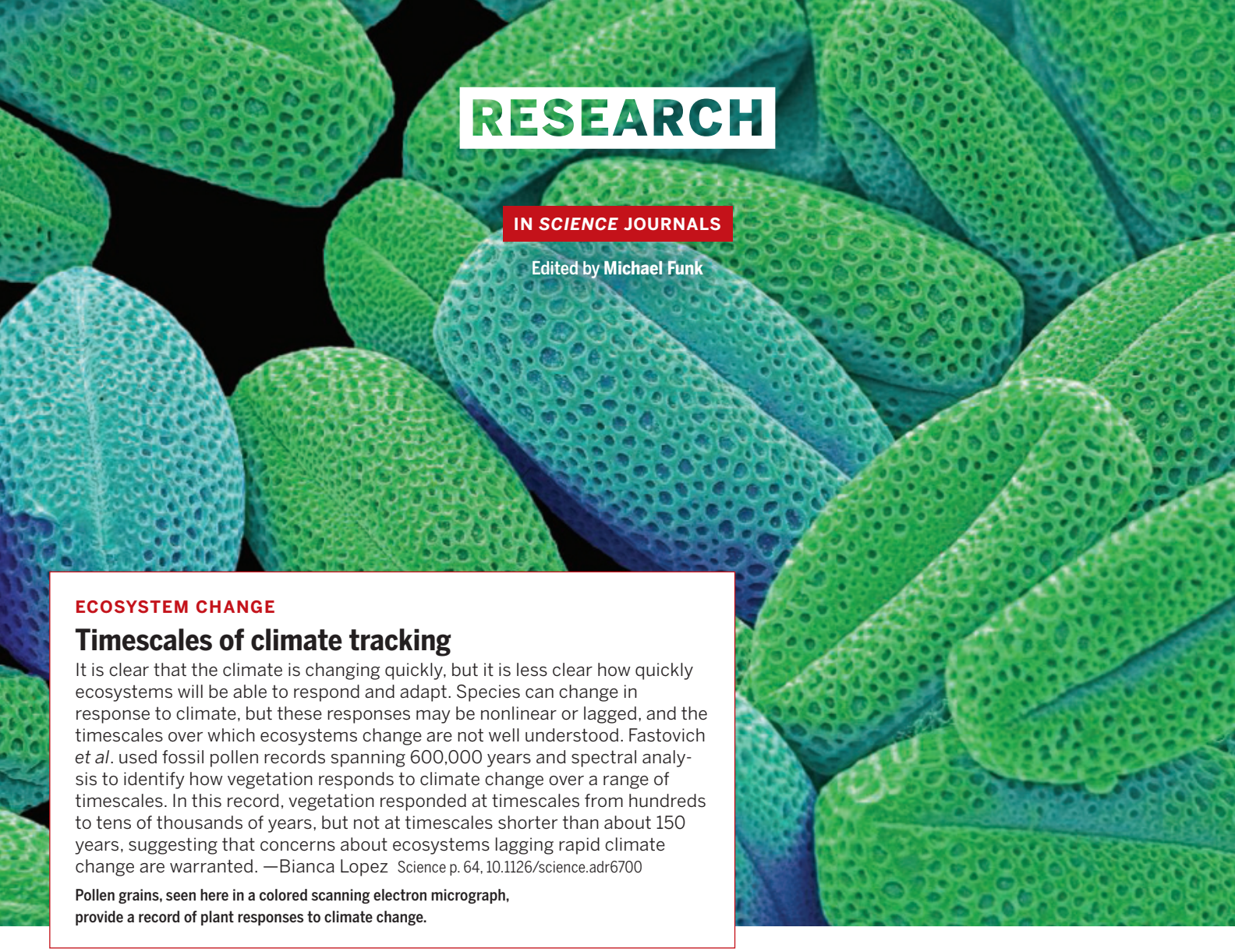

RESEARCH

IN *SCIENCE* JOURNALS

Edited by **Michael Funk**

ECOSYSTEM CHANGE

Timescales of climate tracking

It is clear that the climate is changing quickly, but it is less clear how quickly ecosystems will be able to respond and adapt. Species can change in response to climate, but these responses may be nonlinear or lagged, and the timescales over which ecosystems change are not well understood. Fastovich *et al*. used fossil pollen records spanning 600,000 years and spectral analysis to identify how vegetation responds to climate change over a range of timescales. In this record, vegetation responded at timescales from hundreds to tens of thousands of years, but not at timescales shorter than about 150 years, suggesting that concerns about ecosystems lagging rapid climate change are warranted. —Bianca Lopez Science p. 64, 10.1126/science.adr6700

Pollen grains, seen here in a colored scanning electron micrograph, provide a record of plant responses to climate change.

NEUROSCIENCE

Neocortical synaptic transmission

Calcium-dependent neurotransmitter release from presynaptic terminals is one of the main mechanisms mediating neuronal communication. Synaptotagmin 1 (Syt1) is the main calcium sensor in the neocortex. Bornschein *et al*. examined the calcium sensitivity of neurotransmitter release at small neocortical synapses in rodent brain slices using electrophysiology, quantitative analysis, and modeling. Syt1-mediated release has high affinity for calcium and a steep dose-response curve in the range of action potential–evoked calcium concentrations, suggesting substantial differences to the published work on Syt2-triggered neurotransmitter release in the hindbrain. These results pave the way for a better understanding of neocortical synaptic transmission. —Mattia Maroso

Science p. 48, 10.1126/science.adp0870

GENETIC DISEASE

A failure to recycle

Ritscher-Schinzel syndrome (RSS) is a congenital malformation syndrome associated with multiorgan dysfunction. Causes of the tissue malformation and dysfunction have not been established, but mutations in the Commander and WASH complex are associated with RSS. Kato *et al*. analyzed genetic and proteomic data from patient cohorts to find causative mutations that disrupt Commander- and/or WASH-dependent endosomal recycling of many proteins essential for organ development. Using this information, the authors generated new mouse models to replicate the phenotypes of RSS and to demonstrate the mechanistic underpinnings of the tissue dysfunction. Together, their data show that RSS can be considered a recyclinopathy that stems from dysfunctional assembly and stability of the Commander complex and subsequently dysfunctional endosome recycling. —Brandon Berry

Sci. Transl. Med. (2025) 10.1126/scitranslmed.adt2426

NEUROSCIENCE

Reversing the pathology of mutant LRRK2

Parkinson's disease (PD)–linked mutations in the kinase LRRK2 cause the loss of cilia in cells in the striatum of the brain, disrupting a signaling circuit critical to the survival of dopaminergic neurons. Jaimon *et al*. tested the LRRK2 inhibitor MLi-2 in a mouse model of early-stage, LRRK2 mutation–associated PD. Dietary supplementation with

IMAGE: STEVE GSCHMEISSNER/SCIENCE SOURCE

MLi-2 for 3 months restored cilia formation in striatal neurons and astrocytes, and thus increased their production of the neuroprotective factors that promoted regeneration in nigral dopaminergic neurons. —Leslie Ferrarelli

Sci. Signal. (2025) 10.1126/scisignal.ads5761

POLYMER FILMS

Thin, spongy membranes

Electropolymerization normally creates dense films. By contrast, Itoh *et al*. found that electropolymerization of deprotonated resorcinol and aldehydes in the absence of supporting electrolytes formed low-density, "loofah-like" ultrathin films. The reaction self-limits such that the monomers react only in the electrical double layer and the membrane releases when the bias is removed. Large-area membranes could be used for separations, and the films could be annealed to form carbon membranes. —Phil Szuromi

Science p. 74, 10.1126/science.adq0782

PALEOANTHROPOLOGY

Not just for hunting

Wooden tools from the early Paleolithic Period are extremely rare, with only two previously known discoveries, one in Europe and one in Africa. In both cases, the tools were hunting implements, spears, and spear tips. Liu *et al.* describe several wooden tools from a 300,000-year-old site in China. These tools were not used for hunting, but rather appear to have been designed to obtain and process plant foods. This finding shows that wooden tools were being used across a much wider range at the time, and also provides insight into how cultures from different environments may have developed locally useful implements. —Sacha Vignieri

Science p. 78, 10.1126/science.adr8540

IMMUNE SIGNALING

Flipping immune signals

The mitochondrial antiviral signaling (MAVS) protein is part of the cellular machinery that helps to protect mammalian cells from viral infection. Okazaki *et al*. found that the amino acids in MAVS are carboxylated, and this modification is dependent on γ-glutamyl carboxylase (GGC), a membrane protein found in the endoplasmic reticulum that can invert its orientation so that its active site faces the cytosol. In the presence of activating signals, the authors found that GGC-dependent carboxylation of MAVS stimulated cells to produce type 1 interferon but suppressed signals leading to apoptosis. Mice in which GGC was inhibited, either by genetic knock-out in neurons or by depleting its cofactor vitamin K, had dysregulated responses to viral infection of the brain. —Sarah H. Ross

Science p. 84, 10.1126/science.adk9967

FERROELECTRICS

Ditching fluoropolymers

The vast majority of ferroelectric polymers are based on poly(vinylidene fluoride) (PVDF) chemistry because of their superior performance. However, concerns about fluorine-based "forever chemicals" have encouraged searches for alternative materials. Huang *et al*. investigated the synthesis, structure, ferroelectricity, and electromechanical and electrocaloric effects of side-chain polymers without fluorine or mesogenic groups. They developed a relaxor ferroelectric liquid crystal polymer that features highly polar disulfonyl groups in which the side chains form a layered structure. Their material demonstrates superior electrostriction and electrocaloric properties at low electric fields comparable to state-of-the-art PVDF-based tetrapolymers. —Marc S. Lavine

Science p. 69, 10.1126/science.ads4702

IN OTHER JOURNALS

Edited by **Corinne Simonti** and **Jesse Smith**

DEVELOPMENT

Building life's tubes with precision

In living organisms, tubular structures such as blood vessels and airways are essential for transporting fluids and gases, but how their precise shapes and sizes are controlled has long been a mystery. A new study examined how cells coordinate the expansion of tubes. Using the notochord tube in ascidian embryos as a model, Shi *et al.* discovered that both cell cortex tension, which is regulated by Cdc42 signaling, and the stability of tight junctions are crucial for proper tube growth. Their new theoretical model accurately predicted tube expansion dynamics. These insights could inspire advances in understanding organ development and treating diseases caused by tube malformation. —Di Jiang

Proc. Natl. Acad. Sci. U.S.A. (2025) 10.1073/pnas.2419960122

PHYSICS

Halo trimers

In quantum mechanics, pairs and triplets of particles can form bound states with a spatial extent greater than the range of the interparticle potential. The characteristics of such "halo" states depend on the ratios of the particle masses as well as their interactions. Chuang *et al.* used radiofrequency spectroscopy to detect halo trimers in a mixture of heavy (potassium) and light (sodium) atoms. They tuned a magnetic field to achieve strong potassium-sodium interactions in the presence of mutually weakly repelling sodium atoms. This resulted in trimers consisting of a tightly bound dimer with a weakly bound third particle. Future directions include cooling the system into quantum degeneracy and looking for larger bound states such as halo tetramers. —Jelena Stajic

Phys. Rev. X (2025) 021098

OPTICS

Viewing the out of sight

Non-line-of-sight imaging allows an observer to view an obscured scene. Active methods bounce pulses of light off a relay wall that illuminate the hidden scene. Some light makes its way back to the sender, and computational methods are then used to reconstruct the scene. Such methods can be complex and require expensive components. Li *et al.* have developed a method that uses the rough surface of the relay wall itself as the camera, modeling the microscopic roughness of the relay wall surface and how light from the hidden scene interacts with it. The authors were able to obtain an accurate picture of the hidden scene with submillimeter resolution, video rate capture, and full-color reconstruction capability. Such a passive method should find applications in many scenarios requiring non-line-of-sight imaging. —Ian S. Osborne

Optica (2025) 10.1364/OPTICA.544275

NEUROSCIENCE

Slowing binge drinking

Alcohol dependence affects the function of a brain region called the medial orbitofrontal cortex (mOFC), which is involved in higher-level cognitive functions such as the suppression of impulsive actions. However, the effects of alcohol on specific mOFC circuits are unclear. Gimenez-Gomez *et al.* used genetically modified mice to identify a group of neurons in the mOFC that showed an increase in activity when blood alcohol levels were high. Optogenetic stimulation of these neurons

Seasonal shifts, including dietary changes, alter the gut microbiota of fruit flies.

MICROBIOME

Seasonal gut feelings

The fruit fly, *Drosophila melanogaster,* can survive winter by entering diapause. Like most other organisms, fruit flies carry communities of microbial symbionts, some of which are essential for the host organism's health. Lemoine et al. investigated the effect of seasonal dietary and temperature changes on the bacterial and fungal microbiota of fruit flies in German orchards. Sequencing showed how the microbial communities and certain indicator species changed with time and between orchard sites. The authors interpreted location differences as reflecting differences in microclimate and changes in indicator species as reflecting larger seasonal changes. However, season dictates diet, and diet also has a strong effect on microbiota composition.
—Caroline Ash *Environ. Microbiol.* (2025) 10.1111/1462-2920.70104

decreased alcohol intake, whereas ablating them increased alcohol consumption. This effect was mediated by projections to the mediodorsal thalamus. These findings suggest that this brain circuit protects against binge drinking and could represent a target for the treatment of alcohol addiction. —Sarah Lemprière

Nat. Neurosci. (2025) 10.1038/s41593-025-01970-x

REGENERATION

Understanding healthy bones

Strong bones are critical for health and balance and to protect vital organs. Human skeletal stem cells (hSSCs) fuel bone repair and maintenance through the production of bone, cartilage, and supporting tissues. Ambrosi *et al.* investigated stem cell diversity in the human skeleton to better understand bone formation and the possibility of intercepting age-related defects. The researchers isolated hSSCs from different skeletal sites and identified four major subtypes that could generate specific skeletal tissues. A fibroblastic hSSC subtype was linked to age-related bone alterations and regenerative disorders, and their abnormal expansion resulted in poor bone healing. Understanding how changes in skeletal stem cells occur with age may provide insights into ways to restore function and improve bone repair. —Priscilla N. Kelly

Cell Stem Cell (2025) 10.1016/j.stem.2025.02.013

BATTERY ELECTROLYTES

Visualizing battery shorting

Inorganic solid-state ionic conductors with high elastic modulus and ionic conductivity are promising electrolytes for all-solid-state batteries. However, their chemomechanical instabilities remain a significant hurdle for practical applications. Wang *et al.* explored short-circuit transitions in several inorganic solid-state electrolytes using in situ electron microscopy. They showed that local deposition and infiltration of lithium along grain boundaries or defects in the electrolytes lead to the formation of transient short circuits. The extended lithium precipitation eventually forms a percolating electronic pathway, resulting in battery failure. Inspired by these observations, the authors developed a composite electrolyte by incorporating a more electronically insulating and mechanically resilient polymer that helps to mitigate electronic leakage and improve battery stability. —Jack Huang

J. Am. Chem. Soc. (2025) 10.1021/jacs.5c04113

PHOTO: ROD WILLIAMS/MINDEN PICTURES

RESEARCH ARTICLE SUMMARY

MOLECULAR BIOLOGY

Zincore, an atypical coregulator, binds zinc finger transcription factors to control gene expression

Daniëlle Bianchi *et al.*

Full article and list of author affiliations: https://doi.org/10.1126/science.adv2861

INTRODUCTION: Gene expression is controlled by transcription factors (TFs) that bind to specific sequences in promoter regions and activate transcription. TFs typically function as modular proteins, featuring distinct DNA binding domains and effector domains. Zinc finger transcription factors (ZNFs), the largest family of transcription factors, often lack well-defined effector domains, rendering the mechanisms of how they activate transcription poorly understood.

RATIONALE: Regulatory protein complexes play a crucial role in modulating key cellular processes and functions. We used a compendium-based approach to identify genes that work together to regulate a wide range of phenotypes across a collection of haploid genetic screens. We hypothesized that such genes may encode critical components of undiscovered regulatory complexes.

RESULTS: We identified *QRICH1* and *SEPHS1* as a gene pair influencing diverse cellular phenotypes. Characterization of the encoded proteins revealed that they form a protein complex that we call Zincore. In keeping with a shared physiological function, heterozygous mutations in these genes cause similar neurodevelopmental syndromes in humans, which are characterized by developmental delay and dysmorphic facial features. Furthermore, in mice, homozygous QRICH1 inactivation resulted in high levels of apoptosis in the developing brain, as well as embryonic lethality. Chromatin immunoprecipitation sequencing and functional experiments show that Zincore binds to many regions in the genome, including highly conserved promoter motifs, activating gene expression. Using a genetic screen, we demonstrated that Zincore is recruited to promote transcription by different ZNFs, including ZFP91, ZNF652, ZNF526, and PRDM15. Cryo–electron microscopy analysis of Zincore bound to ZFP91 on its cognate target DNA motif demonstrates that Zincore engages ZFP91 through an arginine clamp formed by two SEPHS1 residues. Notably, one of the two arginines (Arg371) is mutated in patients with the aforementioned neurodevelopmental syndrome, linking its role in gene expression to human development. Zincore recognizes the characteristic and highly conserved ZNF fold rather than specific residues within ZFP91, which explains its broad compatibility with diverse ZNF proteins. In line with this finding, the four ZNF proteins that we identified as factors that recruit Zincore to DNA could explain only 12% of Zincore binding sites. This suggests that additional transcription factors are involved in recruiting Zincore to the genome. In contrast to conventional transcription factor–coregulator interactions, Zincore interacts directly with the DNA binding domain of the ZFP91 and stabilizes its interaction with DNA. Because transcription factors typically bind to only a fraction of their motifs in the genome, Zincore likely contributes to the understanding of how ZNFs occupy specific promoter sites.

CONCLUSION: The discovery of Zincore uncovers an unconventional coregulator complex. Unlike traditional coregulators, Zincore interacts with the structurally conserved DNA binding domain of ZNF proteins. This interaction results in a distinctive locking mechanism that stabilizes ZNF proteins on their genomic consensus motifs. Given Zincore's essential role in development, its ability to lock ZNF transcription factors on DNA may contribute to the establishment of stable gene expression profiles that are critical for healthy development. □

Corresponding author. Anastassis Perrakis (a.perrakis@nki.nl); Sebastian M. B. Nijman (sebastian.nijman@gmail.com); Thijn R. Brummelkamp (t.brummelkamp@nki.nl)
Cite this article as D. Bianchi *et al.*, *Science* **389**, eadv2861 (2025). DOI: 10.1126/science.adv2861

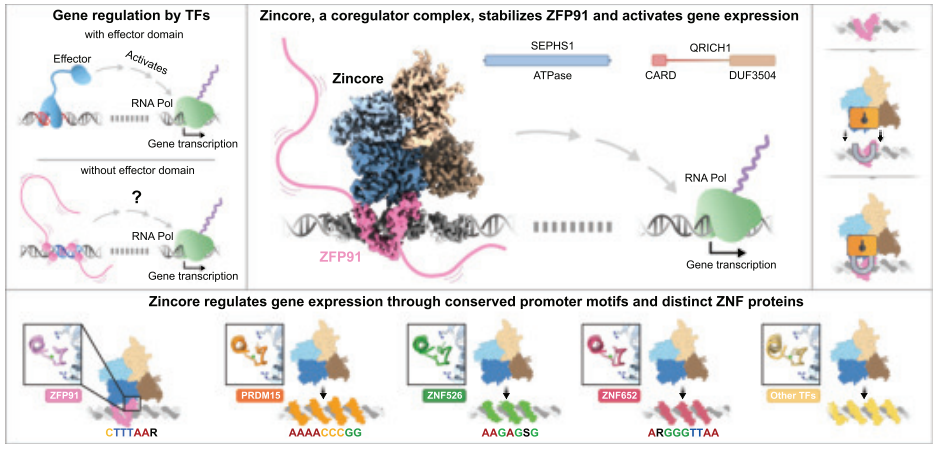

Zincore functions as a transcriptional coregulator, stabilizing zinc finger transcription factors to their consensus motif. Traditional transcription factors (TFs) are modular proteins consisting of a separate DNA binding domain and effector domain. Zinc finger transcription factors (ZNFs) often lack effector domains, rendering their activation mechanisms unclear. Zincore, a complex of QRICH1 and SEPHS1, binds to ZNFs, stabilizes their binding to the DNA, and activates gene expression. RNA Pol, RNA polymerase; ATPase, adenosine triphosphatase; CARD, caspase activation and recruitment domain; DUF, domain of unknown function.

RESEARCH ARTICLE SUMMARY

CENTROMERES

Chromosome-specific centromeric patterns define the centeny map of the human genome

Luca Corda and Simona Giunta*

Full article and list of author affiliations: https://doi.org/10.1126/science.ads3484

INTRODUCTION: Centromeres, composed of long stretches of highly repetitive and rapidly evolving DNA, remain among the most challenging regions of the human genome to resolve and study. Experimental studies indicate that specialized chromatin, rather than the underlying DNA, underpins centromere function in chromosome segregation. Indeed, DNA at centromeres varies in size, structure, and composition between chromosomes and haplotypes as well as across the population. These inherent complexities, coupled with the lack of scalable and reliable methods to interrogate such large repetitive loci, have hindered their systemic study, annotation, and comparison across individuals and species.

RATIONALE: Beyond common methods based on sequence alignment or motif search, we reasoned that an approach leveraging genomic distances between conserved DNA elements could facilitate analyses within highly repetitive regions. We hypothesized that the binding motif of centromere protein B (CENP-B) might exhibit conserved properties among individuals, given its functional relevance, despite being located within highly variable loci. Akin to fragment length analysis, this strategy would allow us to bypass the complexities of the underlying DNA by decoding the content of each centromere into numerical values.

RESULTS: Using our series of computational methods collectively referred to as the Genomic Centromere Profiling (GCP) pipeline, we defined the placement of CENP-B boxes at base-pair resolution in recently available chromosome-level human genome assemblies and calculated the distances between consecutive boxes. We discovered a chromosome-specific pattern of CENP-B boxes within centromeric DNA repeats that is notably conserved across haplotypes and individuals in spite of underlying sequence divergence. We extended our analysis to the whole genome and found conserved distribution of CENP-B boxes outside of centromeres in all chromosomes. The chromosome-specific genomic position, orientation, distribution, and organization of the motif in these ectocentromeric sequences (ECSs) form a conserved pattern that we named the "centeny map." The centeny map of human chromosomes can be leveraged for rapid annotation and characterization of genomic assemblies. The GCP suite presents distinct computational tools to reclassify human chromosomal clusters, mark sites of centromere expansion, identify structural variations and misassembled regions, and perform rapid-read retrieval and annotation. Comparing the centromeric patterns of nonhuman primates, we found the distance values between consecutive centromeric sites to be conserved, especially in evolutionarily related species.

CONCLUSION: In this study, we discovered an ancestral genomic architecture buried within our genome. The conserved chromosome-specific framework enables simplification of DNA sequences into numerical values based on distances between conserved, functionally relevant motifs, resulting in distinct barcodes for chromosomes and centromeres. The GCP suite of computational models that we generated by using these barcodes will not only facilitate the analysis of centromeres across evolution and disease, it will also be utilized for their rapid annotation from raw sequencing reads to contigs and assemblies. Moreover, the identification and characterization of ectocentromeric sites associated with specific epigenetic states along chromosome arms indicate a possible moonlighting function of CENP-B protein beyond centromeres. Our findings open new avenues to understand the pattern's evolutionary dynamics and functional significance within centromeres and beyond. □

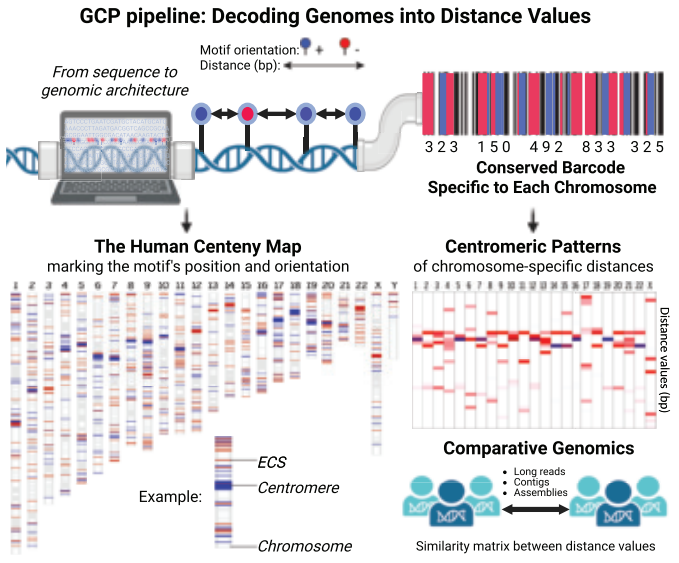

Chromosome-specific barcoding reveals ancestral centromere architecture conserved across humans. We present a new approach for characterization of genome assemblies and raw reads using distances and patterns of a functional DNA motif. Using the GCP computational pipeline, we identified a chromosome-specific framework based on position (lollipops) and orientation (blue or red) of CENP-B boxes (motifs) not only at centromeres but also throughout the genome as ECSs. We named this conserved distribution the "human centeny map." Within centromeres, distance values are conserved and chromosome specific. Decoding genome and centromere complexity in numerical form enables exploration of variation and evolution across species and individuals. bp, base pairs.

*Corresponding author. Email: simona.giunta@uniroma1.it Cite this article as L. Corda and S. Giunta, *Science* **389**, eads3484 (2025). DOI: 10.1126/science.ads3484

RESEARCH ARTICLE SUMMARY

PROTEIN DEGRADERS

Mining the CRBN target space redefines rules for molecular glue–induced neosubstrate recognition

Georg Petzold†, Pablo Gainza†, *et al.*

Full article and list of author affiliations: https://doi.org/10.1126/science.adt6736

INTRODUCTION: Molecular glue degraders (MGDs) are an emergent class of small molecules that induce proximity between a target protein and an E3 ubiquitin ligase, causing target protein ubiquitination and degradation. Clinically active MGDs that repurpose the $CRL4^{CRBN}$ ubiquitin ligase recruit their efficacy targets through a common recognition motif known as the β-hairpin G-loop degron, which is a simple secondary structure element with a high prevalence in the human proteome. The G-loop defines surface features that create overall complementarity to the cereblon (CRBN)–MGD interface and enable protein-protein interactions that potentially mimic the recognition of an endogenous CRBN substrate.

RATIONALE: Given the simplicity of the G-loop interface with CRBN, the dependence of these interactions on an MGD molecule, and the overall abundance of G-loop–like motifs within the human proteome, we expected many more proteins to be amenable to this modality. To identify compatible human proteins, we performed proteome-wide CRBN target space analyses using computational matchmaking algorithms that detect structural or surface similarities to known CRBN degrons. We sought to validate predictions through biochemical, cellular, and structural readouts to systematically explore the CRBN target space and define rules for target engagement.

RESULTS: To map the CRBN target space, we defined different G-loop templates capturing key elements that delineate compatibility with CRBN. The templates were computationally matched against the available structural proteome (Protein Data Bank and AlphaFold2 models), which identified 1633 human proteins that are predicted to be compatible with CRBN through surface-exposed G-loop–like motifs. The predicted G-loops are distributed over >250 domain types and nearly 100 different target classes, many new to this modality and currently perceived as inaccessible to small-molecule ligands. This mining approach not only identified β-hairpin G-loops across the human proteome but also uncovered helical G-loops as a structurally distinct CRBN recognition motif. Because G-loops mimic interactions of an endogenous CRBN substrate through surface features with overall compatibility to CRBN, we reasoned that other mimicry mechanisms exist that are independent of a structurally predefined G-loop–like motif. To this end, we identified VAV1, an undruggable target with broad therapeutic potential in autoimmune and chronic inflammatory indications. The C-terminal SH3 (SH3c) domain of VAV1 lacks structural features of G-loop degrons but engages CRBN in an MGD-dependent manner through molecular surface mimicry of GSPT1, a well-established CRBN G-loop target. Structural analysis revealed that the VAV1 SH3c domain uses a distinct fold to form key hydrogen bond contacts with CRBN that are normally satisfied by G-loop interactions. These findings redefine rules for MGD-induced target engagement and suggest that other mechanisms exist that create complementarity to CRBN through molecular surface mimicry.

CONCLUSION: Our systematic exploration of the CRBN target space unveils an extraordinary plasticity of CRBN, redefines rules for target engagement, and provides opportunities for target space expansion within and beyond the β-hairpin G-loop paradigm. We demonstrate that target complementarity depends on CRBN surface features that are modulated by its central MGD binding site, which allows for the elimination of challenging drug targets by the next generation of MGDs. □

Corresponding author: John C. Castle (jcastle@monterosatx.com); Sharon A. Townson (stownson@monterosatx.com) †These authors contributed equally to this work. Cite this article as G. Petzold *et al.*, *Science* **389**, eadt6736 (2025). DOI: 10.1126/science.adt6736

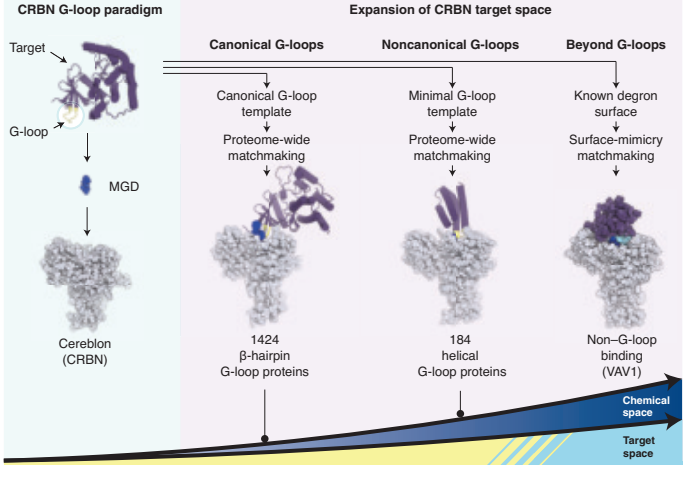

CRBN target space expansion within and beyond G-loops. MGDs are small-molecule compounds that recruit target proteins to CRBN through a generalizable G-loop recognition motif. Computational matchmaking algorithms using structural G-loop templates predict >1600 human proteins with surface-exposed and CRBN-compatible β-hairpin or helical G-loop motifs. Surface-based mimicry searches overcome the G-loop paradigm and provide opportunities to expand the CRBN target space beyond G-loop degrons.

RESEARCH ARTICLE SUMMARY

MESOSCOPIC PHYSICS

Time-domain braiding of anyons

M. Ruelle, E. Frigerio, E. Baudin, J.-M. Berroir, B. Plaçais, B. Grémaud, T. Jonckheere, T. Martin, J. Rech, A. Cavanna, U. Gennser, Y. Jin, G. Ménard, G. Fève*

Full article and list of author affiliations: https://doi.org/10.1126/science.adm7695

INTRODUCTION: Unlike fermions and bosons, anyons are quasiparticles that retain a robust memory of particle exchanges through a braiding phase factor, a property called fractional statistics. This memory is at the heart of topological quantum computing, where quantum information can be processed by braiding anyons. It also provides anyons with distinctive dynamical properties that are so far unexplored. Anyon fractional statistics have recently been evidenced by several experiments that all focused on the stationary regime. As such, they did not provide any information on anyon dynamics. However, when manipulating anyons at the single-particle level, it becomes important to understand how braiding affects the timescales of anyon transfer in a circuit.

RATIONALE: In a fractional quantum Hall (FQH) fluid, braiding plays a prominent role when studying the scattering of an anyon emitted toward a narrow constriction called a quantum point contact (QPC). In this case, the dominant mechanism for particle transfer across the constriction is not the direct tunneling of the incoming excitation, but rather a braiding process between the incoming excitation and an anyon–anti-anyon pair created at the QPC. The creation of the pair, triggered by the incoming excitation, can be understood as a tunneling event across the QPC where an anyon is created on one side, leaving an anyon hole on the other. As a consequence of the robust memory of braiding, these tunneling events may occur long after the incoming anyon has exited the QPC. By contrast, if the incoming particle is an electron with trivial braiding, tunneling occurs at the same time as the electron crosses the QPC. In this work, we used a triggered source of anyon pulses (of temporal width of a few tens of picoseconds) to investigate the dynamics of anyon tunneling at a QPC in a FQH fluid at filling factor $\nu = 1/3$. In the experiment, we used Hong-Ou-Mandel interferometry, where two mutually time-shifted anyon pulses are emitted toward the QPC. By measuring the correlations of the electrical current fluctuations at the QPC output as a function of the time delay between pulses, we directly probed the characteristic anyon tunneling timescale τ_δ.

RESULTS: We observed that anyon braiding increases the characteristic timescale τ_δ for anyon tunneling. Our findings demonstrate that τ_δ is set by the temporal decay of the anyon correlation function and can be understood as the characteristic time at which the anyon memory is erased. It grows when the temperature and the scaling dimension δ (the parameter characterizing the dynamics at the edge of a FQH fluid) decrease. Our study allowed us to extract the value of $\delta = 0.66 \pm 0.08$ by measuring the evolution of the tunneling dynamics with temperature. It differed from the expected value for a Laughlin state, $\delta = 1/3$, indicating that δ is nonuniversal. By varying the number of anyons contained in each pulse, we observed that braiding effects are suppressed for pulses containing three anyons, confirming the quantized value of $\theta = 2\pi/3$ of the braiding phase at filling factor 1/3.

CONCLUSION: Our work provides an experimental signature of the role of braiding in anyon dynamics, highlighting the distinctive properties of anyons compared with those of fermions or bosons. It introduces time-domain measurements for characterizing the properties of anyons—their braiding phase and their scaling dimension—therefore setting the stage for further exploration of more complex FQH states such as those hosting non-Abelian anyons. □

*Corresponding author. Email: gwendal.feve@ens.fr Cite this article as M. Ruelle *et al.*, *Science* **389**, eadm7695 (2025). DOI: 10.1126/science.adm7695

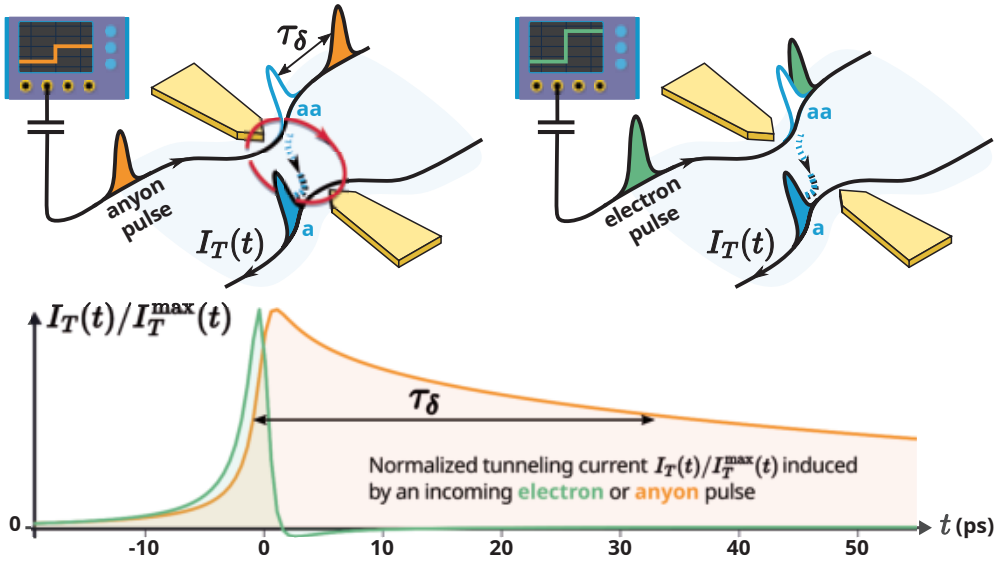

Tunneling dynamics of electrons and anyons. (Top left) A generator emits an anyon pulse (orange) propagating toward the QPC (gold). Anyon braiding leads to the tunneling of an anyon–anti-anyon pair (a-aa; blue) long after the anyon pulse has exited the QPC. (Top right) For electron emission (green), tunneling occurs immediately after the electron crosses the QPC. Consequently, the tunneling current $I_T(t)$ decays rapidly for electrons and slowly for anyons.

RESEARCH ARTICLE SUMMARY

NEUROSCIENCE

Representation of sex-specific social memory in ventral CA1 neurons

Akiyuki Watarai†, Kentaro Tao†, Teruhiro Okuyama*

Full article and list of author affiliations: https://doi.org/10.1126/science.adp3814

INTRODUCTION: The ability to recognize familiar individuals is fundamental to social behavior in animals because it enables them to navigate complex social environments. In mammals, social memory involves not only recognition of individuals, but also of a range of social attributes including genetic and physical traits such as sex. Prior studies have shown that different parts of the hippocampus are involved in storing and processing social information, but how individual neurons combine multiple social features into cohesive memories is not fully understood. In particular, the role of hippocampal circuits in encoding sex-specific features of familiar conspecifics remains unclear.

RATIONALE: We hypothesized that the activities of ventral CA1 (vCA1) neurons in the hippocampus reflect the rich, multidimensional nature of social information about familiar individuals. This information, including their sex and genetic background, may be encoded by distinct neural populations, activity patterns, or both. To test this, we recorded vCA1 neuronal activity in male mice as they interacted with familiar individuals that differed in sex and strain. We then assessed whether reactivating these memories would modulate behavior depending on the sex of the familiar individual.

RESULTS: We found that vCA1 neurons encoded both the individual identity and general properties of familiar individuals. Some neurons responded selectively to a specific sex or strain ("social property cells"), whereas others responded to nonlinear combinations of sex and strain ("social identity cells"). These neurons encoded social information through both changes in firing rate and precise spike timings relative to the hippocampal theta rhythm. Additionally, activity-dependent genetic labeling and optogenetic reactivation of female-associated, but not male-associated, social memories induced place preference in mice. Activation of overlapping populations of neurons representing two distinct female-associated social memories recapitulated this positive reinforcing effect. Furthermore, ablating two brain regions upstream of vCA1, the dorsal CA2 (dCA2) and the medial amygdala (MeA), disrupted the population coding of sex embedded within social memory.

CONCLUSION: Our findings demonstrate that the vCA1 neurons encode social memories across multiple representational dimensions, using distinct neuron populations to represent individual identity and social properties such as sex. These neurons use both rate and temporal coding schemes, with social property cells organizing a generalized map of social information that is temporally compressed within hippocampal theta cycles. We further discovered that these social memories convey sexually dichotomous emotional valence emerging from population coding of sex shaped by inputs from upstream dCA2 and MeA. Our study thus illustrates a neural mechanism by which the brain coordinates diverse social attributes to form unified memory representations, offering a perspective on how social information is integrated into hierarchical episodic memory systems. □

*Corresponding author. Email: okuyama@iqb.u-tokyo.ac.jp †These authors contributed equally to this work. Cite this article as A. Watarai *et al.*, *Science* **389**, eadp3814 (2025). DOI: 10.1126/science.adp3814

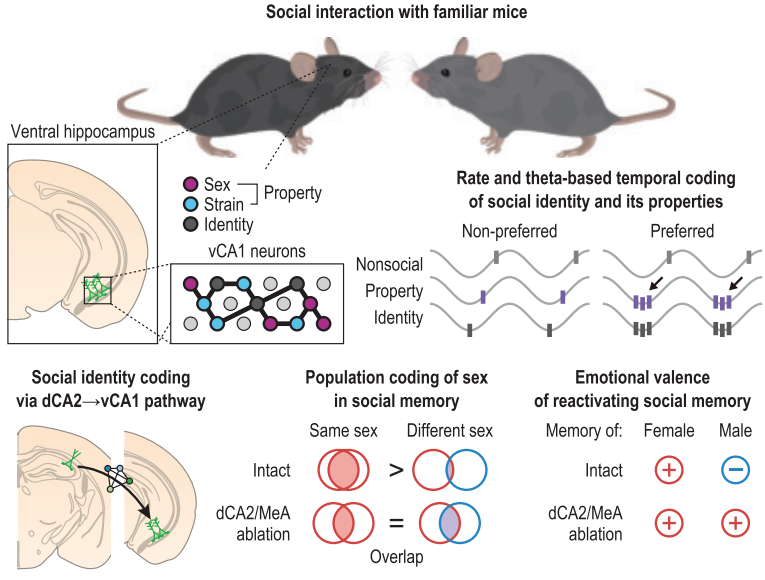

Multifaceted social memory coding by ventral hippocampal neurons. vCA1 neurons in the hippocampus encode the identity and social properties (sex and strain) of familiar individuals, with activity temporally coordinated by hippocampal theta rhythms. Social memory engrams carry sexually dichotomous emotional valence through population coding of sex shaped by inputs from upstream dCA2 and the MeA. [Mouse illustrations: Hiromasa Ono (© 2016 DBCLS TogoTV, CC-BY-4.0)]

NEUROSCIENCE

The intracellular Ca^{2+} sensitivity of transmitter release in glutamatergic neocortical boutons

Grit Bornschein[1]†, Simone Brachtendorf[1]†, Anja Reinert[1], Abdelmoneim Eshra[1], Robert Kraft[1], Johannes Hirrlinger[1,2], Jens Eilers[1], Stefan Hallermann[1], Hartmut Schmidt[1]*

Synaptotagmin-1 (Syt1) and Syt2 are the main calcium (Ca^{2+}) sensors triggering synchronous release in the brain. In this work, we studied the mechanisms mediating Syt1-triggered release from neocortical synapses. We measured the Ca^{2+} dependency of release in layer 5 pyramidal neuron synapses by laser photolysis of caged Ca^{2+}. Release had high Ca^{2+} affinity and positive cooperativity. Measurements at cerebellar Purkinje cell synapses and kinetic models indicate substantial differences compared with Syt2-triggered release. Our results suggest that Syt1-controlled release machineries are optimized for high reliability at moderate Ca^{2+} elevations and high plastic controllability.

Action potentials (APs) trigger neurotransmitter release by opening Ca^{2+} channels. Ca^{2+} activates a sensor protein, which then triggers the release process (*1*). Because of the steepness and short duration of the Ca^{2+} gradient, chemical equilibrium is not established in this process. This makes the physical coupling distance between the Ca^{2+} channels and the sensor protein as well as the intracellular Ca^{2+} sensitivity of the release process central in the control of speed, reliability, and plasticity of release (*2*–*7*).

Whereas coupling distances have been studied in detail at different synapses (*8*–*14*), the intracellular Ca^{2+} sensitivity of release has been less intensively investigated. Synaptotagmin-1 (Syt1) and Syt2 are the main Ca^{2+} sensors for synchronous release in the brain (*1*, *15*). Syt2 is the dominating sensor in hindbrain synapses, whereas in forebrain synapses, particularly in the neocortex, the principal sensor is Syt1 (*15*–*19*). At the giant calyx of Held, the Ca^{2+} sensitivity of Syt2-triggered glutamate release has been quantified from presynaptic Ca^{2+} elevations and transmitter release rates in detail, resulting in a kinetic model of Ca^{2+} binding and release with five cooperative Ca^{2+} binding sites (*2*, *3*, *20*). In subsequent work, this Syt2 model has been extended to account for release at low intracellular Ca^{2+} concentration increases ($\Delta[Ca^{2+}]_i$) (*21*) relevant for asynchronous release (*18*), for developmental alterations (*22*, *23*), for Syt2-triggered γ-aminobutyric acid (GABA) release (*6*), and for priming and synaptic plasticity (*6*, *24*–*26*).

At present, corresponding quantitative detail is lacking for the Ca^{2+} sensitivity of Syt1-triggered release at neocortical synapses. Owing to their small size and axo-dendritic location, glutamatergic neocortical synapses provide less favorable experimental conditions compared with giant (*2*, *3*, *26*) or axo-somatic (*6*) Syt2-expressing synapses. In particular, the axo-dendritic locations of the small boutons pose a substantial hurdle for the identification of the connected boutons. In this work, we quantified the Ca^{2+} dependency of Syt1-triggered release at synapses connecting layer 5 pyramidal neurons (L5PNs) and provided a direct comparison with release from small, Syt2-expressing cerebellar cortical synapses connecting Purkinje cells (PCs).

[1]Carl Ludwig Institute for Physiology, Medical Faculty, Leipzig University, Leipzig, Germany. [2]Department of Neurogenetics, Max Planck Institute for Multidisciplinary Sciences, Göttingen, Germany. ***Corresponding author. Email: hartmut.schmidt@medizin.uni-leipzig.de**
†These authors contributed equally to this work.

Identifying boutons connecting Syt1-expressing L5PNs with ultraviolet laser photolysis

Single-cell RNA sequencing data from the mouse primary somatosensory cortex (S1) showed that L5PNs express Syt1 but not Syt2 (*19*), which is supported by RNA sequencing data from whole-cortex and purified cortical neurons (*27*, *28*). We confirmed this on the protein level using immunohistochemistry (fig. S1).

We combined ultraviolet (UV) laser Ca^{2+} uncaging with quantitative green over red (G/R) two-photon Ca^{2+} imaging at L5PN synapses in the S1 (Fig. 1 and fig. S2). The typical synaptic connection between L5PNs is formed by a few boutons distributed over the basal dendrites. The boutons are situated close to postsynaptic somata (<100 μm) and are well separated from each other (≥100 μm) (*29*, *30*). To identify the connecting boutons on an axon collateral, we performed axonal walking: Using the bright red fluorescence, we followed axon collaterals toward the soma of the postsynaptic neuron and applied UV flashes to boutons at distances ≤100 μm from the soma until photolysis induced both a presynaptic Ca^{2+} signal and a UV-induced excitatory postsynaptic current (uvEPSC) (Fig. 1 and fig. S3). Subsequently, brief UV laser flashes of different intensity and duration were applied to yield different $\Delta[Ca^{2+}]_i$ that were monitored from individual boutons at high–temporal resolution point-mode recordings. The diameter of our uncaging spot was ~10 μm, which is a tenth of the size of the typical ≥100-μm spacing between boutons forming the synaptic connection. Hence, it is most likely that we measured mainly uvEPSCs resulting from release from single boutons.

Occasionally the UV spot covered more than one bouton in the *xy* plane. Therefore, we probed for homogeneity in UV-induced $\Delta[Ca^{2+}]_i$ between boutons within the photolysis area, using line-scan recordings that simultaneously assessed the fluorescence changes in these boutons. We found that ΔG/R were rather homogeneous with an average deviation of 11% between boutons (fig. S4). Although we may not always have imaged the connected bouton that evoked the uvEPSCs, these data suggest that the corresponding error in the $\Delta[Ca^{2+}]_i$ estimate is moderate and that the correlation between $\Delta[Ca^{2+}]_i$ and uvEPSCs is reliable.

Dose-response curve for the dependency of release on presynaptic Ca^{2+}

The transmitter release activity was monitored by recording uvEPSCs (Fig. 1 and Fig. 2A).We obtained presynaptic release rates from multiquantal uvEPSCs by the deconvolution method (*2*, *31*), using an average quantal EPSC (qEPSC) evoked by APs in low extracellular $[Ca^{2+}]_e$ (*11*) (fig. S5). To increase the signal-to-noise ratio, we integrated the release rates over time, which resulted in smooth cumulative release curves. These cumulative curves were typically monoexponential for uvEPSCs evoked by small to intermediate $\Delta[Ca^{2+}]_i$. They occasionally became biexponential for large presynaptic $\Delta[Ca^{2+}]_i$ (>~18 to 20 μM; Fig. 2B). In the slow phase of the biexponential curves, individual steps were frequently visible that may indicate fusion of few or individual vesicles. The cumulative curves were fit with either mono- or biexponential functions. The fit curves were subsequently differentiated, giving rise to smooth release rate curves from which peak release rates were obtained (Fig. 2C). The peak release rates were used to quantify the Ca^{2+} sensitivity of release by dose-response curves.

Increases in the amplitude and/or duration of the UV flashes induced increasing $\Delta[Ca^{2+}]_i$ and concomitantly increasing release rates (Fig. 3, A to D). uvEPSCs were typically detected at presynaptic $\Delta[Ca^{2+}]_i$ above ~4 μM. Below this value, release failures and qEPSCs dominated. Peak release rates increased until $\Delta[Ca^{2+}]_i$ of ~35 μM with subsequent saturation. The increase was steepest in a narrow dynamic range between ~10 and ~30 μM of $\Delta[Ca^{2+}]_i$. Overall, the

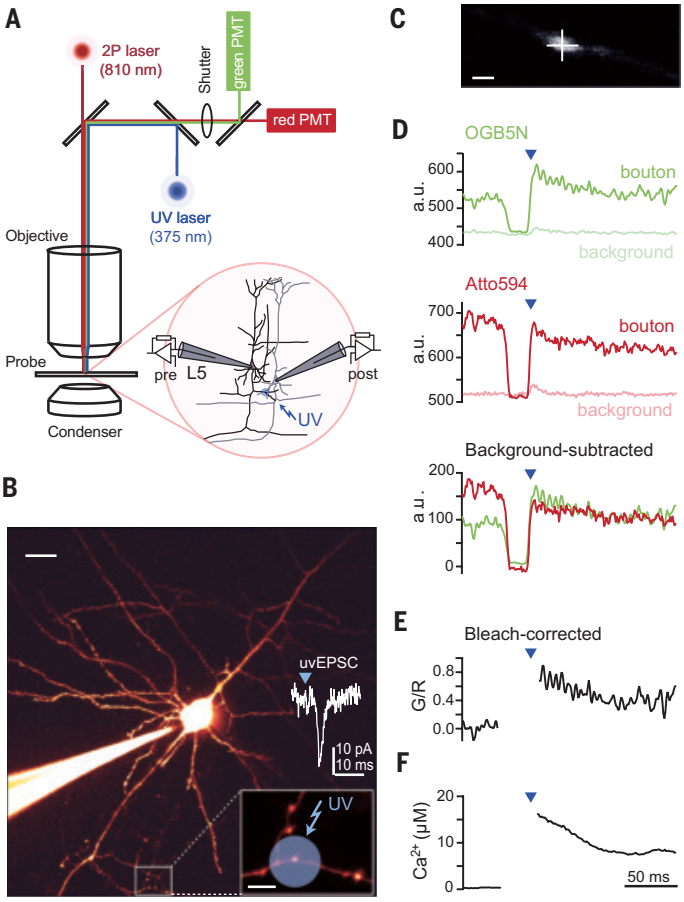

Fig. 1. UV photolysis induced $\Delta[Ca^{2+}]_i$ and uvEPSCs at pairs of connected L5PNs. (**A**) Scheme of the experimental setup showing the light path of the two-photon (2P) laser excitation (dark red), the UV laser illumination (blue), and the emitted red and green fluorescence detected by gateable photomultiplier tubes (PMTs) (red and green, respectively). (Inset) Illustration of connected L5PNs that were identified by paired recordings. (**B**) Two-photon image of a presynaptic L5PN (scale bar, 20 μm) and its axonal boutons (inset; scale bar, 5 μm). The presynaptic neuron was loaded with OGB5N, Atto594, and DMn/Ca^{2+} through the patch pipette; Ca^{2+} elevations were induced by application of brief UV flashes to presumed presynaptic boutons until corresponding uvEPSCs (inset) were recorded from the postsynaptic neurons (not labeled). (**C**) Two-photon image of a bouton located on an axon collateral from which flash-induced green (G) and red (R) fluorescence were recorded in the point-mode (cross) (scale bar, 1 μm). (**D**) Two-photon point-mode recordings showing the green (top) and red (middle) fluorescence as detected by the two PMTs and after background subtraction (bottom). The time of the UV flash is indicated by the blue arrowheads. The background was measured in separate point-mode recordings, and the subtraction of the background eliminated a residual flash-induced artifact (*26*). a.u., arbitrary units. (**E**) Calculated G/R signals with correction for bleaching in the red fluorescence (see materials and methods). (**F**) $[Ca^{2+}]_i$ calculated from the G/R signal based on a cuvette calibration.

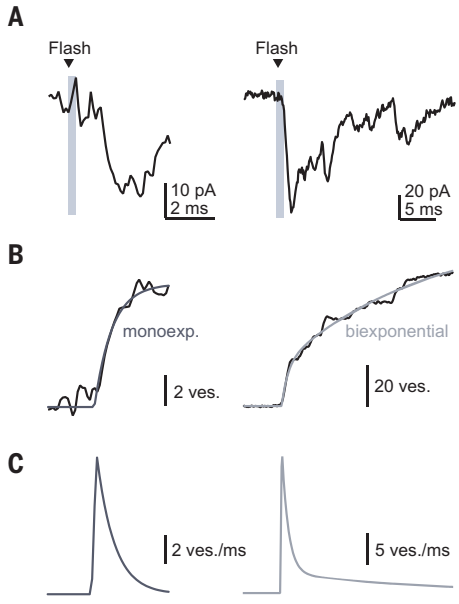

Fig. 2. Quantifying release rates from uvEPSCs. (**A**) Examples of uvEPSCs evoked by Ca^{2+} uncaging in a connected bouton. UV flashes (gray bars) of 0.2-ms (left) or 1-ms (right) duration were applied to the bouton. (**B**) Cumulative release rates from (A) fitted with a mono- (left; dark gray) or a biexponential (right; light gray) function. ves., vesicles. (**C**) Fit curves from (B) after differentiation.

peak release rate versus $\Delta[Ca^{2+}]_i$ dose-response curve was sigmoidal with positive cooperativity [Hill coefficient (n_H), 3.57; half-maximal effective concentration (EC_{50}), 20 μM; Fig. 3E]. Whereas peak release rates increased with $\Delta[Ca^{2+}]_i$, the corresponding synaptic delays decreased (Fig. 3F).

We tested whether saturation of the peak release rates could result from systematically slower rise times of larger EPSCs (*32*) by plotting peak uvEPSC amplitudes against the corresponding peak release rates (fig. S6). If larger uvEPSCs would have slower rise times compared with smaller uvEPSCs, one would expect a nonlinear relationship. However, we found the relationship to be linear over the whole range, which indicates that no systematic error is responsible for the saturation of the dose-response curve.

Photolysis- versus AP-evoked release

To understand whether the dynamic range of the dose-response curve is the physiologically relevant range, we quantified the Ca^{2+} dependency of AP-mediated release (Fig. 4 and fig. S7). First, we analyzed the dependency of release on the extracellular Ca^{2+} concentration by recording AP-mediated EPSCs in different $[Ca^{2+}]_e$. The corresponding cumulative release rates were typically monoexponential in lower $[Ca^{2+}]_e$ (≤2 mM) and typically became biexponential in higher $[Ca^{2+}]_e$ (≥5 mM), which is reminiscent of the uvEPSCs (see previous section). We plotted the peak amplitudes of the EPSCs and the corresponding peak release rates against the respective $[Ca^{2+}]_e$. Both curves were sigmoidal, with n_H values similar to those for the intracellular Ca^{2+} dependency of flash-evoked release. Similar results and parameters for the dependency of AP-evoked release on $[Ca^{2+}]_e$ were obtained in a previous study on cultured cortical neurons from Syt1 knockout mice that were rescued by Syt1 (*15*).

We had previously found that postsynaptic receptor saturation is not an issue at L5PN synapses, even under conditions of very high p_v (*11*). We recorded AP-mediated EPSCs in different $[Ca^{2+}]_e$ in the presence of γ-D-glutamylglycine (γDGG), which relieves glutamate receptor saturation and desensitization (*33*). The resulting dose-response curves for EPSC amplitudes and peak release rates were characterized by Hill parameters similar to those obtained in the absence of γDGG (fig. S7). This suggests that neither the dose-response curve for the photolysis-evoked release nor that for the AP-mediated release were strongly affected by postsynaptic receptor saturation.

For more direct comparison between flash- and AP-evoked release, we first corrected the photolysis dose-response curve (Fig. 3E) for differences in the readily releasable pool (RRP) of vesicles by dividing the peak release rates by the corresponding size of the RRP of each

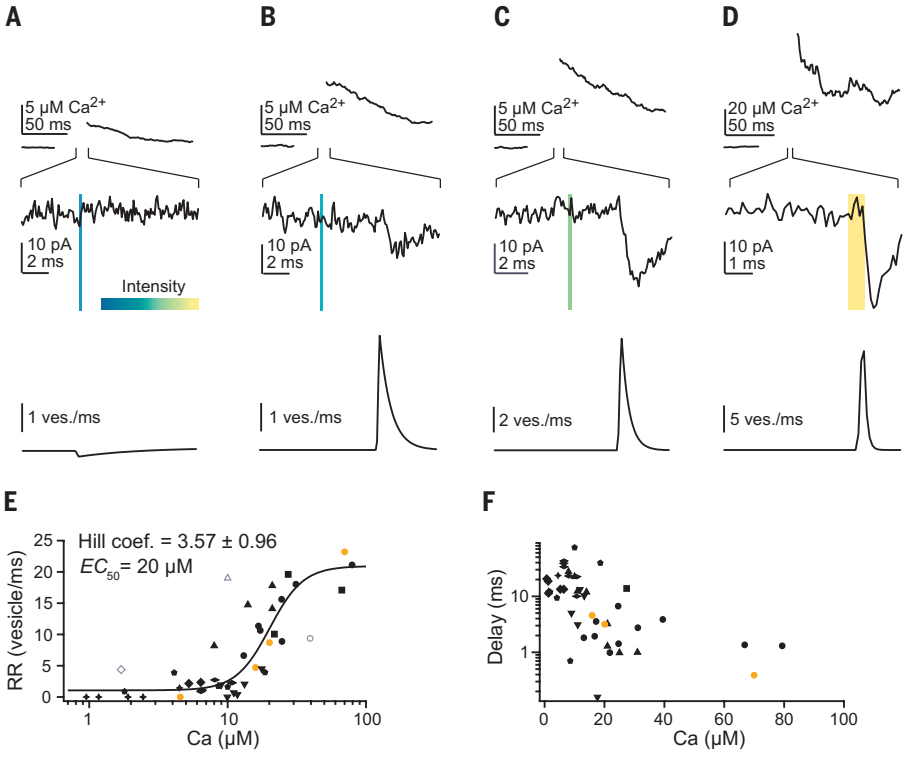

Fig. 3. Ca^{2+} dependency of transmitter release from L5PN presynaptic boutons. (**A** to **D**) UV flash–induced $\Delta[Ca^{2+}]_i$ signals (top) recorded from an individual bouton and the corresponding uvEPSCs (middle) and release rates (bottom). Bars indicate flash intensities (color code, 0 to 100%) and durations (bar width). (**E**) Dose-response curve for the dependency of peak release rates (RRs) on the corresponding elevations in presynaptic $[Ca^{2+}]_i$ ($n = 45$ recordings from 8 cells). Data from individual cells are shown as different symbols. The orange points are from the example shown in (A). The solid line shows a fit with a Hill function to the data. Open symbols indicate outliers from different cells that were excluded during fitting. (**F**) Dependency of synaptic delays on presynaptic $\Delta[Ca^{2+}]_i$. Data from individual cells are shown using the same symbols as in (E). Again, the orange points belong to the example shown in (A).

bouton, giving rise to peak release rates per vesicle per millisecond (*3*, *6*) (Fig. 4D). The size of the RRP was estimated from the amplitude of cumulative release curves or, in the case of the biexponential curves, from the amplitude of the fast component (*6*, *26*). On average, the RRP estimate was 4.9 ± 2.5 (mean ± SD) vesicles per bouton. Given that the total synaptic connection is formed by ~3.5 boutons (*30*), we obtain a total RRP of ~17 vesicles.

Next, we quantified AP-mediated release rates in the same way from a subset of pairs of L5PNs from which the flash-evoked release rates were obtained. We found a median peak release rate of 2.1 per vesicle per millisecond (1.3 to 3.0 per vesicle per millisecond, $n = 5$ cells). Superimposing these values with the Hill fit to the dose-response curve of the flash-induced release rates showed that the local $\Delta[Ca^{2+}]_i$ at Syt1 during an AP reached a median peak value of 20.4 μM and that AP-mediated $\Delta[Ca^{2+}]_i$ span a range of 14.7 to 31.8 μM (Fig. 4D). These data indicate that AP-evoked release rates span the dynamic range of the dose-response curve for photolysis-evoked release, with a median value corresponding to its EC_{50}. Thus, the dynamic range of the curve reflects the physiologically most relevant range.

Functional differences between Syt1- and Syt2-triggered release

To gain quantitative insights into the kinetics of Ca^{2+}-triggered release at L5PN synapses and for comparison with Syt2-triggered release, we established a kinetic model able to describe the experimental photolysis dose-response curve (Fig. 5). We first modeled the expected $\Delta[Ca^{2+}]_i$ time course after flash photolysis, using a detailed model of DM-nitrophen (DMn) uncaging (*34*) that included the indicator dye (fig. S8). This model indicated that, similar to previous reports (*2*, *26*), under our recording conditions, the simulated time course of $\Delta[Ca^{2+}]_i$ was reliably reported by the indicator dye ~0.5 ms after the flash. Hence, as for the experimental data, for modeling the Ca^{2+} dependency of release, we used the $\Delta[Ca^{2+}]_i$ reported by the dye.

Similar to Syt2, Syt1 comprises five Ca^{2+} binding sites (*35*), and the n_H value that we obtained is consistent with at least four binding steps. Therefore, we assumed five Ca^{2+} binding steps for Syt1, followed by fusion from the fully Ca^{2+}-bound sensor (Fig. 5A and fig. S9). First, we tested several previously published Syt2 models (*2*, *6*, *18*, *23*) but found that none of them could describe our data. Attempts to adjust the parameters to obtain a satisfactory fit failed for any of these models. To exclude methodological reasons for the discrepancy compared with our data, we quantified presynaptic release rates and $\Delta[Ca^{2+}]_i$ at Syt2-expressing synapses connecting PCs in the cerebellar cortex, using the same methodology as that used for the L5PNs (Fig. 5C). The dose-response curve obtained showed a shallow and nonsaturating dependency of release onto $\Delta[Ca^{2+}]_i$. In particular in the dynamic range, the Syt2 curve was much shallower than the Syt1 curve, without saturation at $\Delta[Ca^{2+}]_i$ up to 75 μM. Notably, published Syt2 models fit the data from PC-PC synapses well (Fig. 5C), which suggests that methodological reasons are unlikely to be the cause of the observed differences between our Syt1 data and the published Syt2 models.

We identified the realization of cooperativity in the Ca^{2+} unbinding rates in the Syt2 models as the main reason. When we instead implemented positive cooperativity in the forward binding rates, we readily obtained a model that well fit the L5PN dose-response curve as well as the Ca^{2+} dependency of the synaptic delays (fig. S9). The fit could be improved for high $\Delta[Ca^{2+}]_i$, if a Ca^{2+}-dependent priming step with Michaelis-Menten kinetics was added to the model (Fig. 5; Pearsons $\Delta p\chi^2 = 0.27$ between models). This may indicate that during larger Ca^{2+} elevations (>~18 to 20 μM), release is boosted through vesicle recruitment, consistent with the occasional occurrence of biexponential uvEPSCs at larger $\Delta[Ca^{2+}]_i$ (Fig. 2B). It appears that both processes, release and recruitment, cannot be accelerated further by Ca^{2+} elevations above ~35 μM.

The Ca^{2+} dependency of release as quantified at cerebellar PC synapses and reported by the Syt2 models was rather shallow in the dynamic range, with slow saturation at high $\Delta[Ca^{2+}]_i$. Hill fits to the simulations with the Syt2 models (Fig. 5C) gave EC_{50} values between 63 and 82 μM. These results indicate that Syt1-triggered release from L5PN boutons has three- to fourfold higher Ca^{2+} sensitivity with a much stronger Ca^{2+} dependency in the dynamic range compared with Syt2-triggered release.

Discussion

Our results provide a kinetic description of the Ca^{2+} dependency of Syt1-triggered release from neocortical boutons. We identified major differences to Syt2-triggered release from cerebellar boutons. Our

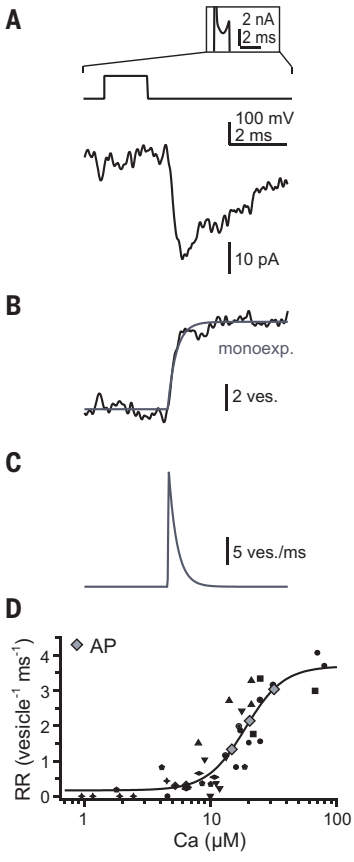

Fig. 4. AP-evoked release rates. (**A**) Example of an action current (inset, top)–evoked EPSC (bottom) from the same L5PN pair as in Fig. 2. (**B**) Cumulative release rate obtained from the EPSC in (A) fit with an exponential function. (**C**) Time course of the release rate derived by differentiation of the fit in (B). (**D**) Dose-response curve from Fig. 3E with peak release rates being normalized to the size of the RRP of each bouton. Outliers were omitted for clarity (open symbols in Fig. 3E). Diamonds represent AP-mediated peak release rates (25%, 50%, and 75% quartiles) superimposed on the Hill fit.

findings account for differential release properties of neocortical and hindbrain synapses, in particular the high p_v (~0.63) and high synaptic reliability observed in the neocortex (*11*, *29*, *30*, *36*, *37*). Furthermore, the dynamic range could provide a framework for enhanced plasticity induced by Ca^{2+} buffers (figs. S10 and S11).

The EC_{50} of 20 μM that we found is ~10-fold lower than for the isolated C2B domain of Syt1 but approximately fourfold higher than for the C2B domain in the presence of PIP_2 (*38*). Therefore, the details of the context into which Syt1 is embedded are critical for determining the Ca^{2+} sensitivity of release. In vivo, Ca^{2+} sensors are integrated in a supramolecular protein complex and interact with lipids, which further influence their Ca^{2+} binding (*35*, *38*–*40*). Thus, it was required to quantify the Ca^{2+} sensitivity of Syt1-triggered release at synaptic boutons in brain tissue with intact presynaptic release machinery. Phrases such as "Syt1 curve" or similar in the manuscript are simplifications used to improve readability. Our results show that the rate constants for Ca^{2+} binding and fusion in neocortical boutons are orders of magnitude higher than those of Syt1-triggered fusion of dense core vesicles in chromaffin cells (*41*, *42*). Furthermore, our results differ from those obtained previously with the uncaging method for Syt1-triggered release in cultured autaptic hippocampal neurons (*43*). There, the dose-response curve could be fitted with a classical Syt2 model. First, differences between cell culture and acute slices and differences between synapses in archicortex and neocortex may contribute to the differential findings. Results obtained in culture may in particular reflect a developmentally more immature state. In acute slices, a developmentally transient contribution of Syt1 to triggering release showed a shallow and nonsaturating Ca^{2+} dependency in the immature calyx (age-dependent slope of 0.85 or 1.57) (*20*). Second, in the hippocampal cultures, simultaneous measurements of the uncaging-induced $\Delta[Ca^{2+}]_i$ in boutons had not been feasible, and peak release rates were correlated to the dendritic $\Delta[Ca^{2+}]_i$. Our data suggest that the previous findings from immature or cultured synapses are not representative for the Ca^{2+} sensitivity of Syt1-triggered release in the matured cortex.

Our results from L5PNs and PCs indicate that the Ca^{2+} dependency of Syt1-triggered release deviates substantially from that of Syt2-triggered release, with our results from PCs being consistent with previous results for Syt2 [(*2*, *6*, *18*, *20*, *26*), but see (*3*)]. First, Syt1-triggered release had approximately three- to fourfold higher affinity. Second, the dose-response curve for Syt1 was steeper in the dynamic range between ~10 and ~30 μM $\Delta[Ca^{2+}]_i$ compared with the corresponding Syt2 curves. Finally, Syt1-triggered release showed pronounced saturation above the dynamic range, whereas the Syt2 curve did not saturate for $\Delta[Ca^{2+}]_i$ up to 75 μM. Overall, these differences necessitated establishing a model to describe the Ca^{2+} dependency of Syt1-triggered release in the neocortex.

The estimates of peak release rates and the degree of saturation can be influenced by priming (*6*, *26*). At synapses with rapid vesicle recruitment and sizable replenishment pools, this can even prevent dose-response curves from saturation (*26*). We also found that the Syt1 curve was better described in the upper range of the $\Delta[Ca^{2+}]_i$ by a model that incorporated a Ca^{2+}-dependent priming step. Yet, priming did not prevent saturation of the curve. This is consistent with observations suggesting that the immediate replenishment pool of L5PN boutons is rather limited (*44*).

Release sensor models are important tools for quantifying functional presynaptic nanotopographies (*4*, *5*, *8*–*13*). We previously measured the median AP-mediated Ca^{2+} transient amplitude in individual boutons to be 124 nM (77 to 208 nM) and estimated the nanodomain coupling distance between a single $Ca_v2.1$ channel and the vesicular release sensor to be ~7 nm (*11*) at the L5PN synapse using a Syt2 model (*23*). With the Syt1 models established in this work, we refine this estimate to a range of 11 to 16 nm (fig. S10), which is still a tight nanodomain coupling. The corresponding estimates for the amplitudes of the local AP-mediated $\Delta[Ca^{2+}]_i$ at the sensor are 35 to 21 μM. In line with this estimate of $\Delta[Ca^{2+}]_i$, we found that AP-mediated release rates cover the dynamic range of the Syt1 dose-response curve with a median value almost identical to the EC_{50} of 20 μM. Thus, AP-mediated release from neocortical boutons will be highly sensitive to modulations in $\Delta[Ca^{2+}]_i$ in the dynamic range.

To further pursue this notion, we incorporated either Syt1 or Syt2 into previously published models of L5PN active zones (*11*) with nanodomain or microdomain coupling (fig. S11). Irrespective of the coupling topography, Syt1-triggered release was less sensitive to variations in the channel to sensor distances compared with Syt2-triggered release. This is due to the higher Ca^{2+} affinity of Syt1 and provides an explanation for the high reliability of neocortical synapses that was found to be independent of age and the details of the presynaptic coupling topography (*11*, *30*, *45*). In loose microdomain coupling, which was found in the young developing neocortex (*11*, *45*), Syt1-triggered release was approximately twofold more sensitive to the presence of a slow Ca^{2+} buffer compared with Syt2-triggered release. This is because of the steep slope of the Ca^{2+} sensitivity of Syt1 in the dynamic range. For Syt2-triggered release, loose microdomain coupling has previously been shown to provide a framework for enhanced plasticity resulting from Ca^{2+} buffering (*13*). We show that the properties of Syt1 further expand the possibilities for plastic regulation of release through Ca^{2+} buffering in the regime of loose microdomain coupling.

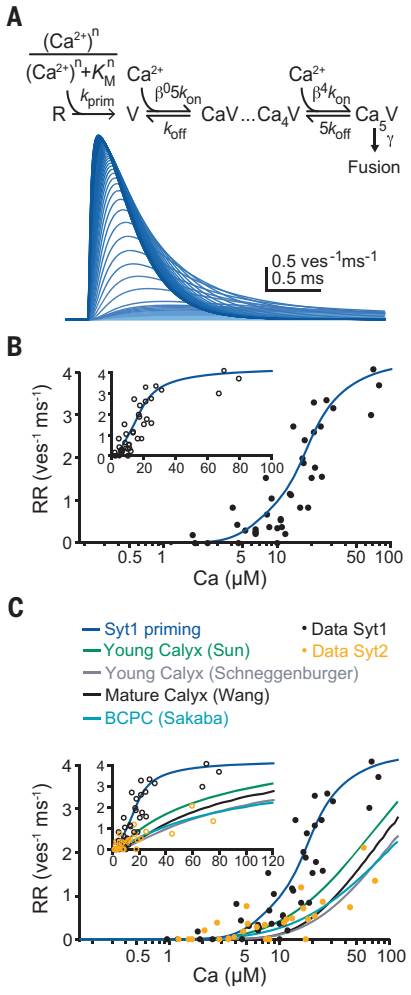

Fig. 5. The Ca^{2+} dependency of Syt1- versus Syt2-triggered release. (**A**) (Top) Scheme of the priming model of the Ca^{2+} dependency of release from L5PN boutons. The model covers a Ca^{2+}-dependent priming step, five steps for binding of Ca^{2+} to Syt1 with positive cooperativity (β), and Ca^{2+}-independent fusion from the fully Ca^{2+}-occupied sensor (γ). (Bottom) Release rates simulated for increasing $[Ca^{2+}]_i$ with the model. (**B**) Fit of the priming model (blue curve) to the dose-response curve of the peak release rates (RRs) from Fig. 4D (inset; linear scaling). (**C**) Comparison of experimental data and models of the Ca^{2+} dependency of release triggered by Syt1 or Syt2. Syt1 data (black points) from Fig. 4D are compared with data for Syt2-triggered release from PC boutons (orange points). The Syt1 priming model (blue curve) is compared with four different Syt2 models: Young calyx of Held in gray (*2*) and green (*18*), mature calyx (black) (*22*), and GABAergic basket cell (BC) to PC synapse (light blue) (*6*). Note that the published models cover our data from PC boutons well without further fitting.

Thus, the combination of high affinity with steep Ca^{2+} dependency of Syt1-triggered release can promote both high-fidelity synaptic transmission at moderate local presynaptic Ca^{2+} elevations as well as enhanced plasticity. This will make neocortical synapses more complex computational devices, which could expand the computational power of cortical microcircuits.

REFERENCES AND NOTES

1. T. C. Südhof, *Angew. Chem. Int. Ed.* **53**, 12696–12717 (2014).
2. R. Schneggenburger, E. Neher, *Nature* **406**, 889–893 (2000).
3. J. H. Bollmann, B. Sakmann, J. G. Borst, *Science* **289**, 953–957 (2000).
4. E. Eggermann, I. Bucurenciu, S. P. Goswami, P. Jonas, *Nat. Rev. Neurosci.* **13**, 7–21 (2012).
5. G. Bornschein, H. Schmidt, *Front. Mol. Neurosci.* **11**, 494 (2019).
6. T. Sakaba, *Neuron* **57**, 406–419 (2008).
7. H. Taschenberger, A. Woehler, E. Neher, *Proc. Natl. Acad. Sci. U.S.A.* **113**, E4548–E4557 (2016).
8. I. Bucurenciu, A. Kulik, B. Schwaller, M. Frotscher, P. Jonas, *Neuron* **57**, 536–545 (2008).
9. N. Rebola *et al.*, *Neuron* **104**, 693–710.e9 (2019).
10. H. Schmidt *et al.*, *Curr. Biol.* **23**, 244–249 (2013).
11. G. Bornschein, J. Eilers, H. Schmidt, *Cell Rep.* **28**, 1410–1418.e4 (2019).
12. Y. Nakamura *et al.*, *Neuron* **85**, 145–158 (2015).
13. N. P. Vyleta, P. Jonas, *Science* **343**, 665–670 (2014).
14. J. J. Chen *et al.*, *Neuron* **112**, 755–771.e9 (2024).
15. J. Xu, T. Mashimo, T. C. Südhof, *Neuron* **54**, 567–581 (2007).
16. F. Berton, C. Iborra, J. A. Boudier, M. J. Seagar, B. Marquèze, *J. Neurosci.* **17**, 1206–1216 (1997).
17. A. Maximov, T. C. Südhof, *Neuron* **48**, 547–554 (2005).
18. J. Sun *et al.*, *Nature* **450**, 676–682 (2007).
19. A. Zeisel *et al.*, *Science* **347**, 1138–1142 (2015).
20. O. Kochubey, N. Babai, R. Schneggenburger, *Neuron* **90**, 984–999 (2016).
21. X. Lou, V. Scheuss, R. Schneggenburger, *Nature* **435**, 497–501 (2005).
22. L. Y. Wang, E. Neher, H. Taschenberger, *J. Neurosci.* **28**, 14450–14458 (2008).
23. O. Kochubey, Y. Han, R. Schneggenburger, *J. Physiol.* **587**, 3009–3023 (2009).
24. F. Felmy, E. Neher, R. Schneggenburger, *Neuron* **37**, 801–811 (2003).
25. G. Bornschein *et al.*, *J. Physiol.* **591**, 3355–3370 (2013).
26. A. Eshra, H. Schmidt, J. Eilers, S. Hallermann, *eLife* **10**, e70408 (2021).
27. Y. Zhang *et al.*, *J. Neurosci.* **34**, 11929–11947 (2014).
28. Y. Zhang *et al.*, *Neuron* **89**, 37–53 (2016).
29. H. Markram, J. Lübke, M. Frotscher, A. Roth, B. Sakmann, *J. Physiol.* **500**, 409–440 (1997).
30. A. Frick, D. Feldmeyer, M. Helmstaedter, B. Sakmann, *Cereb. Cortex* **18**, 397–406 (2008).
31. W. Van der Kloot, *J. Physiol.* **402**, 595–603 (1988).
32. J. C. Magee, E. P. Cook, *Nat. Neurosci.* **3**, 895–903 (2000).
33. S. Chanda, M. A. Xu-Friedman, *J. Neurophysiol.* **103**, 1915–1926 (2010).
34. G. C. Faas, K. Karacs, J. L. Vergara, I. Mody, *Biophys. J.* **88**, 4421–4433 (2005).
35. T. C. Südhof, *Neuron* **80**, 675–690 (2013).
36. H. Markram, M. Tsodyks, *Nature* **382**, 807–810 (1996).
37. R. A. Silver, J. Lubke, B. Sakmann, D. Feldmeyer, *Science* **302**, 1981–1984 (2003).
38. G. van den Bogaart, K. Meyenberg, U. Diederichsen, R. Jahn, *J. Biol. Chem.* **287**, 16447–16453 (2012).
39. Z. Xia, D. R. Storm, *Nat. Rev. Neurosci.* **6**, 267–276 (2005).
40. A. T. Brunger, U. B. Choi, Y. Lai, J. Leitz, Q. Zhou, *Annu. Rev. Biophys.* **47**, 469–497 (2018).
41. T. Voets, *Neuron* **28**, 537–545 (2000).
42. J. B. Sørensen, R. Fernández-Chacón, T. C. Südhof, E. Neher, *J. Gen. Physiol.* **122**, 265–276 (2003).
43. A. Burgalossi *et al.*, *Neuron* **68**, 473–487 (2010).
44. G. Bornschein, S. Brachtendorf, H. Schmidt, *Front. Synaptic Neurosci.* **11**, 36 (2020).
45. O. Ohana, B. Sakmann, *J. Physiol.* **513**, 135–148 (1998).
46. H. Schmidt, Hartmut-Schmidt/Science-2025: Syt1_v1.0, Zenodo (2025). https://doi.org/10.5281/zenodo.15064640.

ACKNOWLEDGMENTS

We thank G. Bethge for technical assistance and C. Simon for providing antibodies. We thank M. Morawski and R. Stassart for supporting this work with the free use of a Zeiss Airyscan LSM 880 and their technical expertise. **Funding:** This work was supported by grants from the German Research Foundation (DFG SCHM1838/2-1 to H.S.) and the European Research Council (ERC CoG 865634 to S.H.). **Author contributions:** Conceptualization: H.S.; Data analysis: G.B., S.B., H.S., A.R., J.H.; Funding acquisition: H.S., S.H.; Investigation: G.B., S.B., A.E., A.R.; Methodology: all authors; Modeling: S.H., H.S.; Resources: J.E., R.K., H.S., J.H.; Supervision: H.S.; Visualization: G.B., S.B., H.S., A.R., J.H.; Writing – original draft: G.B., S.B., H.S.; Writing – review & editing: all authors. **Competing interests:** The authors declare that they have no competing interests. **Data and materials availability:** All data are available in the main text or supplementary materials. The Mathematica code of the models is available through Github (https://github.com/Hartmut-Schmidt/Science-2025/tree/Syt1_v1.0) and Zenodo (*46*). **License information:** Copyright © 2025 the authors, some rights reserved; exclusive licensee American Association for the Advancement of Science. No claim to original US government works. https://www.science.org/about/science-licenses-journal-article-reuse. This research was funded in whole or in part by the European Research Council (ERC CoG 865634); as required, the author will make the Author Accepted Manuscript (AAM) version available under a CC BY public copyright license.

SUPPLEMENTARY MATERIALS

science.org/doi/10.1126/science.adp0870
Materials and Methods; Figs. S1 to S11; Table S1; References (*47*–*65*);
MDAR Reproducibility Checklist

Submitted 7 March 2024; resubmitted 10 February 2025; accepted 25 April 2025
10.1126/science.adp0870

MACROECOLOGY

Consistent energy-diversity relationships in terrestrial vertebrates

Marco Túlio P. Coelho[1]*, Elisa Barreto[1], José Alexandre F. Diniz-Filho[2], Thiago F. Rangel[2], Eliška Bohdalková[3,4], David Storch[3,4], Yun-Ting Jang[5,6], Mikael Pontarp[5], Fernanda Cassemiro[2], Matheus Lima de Araujo[2], Pincelli M. Hull[1,7,8], Catherine H. Graham[1]

Ecologists have long proposed that environments providing more energy can support more species, yet empirical evidence frequently contradicts this expectation. We argue that such inconsistencies result from confounding geographical influences that mask the true relationship between species richness and energy-related factors. Here, by comparing species richness across different climate conditions, we disentangle the direct effects of temperature, precipitation, and primary productivity from the confounding impacts of the area and isolation of various climates. Using a global analysis of terrestrial vertebrates, we reveal clear and consistent relationships between energy-related factors and species richness. Our findings clarify existing ecological theory and illustrate how adopting a climate space perspective advances biodiversity research, providing critical insights into biodiversity patterns and their responses to environmental change.

It has long been hypothesized that biodiversity is highest in warm, wet environments where ecosystem productivity is high (*1*–*3*). According to the species-energy theory, increased energy availability supports greater biodiversity through mechanisms involving solar energy and water-energy dynamics (*4*–*6*). Solar energy accelerates biological processes, influencing rates of reproduction, evolution, and metabolism (*7*, *8*). Specifically, species richness is expected to increase with temperature, with one precise prediction from the metabolic theory of ecology (MTE) proposing that the rate of this increase should match the activation energy of metabolic processes (*9*, *10*). However, temperature alone does not fully account for patterns of biodiversity. Water availability is equally crucial because it enables photosynthesis and nutrient storage, effectively converting solar energy into productivity (*11*, *12*). Increased productivity supports larger populations, thus facilitating greater species richness compared with less-productive environments (*5*, *13*). Accordingly, the general expectation is that species richness should be higher in environments with greater water availability and productivity.

Despite these expectations, empirical studies reveal considerable variability in the relationship between energy availability and species diversity across regions and taxa, often challenging theoretical predictions (*14*–*16*). A comprehensive global analysis of terrestrial vertebrates showed substantial regional variation in the causal pathways linking temperature, water availability, and productivity to species richness, with effects being both positive and negative (*16*). Although many taxa peak in species richness in regions with high productivity, others do so in areas with low to moderate productivity (*17*). In colder climates, water scarcity is generally less critical than solar radiation deficits (*15*, *18*), but at the global scale, this pattern is observed only in reptiles among all terrestrial vertebrates (*16*). In addition, associations between species richness and productivity are less variable than those between species richness and temperature (*15*). Finally, empirical data often challenge the MTE's prediction that the relationship between species richness and temperature reflects metabolic activation energy (*14*, *19*, *20*). These variations and discrepancies between theory and empirical data suggest that the investigation of species-energy theory needs a fresh perspective.

The conventional approach to studying the species-energy relationship is to correlate species richness across different geographic locations with an energy-related measure from the same locations (*15*, *16*, *18*). However, additional local, regional, and continental factors, such as dispersal limitation, lineage splitting, species interactions, and historical events, also influence local species richness (*21*, *22*). Therefore, this traditional approach struggles to separate location-specific geographic confounds from the direct effects of energy-related variables (*23*).

An alternative is to study species-energy relationships using a climate space approach, which explicitly accounts for geographical confounds. This approach groups regions sharing similar environmental conditions into discrete "climate bins," defined by equal intervals of temperature and precipitation irrespective of their geographical position (*24*, *25*). Thus, each climate bin represents a narrow range of climate conditions, potentially encompassing multiple geographically disconnected areas experiencing that specific climate (e.g., hot and wet regions in the Amazon and Borneo; cold and dry regions in Patagonia and the Gobi). However, we do not attempt classification of all of the narrowly defined climate types. Instead, we quantify the number of species currently existing under each climate condition, in addition to two key geographic factors: (i) climate area, the total terrestrial extent occupied by a climate condition, and (ii) climate isolation, describing how geographically dispersed a climate condition is globally. These metrics matter because if specific energy-related conditions are rare or ephemeral on Earth, then few species will be found in these conditions due to the limited ability of species to disperse to, persist in, or adapt to these conditions (*23*, *24*, *26*, *27*). Therefore, fully understanding species-energy relationships requires knowledge of both the area and geographic distribution of energy-related conditions.

Here, we evaluated species-energy relationships across environmental dimensions using global terrestrial vertebrate distribution data and environmental variables compiled from publicly available datasets (*28*–*33*). First, we tested the predictions of the MTE (*9*, *10*), which considers a single energy dimension based on the association between temperature and species richness. Then, we broadened our analysis to include various energy factors commonly used to define energy pathways (*16*), including temperature, precipitation, and productivity, as well as geographical properties of climate such as climate area and isolation (*24*). We anticipated that general patterns of species-energy relationships would emerge when the environment directly defines the units of analysis.

A single energy pathway to biodiversity through the MTE

The MTE provides a precise theoretical prediction for how temperature influences species richness: The logarithm of species richness should decrease linearly with the inverse of temperature ($1/kT$), where k is the Boltzmann constant and T is temperature in kelvin (*9*, *10*). This prediction was initially proposed for ectotherms because of their reliance on external temperatures, with an expected slope between −0.6 and −0.7 (*9*, *10*). Consequently, endotherms, which regulate their internal body temperature independently of environmental temperatures, are not expected to conform to this prediction (*33*).

When we defined geographic space using equal-area grid cells of 110 × 110 km, an optimal resolution for minimizing errors such as false presences in global macroecological analyses (*16*, *34*), and evaluated the relationship between the logarithm of species richness and the inverse of temperature of a given cell, both the form of the relationship

[1]Swiss Federal Institute for Forest, Snow and Landscape Research, Birmensdorf, Switzerland. [2]Departamento de Ecologia, Universidade Federal de Goiás, Goiânia, Brazil. [3]Center for Theoretical Study, Charles University and the Academy of Sciences of the Czech Republic, Prague, Czech Republic. [4]Department of Ecology, Faculty of Science, Charles University, Prague, Czech Republic. [5]Department of Biology, Lund University, Lund, Sweden. [6]Department of Plant Physiology, Umeå Plant Science Centre, Umeå Universitet, Umeå, Sweden. [7]Department of Earth and Planetary Sciences, Yale University, New Haven, CT, USA. [8]Yale Peabody Museum, New Haven, CT, USA. ***Corresponding author. Email: marcotpcoelho@gmail.com**

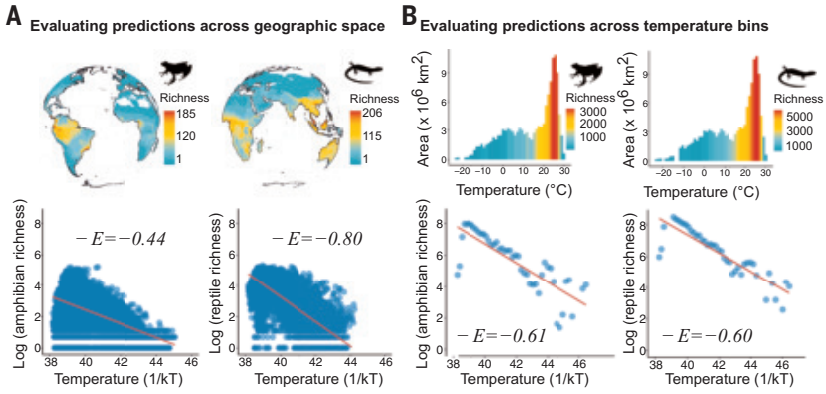

Fig. 1. Evaluating the predictions of the MTE. The MTE posits that species richness logarithmically decreases with the inverse of temperature ($1/kT$), where k is the Boltzmann constant and T is the temperature in kelvin. The expected slope, determined by metabolic activation energy, lies between −0.6 and −0.7. (**A**) Test of this prediction in geographic space by dividing the world into 110 × 110 km cells. The estimated slopes for ectotherms (amphibians: $\beta = -0.44$; reptiles: $\beta = -0.80$) show variation and deviate from the expected slopes of −0.6 to −0.7. (**B**) Evaluation of predictions within temperature bins, where empirical data show slopes (amphibians: $\beta = -0.607$, reptiles: $\beta = -0.602$) that align closely with the theoretical predictions. These results remain robust across different numbers of temperature bins [fig. S1 and tables S1 to S6 (*33*)]. This analysis highlights that when the primary focus is on climate, making spatial processes secondary, the empirical data align well with the predictions of the MTE.

and the estimated slopes for ectotherms (amphibians: $\beta = -0.44$ and reptiles: $\beta = -0.80$; Fig. 1A) were inconsistent with the MTE but consistent with previous research (*14*, *35*). The triangular distribution of residuals, indicating non-homoscedasticity, and the slopes falling outside of the expected range of metabolic activation energy provide clear evidence that the theory's predictions fail when tested in geographical space (Fig. 1A). These results align with previous empirical analyses that consistently found slopes deviating from MTE's expectations across different organism groups and regions (*14*, *19*, *20*).

By contrast, when temperature was the primary focus of analysis and we calculated the number of species within temperature bins, the empirical data yielded a pattern much more consistent with the predictions of the MTE (Fig. 1B), with slopes falling within the expected range for the activation energy of metabolic reactions (amphibians: $\beta = -0.607$; reptiles: $\beta = -0.602$; Fig. 1B). These results remained robust across different numbers of temperature bins [fig. S1 and tables S1 to S6 (*33*)]. Deviations from the expected linear model appeared in the residuals at the highest and lowest temperatures (Fig. 1B), suggesting that additional energy-related pathways are necessary to fully capture empirical richness patterns (see the "Multiple energy pathways to biodiversity" section below). Nonetheless, the marked differences between geographic and climate space analyses indicate that the expected relationship between species richness and temperature is obscured in geographic space because a multitude of factors such as dispersal limitation, species interactions, and local historical contingencies influence geographic patterns of species richness.

Multiple energy pathways to biodiversity

Building on the role of temperature, we incorporated precipitation to define a climate space (Fig. 2), capturing multiple energy-related pathways to biodiversity because both warmth and water availability shape ecosystem productivity and influence species richness. To test multiple energy pathways to biodiversity, we used a structural equation model (*33*). We defined climate space based on temperature and the square root of precipitation (Fig. 2). This transformation was applied to precipitation because small differences in precipitation can have large biological significance in low-precipitation environments (*36*).

In this temperature-precipitation climate space (Fig. 2), we demarcated climate bins and calculated species richness, geographical area, and the isolation of each climate (Fig. 2). We also included three

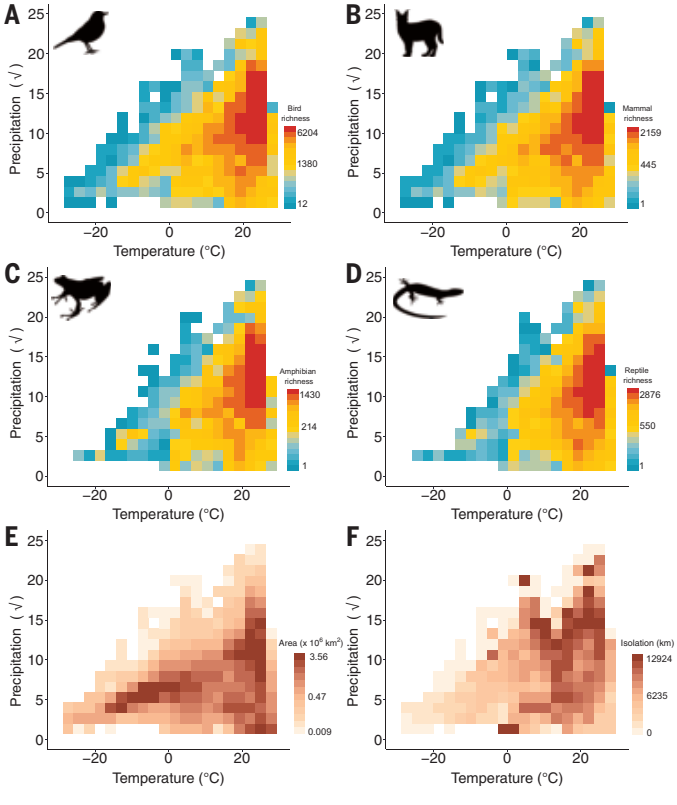

Fig. 2. Species richness, climate area, and climate isolation measured within temperature (°C) and precipitation ($\sqrt{}$kg/m^2) bins. (**A** to **D**) Diversity of terrestrial vertebrate groups within each environmental bin quantifying the number of species that share similar temperature and precipitation conditions. (**E** and **F**) Geographical area (E) and isolation of temperature and precipitation bins (F). Climate area is quantified by the total terrestrial surface area covered by the climatic condition. Isolation is assessed through the average geodesic distance between separate areas experiencing the same climatic conditions, highlighting the physical gaps between habitats with similar climate characteristics.

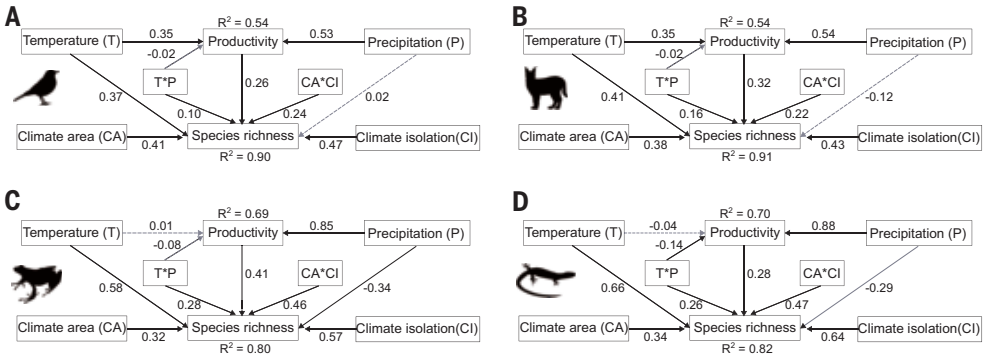

Fig. 3. Structural equation modeling of energy factors on terrestrial vertebrates. The analysis breaks down direct influences, indirect pathways, and variable interactions for various tetrapod groups: birds (**A**), mammals (**B**), amphibians (**C**), and reptiles (**D**). Standardized effect sizes were used, allowing for comparison of the magnitude of the importance of each variable across groups. Before standardization, some variables, such as species richness, net primary productivity, climate area, and isolation, were log-transformed to ensure linear relationships and to improve model fit (*33*). Additionally, because the climate space is based on the square root of precipitation, precipitation is represented by its square root in the models (*33*). Despite a consistent directional effect of variables across all groups, differences in the magnitude of temperature, area, and isolation effects are observed between endothermic species (birds and mammals) and ectothermic species (amphibians and reptiles). The R^2 values presented above the diagrams quantify the proportion of variance in productivity explained by temperature and precipitation, whereas the R^2 values shown below the diagrams reflect the cumulative direct effects of all variables on species richness. In the structural diagrams, solid lines denote statistically significant effects, indicating robust relationships between variables, and dashed lines represent nonsignificant effects [table S7 (*33*)]. Although not shown directly in the diagrams, indirect effects are derived from the product of direct effects along linked pathways. All variables exhibit low collinearity within this resolution of climate space (20 equal-interval bins for each variable; Fig. 2), as demonstrated by their variance inflation factor [VIF <5; table S7 (*33*)]. Analyses at finer resolutions of climate space were not conducted due to high collinearity among temperature, precipitation, and productivity, which affects model coefficient estimation [figs. S2 to S9 (*33*)]. Spatial autocorrelation tests confirmed that no significant autocorrelation was present in the residuals of the models [fig. S26 (*33*)].

energy-related factors in our models: temperature, precipitation, and productivity. Indirectly, temperature and precipitation can influence species richness through their effects on productivity [Fig. 3 (*11*, *12*, *16*)]. Beyond direct and indirect pathways, previous studies support modeling interaction terms as multiplicative combinations such as temperature × precipitation, where water availability is expected to have a stronger influence in warmer environments (*18*), and climate area × isolation, where larger and more isolated climates are predicted to support greater species richness through reduced connectivity and enhanced diversification (*24*).

Despite the high degree of variability and context dependence observed in geographical analyses [Fig. 1A (*15*, *16*)], energy effects in climate space are consistently detected across different terrestrial vertebrate groups. The strength of these effects differs between endothermic and ectothermic species. Temperature shows a strong positive relationship with species richness across all groups (Fig. 3), particularly in ectotherms (amphibians: $\beta_{std} = 0.58$; reptiles: $\beta_{std} = 0.66$; mammals: $\beta_{std} = 0.41$; birds: $\beta_{std} = 0.37$, where β_{std} denotes standardized regression coefficients from the structural equation model). Temperature directly influences species richness in ectotherms by regulating physiological performance (*9*, *37*), and this effect occurs without a significant dependence on productivity. Therefore, there is no indirect effect of temperature on ectothermic groups through productivity (amphibians: $\beta_{std} = 0.004$; reptiles: $\beta_{std} = -0.011$), because this indirect effect reflects the product of the direct effect of temperature on productivity and the direct effect of productivity on species richness in the structural equation model.

By contrast, for endotherms, temperature indirectly affects species richness through its enhancement of ecosystem productivity (mammals: $\beta_{std} = 0.11$; birds: $\beta_{std} = 0.09$) in addition to its direct effects. This finding is consistent with early ecological literature suggesting that temperature supports endothermic species by increasing productivity (*37*, *38*), thereby providing the energy resources necessary to meet their high metabolic demands for thermoregulation.

In contrast to temperature, the direct effect of precipitation negatively affects species richness, particularly in ectotherms (amphibians: $\beta_{std} = -0.34$; reptiles: $\beta_{std} = -0.29$; mammals: $\beta_{std} = -0.12$; birds: $\beta_{std} = 0.02$). A similar pattern has been observed in plants inhabiting high-precipitation climates, where elevated water availability favors more competitive species, thus reducing coexistence and ultimately lowering species richness (*39*). This suggests that excessive precipitation can shift community dynamics by promoting competitive exclusion and decreasing biodiversity. However, precipitation remains essential for ecosystem productivity. Across all groups, precipitation exerts a positive indirect effect on species richness through its influence on productivity (amphibians: $\beta_{std} = 0.34$; reptiles: $\beta_{std} = 0.25$; mammals: $\beta_{std} = 0.17$; birds: $\beta_{std} = 0.13$). This positive indirect effect aligns with the water-energy dynamics theory (*11*, *12*), which posits that precipitation enhances biodiversity by facilitating the conversion of physical energy into ecosystem productivity, thereby supporting population growth and species diversity. Furthermore, productivity itself directly and positively affects species richness across all groups (amphibians: $\beta_{std} = 0.41$; reptiles: $\beta_{std} = 0.28$; mammals: $\beta_{std} = 0.32$; birds: $\beta_{std} = 0.26$).

The positive interaction between temperature and water availability also underscores the enhanced effect of water availability on biodiversity in warmer climates (amphibians: $\beta_{std} = 0.28$, reptiles: $\beta_{std} = 0.26$, mammals: $\beta_{std} = 0.16$, birds: $\beta_{std} = 0.10$). These results support Hawkins's proposition that water plays a greater role in limiting diversity in warmer climates than in colder ones (*18*). Geographically, this hypothesis was supported when colder climates were categorized as near the poles and warm climates as near the equator (*18*), but not for most terrestrial vertebrate groups when evaluated in a continuous way across the globe (*16*). However, in climate space, we found consistent support for Hawkins's hypothesis for all terrestrial vertebrates.

The weak negative interaction between temperature and precipitation on productivity indicates that high levels of both factors do not synergistically increase productivity, but rather tend to reduce it (amphibians: $\beta_{std} = -0.08$; reptiles: $\beta_{std} = -0.14$; mammals: $\beta_{std} = -0.02$; birds: $\beta_{std} = -0.02$). Our results are consistent with empirical studies showing that net primary productivity does not increase under simultaneous high temperature and precipitation because heat

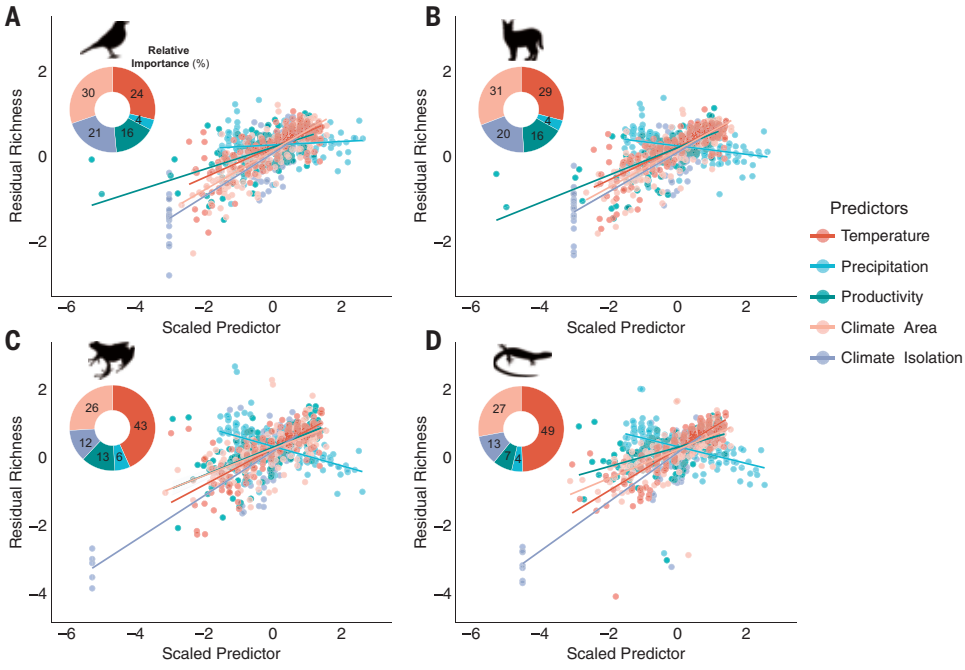

Fig. 4. Partial residual plots demonstrating predictor impact on species richness. Partial residual plots, where species richness, adjusted for the influence of other predictors, is plotted against each predictor for birds (**A**), mammals (**B**), amphibians (**C**), and reptiles (**D**). In this figure, partial residuals for each variable are overlaid on the same plot for each group, with different colors representing different predictors. As a result, residuals are repeated five times, once for each variable. Separate plots for individual predictors and species groups are provided in fig. S27 (*33*), where each partial residual plot is shown separately for better visualization. By standardizing both response variables and predictors, we align all relationships to showcase the recurrent direct influence of each variable on species richness. Accompanying donut plots illustrate the relative significance (percent variance explained) of each predictor in elucidating species richness patterns within climate space, with larger segments denoting greater importance.

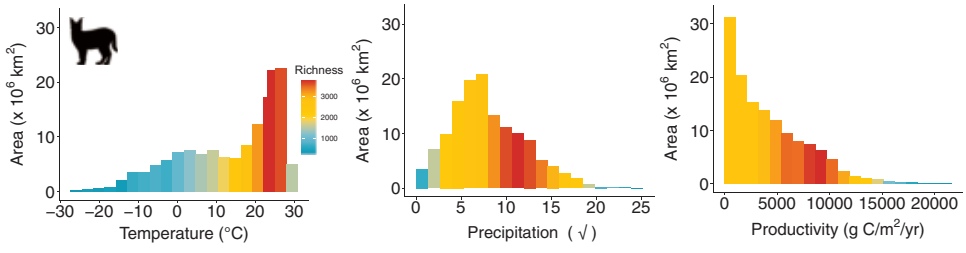

Fig. 5. Prevalence of high temperatures compared with the rarity of high precipitation and productivity on Earth. The area of climate bins is depicted by the heights of the bars, which are color-coded based on the number of mammal species per climate bin. Patterns are consistent for other groups of terrestrial vertebrates and are independent of the number of bins [figs. S10 to S21 (*33*)].

inhibits photosynthesis and excessive rainfall reduces light availability or leaches nutrients (*40*–*42*).

The positive effects of climate area (amphibians: $\beta_{std} = 0.58$; reptiles: $\beta_{std} = 0.66$; mammals: $\beta_{std} = 0.38$; birds: $\beta_{std} = 0.41$) and isolation (amphibians: $\beta_{std} = 0.57$; reptiles: $\beta_{std} = 0.64$; mammals: $\beta_{std} = 0.43$; birds: $\beta_{std} = 0.47$) are strong and more pronounced in ectotherms. This stronger effect is likely due to ectotherms' lower dispersal capacity and slower rates of niche evolution compared with endotherms (*43*). By contrast, endotherms exhibit greater physiological plasticity and environmental tolerance, allowing them to regulate body temperature more effectively, which alleviates some of the dispersal limitations imposed by climatic niche constraints (*44*). With fewer dispersal barriers, endotherms maintain higher gene flow among populations occupying different climatic regions, thereby reducing the influence of climate area and isolation on species richness. Consequently, endotherms are less likely to experience speciation driven by climatic isolation than ectotherms.

Recurrent patterns of species-energy relationships become more apparent when partial relationships, those in which the effect of each predictor is controlled by all other predictors, are visually inspected (Fig. 4). Direct effects on species richness account for ~90% of the variation in endotherm richness (birds: $R^2 = 0.90$; mammals: $R^2 = 0.91$) and ~80% of the variation in ectotherm richness (amphibians: $R^2 = 0.80$; reptiles: $R^2 = 0.82$) in climate space (Figs. 3 and 4). A large portion of the variation in species richness among endotherms and ectotherms can be explained by climate area and temperature, accounting for ~55% of the variation in endotherms and 75% in ectotherms [Fig. 4 and fig. S27 (*33*)]. This result emphasizes the critical role of both climate area and temperature in shaping species richness across thermoregulatory strategies. It also reinforces the importance of considering the geographical area occupied by energy-related conditions when studying species-energy relationships. Differences in the spatial extent of these conditions are evident: Whereas warmer conditions occupy larger areas, high-humidity and highly productive environments cover much smaller areas. This discrepancy likely influences the number of species that can inhabit such environments (Fig. 5).

Conclusions

Ecologists have long proposed that energy availability shapes biodiversity, yet decades of research have yielded inconsistent results, largely due to the confounding effects of geography. Traditional geographic units combine environmental gradients with spatially structured processes associated with the generation of species pools and dispersal histories, obscuring general patterns. By shifting to a climate space approach, we isolated environmental dimensions from geography, revealing clearer and more consistent species-energy relationships.

One such relationship is the link between temperature and species richness in ectotherms, the only energy pathway with a specific theoretical prediction from the MTE (*9*, *10*). This relationship becomes apparent within climate space, where observed slopes align with the predicted metabolic activation energy. Although this result does not resolve longstanding criticism of the theory's simplicity (*37*), it underscores the value of situating theory within its appropriate environmental context.

Incorporating precipitation, productivity, and the spatial properties of climate types further clarifies energy-richness patterns. For instance, warm climates occupy larger areas globally, whereas humid and highly productive climates are more spatially restricted. These geographic

characteristics, quantified here as climate area and isolation, capture key dimensions of how geography mediates biodiversity patterns. Controlling for them enables a clearer view of the underlying influence of energy. As ecological theory increasingly informs biodiversity projections under climate change, it is essential that models account for geographic confounders to accurately estimate the effect of energy on biodiversity patterns.

REFERENCES AND NOTES

1. J. R. Forster, in *Foundations of Biogeography: Classic Papers with Commentaries*, M. V. Lomolino, D. F. Sax, J. H. Brown, Eds. (Univ. of Chicago Press, 2004), pp. 19–27.
2. A. von Humboldt, *Views of Nature: Or Contemplations on the Sublime Phenomena of Creation* (Henry G. Bohn, 1808).
3. A. R. Wallace, *Tropical Nature, and Other Essays* (MacMillan & Co., 1878).
4. G. E. Hutchinson, *Am. Nat.* **93**, 145–159 (1959).
5. J. H. Brown, *Am. Zool.* **21**, 877–888 (1981).
6. D. H. Wright, *Oikos* **41**, 496–506 (1983).
7. K. L. Evans, P. H. Warren, K. J. Gaston, *Biol. Rev. Camb. Philos. Soc.* **80**, 1–25 (2005).
8. R. Carrara, D. P. Vázquez, *Ecography* **33**, 942–948 (2010).
9. A. P. Allen, J. H. Brown, J. F. Gillooly, *Science* **297**, 1545–1548 (2002).
10. J. H. Brown, J. F. Gillooly, A. P. Allen, V. M. Savage, G. B. West, *Ecology* **85**, 1771–1789 (2004).
11. E. O'Brien, *J. Biogeogr.* **25**, 379–398 (1998).
12. E. M. O'Brien, *J. Biogeogr.* **33**, 1868–1888 (2006).
13. D. Storch, E. Bohdalková, J. Okie, *Ecol. Lett.* **21**, 920–937 (2018).
14. B. A. Hawkins *et al.*, *Ecology* **88**, 1877–1888 (2007).
15. E. Bohdalková, A. Toszogyova, I. Šímová, D. Storch, *Ecography* **44**, 1366–1378 (2021).
16. E. Barreto *et al.*, *Glob. Ecol. Biogeogr.* **30**, 1899–1908 (2021).
17. J. Cusens, S. D. Wright, P. D. McBride, L. N. Gillman, *Ecology* **93**, 2241–2252 (2012).
18. B. A. Hawkins *et al.*, *Ecology* **84**, 3105–3117 (2003).
19. B. A. Hawkins *et al.*, *Ecology* **88**, 1898–1902 (2007).
20. A. C. Algar, J. T. Kerr, D. J. Currie, *Glob. Ecol. Biogeogr.* **16**, 170–178 (2007).
21. J. A. F. Diniz-Filho, in *The Macroecological Perspective: Theories, Models and Methods*, J. A. F. Diniz-Filho, Ed. (Springer International Publishing, 2023), pp. 203–249.
22. P. V. A. Fine, *Annu. Rev. Ecol. Evol. Syst.* **46**, 369–392 (2015).
23. M. L. Rosenzweig, *Species Diversity in Space and Time* (Cambridge Univ. Press, 1995).
24. M. T. P. Coelho *et al.*, *Nature* **622**, 537–544 (2023).
25. C. H. Graham *et al.*, *Ecol. Lett.* **28**, e70008 (2025).
26. R. H. Macarthur, E. O. Wilson, *The Theory of Island Biogeography* (Princeton Univ. Press, 1967).
27. J. Terborgh, *Am. Nat.* **107**, 481–501 (1973).
28. International Union for Conservation of Nature (IUCN), "The IUCN red list of threatened species" (2025); https://www.iucnredlist.org/en.
29. BirdLife International, "Bird species distribution data" (2025); https://datazone.birdlife.org/dataset-information.
30. U. Roll *et al.*, *Nat. Ecol. Evol.* **1**, 1677–1682 (2017).
31. D. N. Karger *et al.*, *Sci. Data* **4**, 170122 (2017).
32. M. T. P. Coelho, Species-energy relationships across environmental gradients: Data and analysis code, Figshare (2024); https://doi.org/10.6084/m9.figshare.26781022.v3.
33. See the supplementary materials.
34. J. Belmaker, W. Jetz, *Glob. Ecol. Biogeogr.* **20**, 464–474 (2011).
35. F. A. S. Cassemiro, J. A. F. Diniz-Filho, *Ecology* **91**, 3729–3738 (2010).
36. T. Raz *et al.*, *J. Zool.* **322**, 126–140 (2024).
37. A. P. Allen, J. Gillooly, J. H. Brown, in *Scaling Biodiversity*, D. Storch, P. A. Marquet, J. H. Brown, Eds. (Cambridge Univ. Press, 2007), pp. 283–299.
38. D. J. Currie, *Am. Nat.* **137**, 27–49 (1991).
39. S. Fei *et al.*, *Nat. Commun.* **9**, 5436 (2018).
40. L. R. Holdridge, *Science* **105**, 367–368 (1947).
41. E. A. G. Schuur, *Ecology* **84**, 1165–1170 (2003).
42. K. Zhu, N. R. Chiariello, T. Tobeck, T. Fukami, C. B. Field, *Proc. Natl. Acad. Sci. U.S.A.* **113**, 10589–10594 (2016).
43. J. Rolland *et al.*, *Nat. Ecol. Evol.* **2**, 459–464 (2018).
44. J. G. Boyles, F. Seebacher, B. Smit, A. E. McKechnie, *Integr. Comp. Biol.* **51**, 676–690 (2011).

ACKNOWLEDGMENTS

We thank R. Field for valuable comments on early versions of this manuscript. **Funding:** This work was supported by the Swiss National Science Foundation (SNSF grant 315230_197753 to M.T.P.C. and C.H.G.); Conselho Nacional de Desenvolvimento Científico e Tecnológico (CNPQ grants PQ304923/2023-0, PQ303467/2021-5, and 465610/2014-5 to T.F.R. and J.A.F.D.-F.); Fundação de Amparo à pesquisa do Estado de Goiás (grant 201810267000023 to T.F.R. and J.A.F.D.-F.); the Czech Science Foundation (grant GAČR 20-29554X to D.S. and E.B.); the Swedish Research Council (VR grant 2018-05115 to M.P.); Schmidt Sciences (P.M.H.); and the Swiss Federal Institute for Forest, Snow and Landscape Research (P.M.H.). **Author contributions:** Conceptualization: M.T.P.C., C.H.G., E.B., T.F.R., J.A.F.D.-F.; Formal analysis: M.T.P.C.; Funding acquisition: C.H.G.; Investigation: M.T.P.C.; Methodology: M.T.P.C.; Project administration: C.H.G.; Visualization: M.T.P.C.; Writing – original draft: M.T.P.C.; Writing – review & editing: M.T.P.C., C.H.G., E.B., J.A.F.D.-F., T.F.R., E.B., D.S., Y.-T.J., M.P., F.C., M.L.d.A., P.M.H. **Competing interests:** The authors declare no competing interests. **Data and materials availability:** Climate data and terrestrial vertebrate range maps are publicly accessible (*28*–*33*). Datasets and code for reproducibility are available at figshare (*32*).

SUPPLEMENTARY MATERIALS

science.org/doi/10.1126/science.adu2590
Materials and Methods; Supplementary Text; Figs. S1 to S27; Tables S1 to S7; References (*45*–*49*)

Submitted 30 October 2024; accepted 8 May 2025

10.1126/science.adu2590

NEUROSCIENCE

Identification of proliferating neural progenitors in the adult human hippocampus

Ionut Dumitru[1]†, Marta Paterlini[1]†, Margherita Zamboni[1], Christoph Ziegenhain[1]‡, Sarantis Giatrellis[1], Rasool Saghaleyni[2], Åsa Björklund[2], Kanar Alkass[3], Mathew Tata[1]§, Henrik Druid[3], Rickard Sandberg[1], Jonas Frisén[1]*

Continuous adult hippocampal neurogenesis is involved in memory formation and mood regulation but is challenging to study in humans. Difficulties finding proliferating progenitor cells called into question whether and how new neurons may be generated. We analyzed the human hippocampus from birth through adulthood by single-nucleus RNA sequencing. We identified all neural progenitor cell stages in early childhood. In adults, using antibodies against the proliferation marker Ki67 and machine learning algorithms, we found proliferating neural progenitor cells. Furthermore, transcriptomic data showed that neural progenitors were localized within the dentate gyrus. The results contribute to understanding neurogenesis in adult humans.

Most studies on human hippocampal neurogenesis have assessed the presence of proteins associated with neurogenesis at different stages from neural stem cells, through intermediate neural progenitor cells (INPs) and neuroblasts (hereafter referred collectively to as neural progenitor cells) to new neurons (*1*). Several studies have reported immunohistochemical evidence of neural progenitor–associated markers in the human dentate gyrus throughout life (*2*–*8*), whereas others report their absence beyond childhood, questioning the existence of adult hippocampal neurogenesis in humans (*9*–*11*). Methodological differences likely contribute to these conflicting results (*1*, *12*) and it remains open whether these markers, despite their validation in other species, reliably identify neural progenitors in humans.

Single-nucleus RNA sequencing (snRNA-seq) provides an unbiased investigation of cell types and states, surpassing marker limitations and enabling cross-species and developmental trajectory comparisons (*13*). Recent snRNA-seq studies of the adult human hippocampus identified immature neurons (*14*) but failed to identify proliferating progenitor cells (*14*, *15*), suggesting that new neurons arise through slow maturation of neuronal progenitors generated during development (*14*, *15*). Bromodeoxyuridine (BrdU) labeling, carbon dating (*16*, *17*), and mitotic generation of neurons in adult human dentate gyrus explants (*14*) support the presence of proliferating progenitors in the adult human hippocampus. Nevertheless, proliferating progenitors and a neurogenic cell trajectory remained elusive and a missing link for understanding adult hippocampal neurogenesis in humans.

Characterization of hippocampal neural progenitor cells in childhood

To identify neural progenitors in the human hippocampus, we first focused on young individuals (ages 0 to 5 years); based on previous data, we expected to find high number of neural progenitors in this population (*5*, *17*). We performed droplet-based snRNA-seq of hippocampal nuclei obtained from six individuals (referred to as the childhood group), obtaining a dataset of 115,861 nuclei (table S1). After sample integration to account for batch and individual effects, we manually annotated major cell types based on marker expression (Fig. 1A and figs. S1 and S2) (*17*–*22*).

We selected Louvain clusters containing nuclei expressing genes characteristic of the mouse hippocampal neurogenic lineage (fig. S2) (*23*). Reintegration of these selected cells revealed two large clusters, one dominated by astrocytes and the other by granule neurons (Fig. 1B). These clusters were connected by a trail of nuclei expressing the cell proliferation marker *MKI67* and/or *EOMES* (Fig. 1C), associated with INPs and neuroblasts (*24*). RNA velocity analysis indicated a progressive differentiation trajectory from the cells expressing INP markers, through the trail of cells expressing neuroblast markers into the granule neuron cluster (Fig. 1D), indicative of a neurogenic lineage and resembling the RNA velocity pattern of mouse hippocampal neurogenesis (*25*).

We delineated different cell stages in the neurogenic trajectory by Louvain clustering and marker expression (Fig. 1E and fig. S3). INPs and neuroblasts formed discrete clusters whereas putative neural stem cells were dispersed within the astrocyte cluster and were identified by coexpression of *NESTIN*, *PAX6*, *ASCL1*, *SOX2* and low expression of *S100*β. Putative immature neurons, expressing granule neuron and plasticity markers *PROX1*, *ST8SIA2*, *DCX*, and low GAD2, were identified near neuroblasts in the granule neuron cluster (fig. S3).

Diffusion map analysis corroborated a trajectory from neural stem cells, to proliferating INPs, neuroblasts, and granule neurons (Fig. 1, F and G, and figs. S4 and S5) (*26*). Through differential gene expression analysis, we identified additional genes which have not been thoroughly studied in postnatal neurogenesis but are enriched in human INPs and neuroblasts, such as *EZH2*, or in neuroblasts and immature neurons such as *GLRA2*, *EPHA3*, *KCNH7*, and *SEMA3C* (fig. S6, A to D).

Similarities and differences between neural progenitors in young mice and humans

We integrated the human childhood dataset with a juvenile mouse hippocampus dataset (*27*). Several cell types were fully overlapping in uniform manifold approximation and projection (UMAP) visualization (e.g., the INPs and neuroblasts) whereas others were not (e.g., the putative neural stem cells and immature neurons), suggesting species-specific nuances in gene expression (Fig. 2A and figs. S7 and S8). Hierarchical clustering showed that INPs and neuroblasts were more similar to their mouse counterparts than to other human cell types, indicating transcriptional similarity between human and mouse neurogenic cells (Fig. 2B and figs. S7 and S8).

We compared the neurogenic trajectories between species by plotting human and mouse neural progenitors and immature neurons in diffusion map space, obtaining a combined neurogenic trajectory in which human cells recapitulate the transition stages characteristic of mouse neurogenesis (Fig. 2, C and D). We assessed the distribution of canonical neurogenic markers along the neurogenic trajectory in humans and mice and found expression in both species. However, their dynamics varied during progression from stem cells to immature neurons. *HES6*—specific to INPs and neuroblasts in mice—was expressed in both stem cells and INPs in the childhood human hippocampus. *EOMES*, specific to INPs in mice, was found in both INPs and neuroblasts in humans (Fig. 2, E to H, and fig. S9).

Enrichment and identification of neural progenitors

To identify neural progenitors in the adolescent and adult human hippocampus, we performed snRNA-seq on whole hippocampi or dentate gyri from 19 individuals in the range of 13 to 78 years old (y.o.) In 12 of these individuals (20 to 78 y.o.), neural progenitors were enriched using flowcytometric sorting (for details, see materials and methods and

[1]Department of Cell and Molecular Biology, Karolinska Institutet, Stockholm, Sweden. [2]Dept of Biology and Biological Engineering, National Bioinformatics Infrastructure Sweden, Science for Life Laboratory, Chalmers University of Technology, Göteborg, Sweden. [3]Department of Oncology-Pathology, Karolinska Institutet, Stockholm, Sweden. ***Corresponding author. Email: jonas.frisen@ki.se** †These authors contributed equally to this work. ‡Present address: Department of Medical Biochemistry and Biophysics, Karolinska Institutet, Stockholm, Sweden. §Present address: Cancer Research UK, 2 Redman Place, London, UK.

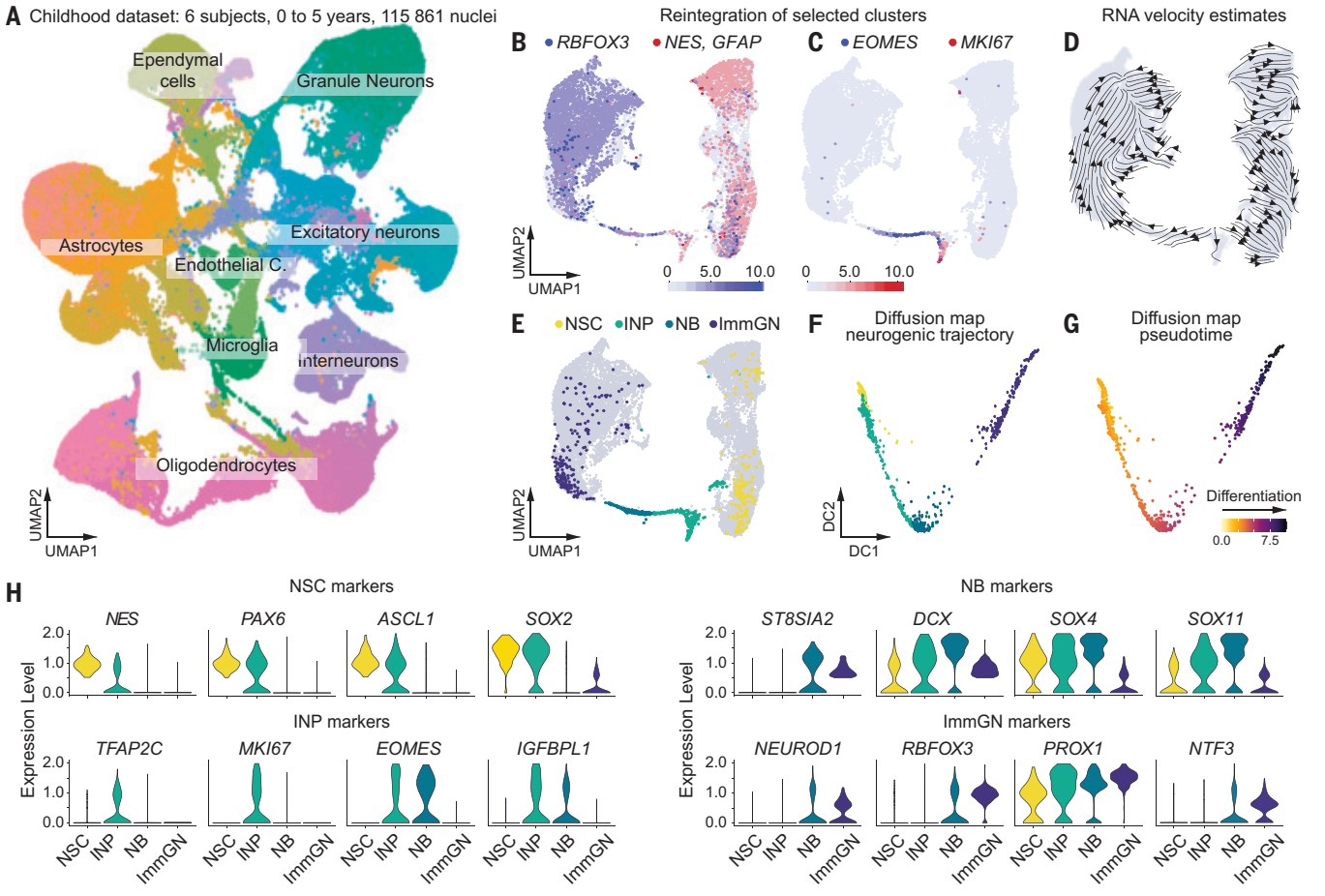

Fig. 1. Delineation of a neurogenic trajectory in the human childhood hippocampus. (**A**) UMAP projection of the integrated dataset after snRNA-seq of whole hippocampi from individuals ranging from 0 to 5 y.o. (**B** and **C**) Clusters coexpressing neurogenic markers were reintegrated. Expression of cluster specific markers projected on the UMAP: (B) *RBFOX3* for neurons and *NES* and *GFAP* for astrocytes/neural stem cells; (C) *EOMES* for INPs and neuroblasts and *MKI67* for dividing cells.(**D**) RNA velocity estimates derived from the stochastic model projected onto the UMAP-based embedding. (**E**) Cluster annotation for the reintegrated cells. The separations between astrocytes and neural stem cells (NSC) and between granule neurons (GN) and immature granule neurons (ImmGN) are based on marker expression in which a NSC is defined by *NES*, *ASCL1*, *SOX2*, and *PAX6* expression, whereas an ImmGN is defined by *ST8SIA2*, *DCX*, *PROX1*, and *GLRA2* expression. (**F** and **G**) Diffusion map organizing neural stem cells, INPs, neuroblasts, and immature granule neurons in a trajectory that recapitulates their differentiation. (F) Display of how clusters of progenitors are distributed along the trajectory; (G) is a representation of their pseudotemporal ordering. (**H**) Violin plots displaying gene expression patterns characteristic of NSC, INP, and NB in the clusters obtained after reintegration.

table S1). Of the enrichment protocols tested, the sorting of *Ki67*+ nuclei performed in eight samples proved to be efficient, resulting in a 37-fold enrichment of *MKI67* mRNA-expressing nuclei ($P = 0.018$, Wilcoxon rank sum exact test corrected using the Bonferroni method, fig. S10). Each sorted sample was supplemented with unsorted dentate gyrus cell nuclei from the same donor to enable droplet-based snRNA-seq, yielding 141,021 nuclei (fig. S11). Nuclei from the remaining seven individuals (13 to 31 y.o.) were processed without sorting. The final dataset included 286,799 nuclei, leading—after integration with the childhood dataset—to a 402,660-nuclei dataset from individuals ranging in age from 0 to 78 years, in which we identified all major hippocampal cell types through unbiased clustering and manual annotation (fig. S12).

We faced challenges in identifying progenitor cells in the adolescent and adult cohorts when using the same strategy as in the childhood group, and so we instead trained machine learning algorithms (scPred, LMN, and scANVI) (*14*, *28*–*30*) to identify nuclei transcriptionally similar to childhood INPs and neuroblasts. Nuclei from the adolescent and adult datasets were annotated as progenitors if predicted by at least two algorithms.

The strategy was tested in a juvenile mouse dataset (*27*), where it identified 83% of the INPs, 49% of the neuroblasts and 91% of all proliferating progenitors, with only 2 cells misannotated out of 540 cells predicted, indicating a 0.37% false prediction rate (fig. S13). We further applied this analysis strategy to the adult human cortex, in which there is no evidence of postnatal neurogenesis (*31*, *32*). We analyzed 12 cortical datasets (*19*, *33*, *34*) with a total of 108,285 nuclei; our strategy predicted one potential progenitor cell, later excluded based on the canonical oligodendrocyte lineage marker expression (fig. S13). Taken together, the data suggest that this strategy conservatively identifies putative neural progenitors with high specificity.

Neural progenitor cells in the adolescent and adult human hippocampus

We applied machine learning to the adolescent and adult hippocampal snRNA-seq dataset and identified a total of 354 progenitor cells (Fig. 3A), which we determined based on their expression patterns and cluster identity to be neural stem cells (12 adolescent, 65 adult), INPs (4 adolescent, 71 adult), and neuroblasts (202 adult) (Fig. 3G). To further characterize the predicted cells and to determine how they compare with neural progenitors of other species, we integrated the whole human dataset generated in this study with published mouse, pig, and rhesus monkey hippocampal snRNA-seq datasets, using the

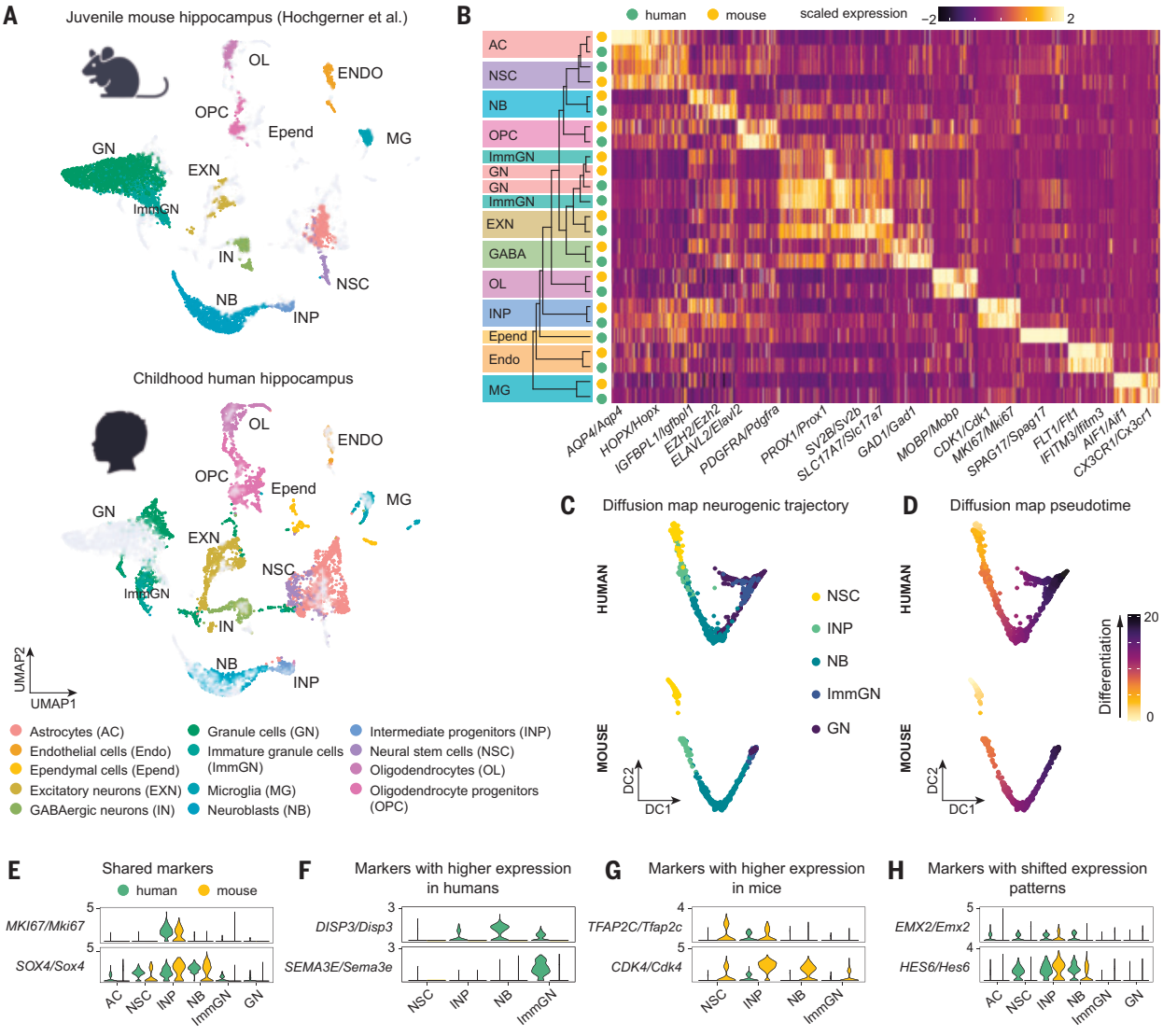

Fig. 2. Comparison of the neural progenitors in the human childhood and juvenile mouse hippocampus. (**A**) UMAP plots displaying the collection of cell types composing the mouse dentate gyrus and young human dentate gyrus. (**B**) Heatmap representing the top 50 cell type markers that are conserved across species. Hierarchical clustering on the lefthand side of the plot emphasizes transcriptional similarities of the different cell types between mouse and human. (**C** and **D**) Diffusion map organizing the human and mouse neural progenitors from both species in a trajectory that recapitulates their differentiation. (C) shows the cluster distribution along the trajectory, whereas (D) displays the pseudotemporal ordering. (**E** to **H**) Violin plots displaying gene expression patterns in mouse and human progenitor cells. They display examples of genes with similar expression (E), enriched in humans (F), enriched in mice (G), or genes that display interspecies differences in the pattern of expression across the neurogenic cells (H).

mouse as reference (*15*, *27*). The human neural progenitors identified in all ages organized along the same neurogenic trajectory as the neural progenitors from the other species (Fig. 3, B to G).

Hierarchical clustering analysis demonstrated that the human adolescent and adult neural stem cells, INPs, and neuroblasts had the highest similarity to the corresponding cell types in the mouse, pig, rhesus monkey, and human childhood datasets (Fig. 3H). We further integrated the human dataset generated in this study with a human fetal hippocampus dataset (*35*) and the mouse dataset, again using the mouse as a reference (fig. S14) (*35*). The human neural progenitors identified in this study aligned not only with the mouse progenitors as already described, but also with the human fetal progenitors (fig. S14). This was validated by the hierarchical clustering analysis, which showed that the human childhood and adolescent/adult INPs and neuroblasts were more similar to the corresponding cells in the mouse and human fetal datasets than to any other cell type in the integrated dataset (fig. S14, E to J).

Similar to childhood progenitors, proliferating adolescent and adult progenitors were also enriched in *NES* and *VIM*, likely reflecting their neural stem cell origin, and also show *EZH2*, *SYNE2*, *SOX11*, *SOX4*, *DRAXIN*, and *HES6* (fig. S15). However, adolescent and adult proliferating progenitors present *EOMES* and *TFAP2C* at low amounts compared with the childhood progenitors, whereas *EZH2*, *SYNE2* and *SOX4* showed similar levels between the two groups (fig. S15 and S16). We found human progenitors to express markers similar to neural progenitors of other species such as those described above, but also genes that appear to be specific to the adult human cells such as *APOLD1* and *RRM2* (fig. S15 and S16). The former gene is expressed in human cortical INPs during development (*36*), whereas the latter is induced by *ASCL1* expression in INPs (*37*).

Pseudotemporal analysis (*26*) in mouse, pig, rhesus monkey, and human nuclei revealed a differentiation trajectory from the neural stem cell cluster, through the INPs and neuroblast clusters and toward the granule neurons with adolescent and adult progenitors distributed along

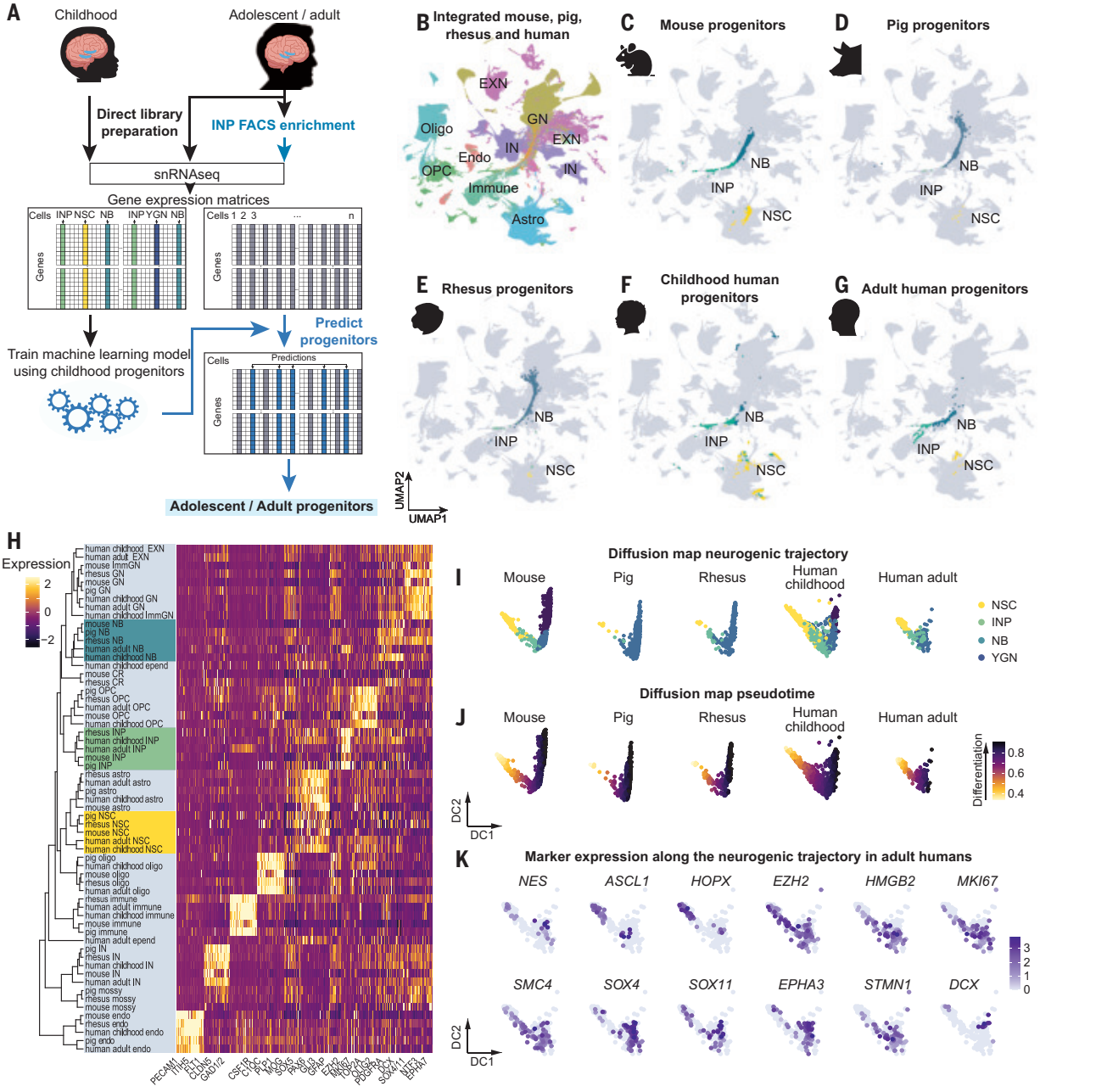

Fig. 3. Neural progenitors in the adult human hippocampus. (**A**) Scheme depicting the identification of neural progenitors in the adolescent and adult human brain. The transcriptional profiles of the neural progenitors identified in human childhood were used to train machine learning models, which were applied to the adolescent/adult human dataset generated in this study. The adolescent and adult human dataset includes human hippocampi or dentate gyrus samples directly processed to obtain 10x libraries as well as samples subjected to fluorescence-activated cell sorting enrichment for proliferating and/or neural progenitor markers. (**B** to **G**) Characterization of the neural progenitors present in the integrated dataset across species. We aligned the human dataset generated in this study with rhesus monkey, pig (*15*), and mouse data (*27*), using the latter as a reference for integration. The neural progenitors annotated according to the study of origin are highlighted in the UMAP plot of the integrated dataset: mouse (C), pig (D), rhesus monkey (E), childhood human (F), and adult human (G). (**H**) Heatmap representing the top 50 cell type markers that are conserved between the mouse, pig, rhesus monkey, childhood, and adolescent/adult human neural progenitors. Hierarchical clustering on the lefthand side of the plot emphasizes the transcriptional similarities of progenitors across species and age groups. (**I** to **K**) Diffusion map organizing neural progenitors across species and ages in a continuous trajectory that recapitulates their differentiation. The cluster distribution along the trajectory is presented in (I) and the pseudotemporal ordering in (J). (K) Gene expression patterns of neurogenesis markers along the pseudotemporal ordering of the human adult progenitors as determined with diffusion map.

this route, indicating the presence of a neurogenic trajectory in the adult human hippocampus (Fig. 3, I to K, and fig. S15).

The majority of the neural progenitor cell nuclei in the adolescent and adult dataset were in cell cycle (70% compared with 22% in the childhood dataset). This reflects the flow cytometric enrichment for *Ki67*+ nuclei in many samples, and neural progenitors that are not in cell cycle are selected against in these individuals, resulting in their underrepresentation in relation to the proliferating cells. Almost all INPs were in cell cycle in the adolescent/adult group, regardless of the proliferation marker Ki67 enrichment (table S1). Differential gene expression analysis showed that, similar to childhood proliferating progenitors, the adolescent/adult progenitors in

cell cycle expressed several proliferation markers in addition to *MKI67*, such as *TOP2A*, *CENPF*, *PCNA*, *MCM2*, as well as *SMC4* and *HMGB2* (cell cycle genes described in neural progenitors), corresponding to gene ontology terms related to cell division (fig. S15).

There was substantial interindividual variation in the number of progenitors within the adolescent and adult cohorts (table S1). In the samples that were not enriched for Ki67+ nuclei, adolescents generally had higher numbers compared with adults. However, the highest numbers were seen in some of the adult subjects in whom dentate gyrus nuclei were enriched with antibodies against Ki67 (table S1). Two individuals (40 and 58 y.o.) stood out for having much higher numbers of INPs and neuroblasts than other adults. The younger of these two subjects (40 y.o.) had a known history of epilepsy, potentially explaining the higher number of progenitor cells (*38*), whereas the older individual (58 years) had no known pathology. Neural progenitors were identified in all childhood subjects in the group but were absent in 2 out of 4 adolescents and 5 out of the 14 adults (table S1). However, in 6 of the subjects in which we failed to find progenitor cells we could identify immature granule neurons by marker expression (fig. S17 and table S1). One of the samples with no detectable progenitors also had no immature neurons, suggesting both technical as well as biological sources of variation.

Spatial localization of neural progenitor cells in the adult human dentate gyrus

We used RNAscope in situ hybridization (*39*) and Xenium, a spatially resolved transcriptomics platform with single-cell resolution (*40*), to localize neural progenitor cells in the adult human hippocampus. RNAscope offers very high sensitivity and specificity but allows the analysis of only a few genes simultaneously, limiting the ability to identify cells based on multiple markers. Xenium, on the other hand, allows the multiplexing of hundreds of genes, enabling the identification of major hippocampal cell types through graph-based clustering. Rare cell types do not cluster separately in unsupervised analysis but can be distinguished by their spatial localization in the tissue (for instance, dentate gyrus neural progenitor cells, fig. S18).

In snRNA-seq analysis, identifying progenitor cells based on a small number of marker combinations was challenging. Adding spatial context and narrowing the focus to the granule cell layer of the dentate gyrus and its immediate vicinity partially helped. However, even within this limited region, it is necessary to assess the presence and absence of multiple markers to reliably identify progenitors, which was possible using Xenium (fig. S19). For example, *NES*, *SOX4*, and *SOX11* are expressed by neural progenitors, but other markers are needed as these genes are also expressed by some oligodendrocyte progenitors (*PDGFRA*+, *CSPG4*+) and endothelial cells (*PECAM1*+, *FLT1*+) (fig. S19).

Using Xenium and RNAscope in the dentate gyrus, we identified neural stem cells coexpressing *NESTIN*, *SOX2*, and *ASCL1*, INPs expressing combinations of *ASCL1*, *EOMES*, *SOX2*, *SOX11*, *EZH2*, and *DCX*, and neuroblasts expressing sets of the markers *EZH2*, *EOMES*, *DCX*, *ST8SIA2*, *SOX11*, *IGFBPL1*, *ELAVL4*, *CALB2*, and *STMN1* (Fig. 4 and figs. S19, S20, and S21). We also localized cells expressing the new markers, which we found to be enriched in human neural progenitors such as *EZH2* in proliferating early INPs and in neuroblasts at different maturation stages (fig. S22, A to C and H), and *GLRA2*, *EPHA3*, and *KCNH7* in neuroblasts and/or immature granule neurons, coexpressing *DCX* and/or *CALB2* (fig. S22, D to G). Furthermore, we found that cells expressing combinations of neurogenic and proliferation markers, without markers of other cell identities, were mostly localized in the dentate gyrus and adjacent hilus region (fig. S23).

DCX has been the most often-used marker to identify neuroblasts and immature neurons in many species, including humans. In snRNA-seq of the whole human hippocampus, *DCX* is broadly expressed and is not in itself informative for identifying neuroblasts (fig. S2F) (*12*, *14*, *41*). Within the dentate gyrus granule cell layer, *DCX* expressing cells are very sparse, with 21.8% being *GAD2*-expressing GABAergic interneurons. Of the *DCX*-expressing cells lacking *GAD2*, 22.0% coexpress *CALB2*, associated with more mature neuroblasts (*4*) ($n = 4$, ages 27 to 53 years, fig. S24). RNAscope for *DCX* and *CALB2* was combined with immunohistochemistry, confirming overlapping gene and protein expression (fig. S25). Using both RNAscope and Xenium, we identified neural stem cells, INPs, and neuroblasts expressing proliferation markers (Fig. 4 and figs. S21 and S26). Proliferating neural stem cells and INPs were often located in pairs or small clusters (Fig. 4 and fig. S22H) and several neuroblasts were often found within a limited area, suggesting ongoing cell division and active neurogenesis. Although several markers were consistently observed (*NES*, *EZH2*, *GLRA2*, *DCX*, or *CALB2)*, some were detected less frequently (*EOMES*, *IGFBPL1*, *SOX11*, and *MKI67)*, likely reflecting biological heterogeneity. With the enhanced sensitivity of RNAscope and Xenium compared with scRNA-seq, we detected neural progenitors in all 10 cases tested (table S1).

Discussion

We report the identification and molecular characterization of neural progenitor cells from birth through adulthood in the human hippocampus. These cells are more abundant and readily identifiable early in life and become sparser in adolescents and adults. The dentate gyrus is the primary gateway of the hippocampus, controlling how information flows from the cortex to the hippocampus proper. To maintain normal function, granule neurons receive fine-tuned inhibition from local-circuit GABAergic interneurons, with only few responding to activation (*42*). Immature granule neurons have a period of enhanced

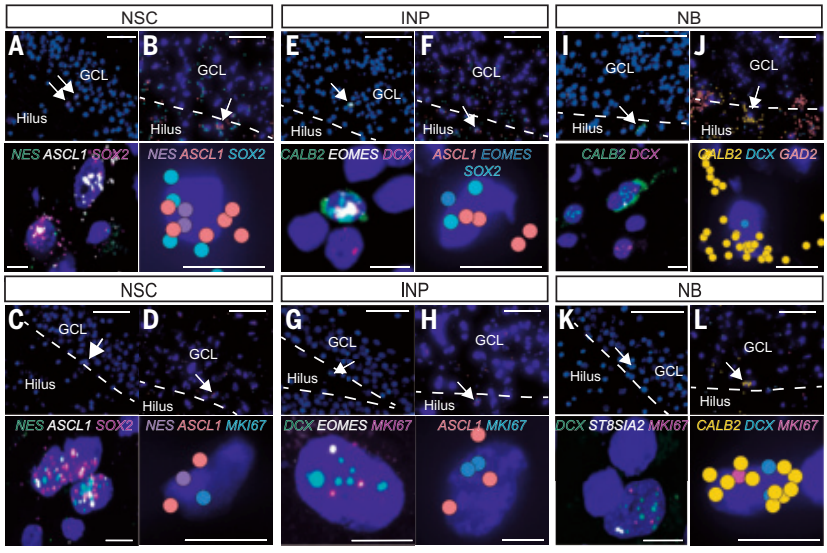

Fig. 4. Single-cell transcriptomic characterization of adult human neural progenitors and of the human neurogenic niches with spatial resolution. (**A** to **D**) Example NSCs expressing characteristic markers detected with RNAscope (A) and (C) and Xenium (B) and (D). (**E** to **H**) Example INPs expressing characteristic markers detected with RNAscope (E) and (G) and Xenium (F) and (H). (**I** to **L**) Example NBs expressing characteristic markers detected with RNAscope (I) and (K) and Xenium (J) and (L). Xenium spatial transcriptomics was performed on brain tissue from a 34-year-old male subject. The cells shown are negative for *PDGFRA*, *CSPG4*, *GAD2*, *ADARB2*, *SOX10*, *MOBP*, *MBP*, *FLT1*, *PECAM1*, and *CD4*. GCL, granular cell layer. Hatched lines indicate the border between the GCL and the hilus. Arrows in the upper panels indicate cells shown in higher magnification in the lower panels.

plasticity when they are highly responsive to excitation, and therefore even a small number of newly generated cells can have a functional impact on the hippocampus (*42*).

The difficulty in identifying neural progenitors in the human hippocampus has led some to question the existence of neurogenesis. A recent study using snRNA-seq identified and characterized immature granule neurons in the dentate gyrus (*14*). However, neural stem cells, INPs, and neuroblasts have not been identified in adult humans using unbiased transcriptomics. Our data integrate snRNA-seq with spatially resolved transcriptomics at a single-cell resolution, allowing the identification and visualization of neural progenitors in the adult human hippocampus. It complements the identification of immature granule neurons by capturing and characterizing proliferative neural progenitors, together delineating a full cell trajectory for adult neurogenesis in humans.

The number of nuclei sequenced is critical to the ability to identify very small cell populations, and previous studies have been suggested to be underpowered for identifying neural progenitors (*12*). Analyzing a large number of subjects and nuclei, specifically isolating nuclei from the dentate gyrus rather than the whole hippocampus, and most importantly enriching for proliferating cells, increased the power to identify rare neural progenitors. Moreover, using machine learning algorithms as previously done by Zhou *et al.* to identify immature neurons (*14*) was necessary to confidently detect neural progenitor cells in adolescent and adult subjects.

We found that neural progenitor cells in the adult human hippocampus are transcriptionally similar to those in mice, pigs, macaques, and in humans during childhood, with slight species-specific nuances in gene expression, with unclear functional relevance. The identification of a neurogenic cell trajectory with proliferating neural progenitor cells provides a cellular underpinning for the mitotic generation of neurons in the adult human hippocampus, which previously has been demonstrated by BrdU labeling and radiocarbon dating (*16*, *17*). It is unclear whether the generation of immature granule neurons by proliferating progenitors is the main mechanism for adult neurogenesis and to what extent mitotic generation earlier in life and protracted neuronal maturation are complementary pathways.

As expected, the highest number of neural progenitor cells was found in the youngest subjects in the childhood group (*5*, *17*). However, differences in nuclear enrichment protocols make it difficult to draw conclusions about the number of neural progenitor cells at different ages in adulthood. Nevertheless, substantial variation was detected across individuals processed using the same enrichment approaches and variation in the numbers of immature granule neurons was also observed in parallel, consistent with prior reports of variability of neurogenesis among macaques, humans, and inbred mouse strains (*12*, *14*, *17*, *41*).

Several of the donors had a history of psychiatric or neurological diseases, which have been associated with differences in neurogenesis (*2*, *3*, *42*). However, the current study was not powered to draw conclusions about a potential relationship between pathology and neurogenesis. The identification of neural progenitor cells in the adult human brain will facilitate further studies on possible effects of pathology and genetic predisposition on neurogenesis.

REFERENCES AND NOTES

1. G. Kempermann *et al.*, *Cell Stem Cell* **23**, 25–30 (2018).
2. J. Terreros-Roncal *et al.*, *Science* **374**, 6571 (2021).
3. E. P. Moreno-Jiménez *et al.*, *Nat. Med.* **25**, 554–560 (2019).
4. E. P. Moreno-Jiménez, J. Terreros-Roncal, M. Flor-García, A. Rábano, M. Llorens-Martín, *J. Neurosci.* **41**, 2541–2553 (2021).
5. R. Knoth *et al.*, *PLOS ONE* **5**, e8809 (2010).
6. M. Boldrini *et al.*, *Cell Stem Cell* **22**, 589–599.e5 (2018).
7. M. K. Tobin *et al.*, *Cell Stem Cell* **24**, 974–982.e3 (2019).
8. A. Ammothumkandy *et al.*, *Nat. Neurosci.* **25**, 493–503 (2022).
9. S. F. Sorrells *et al.*, *J. Neurosci.* **41**, 2554–2565 (2021).
10. S. F. Sorrells *et al.*, *Nature* **555**, 377–381 (2018).
11. S. Cipriani *et al.*, *Cereb. Cortex* **28**, 2458–2478 (2018).
12. G. Tosoni *et al.*, *Neuron* **111**, 1714–1731.e3 (2023).
13. M. Sepp *et al.*, *Nature* **625**, 788–796 (2024).
14. Y. Zhou *et al.*, *Nature* **607**, 527–533 (2022).
15. D. Franjic *et al.*, *Neuron* **10**, P452–469.E14 (2022).
16. P. S. Eriksson *et al.*, *Nat. Med.* **4**, 1313–1317 (1998).
17. K. L. Spalding *et al.*, *Cell* **153**, 1219–1227 (2013).
18. F. Ayhan *et al.*, *Neuron* **109**, 2091–2105.e6 (2021).
19. N. Habib *et al.*, *Nat. Methods* **14**, 955–958 (2017).
20. T. Stuart *et al.*, *Cell* **177**, 1888–1902.e21 (2019).
21. Y. Hao *et al.*, *Cell* **184**, 3573–3587.e29 (2021).
22. L. McInnes, J. Healy, N. Saul, L. Großberger, *J. Open Source Softw.* **3**, 861 (2018).
23. L. Waltman, N. J. Van Eck, *Eur. Phys. J. B* **86**, 471 (2013).
24. R. D. Hodge *et al.*, *J. Neurosci.* **32**, 6275–6287 (2012).
25. V. Bergen, M. Lange, S. Peidli, F. A. Wolf, F. J. Theis, *Nat. Biotechnol.* **38**, 1408–1414 (2020).
26. P. Angerer *et al.*, *Bioinformatics* **32**, 1241–1243 (2016).
27. H. Hochgerner, A. Zeisel, P. Lönnerberg, S. Linnarsson, *Nat. Neurosci.* **21**, 290–299 (2018).
28. G. La Manno *et al.*, *Cell* **167**, 566–580.e19 (2016).
29. J. Alquicira-Hernandez, A. Sathe, H. P. Ji, Q. Nguyen, J. E. Powell, *Genome Biol.* **20**, 264 (2019).
30. A. Gayoso *et al.*, *Nat. Biotechnol.* **40**, 163–166 (2022).
31. H. B. Huttner *et al.*, *Nat. Neurosci.* **17**, 801–803 (2014).
32. R. D. Bhardwaj *et al.*, *Proc. Natl. Acad. Sci. U.S.A.* **103**, 12564–12568 (2006).
33. C. Nagy *et al.*, *Nat. Neurosci.* **23**, 771–781 (2020).
34. K. Siletti *et al.*, *Science* **382**, 6667 (2023).
35. S. Zhong *et al.*, *Nature* **577**, 531–536 (2020).
36. X. Fan *et al.*, *Sci. Adv.* **6**, eaaz2978 (2020).
37. J. Andersen *et al.*, *Neuron* **83**, 1085–1097 (2014).
38. S. Jessberger, J. M. Parent, *Cold Spring Harb. Perspect. Biol.* **7**, 1–10 (2015).
39. F. Wang *et al.*, *J. Mol. Diagn.* **14**, 22–29 (2012).
40. A. Janesick *et al.*, *Nat. Commun.* **14**, 8353 (2023).
41. P. J. Lucassen, C. P. Fitzsimons, E. Salta, M. Maletic-Savatic, *Behav. Brain Res.* **381**, 112458 (2020).
42. S. B. McHugh *et al.*, *Nat. Neurosci.* **25**, 1481–1491 (2022).
43. I. Dumitru, snRNAseq_human_hippocampus, Version v1, Zenodo (2025); https://zenodo.org/records/14879680.
44. I. Dumitru, Xenium_1_2_3, Version v1, Zenodo (2025); https://zenodo.org/records/14879552.
45. I. Dumitru, Xenium_4_5_6, Version v1, Zenodo (2025); https://zenodo.org/records/14879626.
46. I. Dumitru, Computational Code Human Neurogenesis, Version v1, Zenodo (2025); https://zenodo.org/records/14882965.

ACKNOWLEDGMENTS

We thank E. Llorens-Bobadilla and J. Mold for valuable discussions. We thank N. Eckerdal, the Biostatistics Core Facility, and the Karolinska Institutet for help regarding the statistical comparisons present in the study. The tissue used in this research was obtained from the Human Brain Collection Core, Intramural Research Program, NIMH (https://www.nimh.nih.gov/research/research-conducted-at-nimh/research-areas/research-support-services/hbcc). Human tissue was also received from KI Donatum, the NIH NeuroBioBank at the University of Maryland, the University of Miami, and from the Medical Research Council Biobank in UK, from King's College London. The authors acknowledge the In Situ Sequencing Facility at SciLifeLab, funded by Science for Life Laboratory; the authors also acknowledge the Swedish Research Council for providing in situ sequencing services. **Funding:** This work was funded by the following: The Swedish Research Council, ERC (ERC-2015-AdG-695096) (to J.F.); the Swedish Cancer Foundation (to J.F.); Knut och Alice Wallenbergs Stiftelse (to J.F.); The Swedish Society for Strategic Research and the Strategic Research Programme in Stem Cells and Regenerative Medicine at Karolinska Institutet (StratRegen) (to J.F.); the EMBO long term fellowship and a Marie Sklodowska-Curie Action (to I.D.); and the Knut and Alice Wallenberg Foundation as part of the National Bioinformatics Infrastructure Sweden at SciLifeLab (to Å.B. and R.S.). **Author contributions:** Conceptualization and methodology: I.D., J.F., M.P., M.Z., C.Z., and R.S. Methodology: I.D., J.F., M.P., M.Z., C.Z., K.A., H.D., R.S., and S.G. Primary analysis: I.D. and C.Z.; Secondary analysis: I.D., M.Z., and C.Z. Visualization: I.D., M.Z., C.Z., and M.P.; Funding acquisition: J.F. Project administration: I.D. and J.F. Writing – original draft: I.D. Writing – review & editing: I.D. and J.F. and all authors; Supervision: J.F. and R.S. **Competing interests:** J.F. and M.Z. are consultants to 10x Genomics. I.D. started working at AAX Biotech AB in December 2024. C.Z. has been the CEO of Xpress genomics since 2022. **Data and materials availability:** All sequencing data in the study and the Xenium data are freely available and are deposited at Zenodo: snRNA-seq dataset (*43*) and Xenium datasets (*44*) and (*45*). The computational code used in this study is available at Zenodo (*46*). The raw FASTQ files have been deposited in the European Nucleotide Archive (ENA) under study accession number ERP173468.

SUPPLEMENTARY MATERIALS

science.org/doi/10.1126/science.adu9575
Materials and Methods; Figs. S1 to S26; Tables S1 and S2; References (*47*–*56*); MDAR Reproducibility Checklist

Submitted 28 November 2024; accepted 25 April 2025

10.1126/science.adu9575

ECOSYSTEM CHANGE

Coupled, decoupled, and abrupt responses of vegetation to climate across timescales

David Fastovich[1,2]*, Stephen R. Meyers[3], Erin E. Saupe[4], John W. Williams[5,6], Maria Dornelas[7,8], Elizabeth M. Dowding[9], Seth Finnegan[10,11], Huai-Hsuan M. Huang[12], Lukas Jonkers[13], Wolfgang Kiessling[9], Ádám T. Kocsis[9], Qijian Li[14,15], Lee Hsiang Liow[16,17], Lin Na[14,15], Amelia M. Penny[18], Kate Pippenger[19], Johan Renaudie[20], Marina C. Rillo[21], Jansen Smith[22], Manuel J. Steinbauer[23], Mauro Sugawara[24,25], Adam Tomašových[26], Moriaki Yasuhara[27,28,29,30,31], Pincelli M. Hull[19,32,33]

Climate and ecosystem dynamics vary across timescales, but research into climate-driven vegetation dynamics usually focuses on singular timescales. We developed a spectral analysis–based approach that provides detailed estimates of the timescales at which vegetation tracks climate change, from 10^1 to 10^5 years. We report dynamic similarity of vegetation and climate even at centennial frequencies (149^{-1} to $18{,}012^{-1}$ year^{-1}, that is, one cycle per 149 to 18,012 years). A breakpoint in vegetation turnover (797^{-1} year^{-1}) matches a breakpoint between stochastic and autocorrelated climate processes, suggesting that ecological dynamics are governed by climate across these frequencies. Heightened vegetation turnover at millennial frequencies (4650^{-1} year^{-1}) highlights the risk of abrupt responses to climate change, whereas vegetation-climate decoupling at frequencies >149^{-1} year^{-1} may indicate long-lasting consequences of anthropogenic climate change for ecosystem function and biodiversity.

Characterizing ecological dynamics across timescales is urgently required to understand how and at what rates ecosystems are likely to respond to anthropogenic climate change. Species and ecosystems differ in their responses to changing climates, and these dynamics are timescale dependent (*1*–*4*). The climate system exhibits two interconnected modes of variability: short-term, stochastic weather variations that scale to large, autoregressive climate fluctuations at timescales longer than 100 to 1000 years (*5*, *6*). Yet most studies of climate-driven ecological dynamics have focused on narrow ranges of timescales (*7*).

Global networks of ecological and paleontological data (*8*, *9*) now enable us to characterize, in ways not previously possible, ecological responses to climate forcing across timescales and modes of climate variability. Former research has shown that fast ecological dynamics track climate change (*10*, *11*), whereas slow dynamics are lagged or decoupled from climate (*12*–*15*). Ecosystems can also linearly or nonlinearly respond to forcing, with the potential to lead to unexpected species' compositional changes (*16*).

In this work, we focused on the relationships among temperature, precipitation, and vegetation compositional turnover in paleoecological records spanning hundreds to hundreds of thousands of years over the past 600,000 years. To quantify the coupling, decoupling, and scaling of climate drivers and ecological responses across timescales, we created and applied a conceptual and analytical framework rooted in spectral analysis (*17*). Whereas many time-series methods are only capable of examining vegetation-climate coupling at discrete temporal lags, spectral analysis overcomes this limitation in the frequency domain by comprehensively decomposing time-series variability into specific timescales of observation. This decomposition is quantified in the power spectrum and provides insights into the relative contributions of different timescales to overall climate or vegetation variability.

Through this approach, we generated global power spectra of vegetation variability by averaging site-level power spectra for fossil pollen assemblages across a global compilation of 1321 sites (*8*, *9*), with the densest coverage for the past 20,000 years (figs. S1 and S2). We compared these global vegetation compositional changes to power spectra of temperature and precipitation from a climate model simulation of the past 21,000 years (TraCE-21ka; figs. S3 to S6) (*18*, *19*). To capture lower-frequency climate variability, we included proxy temperature reconstructions that approximate global climate over the past 2 million years (*20*, *21*).

Paired spectral analysis of climate and vegetation: Analytical and conceptual framework

The exponential coefficient (β) of the power-law relationship [$S(f) \propto f^{-\beta}$] between spectral power (S) and frequency (f) defines the spectral continuum, quantifies how variance is partitioned across frequencies in power spectra of climate and ecological turnover, and identifies dynamic similarity between these systems across timescales (fig. S7) (*22*, *23*). If vegetation composition changes in parallel with climate variability, the βs for vegetation should be similar to those for climate variability. For instance, a shift in low-frequency climate variability will induce a change in vegetation turnover at the same frequencies. However, the drivers of vegetation compositional change vary in relative importance across timescales (Fig. 1): Disturbance, biotic interactions, and demographic processes are thought to be more important at short timescales; migration lags and other dispersal limitations, population dynamics, restriction to refugia, and ecosystem transformation dominate at intermediate timescales; and macroevolutionary processes such as speciation and extinction prevail on longer timescales (Fig. 1) (*1*, *2*). These processes modulate vegetation responses to climate and may cause the continuum of vegetation variability to diverge from climate ($\beta_{veg} \neq \beta_{clim}$).

We expect that matching βs for climate and vegetation are likely to emerge at intermediate frequencies (~1000^{-1} to ~$100{,}000^{-1}$ year^{-1}, that is, one cycle per ~1000 to ~100,000 years) given previous work (*10*, *11*) (Fig. 1). At these intermediate frequencies, the processes regulating assemblage composition can keep up with climate change (*10*, *11*), leading to $\beta_{veg} = \beta_{clim}$ (Fig. 1A). Across frequencies when $\beta_{veg} = \beta_{clim}$, we infer that vegetation is tracking climate and use the term "fast tracking" (*11*), even though our methods do not test for causal links.

[1]Department of Earth and Environmental Sciences, Syracuse University, Syracuse, NY, USA. [2]Department of Geography, University of Georgia, Athens, GA, USA. [3]Department of Geoscience, University of Wisconsin–Madison, Madison, WI, USA. [4]Department of Earth Sciences, University of Oxford, Oxford, UK. [5]Department of Geography, University of Wisconsin–Madison, Madison, WI, USA. [6]Center for Climatic Research, University of Wisconsin–Madison, Madison, WI USA. [7]Centre for Biological Diversity, School of Biology, University of St Andrews, St Andrews, UK. [8]Guia Marine Lab, MARE, Faculty of Science of the University of Lisbon, Cascais, Portugal. [9]GeoZentrum Nordbayern, Friedrich-Alexander Universität Erlangen-Nürnberg (FAU), Erlangen, Germany. [10]Department of Integrative Biology & Museum of Paleontology, University of California, Berkeley, Berkeley, CA, USA. [11]Smithsonian Tropical Research Institute, Panama City, Panama. [12]Department of Geosciences, Princeton University, Princeton, NJ, USA. [13]MARUM - Center for Marine Environmental Sciences University of Bremen, Bremen, Germany. [14]State Key Laboratory of Palaeobiology and Stratigraphy, Nanjing Institute of Geology and Palaeontology, Chinese Academy of Sciences, Nanjing, China. [15]Center for Excellence in Life and Paleoenvironment, Chinese Academy of Sciences, Nanjing, China. [16]Natural History Museum, University of Oslo, Oslo, Norway. [17]Centre for Planetary Habitability, Department of Geosciences, University of Oslo, Oslo, Norway. [18]School of GeoSciences, University of Edinburgh, Edinburgh, UK. [19]Department of Earth and Planetary Sciences, Yale University, New Haven, CT, USA. [20]Museum für Naturkunde, Berlin, Germany. [21]ICBM–Institute for Chemistry and Biology of the Marine Environment, University of Oldenburg, Wilhelmshaven, Germany. [22]Department of Earth & Environmental Sciences, University of Minnesota–Duluth, Duluth, MN, USA. [23]Bayreuth Center of Ecology and Environmental Research, University of Bayreuth, Bayreuth, Germany. [24]University of British Columbia, Vancouver, BC, Canada. [25]Mário Schenberg Institute, São Paulo, Brazil. [26]Earth Science Institute, Slovak Academy of Sciences, Bratislava, Slovakia. [27]School of Biological Sciences, Area of Ecology and Biodiversity, The University of Hong Kong, Hong Kong, China. [28]Swire Institute of Marine Science, The University of Hong Kong, Hong Kong, China. [29]Institute for Climate and Carbon Neutrality, The University of Hong Kong, Hong Kong, China. [30]Musketeers Foundation Institute of Data Science, The University of Hong Kong, Hong Kong, China. [31]State Key Laboratory of Marine Pollution, City University of Hong Kong, Hong Kong, China. [32]Yale Peabody Museum, New Haven, CT, USA. [33]Swiss Federal Institute for Forest, Snow and Landscape Research, Birmensdorf, Switzerland. ***Corresponding author. Email: fastovich@uga.edu**

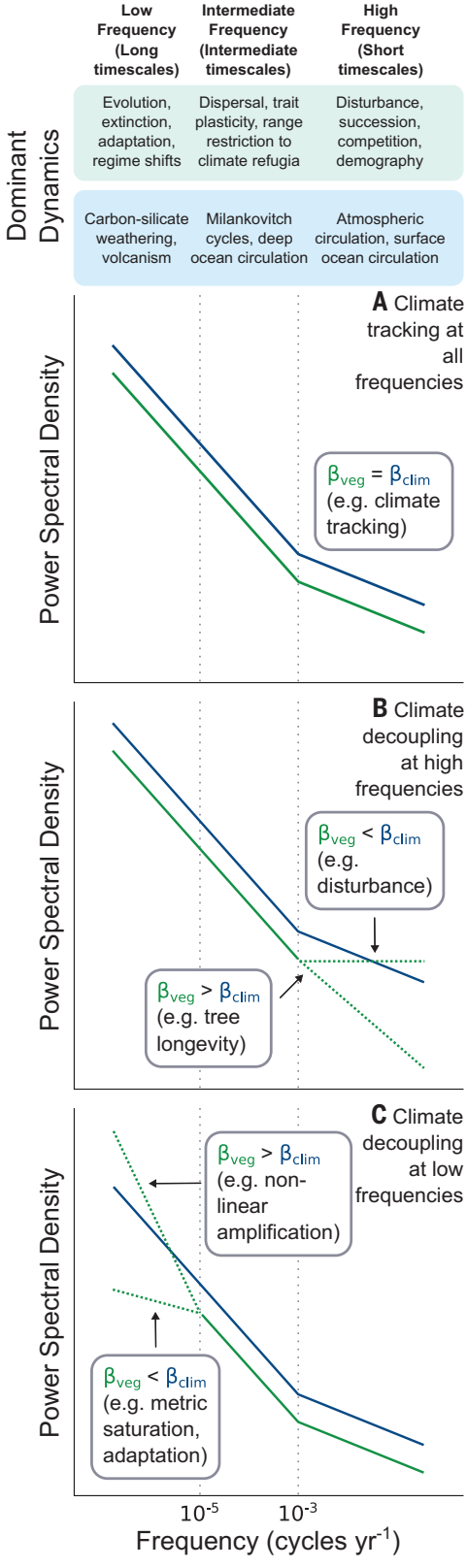

Fig. 1. Conceptual framework for ecoclimate spectral analyses. A conceptual framework for interpreting the relationship between vegetation and climate using power spectra through the power-law scaling relationship between spectral power and frequency [$S(f) \propto f^{-\beta}$]. The blue line corresponds to β for climate variability, and the green line corresponds to β for vegetation compositional turnover. The breakpoint in climate spectral power in all three panels is based on prior work that indicates a breakpoint in climate variability at approximately 100^{-1} to 1000^{-1} $year^{-1}$ (*5*,*6*). Key characteristics include the slope (β, i.e., continuum) of vegetation turnover relative to climate and the placement of breakpoints (dashed vertical lines). Three scenarios illustrate potential relationships between climate and vegetation. (**A**) Vegetation composition exhibits linear responses to climate across all frequencies, and so the slope of vegetation spectral power parallels that of climate (*10*). (**B**) Vegetation linearly tracks climate at intermediate and low frequencies (*10*) but is decoupled from climate at high frequencies (*50*). At high frequencies, a higher β for vegetation than climate suggests that processes such as tree longevity influence vegetation turnover, whereas a lower β for vegetation indicates that disturbance may be a primary control on turnover (*25*). (**C**) Vegetation tracks climate across high and intermediate frequencies but is decoupled at low frequencies from processes such as evolutionary adaptation (lower β for vegetation) or nonlinear amplification through processes such as threshold responses (higher β for vegetation). Other scenarios and biological processes are possible beyond those shown here.

warming, as they examine how ecological and life-history factors may override the influence of climate variability. The vegetation response at high frequencies may be slow, because trees tend to have life spans of 10^2 to 10^3 years (*24*), producing a larger β in vegetation turnover than in climate (Fig. 1B; $\beta_{veg} > \beta_{clim}$). Conversely, disturbance through herbivory, fire, human land use, and disease could increase vegetation turnover at high frequencies, decreasing β relative to climate (Fig. 1B; $\beta_{veg} < \beta_{clim}$) (*25*).

At low frequencies, vegetation dynamics distinct from intermediate and high frequencies may emerge. Climate tracking could persist, as expected at intermediate frequencies (Fig. 1C; $\beta_{veg} = \beta_{clim}$), or adaptive evolution could increase species' tolerances to new climate regimes (*26*), potentially reducing compositional responses to climate forcing. Consequently, vegetation turnover variability would increase minimally relative to climate variations (Fig. 1C; $\beta_{veg} < \beta_{clim}$). Conversely, if vegetation responses to environmental forcings are characterized by strong nonlinearities (*16*, *27*), variability in vegetation turnover would be high relative to climate (Fig. 1C; $\beta_{veg} > \beta_{clim}$).

Spectral continuum of vegetation variability

To meaningfully compare climate and vegetation turnover, we aligned their spatiotemporal characteristics through downsampling and low-pass filtering the climate model simulations (*28*). The proxy estimates of global climate variability cannot undergo this processing, resulting in spatiotemporal characteristics that differ from the fossil pollen records. We assessed the effects of temporal uncertainty and uneven spatiotemporal coverage of the vegetation turnover data on the averaged power spectra (Fig. 2) by resampling sites and their corresponding posterior age estimates to produce an ensemble of power spectra, estimates of β, and estimates of the breakpoints in β (*28*). Lastly, we assessed the sensitivity of our results to sediment deposition (Fig. 2), resolution (fig. S8), dimensionality reduction (figs. S9 to S12), power spectra and β estimation (figs. S9, S10, S13, and S14), and spatiotemporal sampling biases (figs. S15 to S17) and found that our conclusions are insensitive to each (*28*).

We found that the spectral continuum of variability in vegetation turnover carries clear similarities to that of the climate system (Fig. 2), yet the relationship to climate varies with frequency. The power spectrum of vegetation turnover appears to follow the climate system across the scaling breakpoint reported in previous studies (*5*, *6*) and also found here, supporting the interpretation that vegetation dynamically tracks the climate system at intermediate frequencies (Figs. 1 and 2 and table S1; 693^{-1} to 649^{-1} $year^{-1}$ for temperature, 691^{-1} to 660^{-1} $year^{-1}$ for precipitation, and 862^{-1} to 759^{-1} $year^{-1}$ for vegetation turnover) (*10*). However, unlike temperature and precipitation (*5*, *6*), the vegetation turnover power spectrum has two additional breakpoints, at 149^{-1} $year^{-1}$ (95% confidence interval: 154^{-1}, 145^{-1}) and $18{,}012^{-1}$ $year^{-1}$ ($18{,}952^{-1}$, $17{,}254^{-1}$) (uncertainties for all parameters estimated are reported in table S1). The vegetation turnover

The relationship between climate and vegetation dynamics at lower ($<100{,}000^{-1}$ $year^{-1}$) and higher ($>1000^{-1}$ $year^{-1}$) frequencies remains unresolved, as do the frequencies at which the assumption of fast tracking no longer holds (*12*). High frequencies are particularly crucial for predicting vegetation responses to rapid, anthropogenic climate

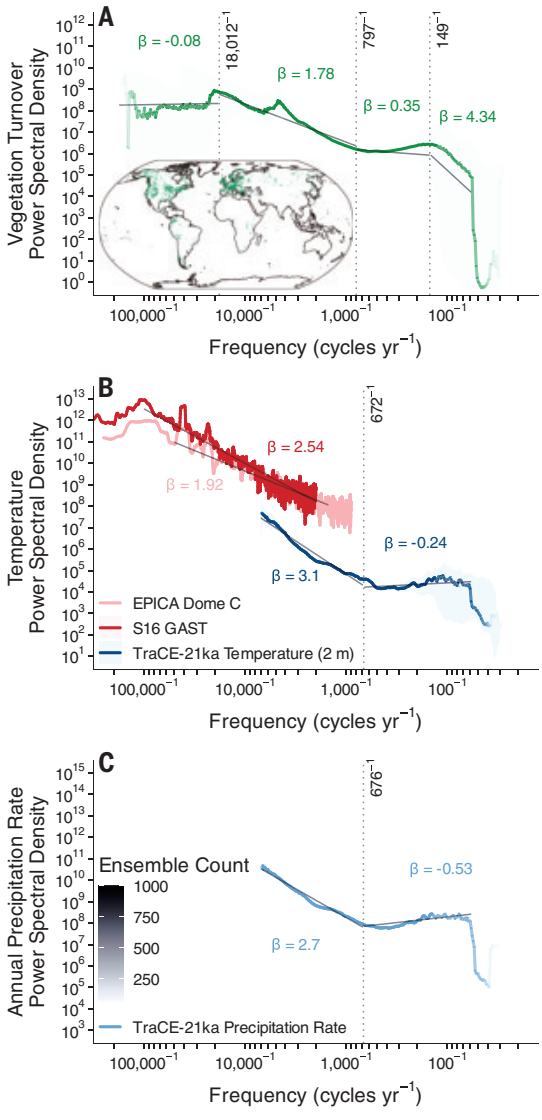

Fig. 2. The continuum of global vegetation turnover and climate variability. The spectral continuum of (**A**) vegetation turnover (green), (**B**) temperature (blue, red, and pink), and (**C**) precipitation (light blue) variability based on the median from an ensemble of spectral power estimates. The transparency of the power spectra indicates the number of ensemble members that resolve each frequency with the corresponding legend for all plots in (C). β in the high-frequency band was fit to the maximum frequency that yielded an unbiased estimate (*28*). Solid gray lines correspond to β from ordinary least squares regressions of log spectral power and log frequency. Vertical dashed lines correspond to breakpoints identified in the spectral continuum. Climate estimates from TraCE-21ka have been downsampled in space and time and low-pass filtered to match the temporal characteristics of the fossil pollen abundances. Shaded regions indicate the 95% confidence interval (CI) for spectral power. Uncertainties for β and breakpoints and permutation tests comparing these parameters are reported in fig. S21 and tables S1 to S3.

power spectra are therefore characterized by four scaling regimes: high frequencies (<149^{-1} $year^{-1}$), high-intermediate frequencies (149^{-1} to 797^{-1} $year^{-1}$), low-intermediate frequencies (797^{-1} to $18{,}012^{-1}$ $year^{-1}$), and low frequencies (>$18{,}012^{-1}$ $year^{-1}$). The additional breakpoints in the continuum of the vegetation turnover power spectrum found in the global average (Fig. 2) are also found in the spectra of individual time series (fig. S18), indicating that the patterns are not an artifact of the ensemble approach. Together, these features of the vegetation turnover power spectra provide evidence that the relationship between plant assemblages and climate is timescale dependent and complex. Ecological communities and climate may co-vary on some timescales but differ in their dynamics on others, which we detail in the next section.

Timescales of ecological dynamics

Coupled dynamics

We show evidence of climate and vegetation coupling between 149^{-1} and $18{,}012^{-1}$ $year^{-1}$ (Fig. 2), which is a narrower range of frequencies than previously theorized (*10*). First, for both vegetation and climate, βs are near zero at frequencies from 149^{-1} to 797^{-1} $year^{-1}$ and ~2 at frequencies from 797^{-1} to $18{,}012^{-1}$ $year^{-1}$. Second, scaling breakpoints are aligned for vegetation and climate between 672^{-1} and 797^{-1} $year^{-1}$ (Fig. 1). This period of vegetation and climate coupling spans the theorized (*29*) and observed scaling break (*5*, *6*) that separates weather and climate variability and suggests that a foundational shift in vegetation turnover from autocorrelated to stochastic at frequencies of around 670 to 800^{-1} $year^{-1}$ is related to coupled atmosphere-ocean-vegetation processes (*29*).

This finding sharpens our understanding of the frequencies at which plant communities rapidly and dynamically adjust composition and structure in response to climate forcing. Prior theory and the observations of orbital signals in pollen records have led to the widespread agreement of fast tracking of climate by vegetation composition at frequencies of 1000^{-1} to $100{,}000^{-1}$ $year^{-1}$ (*10*, *11*). However, whether vegetation rapidly tracks climate at submillennial frequencies (10^{-2} to 10^{-3} $year^{-1}$) was previously unclear, with evidence for and against climate disequilibrium at frequencies of 50^{-1} to 200^{-1} $year^{-1}$ (*12*, *30*). Our work thus expands prior knowledge by suggesting climate tracking by vegetation for frequencies as high as 149^{-1} $year^{-1}$.

The small β for vegetation turnover between 149^{-1} and 797^{-1} $year^{-1}$ indicates that variance is equally partitioned across this frequency range and suggests that stochastic processes, such as extreme weather events or disturbances, yield small changes in abundance without a wholesale change in vegetation composition (Fig. 2). By contrast, a β ~ 2 from 797^{-1} to $18{,}012^{-1}$ $year^{-1}$ indicates more variance at lower frequencies and autocorrelated dynamics. These dynamics can result from vegetation directly tracking autocorrelated processes in the climate system or from ecological processes that increase autocorrelation, such as density-dependent processes and priority effects.

Although the breakpoint for vegetation turnover at 797^{-1} $year^{-1}$ is statistically distinguishable from temperature and precipitation (table S2), these differences likely reflect the limitations of the approach. The nonrandom subset of communities recorded by these vegetation assemblage records, our choice of climate model, or biased local or regional spectral estimates from climate models (*31*) all could affect the precise location of the breakpoint and lead to an apparent offset. However, if this offset between the vegetation and climate breakpoints is real, two hypotheses may explain the brief decoupling of climate and vegetation between frequencies of 676^{-1} to 672^{-1} $year^{-1}$ and 797^{-1} $year^{-1}$: a lag in vegetation response to the transition from low-β to higher-β weather-climate scaling regimes or the greater importance of nonclimatic forcing (such as disturbance regimes) at these frequencies.

Uncoupled dynamics

Vegetation and climate appear decoupled at frequencies higher than 149^{-1} $year^{-1}$ and lower than $18{,}012^{-1}$ $year^{-1}$. β is 4.34 (3.64, 4.96) for vegetation turnover at the highest frequencies, whereas for temperature and precipitation, β is −0.24 (−0.29, −0.18) and −0.53 (−0.58, −0.49), respectively (Fig. 2 and table S1). This finding supports prior observations of higher βs in vegetation turnover at these high frequencies (*32*) but appears sensitive to the amount of weight given to abundant and rare taxa when estimating vegetation turnover with dissimilarity metrics and the fossil pollen record under consideration (fig. S9). Some combination of taphonomy, sampling, and ecological processes could explain higher βs in vegetation turnover at these high frequencies. Decadal-scale mixing of lake sediments and scale gaps caused by discontinuous

sampling of sediments may enhance autocorrelation in vegetation turnover variability from these archives (*33*, *34*). In addition, the large βs at the highest frequencies may result from the long life spans of some plants (e.g., trees, which are well represented in fossil pollen assemblages), limiting the ability of the full assemblage to track high-frequency climate variability because of slow turnover times. Indeed, the median tree life span from the International Tree Ring Data Bank (*35*, *36*) is 246 years (n = 4773) (fig. S19). A long life span may impart a high β, as vegetation turnover would increase when approaching the median tree longevity frequency because trees nearing their median life span would experience higher mortality rates, leading to greater community turnover. Anthropogenic land-use change may also contribute to climate decoupling at high frequencies (*37*, *38*), possibly interacting with tree longevity. Notably, a greater β for vegetation turnover at the highest frequencies is consistent with observations of slow vegetation responses to climate variability and evidence of climate debt (*13*–*15*, *39*). These slow responses are expected to create mismatches between species' climate preferences and climate and thus reduce organismal fitness and ecosystem function.

For frequencies lower than $18{,}012^{-1}$ year^{-1} ($18{,}952^{-1}$, $17{,}254^{-1}$), β equals −0.08 (−0.23, −0.06) for the vegetation turnover power spectrum (Fig. 2). This contrasts with the climate power spectra, which maintain the long-term climate-system βs of ~2 to 3 because of the influence of astronomical forcing (Fig. 2) (*40*). There are two possible explanations for low βs in vegetation turnover at these low frequencies. First, the community dissimilarity metric we used to quantify vegetation turnover within each time series may reach a maximum value (i.e., metric saturation; fig. S20) and fail to record turnover beyond a complete replacement of the vegetation assemblage (*41*). For example, if climate change caused multiple assemblage turnovers (assemblage A replaced by B replaced by C), community dissimilarity metrics will saturate and underestimate the true ecological impact of past climate change, producing an apparent decrease in vegetation turnover with decreasing frequency. Second, fast evolutionary adaptation would increase species' tolerance to environmental variation and result in vegetation communities appearing relatively resistant to climate forcing. Although local adaptation cannot be excluded as an explanation, the hypothesis of metric saturation appears sufficient to explain the reduced vegetation turnover variability at low frequencies (fig. S9).

Nonlinearity in the climate-vegetation relationship

High spectral power at 4650^{-1} year^{-1} is specific to vegetation turnover and is absent in the power spectra of the climate proxies and climate simulations that we evaluated (Fig. 2 and fig. S3). Climate in the North Atlantic has been argued to contain apparent modes of climate variability at 1470^{-1} and 4670^{-1} year^{-1} (*42*) and provides a plausible mechanism for forcing vegetation turnover (*30*, *43*, *44*). However, global compilations of Holocene climate records lack high spectral power at any of these frequencies (fig. S3) (*45*), as do the spectra of simulated temperature and precipitation (Fig. 2). This disconnect at the global scale (and in the subset of sites we investigated) between climate and vegetation turnover leads us to hypothesize that relatively subtle or regional millennial-scale climate variations are amplified in the vegetation response by nonlinear ecological dynamics (*27*, *46*).

However, analytical artifacts may also contribute to high spectral power at 4650^{-1} year^{-1}. Most of our records span 20,000 years, with fewer longer records (186 sites; fig. S1 and data S1). The relatively low number of sites sampled could bias our spatial and environmental coverage at low frequencies, producing a spurious peak in spectral power. Despite these potential artifacts, evidence for nonlinear responses in vegetation assemblages to small environmental changes is well documented (*27*). Our observations suggest slow vegetation responses to climate variability at high frequencies alongside high turnover at 4650^{-1} year^{-1}, demonstrating how gradual vegetation changes can be accompanied by abrupt, nonlinear shifts in vegetation assemblages. Hence, even without clear patterns of climate variability in the North Atlantic at this frequency, the vegetation dynamics over the past 600,000 years underscore the potential for abrupt changes in plant assemblages over the coming decades of warming (*47*).

Latitudinal gradient in assemblage dynamics

We found that the relationship between vegetation turnover variability and climate variability differs across latitudes. Climatically, the high

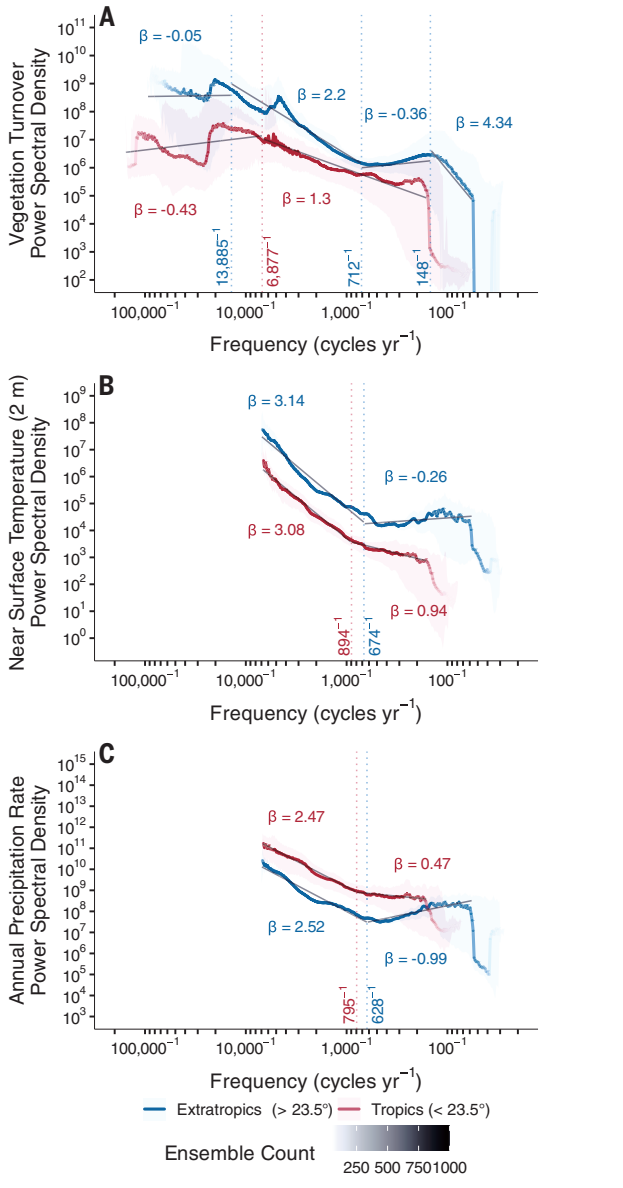

Fig. 3. The continuum of tropical and extratropical vegetation turnover and climate variability. The continuum of (**A**) vegetation turnover, (**B**) near-surface temperature, and (**C**) annual precipitation rate variability, averaged for the extratropics (blue, >23.5°) and tropics (red, <23.5°) based on the median from an ensemble of spectral power estimates. The transparency of the power spectra indicates the number of ensemble members that resolve each frequency. β in the high-frequency band was fit to the maximum frequency that yielded an unbiased estimate (*28*). Vertical dashed lines correspond to breakpoints identified in the spectral continuum and are colored by the corresponding spatial average. All climate estimates are from TraCE-21ka and have been downsampled as in Fig. 2. Shaded regions indicate the 95% CI for spectral power. Uncertainties for β and breakpoints, and permutation tests comparing these parameters, are reported in fig. S22 and tables S1 and S4 to S7.

latitudes experience greater temperature variability than the tropics at all frequencies (*5*), whereas the tropics experience greater precipitation variability (Fig. 3). Even though accurately simulating precipitation remains challenging, vegetation turnover appears to resemble temperature, in that tropical sites (<23.5°) have less vegetation variability than extratropical sites (>23.5°) (Fig. 3A). In addition, at frequencies of 712^{-1} (730^{-1}, 698^{-1}) to $13{,}885^{-1}$ ($14{,}495^{-1}$, $13{,}160^{-1}$) $year^{-1}$, extratropical sites have a β of 2.20 (2.16, 2.26) that is similar to those of temperature and precipitation, whereas tropical sites have a β of 1.30 (1.21, 1.38) (Fig. 3). Thus, tropical vegetation assemblages may be less sensitive to climate forcing across the frequencies investigated, are sensitive to climate forcings other than temperature and precipitation, are affected more by nonclimatic factors, or are more stable and resistant to turnover. Along these lines, recent observations show that although net primary production in low latitudes is constrained by solar radiation and precipitation, high northern-latitude productivity is limited by temperature (*48*), suggesting that these latitudinal differences in β could result from spatially variable climate controls on vegetation variability.

Conclusions

Our theoretical framework, based on spectral analyses, provides a new pathway forward to disentangle a fundamental question in ecology: How closely are ecological dynamics coupled or decoupled with environmental dynamics across timescales? The methods shown here are flexible and adaptable to all ecological systems with observational data across a range of timescales. Through this framework, we show that the relationship between vegetation turnover and climate variability is nonlinear and timescale-dependent over frequencies from 10^{-1} to $100{,}000^{-1}$ $year^{-1}$. The many similarities between vegetation and climate power spectra suggest that vegetation variation is governed by climate variability across intermediate frequencies. Modes of heightened variability in vegetation relative to climate at millennial frequencies underscore the risk of nonlinear and abrupt vegetation responses to present climate change. Conversely, the decoupling of vegetation and climate variability at higher frequencies ($>149^{-1}$ $year^{-1}$) reinforces concerns that biotic processes will be slow to respond to anthropogenic climate change and changing climate variability (*12*, *49*), leading to delayed and widespread ecological transitions that challenge predicting vegetation responses to present global warming.

REFERENCES AND NOTES

1. J. Overpeck, C. Whitlock, B. Huntley, in *Paleoclimate, Global Change and the Future*, Global Change—The IGBP Series, K. D. Alverson, T. F. Pedersen, R. S. Bradley, Eds. (Springer, 2003), pp. 81–103.
2. E. M. Wolkovich, B. I. Cook, K. K. McLauchlan, T. J. Davies, *Ecol. Lett.* **17**, 1365–1379 (2014).
3. D. Jablonski, *Evolution* **62**, 715–739 (2008).
4. R. E. Ricklefs, *Science* **235**, 167–171 (1987).
5. P. Huybers, W. Curry, *Nature* **441**, 329–332 (2006).
6. F. Zhu *et al.*, *Proc. Natl. Acad. Sci. U.S.A.* **116**, 8728–8733 (2019).
7. M. Yasuhara, R. Danovaro, *Biol. Rev. Camb. Philos. Soc.* **91**, 275–287 (2016).
8. J. W. Williams *et al.*, *Quat. Res.* **89**, 156–177 (2018).
9. J. Smith *et al.*, *Glob. Ecol. Biogeogr.* **32**, 1680–1689 (2023).
10. T. Webb III, *Vegetatio* **67**, 75–91 (1986).
11. J. W. Williams, A. Ordonez, J.-C. Svenning, *Nat. Ecol. Evol.* **5**, 17–26 (2021).
12. J.-C. Svenning, B. Sandel, *Am. J. Bot.* **100**, 1266–1286 (2013).
13. M. V. Talluto, I. Boulangeat, S. Vissault, W. Thuiller, D. Gravel, *Nat. Ecol. Evol.* **1**, 0182 (2017).
14. R. Bertrand *et al.*, *Nature* **479**, 517–520 (2011).
15. B. J. Butterfield, R. S. Anderson, C. A. Holmgren, J. L. Betancourt, *Glob. Ecol. Biogeogr.* **28**, 1067–1077 (2019).
16. M. Scheffer, S. Carpenter, J. A. Foley, C. Folke, B. Walker, *Nature* **413**, 591–596 (2001).
17. D. J. Thomson, *Proc. IEEE* **70**, 1055–1096 (1982).
18. F. He, thesis, University of Wisconsin–Madison (2011).
19. Z. Liu *et al.*, *Science* **325**, 310–314 (2009).
20. C. W. Snyder, *Nature* **538**, 226–228 (2016).
21. J. Jouzel *et al.*, *Science* **317**, 793–796 (2007).
22. T. Platt, K. L. Denman, *Annu. Rev. Ecol. Syst.* **6**, 189–210 (1975).
23. M. E. Dillon *et al.*, *Integr. Comp. Biol.* **56**, 14–30 (2016).
24. G. M. Locosselli *et al.*, *Proc. Natl. Acad. Sci. U.S.A.* **117**, 33358–33364 (2020).
25. L. B. Brubaker, *Vegetatio* **67**, 119–130 (1986).
26. R. Rauschkolb *et al.*, *New Phytol.* **235**, 773–785 (2022).
27. J. W. Williams, J. L. Blois, B. N. Shuman, *J. Ecol.* **99**, 664–677 (2011).
28. Materials and methods are available as supplementary materials.
29. K. Hasselmann, *Tellus* **28**, 473–485 (1976).
30. J. W. Williams, D. M. Post, L. C. Cwynar, A. F. Lotter, A. J. Levesque, *Geology* **30**, 971–974 (2002).
31. T. Laepple *et al.*, *Nat. Geosci.* **16**, 958–966 (2023).
32. R. Hébert, L. Schild, T. Laepple, U. Herzschuh, *Ecol. Evol.* **13**, e10585 (2023).
33. R. Hébert, K. Rehfeld, T. Laepple, *Nonlinear Process. Geophys.* **28**, 311–328 (2021).
34. R. B. Davis, *Limnol. Oceanogr.* **19**, 466–488 (1974).
35. H. D. Grissino-Mayer, H. C. Fritts, *Holocene* **7**, 235–238 (1997).
36. S. Zhao *et al.*, *J. Biogeogr.* **46**, 355–368 (2019).
37. O. Mottl *et al.*, *Science* **372**, 860–864 (2021).
38. L. Stephens *et al.*, *Science* **365**, 897–902 (2019).
39. K. Zhu, C. W. Woodall, J. S. Clark, *Glob. Change Biol.* **18**, 1042–1052 (2012).
40. S. R. Meyers, L. A. Hinnov, *Paleoceanography* **25**, PA3207 (2010).
41. S. Ferrier, G. Manion, J. Elith, K. Richardson, *Divers. Distrib.* **13**, 252–264 (2007).
42. G. Bond *et al.*, *Science* **278**, 1257–1266 (1997).
43. D. Fastovich *et al.*, *Geophys. Res. Lett.* **47**, e2020GL090031 (2020).
44. B. Huntley *et al.*, *PLOS ONE* **8**, e61963 (2013).
45. H. Wanner *et al.*, *Quat. Sci. Rev.* **27**, 1791–1828 (2008).
46. D. Magri, *J. Biogeogr.* **35**, 450–463 (2008).
47. M. G. Turner *et al.*, *Philos. Trans. R. Soc. London Ser. B* **375**, 20190105 (2020).
48. R. R. Nemani *et al.*, *Science* **300**, 1560–1563 (2003).
49. J. Aguirre-Gutiérrez *et al.*, *Science* **387**, eadl5414 (2025).
50. M. B. Davis, in *Forest Succession: Concepts and Application*, D. C. West, H. H. Shugart, D. B. Botkin, Eds. (Springer, 1981), pp. 132–153.
51. D. Fastovich, Code and data for Coupled, decoupled, and abrupt responses of vegetation to climate across timescales, Version 1.0. Zenodo (2024); https://doi.org/10.5281/zenodo.12726798.

ACKNOWLEDGMENTS

We thank Y. Kubota for convening the P-SEEDS workshop where the idea for this project began. Many thanks to the Syracuse University High Throughput Computing Campus Grid (OrangeGrid) for providing computational resources and to J. Cheney for technical support. Fossil pollen data were obtained from the Neotoma Paleoecology Database (http://www.neotomadb.org) and its constituent databases: the African Pollen Database, European Pollen Database, Indo-Pacific Pollen Database, Latin American Pollen Database, and North American Pollen Database. The work of data contributors, data stewards, and the Neotoma community is acknowledged. We thank the anonymous reviewers for their feedback, which greatly improved the manuscript. **Funding:** This project is a contribution to the BioDeepTime project, supported by Paleosynthesis Project, which is funded by the Volkswagen Foundation (Az 96 796). D.F. acknowledges postdoctoral support from NSF OCE-2103015, NSF AGS-2402498, and the College of Arts and Sciences at Syracuse University. Funding for OrangeGrid is provided by ACI-1341006. E.E.S. acknowledges support from a Leverhulme Prize and NERC grant NE/V011405/1. L.J. is supported through the German climate modeling initiative PALMOD, funded by the German Federal Ministry of Research, Technology and Space (BMFTR, 01LP1922A and 01LP2308A). M.C.R. acknowledges support from the German Research Foundation (DFG) through the Cluster of Excellence "The Ocean Floor – Earth's Uncharted Interface" (EXC 2077, grant no. 390741603). P.M.H. acknowledges sabbatical support from the Swiss Federal Institute for Forest, Snow and Landscape Research. S.R.M. acknowledges sabbatical support from University of Wisconsin–Madison and a Guggenheim Fellowship. J.W.W. acknowledges sabbatical support from University of Wisconsin–Madison and NSF awards EAR-2410961 and DEB-1855781. M.D. is funded by the European Union (CoralINT, GA 101044975). A.T. was funded by the Slovak Agency for Research and Development (APVV22-0523). Views and opinions expressed are however those of the author(s) only and do not necessarily reflect those of the European Union or the European Research Council. Neither the European Union nor the granting authority can be held responsible for them; and the Leverhulme Trust Research Centre – the Leverhulme Centre for Anthropocene Biodiversity (RC-2018-021). **Author contributions:** D.F. and P.M.H. developed the research questions and study design. D.F., S.R.M., E.E.S., J.W.W., and P.M.H. codeveloped the conceptual and analytical framework. D.F. performed all analyses with help from S.R.M. and E.E.S. D.F. led writing with support from S.R.M., E.E.S., J.W.W., and P.M.H. The ideas for this paper originated from discussions in the BioDeepTime working group. All authors reviewed and contributed to the article. **Competing interests:** J.W.W. declares additional advisory and consultancy roles: "I serve on the external scientific advisory board for the Ancient Environmental Genomics Initiative for Sustainability (AEGIS), a Danish research initiative that is studying species responses to past climate change. And I serve as the Secretary of the Earth-Life Consortium, a US non-profit 501c3 dedicated to the open sharing of paleobiological and paleoecological data. I receive no compensation for either role, except in the form of travel reimbursements from AEGIS." All other authors declare no competing interests. **Data and materials availability:** Data and code needed to reproduce all analyses are available on Zenodo (*51*).

SUPPLEMENTARY MATERIALS

science.org/doi/10.1126/science.adr6700
Materials and Methods; Figs. S1 to S22; Tables S1 to S8; References (*52*–*100*); Data S1

Submitted 11 July 2024; resubmitted 23 December 2024; accepted 8 May 2025

10.1126/science.adr6700

FERROELECTRICS

Fluorine-free strongly dipolar polymers exhibit tunable ferroelectricity

Jiahao Huang[1]†, Guanchun Rui[1,2,3]†, Yueming Yan[4]†, Elshad Allahyarov[5,6,7], Man-Hin Kwok[1]‡, Wenyi Zhu[2], Li Li[8], Shixian Zhang[8], Zhiliang Pan[9], Deyu Li[9], Honghu Zhang[10], Richard R. Mu[11], Bin Zhao[12], Qing Wang[8], Philip L. Taylor[7]*, Richard F. Haglund[4]*, Q. M. Zhang[2]*, Lei Zhu[1]*

Current research on ferroelectric polymers centers predominantly on poly(vinylidene fluoride) (PVDF)–based fluoropolymers because of their superior performance. However, they are considered "forever chemicals" with environmental concerns. We describe a family of rationally designed fluorine-free ferroelectric polymers, featuring a polyoxypropylene main chain and disulfonyl alkyl side chains with a C3 spacer: $-SO_2CH_2CHRCH_2SO_2-$ (R = –H or $-CH_3$). Both experimental and simulation results demonstrate that strong dipole-dipole interactions between neighboring disulfonyl groups induce ferroelectric ordering in the condensed state, which can be tailored by changing the R group: ferroelectric for R = –H or relaxor ferroelectric for R = $-CH_3$. At low electric fields, the relaxor polymer exhibits electroactuation and electrocaloric performance comparable with those of state-of-the-art PVDF-based tetrapolymers.

Ferroelectric (FE) materials feature direct cross couplings between electric polarization and diverse other properties, enabling applications in sensors and actuators, electrocaloric cooling, capacitors, and energy harvesting (*1*–*5*). Compared with FE ceramics, polymer FEs offer several advantages, including good flexibility, easy fabrication into complex shapes, lower weight and cost, and better acoustic impedance matching to biological tissues. Despite decades of research, however, only a limited number of FE polymers have been discovered; the most important are poly(vinylidene fluoride) (PVDF)–based fluoropolymers (*3*, *4*), hydrogen-bonded nylons (*6*), and liquid crystalline polymers (LCPs) with a chiral smectic C (SmC*) phase (*7*, *8*). Among these, only PVDF-based fluoropolymers have emerged as a successful FE polymer platform with a well-defined Curie transition and a large spontaneous polarization (*3*, *4*). However, manipulating the semicrystalline structures of FE fluoropolymers through chemical modifications to achieve tunable FE properties and high performance, such as transitioning from P(VDF-*co*-trifluoroethylene) [P(VDF-TrFE)]–based copolymers to terpolymers and tetrapolymers (*4*), has become increasingly complex and costly. Furthermore, fluoropolymers are often categorized as potential "forever chemicals," raising environmental and health concerns because of their environmental persistence. Thus, a rational design for fluorine-free FE polymers with tunable FE properties is highly desirable.

Beyond direct crystallization into polar crystal structures, as observed in PVDF/P(VDF-TrFE) and odd-numbered nylons, a promising strategy is to use strongly dipolar molecules to induce FE ordering. FE nematic and smectic A liquid crystals (LCs) were realized for rodlike molecules with large dipole moments (μ > ~10 D) (*9*–*12*), a design concept theoretically predicted by Born more than a century ago (*13*). However, the large dipole moment of these rodlike molecules is achieved by their long rod length, d: $\mu = qd$, where q is the partial charge. The substantial losses and heat generation associated with repeated FE switching of long, rodlike molecules underscore the need for an alternative approach. An increase in the partial charge q of small molecular dipoles could minimize these losses while allowing an enhanced dipole moment density (polarization) with tunable FE properties, but this remains an ongoing challenge.

Self-assembly in disulfonylated comb-shaped polymers

We rationally designed fluorine-free FE polymers with small, strongly dipolar disulfonyl groups, whose FE properties can be tailored simply by varying the chemical structure. These polymers feature a comb-shaped structure with a polyoxypropylene main chain and disulfonylated alkyl side chains with a C3 spacer (Fig. 1A). The synthesis procedures are presented in the supplementary materials, materials and methods. The overall dipole moment of two sulfonyl groups in each side chain could reach as high as 9 D [4.5 D for each sulfonyl group (*14*)], when the C3 spacer adopts a zig-zag conformation. We hypothesized that such a large dipole moment would favor FE ordering. By manipulating the methyl branch in the C3 spacer, the dipole-dipole interactions can be tailored to achieve either normal ferroelectricity (for FE-2SO_2P without the methyl branch) or relaxor ferroelectricity (for RFE-2SO_2P with the methyl branch).

Phase transitions of FE-2SO_2P and RFE-2SO_2P powder samples were studied by means of differential scanning calorimetry (DSC) (Fig. 1, B and C). For FE-2SO_2P during the first cooling, two sharp exothermic peaks were seen at 203.4° and 112.0°C, with enthalpy changes of 6.2 and 32.9 J g^{-1}, respectively. During the second heating, a glass transition temperature (T_g) was found at 48°C, together with two endothermic peaks at 140.4°C (33.6 J g^{-1}) and 207.7°C (6.4 J g^{-1}). From the substantially different enthalpy changes and supercoolings of the two transitions during the cooling and heating cycle, the phase below 140.4°C [the melting temperature (T_m)] should be a crystalline (K) phase, whereas the phase between 140.4° and 207.7°C [the isotropization temperature (T_i)] should be a LC phase. This assignment was further confirmed by means of polarized light microscopy (PLM) images of a powder sample (Fig. 1B, inset, and fig. S1). The K and LC structures were studied by means of temperature-dependent x-ray diffraction (XRD). From the fiber patterns of FE-2SO_2P at 25°C (Fig. 1D) and 160°C (fig. S2), lamellar reflections were seen on the equator in both K and LC phases, with layer thicknesses being 4.6 and 4.4 nm, respectively. The inter–side-chain scatterings on the meridian indicated an average distance of 0.45 nm and ~19° side-chain tilting from the polymer main chain in the K phase (fig. S2, B, i, and C, i). However, the average side-chain distance was 0.48 nm, and no side-chain tilting was seen in the LC phase (fig. S2, B, ii, and C, ii). On the basis of previous studies (*14*), this family of comb-shaped LCPs forms thermodynamically stable LC phases above the T_m of crystals because their fiber and powder XRD signatures match. The powder XRD (fig. S3A) also matched the fiber XRD (Fig. 1D and fig. S2) for FE-2SO_2P, indicating that the LC phase was thermodynamically stable and not induced by mechanical stretching.

[1]Department of Macromolecular Science and Engineering, Case Western Reserve University, Cleveland, OH, USA. [2]School of Electrical Engineering and Computer Science, Materials Research Institute, The Pennsylvania State University, University Park, PA, USA. [3]Arkema, King of Prussia, PA, USA. [4]Department of Physics and Astronomy, Vanderbilt University, Nashville, TN, USA. [5]Institut für Theoretische Physik II: Weiche Materie, Heinrich-Heine Universität Düsseldorf, Düsseldorf, Germany. [6]Theoretical Department, Joint Institute for High Temperatures, Russian Academy of Sciences, Moscow, Russia. [7]Department of Physics, Case Western Reserve University, Cleveland, OH, USA. [8]Department of Materials Science and Engineering, Materials Research Institute, The Pennsylvania State University, University Park, PA, USA. [9]Department of Mechanical Engineering, Vanderbilt University, Nashville, TN, USA. [10]National Synchrotron Light Source II, Brookhaven National Laboratory, Upton, NY, USA. [11]TIGER Institute, Tennessee State University, Nashville, TN, USA. [12]Department of Chemistry, University of Tennessee, Knoxville, TN, USA.
***Corresponding author. Email: lxz121@case.edu (L.Z.); plt@case.edu (P.L.T.); richard.haglund@vanderbilt.edu (R.F.H.); qxz1@psu.edu (Q.M.Z.)** †These authors contributed equally to this work. ‡Present address: Department of Chemistry, The Chinese University of Hong Kong, Shatin, N.T., Hong Kong, P. R. China.

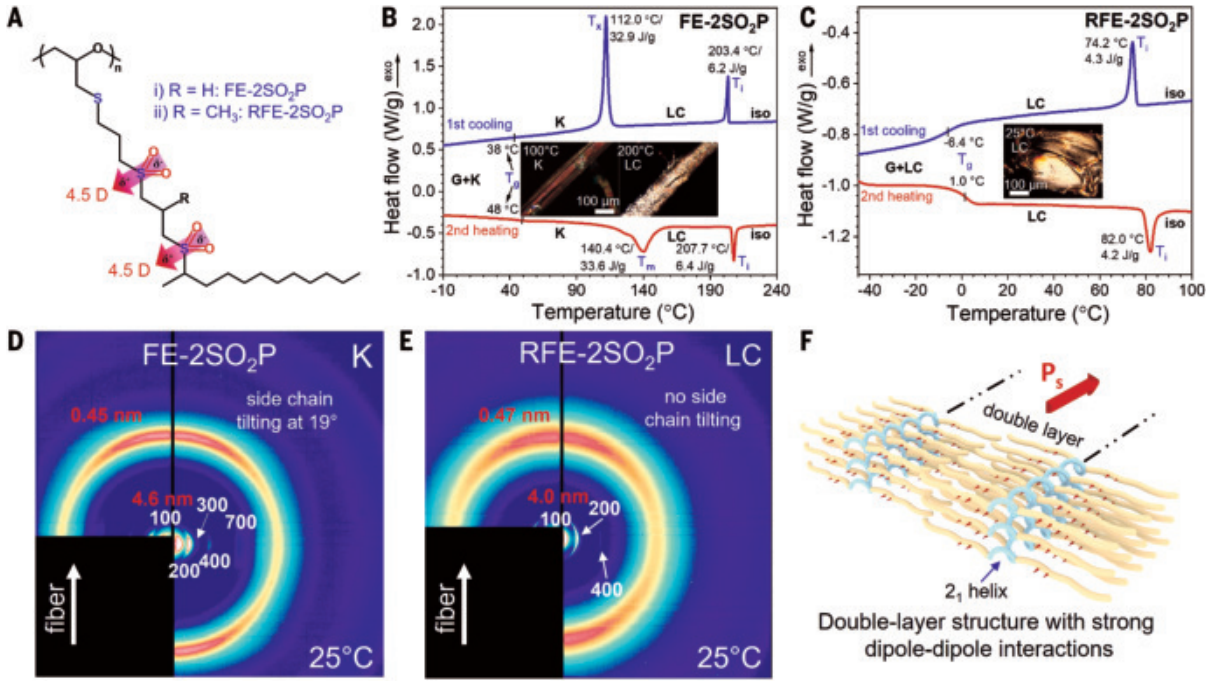

Fig. 1. Structures and phase transitions in FE-2SO$_2$P and RFE-2SO$_2$P. (**A**) Chemical structures of (i) FE (FE-2SO$_2$P) and (ii) RFE (RFE-2SO$_2$P) polymers, showing two parallel sulfonyl dipoles in the side chain with a C3 spacer. (**B** and **C**) First cooling and second heating DSC curves of (B) FE-2SO$_2$P and (C) RFE-2SO$_2$P powder samples. T_g is the glass transition temperature. T_m and T_x are the melting and crystallization temperatures, respectively. T_i is the isotropization temperature. (Insets) The corresponding PLM images at different temperatures. (**D** and **E**) Two-dimensional XRD fiber patterns of (D) FE-2SO$_2$P and (E) RFE-2SO$_2$P melt-drawn fibers at 25°C. (**F**) Proposed double-layer structure. Yellow strings indicate the aliphatic side chains, light-blue springs indicate the main chains with 2_1 helical conformation, and small red arrows indicate aligned sulfonyl dipoles. P_s is the spontaneous polarization from FE ordering of the disulfonyl groups.

The observations of a single endothermic peak at 82.0°C with a small enthalpy change of 4.2 J g^{-1} and birefringence at lower temperatures (Fig. 1C, inset, and fig. S4) reveal that RFE-2SO$_2$P had only an LC phase below T_i at 82.0°C, together with a T_g at 1.0°C during heating. Similarly, RFE-2SO$_2$P also self-assembled into a layered structure ~4.0 nm thick with no side-chain tilting below T_i (Fig. 1E and fig. S5). This fiber XRD matched the powder XRD (fig. S3B), indicating an intrinsic layered LC structure. Given the side-chain length, a double-layer structure is proposed for these two FE dipolar polymers (Fig. 1F and supplementary text 1).

Tunable ferroelectricity

The ferroelectricity of these two dipolar polymers was examined with broadband dielectric spectroscopy (BDS), electric displacement–electric field (D-E) loop test, and second-harmonic generation (SHG) measurements. The real part of the relative permittivity (ε_r') of FE-2SO$_2$P (Fig. 2A) was measured in the temperature-scan BDS during cooling at 2°C/min. The peak in dielectric constant, which was independent of frequency at 118°C, coincided with the crystallization temperature (T_x) at 112°C observed in the DSC cooling scan (Fig. 1B), indicating a paraelectric (PE)–to-FE Curie transition between the PE LC and the FE K phases in FE-2SO$_2$P. The $1/\varepsilon_r'$ versus (T-T_C) exhibited a linear relationship for frequency between 30 kHz and 1 MHz (Fig. 2A, inset), fitting well to the Curie-Weiss law (*15*). Typical FE D-E hysteresis loops of FE-2SO$_2$P were obtained at 75°C (Fig. 2C and fig. S6A). At a poling field of 125 MV m^{-1}, the remanent polarization (P_r) was 33.2 mC m^{-2}, which is much higher than that of typical FE SmC* LCPs (0.1 to 1 mC m^{-2}) (*8*). The coercive field was ~31 MV m^{-1}. From the plot of P_r versus poling field (fig. S6B), the major P_r was attributed to FE switching, rather than ionic conduction, when the poling field was above 75 MV m^{-1}.

Substantially different from FE-2SO$_2$P, RFE-2SO$_2$P exhibited a broad frequency-dependent ε_r' peak in the temperature-scan BDS curves (Fig. 2B). A peak ε_r' as high as 48, comparable with those of PVDF-based terpolymer relaxors (50 to 60) (*16*), was found at 27.6°C and 10 Hz. The temperature at the peak ε_r' is denoted T_{max}. Both the high ε_r' and the apparent frequency dependence of T_{max} suggest typical relaxor ferroelectricity in the RFE-2SO$_2$P near room temperature (RT). The frequency (f) dispersion is well described by the Vogel-Fulcher law: $f = f_0\exp[-E_a/(k_B(T_{max} - T_f))]$, where f_0 is the attempt frequency, E_a is the activation energy, and T_f is the freezing temperature (*17*, *18*). From the Vogel-Fulcher fitting, we obtained T_f = 239 K and E_a = 0.12 eV (Fig. 2B, inset). Unlike normal FEs with large domains, relaxors contain polar nanoregions or nanodomains with random orientations (*17*, *18*). Unfortunately, because the LC RFE-2SO$_2$P was very soft and should contain dynamic nanodomains at RT, piezoresponse force microscopy could not detect the nanodomains. Below T_f, relaxors can change to normal FEs because of enlarged and frozen nanodomains. Both slim RFE and broad FE D-E loops were observed for RFE-2SO$_2$P at 20 and −30°C, respectively (Fig. 2D). The P_r decreased continuously from 28.5 mC/m^2 at −30°C to 4.3 mC m^{-2} at 20°C (Fig. 2D, inset, and fig. S7, D-E loops).

The existence of FE domains in both polymers was confirmed by measuring the SHG signal generated by a near-infrared laser (supplementary text 2). Samples in LC cells were electrically poled (120 MV m^{-1}) at 75°C for FE-2SO$_2$P and −50°C for RFE-2SO$_2$P (supplementary materials, materials and methods), and then, their SHG responses were recorded during heating after removal of the poling field. PE materials, which contain no FE domains, would show no SHG signal once the poling field was removed. However, both samples exhibited clear SHG signals even after the removal of the poling field, indicating the persistence of oriented FE domains due to electric poling.

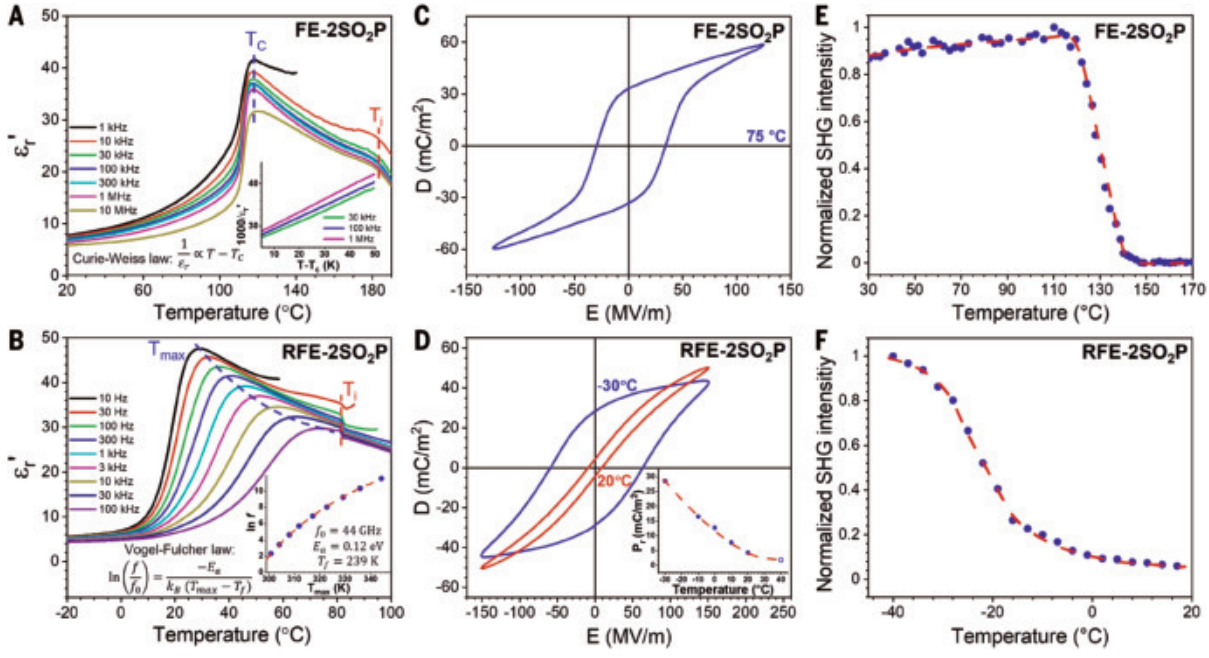

Fig. 2. Ferroelectricity of FE-2SO$_2$P and relaxor ferroelectricity of RFE-2SO$_2$P. (**A** and **B**) Temperature-scan BDS results of the real part of the relative permittivity (ε_r') for (A) FE-2SO$_2$P and (B) RFE-2SO$_2$P during cooling at 2°C min^{-1}. T_C is the Curie temperature. (A) (Inset) The Curie-Weiss plot for frequency between 30 kHz and 1 MHz. (B) (Inset) The Vogel-Fulcher fitting of T_{max}. (**C** and **D**) Bipolar D-E loops of (C) FE-2SO$_2$P and (D) RFE-2SO$_2$P. (D) (Inset) A gradual decrease of P_r with temperature. (**E** and **F**) Normalized SHG intensity after removal of the poling field during heating for poled (E) FE-2SO$_2$P and (F) RFE-2SO$_2$P in LC cells.

Neither should have shown any SHG signal after removal of the poling field, if both samples were PE without any FE domains. For FE-2SO$_2$P, the SHG signal remained almost constant at temperatures below 120°C, which is consistent with a normal FE phase having uniform polarization. The SHG signal showed a rapid drop starting at 125°C (Fig. 2E), which is the onset Curie temperature of the FE-to-PE transition peak (Fig. 2A). Eventually, the SHG signal became zero in the PE phase. By contrast, for RFE-2SO$_2$P, the SHG signal decreased continuously (Fig. 2F) at temperatures far below the T_{max} at 10 Hz (Fig. 2B), which is characteristic of a relaxor FE.

Molecular dynamics simulations

Because single crystals could not be obtained for these polymers and the atomic packing information remained unknown, molecular dynamics (MD) simulations were performed to investigate the mechanism of FE ordering. Details of the MD simulations are given in the supplementary materials, materials and methods. Simulated single-layer molecules of FE-2SO$_2$P and RFE-2SO$_2$P are shown in Fig. 3, A and B (from the 10-layer stacked molecules in fig. S8), respectively. Before MD simulation, the sulfonyl dipoles were initially randomized with an angle α, which is defined in Fig. 3D, inset (α = π/2 for the molecules in Fig. 3, A to C). After MD simulation for each α, the average dipole moments of the inner and the outer sulfonyl groups were calculated. As α decreased from 2π to 0, the average dipole moments of inner and outer sulfonyl groups increased (Fig. 3D). The dipole moment of the inner sulfonyl groups was always higher than that of the outer sulfonyl groups. For example, when α = 0, the average dipole moments of the inner sulfonyl groups for FE-2SO$_2$P and RFE-2SO$_2$P were both 4.49 D, and those of the outer sulfonyl groups were 3.95 and 3.48 D, respectively. The average dipole moment of the outer sulfonyl group in RFE-2SO$_2$P was smaller than that in FE-2SO$_2$P. This can be visualized from the magnified side chains shown in Fig. 3C, where the inner sulfonyl groups were better aligned along the main chain than the outer sulfonyl groups, possibly because of the higher

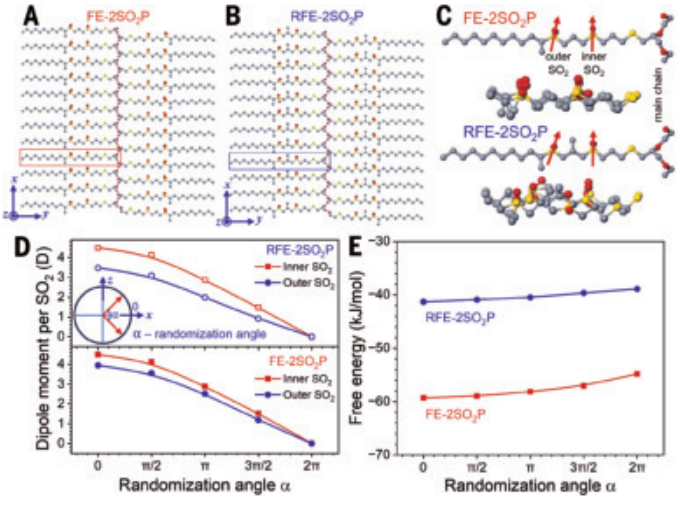

Fig. 3. MD simulations of FE-2SO$_2$P and RFE-2SO$_2$P. (**A** and **B**) MD-simulated full atomistic models of single-layer (A) FE-2SO$_2$P and (B) RFE-2SO$_2$P with the initial dipole randomization angle, α = π/2. (**C**) Magnified single side chains for FE-2SO$_2$P and RFE-2SO$_2$P in the red box in (A) and the blue box in (B), respectively. The magnified side views of the disulfonyl groups in three layers of stacked molecules are also shown. (**D**) Simulated dipole moments of the inner and the outer sulfonyl dipoles as a function of the initial dipole randomization angle α (defined in the inset). (**E**) Free energy as a function of α for FE-2SO$_2$P and RFE-2SO$_2$P.

flexibility of the outer sulfonyl groups. We attribute the difference between FE-2SO$_2$P and RFE-2SO$_2$P to the methyl branch in the C3 spacer of the disulfonyl group in RFE-2SO$_2$P, whose steric hindrance prevents the parallel alignment of the two sulfonyl groups in one side chain. The free energies were calculated for FE-2SO$_2$P and

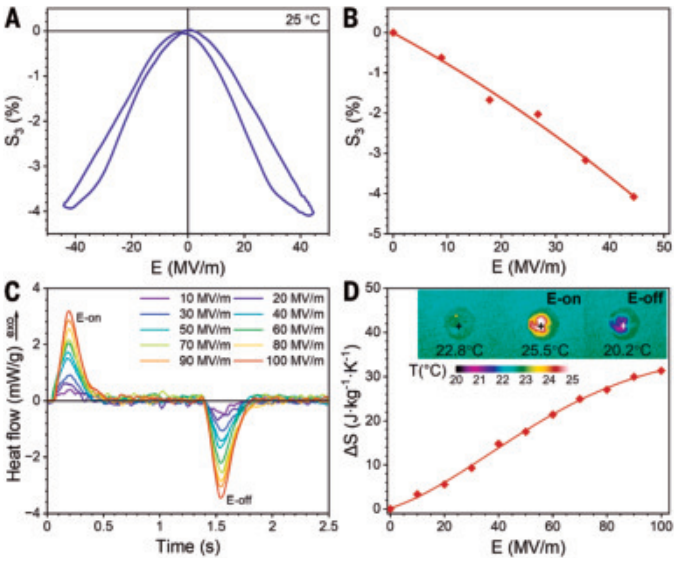

Fig. 4. Electroactuation and ECE of RFE-2SO$_2$P. (**A**) Bipolar S_3-E loop and (**B**) electroactuation of RFE-2SO$_2$P at 25°C. The poling frequency is 1 Hz with a sinusoidal waveform. (**C**) ECE heat flow curves and (**D**) measured ΔS values of RFE-2SO$_2$P measured under different electric fields at RT. (Inset) Infrared images for temperature changes during an on-off poling cycle under 40 MV m^{-1} at RT.

RFE-2SO$_2$P (Fig. 3E). FE-2SO$_2$P had much lower free energy than RFE-2SO$_2$P at all α values. We conclude that the methyl branches in the C3 spacers destabilize RFE-2SO$_2$P as compared with FE-2SO$_2$P, which should explain why FE-2SO$_2$P had much stronger polar ordering (FE) than RFE-2SO$_2$P (RFE). A schematic representation of the self-assembly and FE ordering is shown in fig. S9.

Electroactuation and electrocaloric effect

Given the distinctive RFE behavior of RFE-2SO$_2$P, we further explored electroactuation and electrocaloric effect (ECE), especially under low electric fields at RT for practical applications. The thickness strain (S_3) was measured for a thin film under ac fields at 1 Hz (Fig. 4A). A high strain of −4% was observed at 44 MV m^{-1} (Fig. 4, A and B). The Maxwell strain would also be expected to produce a nonnegligible contribution to the overall electroactuation because of the low modulus of RFE-2SO$_2$P (~1 MPa at 1 Hz) (fig. S10). This electroactuation is superior to that observed in the PVDF-based terpolymers (S_3 = −1.0%) and tetrapolymers (S_3 = −3.6%) at 50 MV m^{-1} (*19*). The ECE of RFE-2SO$_2$P was directly measured for different electric fields under the adiabatic condition at RT—entropy change (ΔS) by means of a calorimeter equipped with a heat flux sensor (*20*) and temperature change (ΔT) with an infrared camera (*21*, *22*). A ΔS of 14.8 J kg^{-1} K^{-1} and a ΔT of 2.7 K were obtained at 40 MV m^{-1} (Fig. 4, C and D). This ECE exceeds that of the PVDF-based terpolymer (ΔS = 4.8 J kg^{-1} K^{-1} and ΔT = 1.1 K) and compares favorably with that of a recently reported PVDF-based tetrapolymer (ΔS = 24.7 J kg^{-1} K^{-1} and ΔT = 4.9 K) at 40 MV m^{-1} (*20*). We attribute the excellent electroactive performance of RFE-2SO$_2$P at low fields to the highly mobile nanodomains in the LC phase at RT.

We have demonstrated a class of fluorine-free FE polymers with tunable ferroelectricity. The strong dipole-dipole interactions among neighboring disulfonyl groups with a C3 spacer in the side chains induced the polar ordering to form FE domains. When the methyl branch in the C3 spacer was absent, FE-2SO$_2$P crystallized into FE crystals. When the C3 spacer was implemented with a methyl branch, the crystalline packing was disrupted, and RFE-2SO$_2$P became relaxor FE and LC at RT. Substantial electroactuation and a promising ECE in RFE-2SO$_2$P were achieved below 50 MV m^{-1}. We anticipate that these polymers will enable a systematic study of the structural dependence of FE behavior. Moreover, their environmentally friendly nature makes them particularly promising for diverse applications, including wearable and biocompatible actuators, thermal management devices, and next-generation flexible electronics.

REFERENCES AND NOTES

1. G. H. Haertling, *J. Am. Ceram. Soc.* **82**, 797–818 (1999).
2. F. Li *et al.*, *Nat. Mater.* **17**, 349–354 (2018).
3. A. J. Lovinger, *Science* **220**, 1115–1121 (1983).
4. X. Qian, X. Chen, L. Zhu, Q. M. Zhang, *Science* **380**, eadg0902 (2023).
5. M. Zhang *et al.*, *Science* **384**, 185–189 (2024).
6. H. S. Nalwa, in *Ferroelectric Polymers: Chemistry, Physics, and Applications*, H. S. Nalwa, Ed. (Marcel Dekker, 1995), pp. 297–323.
7. R. B. Meyer, L. Liebert, L. Strzelecki, P. Keller, *J. Phys. Lett.* **36**, 69–71 (1975).
8. G. Scherowsky, in *Ferroelectric Polymers: Chemistry, Physics, and Applications*, H. S. Nalwa, Ed. (Marcel Dekker, 1995), pp. 435–537.
9. H. Nishikawa *et al.*, *Adv. Mater.* **29**, 1702354 (2017).
10. X. Chen *et al.*, *Proc. Natl. Acad. Sci. U.S.A.* **119**, e2210062119 (2022).
11. H. Kikuchi *et al.*, *Adv. Sci.* **9**, e2202048 (2022).
12. O. D. Lavrentovich, *Proc. Natl. Acad. Sci. U.S.A.* **117**, 14629–14631 (2020).
13. O. M. Born, *Sitzungsber. Preuss. Akad Wiss* **30**, 614–649 (1916).
14. J. Huang, M.-H. Kwok, B. Zhao, L. Zhu, *Giant* **18**, 100257 (2024).
15. D. Viehland, S. J. Jang, L. E. Cross, M. Wuttig, *Phys. Rev. B Condens. Matter* **46**, 8003–8006 (1992).
16. Y. Lu, J. Claude, B. Neese, Q. Zhang, Q. Wang, *J. Am. Chem. Soc.* **128**, 8120–8121 (2006).
17. L. E. Cross, *Ferroelectrics* **76**, 241–267 (1987).
18. Q. M. Zhang, V. Bharti, X. Zhao, *Science* **280**, 2101–2104 (1998).
19. X. Chen *et al.*, *Science* **375**, 1418–1422 (2022).
20. X. Qian *et al.*, *Nature* **600**, 664–669 (2021).
21. R. Ma *et al.*, *Science* **357**, 1130–1134 (2017).
22. D. Han *et al.*, *Nature* **629**, 1041–1046 (2024).

ACKNOWLEDGMENTS

Funding: L.Z. and B.Z. acknowledge initial funding from the US Department of Energy (DOE), Office of Science/Basic Energy Science, Materials Synthesis Program (DE-SC0018075). L.Z. and P.L.T. acknowledge partial funding from the National Science Foundation (NSF), Division of Materials Research (DMR), Polymers Program (2103196 and 2500507) for MD simulations. Q.M.Z. and Q.W. acknowledge financial support from NSF, DMR, Polymers Program (2413150). W.Z. acknowledges financial support from the US Office of Naval Research (grant N00014-23-1-2247). R.R.M. acknowledges partial support by the NSF DMR through the Partnership for Research and Education in Materials (PREM) program (2122169 and 2424463) and by DOE DE-FE0032273 and the RENEW program. B.Z. acknowledges partial support from NSF, DMR, and the Polymers Program (2412257). R.F.H. acknowledges partial funding from the Stevenson Endowment in Physics. XRD experiments were performed at the 11-BM CMS beamline of NSLS-II, BNL, a DOE User Facility operated for the Office of Science by BNL (DE-SC0012704). **Authors contributions:** L.Z., Q.M.Z., P.L.T., R.F.H., B.Z., and Q.W. directed the research; J.H. and M.-H.K. conducted materials synthesis and general characterization; J.H., G.R., W.Z., and S.Z. conducted electroactuation and ECE measurements; Y.Y., J.H., Z.P., D.L., and R.R.M. carried out the SHG experiments; H.Z. and J.H. performed WAXD experiments; E.A., P.L.T., and L.L. performed MD simulations; J.H. and L.Z. performed experimental data analyses, and all authors participated in discussions. J.H. and L.Z. prepared the manuscript with input from all authors. **Competing interests:** J.H., G.R., M.-H.K., and L.Z. have filed a provisional patent application at Case Western Reserve University (US application no. 63/782,698). All other authors declare no competing interests. **Data and materials availability:** All data are available in the manuscript or the supplementary materials.

SUPPLEMENTARY MATERIALS

science.org/doi/10.1126/science.ads4702
Materials and Methods; Supplementary Text; Figs. S1 to S18; References (*23*–*33*)
Submitted 15 August 2024; resubmitted 11 February 2025; accepted 2 May 2025
10.1126/science.ads4702

POLYMER FILMS

Electric double-layer synthesis of a spongelike, lightweight reticular membrane

Yoshimitsu Itoh[1,2]*, Tengfei Fu[1]†, Pier-Luc Champagne[1]†‡, Yudai Yokoyama[1]†, Kunita Numabe[1]†§, You-lee Hong[3]¶, Yusuke Nishiyama[3,4], Hsiao-Fang Wang[5]#, Akemi Kumagai[5], Hiroshi Jinnai[5], Hirohmi Watanabe[6], Teiko Shibata-Seki[7], Asuteka Nagao[1], Tsutomu Suzuki[1], Yukie Saito[8], Keigo Wakabayashi[5], Takeharu Yoshii[5], Atsushi Izumi[9], Katsumi Hagita[10], Junichi Furukawa[1]**, Takuzo Aida[1,11]*

Electrochemical polymer synthesis usually forms dense films bound to the electrode. We report a single-step synthesis of large-area, ultrathin (~70-nanometer) polymeric membranes with a luffa-like, reticular cross-linked network with low density (0.5 grams per cubic centimeter). This particular membrane forms within an electric double layer in water constructed by voltage application without supporting electrolytes—in which deprotonated resorcinol and an aldehyde react three-dimensionally with a self-termination mechanism—and is spontaneously released when the voltage bias is removed. Initially rigid with a Young's modulus of 8.9 gigapascals, this membrane reversibly regains flexibility (0.5 gigapascals) upon wetting and can be used as a large-area membrane for separations. Its shape-persistent carbonization made it possible to yield ultrathin (~22-nanometer) nanoporous carbon membranes.

Amid a variety of emerging concerns related to plastic waste (*1*, *2*), the utilization of low-density, resource-saving polymeric materials is attracting much attention and holds promise for shaping a sustainable future (*3*). In nature, luffa, a member of the cucumber family, has a cross-linked reticular network comprising lignin hybridized with cellulose (*4*, *5*). When dried, the resulting luffa sponge is ultralow-density, but stiff, natural material. Although many synthetic porous lightweight materials (density $D < 0.7$ g cm^{-3}) including polymer foams and aerogels (*6*–*8*) have been reported, they are not robust, because their Young's modulus and tensile strength typically decrease with density (*9*, *10*). By contrast, the luffa sponge is mechanically robust in the dry state and maintains its reticular form under applied pressure, even under heavy weight, but after wetting returns to a markedly flexible and deformable material.

To date, synthetic lightweight reticular materials with similar properties have not been reported. We now demonstrate the direct electrochemical polymer synthesis of low-density (0.4 to 0.6 g cm^{-3}), ultrathin (<70 nm), cross-linked membranes with a luffa-like, lightweight reticular architecture [reticular membranes (RMs)] that are stiff in their dry state yet exhibit high flexibility when wet.

Electrochemical membrane synthesis

We found that the synthesis of this particular membrane from resorcinol and aldehydes by electropolymerization occurred only in pure water in the absence of the usual supporting electrolytes. We used a custom-made reaction cell comprising a highly doped silicon wafer as the working electrode, a Pt mesh as the counter electrode, and Ag/AgCl as the reference electrode (fig. S1) (*11*). In our experiments, we initially filled this custom-made cell with a deionized aqueous solution of a mixture of resorcinol (0.50 M) and formaldehyde (^{CHO}C1, 1.0 M) and applied a DC voltage of +5 V (versus Ag/AgCl) for 1 min at 35°C or 1 hour at 15°C. Application of a voltage to deionized water caused electrostatic accumulation of OH^- and H^+ ions to form their electric double layers (EDLs) on the positively and negatively charged electrodes, respectively. These EDLs are expected to stay near the electrode surfaces without diffusion (*12*–*14*). In a previous study, we used such an electrostatically accumulated EDL for inducing the conformational change of a surface-anchored oligoether by deprotonating and protonating its carboxylate headgroup (*15*). In the present work, we used such an EDL as a medium for activating resorcinol through deprotonation for the cross-linking reaction with formaldehyde as well as longer-chain dialdehydes. As a consequence, deposition of a thin film of ^{C1}RM onto the working electrode surface resulted (Fig. 1, A to C). In marked contrast to conventional electropolymerization (*16*–*19*), removal of the applied voltage resulted in spontaneous delamination of ^{C1}RM from the electrode surface (*20*), affording a free-standing membrane with a smooth surface (Fig. 1, D, F, and G, and movie S1).

Because there were no supporting electrolytes, deprotonated resorcinol and a polyphenolic product were electrostatically paired with a positive charge (hole) in the electrode and did not carry a counter cation in their vicinity. Thus, these species must repel each other. This peculiar circumstance may lead to a low-density, luffa-like reticular architecture (Fig. 1, C and E). Application of an optimized voltage of +5 V for only 1 min to deionized water without addition of supporting electrolytes did not cause electrolysis of water but rather facilitated resorcinol to be deprotonated to form an EDL followed by electrochemical reticular membrane formation. Application of a lower voltage of +4 V and +3 V also produced a membrane after 1 min, whereas the application of +2 V required 10 min for the formation of the membrane (table S1). Contrasting examples reported to date include the resorcinol/formaldehyde cross-linking reaction (*21*) at an applied voltage of +60 V for 1 to 3 days (*22*), in which water is electrolyzed to yield diffusible acids and bases (*23*), which cause a non–site specific cross-linking reaction, resulting in formation of a resorcinol resin.

The formation of a membrane requires only a small amount of resorcinol and formaldehyde in the feed, and we succeeded in obtaining 30 membranes from the same feed solution by simply renewing the working electrode. ^{C1}RMs of high structural integrity still formed, even when the concentrations of resorcinol and formaldehyde were greatly reduced to 0.125 M and 0.25 M, respectively (table S1). With the cell configuration shown in fig. S1, the membrane formed had exactly the same surface area (6 cm^2) as that of the working electrode exposed to the polymerization mixture.

We hypothesized that the negatively charged EDL, which is supposedly constructed electrostatically in the vicinity of the working electrode (according to Fig. 1, B and C), plays a vital role. To confirm the formation of such a particular EDL, we prepared an electric cell filled

[1]Department of Chemistry and Biotechnology, School of Engineering, the University of Tokyo, Bunkyo-ku, Tokyo, Japan. [2]Japan Science and Technology Agency (JST), Precursory Research for Embryonic Science and Technology (PRESTO), Kawaguchi, Saitama, Japan. [3]RIKEN—JEOL Collaboration Center and RIKEN SPring-8 Center, Yokohama, Kanagawa, Japan. [4]JEOL, Akishima, Tokyo, Japan. [5]Institute of Multidisciplinary Research for Advanced Materials, Tohoku University, Aoba-ku, Sendai, Miyagi, Japan. [6]Organic Materials Diagnosis Group, National Institute of Advanced Industrial Science and Technology, Higashihiroshima, Hiroshima, Japan. [7]Administrative Affairs Department of TMU, Tokyo Metropolitan Public University Corporation, Hino, Tokyo, Japan. [8]Graduate School of Agricultural and Life Sciences, the University of Tokyo, Bunkyo-ku, Tokyo, Japan. [9]Corporate Engineering Center, Sumitomo Bakelite Co., Fujieda, Shizuoka, Japan. [10]Department of Applied Physics, National Defense Academy, Yokosuka, Kanagawa, Japan. [11]RIKEN Center for Emergent Matter Science, Wako, Saitama, Japan. ***Corresponding author. Email: itoh@chembio.t.u-tokyo.ac.jp (Y.I.); aida@macro.t.u-tokyo.ac.jp (T.A.)** †These authors contributed equally to this work. ‡Present address: NOVA Chemicals Corporation, Center of Applied Research, Calgary, Alberta, Canada. §Present address: Institut des Matériaux, Laboratoire des Polymères, École Polytechnique Fédérale de Lausanne (EPFL), Lausanne, Switzerland. ¶Present address: LG Energy Solutions, Yuseong-gu, Daejeon, Republic of Korea. #Present address: Department of Chemical and Materials Engineering, National Central University, Zhongli District, Taoyuan City, Taiwan (ROC). **Present address: Kao Corporation, Chuo-ku, Tokyo, Japan.

with a deionized aqueous solution of 1-hydroxypyrene (1-HP, 1 μM), a pH-sensitive dye bearing a phenolic –OH group. The fluorescence emission at 448 nm derived from the deprotonated 1-HP, as expected, appeared and disappeared in response to turning on and off the DC voltage of +5 V (versus Ag/AgCl), respectively (fig. S20) (*11*). In the negatively charged EDL constructed here, not only the resorcinol monomer but also its polymeric network was deprotonated. Thus, the monomer diffusion into the polymeric network could electrostatically be suppressed (*11*), thereby self-terminating the membrane growth (Fig. 1E). Also, such a repulsive environment likely suppressed the molecular packing to give a low-density (0.5 g cm^{-3}) reticular network (Fig. 1E and fig. S6; see below). When the polymerization was conducted in the presence of 0.1 M sodium sulfate, a membrane with an ordinary density of 0.9 g cm^{-3} formed (fig. S11) (*24*). The negative-charged EDL constructed here is composed of sulfate ions, wherein neither the resorcinol monomer nor its polymeric product is deprotonated.

Structural characterization

The Fourier transform infrared spectrum of ^{C1}RM showed distinct bands that were due to the O–H and C–H stretching vibrations at 3250 cm^{-1} and 2850 to 2920 cm^{-1}, respectively (fig. S27). In the lower wave-number region, we observed a C=C stretching vibration at 1600 cm^{-1} (fig. S27). As expected, wide scan x-ray photoelectron spectroscopy (XPS) of ^{C1}RM (fig. S6A) showed only two peaks due to carbon and oxygen, whereas the narrow scan of C1s (fig. S6B) displayed peaks due to C=C originating from the benzene ring of resorcinol together with those due to C–O and C=O.

To enhance the ^{13}C NMR signals of the methylene units derived from formaldehyde, we prepared ^{C1}RM using ^{13}C-enriched (≥99 atomic %) formaldehyde. As shown in Fig. 2A, its cross-polarization magic-angle spinning carbon-13 nuclear magnetic resonance (^{13}C CP-MAS NMR) spectrum (Fig. 2A, figs. S21 to S25, and table S2) displayed CH_2 signals due to Ar–CH_2–Ar (20 to 30 ppm) and Ar–CH_2O– (50 to 60 ppm). These units do not exist in the monomers, which suggests the occurrence of a base-catalyzed addition-condensation reaction between resorcinol and formaldehyde to form ^{C1}RM (Fig. 2B) (*21*). Nevertheless, the ^{13}C NMR signals due to Ar–Ar (110 to 120 ppm) and Ar–O–Ar (150 to 160 ppm) indicate the concomitant occurrence of oxidative resorcinol coupling (Fig. 2B) (*25*). Notably, the integral ratio of the signals due to these methylene units relative to the total aromatic units (90 to 170 ppm) was 1/78, which was smaller than the ratio of 1/4, provided that all aromatic CH units in resorcinol reacted with formaldehyde (fig. S25) (*11*). On the basis of the XPS of trifluoroacetic anhydride–labeled ^{C1}RM (fig. S29), we concluded that 66% of the phenolic–OH groups remained unreacted in the membrane (*11*). Thus, the number of –OH groups in the membrane was as high as that of lignin (*26*). The cross-linked structure of ^{C1}RM was also supported by its characteristic thermoset

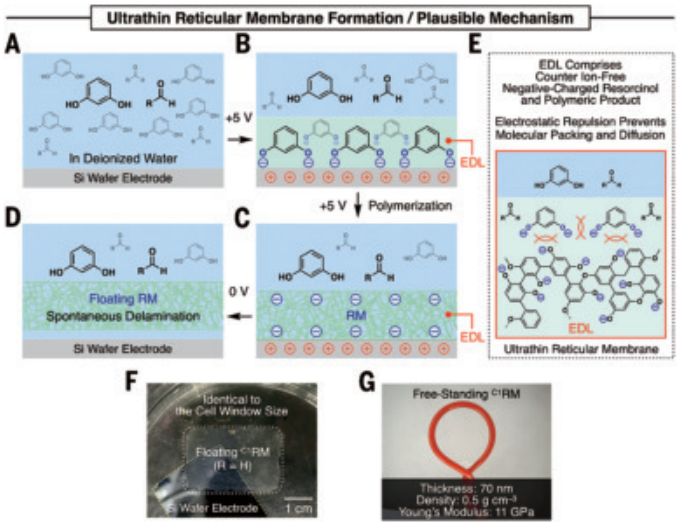

Fig. 1. Supporting electrolyte-free electropolymerization in water for the synthesis of ultrathin low-density reticular membranes (RMs). (**A** to **D**) Proposed mechanism for the formation of an ultrathin RM. (A) Before the application of a voltage. (B) Upon application of +5 V, an EDL containing deprotonated resorcinol is constructed on the positive-charged electrode surface. (C) A RM, formed by oxidative coupling and addition-condensation reaction, is likely deprotonated to comprise the EDL. (D) After the bias is removed, the RM is spontaneously delaminated. The residual solution can be repetitively reused for the RM synthesis more than 30 times by renewing the working electrode. (**E**) Electrostatic repulsion between the deprotonated reactants (resorcinol and its polymeric product) in a negative-charged EDL can account for the formation of a reticular architecture and also the self-termination to suppress its growth along the thickness direction. (**F**) Photograph of a floating ^{C1}RM (bordered by dashed white lines) on water delaminated from the working electrode after the voltage removal. (**G**) Photograph of a free-standing ^{C1}RM supported by a ring-shaped thin wire.

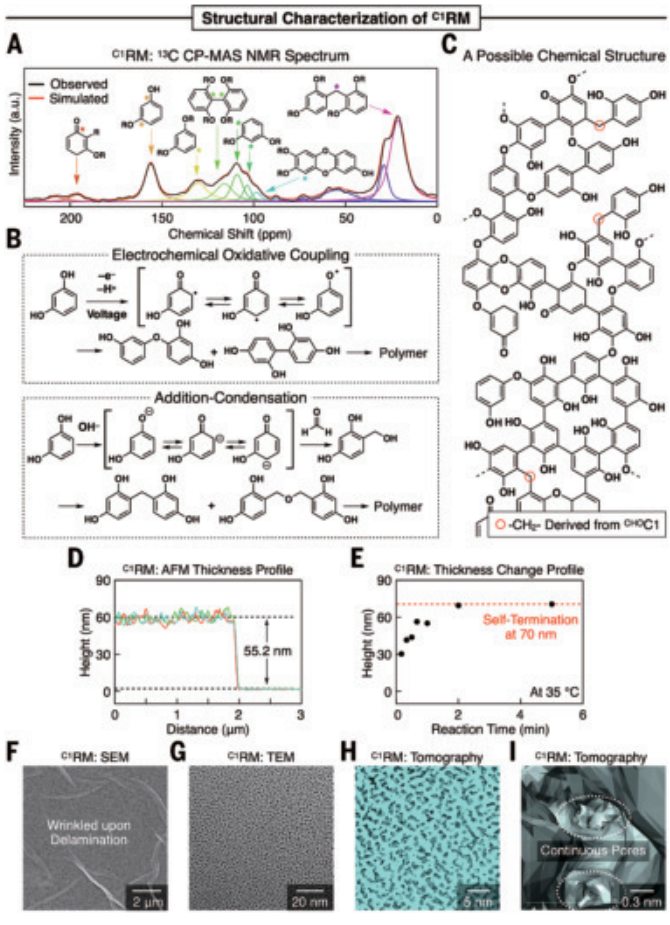

Fig. 2. Structural characterization of ^{C1}RM. (**A**) ^{13}C CP-MAS NMR spectrum (black) of ^{C1}RM prepared with ^{13}C-labeled formaldehyde and its deconvoluted spectra (multiple colors). (**B**) Elementary reactions involved in the membrane formation. (**C**) A possible chemical structure of ^{C1}RM. (**D**) AFM thickness profile of ^{C1}RM synthesized with a voltage-application time of 1 min and (**E**) thickness change profile with the progress of reaction. (**F**) SEM micrograph of ^{C1}RM. The sample was sputtered with platinum. (**G**) TEM micrograph of ^{C1}RM. The sample was stained with ruthenium tetroxide. Electron tomographic images of the surface (**H**) and pore interior (**I**) of ^{C1}RM.

nature in differential scanning calorimetry, by which neither exothermic nor endothermic heat flow was detected in a range from −20°C to 200°C (fig. S34).

Using atomic force microscopy (AFM), we found that ^{C1}RM reached the thickness of 55 nm when the polymerization was allowed to proceed by applying a voltage of +5 V for 1 min at 35°C (Fig. 2, D and E). When the same voltage was applied for 2 min, the membrane thickness reached 70 nm but did not increase further, even when the reaction was continued (Fig. 2E), indicating self-termination. We investigated the resulting membrane with scanning electron microscopy (SEM) (Fig. 2F and fig. S30) and transmission electron microscopy (TEM) (Fig. 2G). Although SEM showed some wrinkles resulting from delamination, no structural defects were observed across any scale. Notably, electron tomography revealed the presence of continuous pores (Fig. 2, H and I, and movie S2) with a considerably narrow pore-size distribution, peaking at 0.5 nm, similar to the strut-size distribution (fig. S32). Roughly estimated, these pores occupied half the volume of the membrane, which is consistent with the density of 0.5 g cm^{-3} as estimated from the x-ray reflectivity (XRR) measurements (fig. S6E). Thus, ^{C1}RM belongs to the category of lightweight polymer materials (< 0.7 g cm^{-3}) (*27*).

Mechanical properties

To investigate the Young's modulus of nanoporous ^{C1}RM, we used nanoindentation that can provide the intrinsic moduli of materials (*11*). Notably, ^{C1}RM exhibited an exceptionally high Young's modulus of 11 GPa (Fig. 3, A and B), markedly higher than those reported for other lightweight two-dimensional (2D) and 3D porous polymers (*11*) (Fig. 3E and fig. S46). Ordinary phenol resins show Young's moduli of 4 GPa at a density of ~1.2 g cm^{-3} (*24*). Unlike ordinary phenol resins, ^{C1}RM contained biphenyl and phenyl ether groups that are partly responsible for the high Young's modulus of ^{C1}RM. Molecular dynamics simulations (fig. S45) (*11*) on a nonporous model of ^{C1}RM allowed us to estimate its density and Young's modulus of 1.4 g cm^{-3} and 19 GPa, respectively. According to the scaling relationship (*9*), the Young's modulus of 11 GPa observed for ^{C1}RM with a density of 0.5 g cm^{-3} is quite reasonable.

Ductility is one of the most important mechanical properties of membranes for practical applications (*28*). We noticed that ^{C1}RM lacked sufficient ductility because it easily fractured, even upon exposure to the air for drying. To tackle this problem, we polymerized resorcinol with glutaraldehyde (^{CHO}C5) and a series of α,ω-formyl polyethylene glycols (PEGs), such as ^{CHO}PEG1K, ^{CHO}PEG2K, and ^{CHO}PEG20K, with number-average molecular weights (M_n) of 1000, 2000, and 20,000, respectively (fig. S2) (*29*). When a voltage of +5 V was applied for 1 hour at 15°C, we obtained thin, delaminable membranes of ^{C5}RM, ^{PEG1K}RM, ^{PEG2K}RM, and ^{PEG20K}RM (figs. S7 to S10) that were sufficiently ductile. On the basis of the C–O bond population observed in narrow-scan XPS of C1s and ^{13}C CP-MAS NMR spectroscopy, the weight fractions of the aldehyde monomers in these membranes were evaluated as 2.4, 31, 30, and 25%, respectively (fig. S2). These membranes were also highly porous because their densities were between 0.4 g cm^{-3} and 0.6 g cm^{-3} (figs. S7 to S10) (*11*). Their Young's moduli ranged from 5 to 10 GPa (Fig. 3, A and B).

We conducted bulge tests for RMs to determine the ductility of these ultrathin (<100-nm) membranes (*30*–*32*). A sample membrane was attached to a flat jig with a 1-mm-diameter hole, and a nitrogen pressure was applied from the backside of the membrane to observe its deformation (Fig. 3C). Using the applied pressure (P), deformation (h), and membrane thickness (t), we obtained stress (σ)–strain (ε) curves of the membranes shown in fig. S19. Whereas ^{C1}RM was extremely fragile for testing, ^{C5}RM exhibited sufficient ductility, although with a low ultimate strain of 0.5%. ^{PEG20K}RM underwent substantial deformation until it ruptured at an applied nitrogen pressure of 2.75 kPa (Fig. 3C). Analysis of the stress-strain curve shown in fig. S19 revealed that ^{PEG20K}RM reached an ultimate strain of 3% (Fig. 3D), which is higher than any of the other thermoset polymers with Young's moduli >5 GPa reported thus far (*24*). Furthermore, as shown in Fig. 3D, the ultimate tensile strengths of four membranes ^{C5}RM to ^{PEG20K}RM, obtained from the bulge tests, ranged from 32 to 46 MPa, which are in the highest class among those reported for 2D and 3D lightweight polymers (Fig. 3E and fig. S47). Instead of α,ω-formyl PEGs, we used methoxy-terminated PEGs (^{MeO}PEGs) with M_n of 1000, 2000, and 20,000 as references for the membrane formation because they are ineligible for the addition-condensation reaction. As expected, the membrane ductility was not enhanced (fig. S37).

Membrane properties

Similarly to luffa sponge, RMs swelled in deionized water, resulting in a notable decrease in Young's moduli (Fig. 4A) (*33*). For example, ^{C1}RM, upon being swollen, showed a 35% increase in thickness, from 53 to 72 nm (Fig. 4A, fig. S38, and table S4). When alkaline water at pH 10 was added to swollen ^{C1}RM, its thickness further increased by 68% to 89 nm (Fig. 4A, fig. S38, and table S4). Such swelling behavior is likely due to the electrostatic repulsion of the deprotonated phenolic –OH groups (Fig. 4B). As observed by AFM, ^{C1}RM showed a substantial decrease in Young's modulus from 8.9 GPa in the dry state to 2.9 GPa in deionized water and further to 0.50 GPa in alkaline water at pH 10

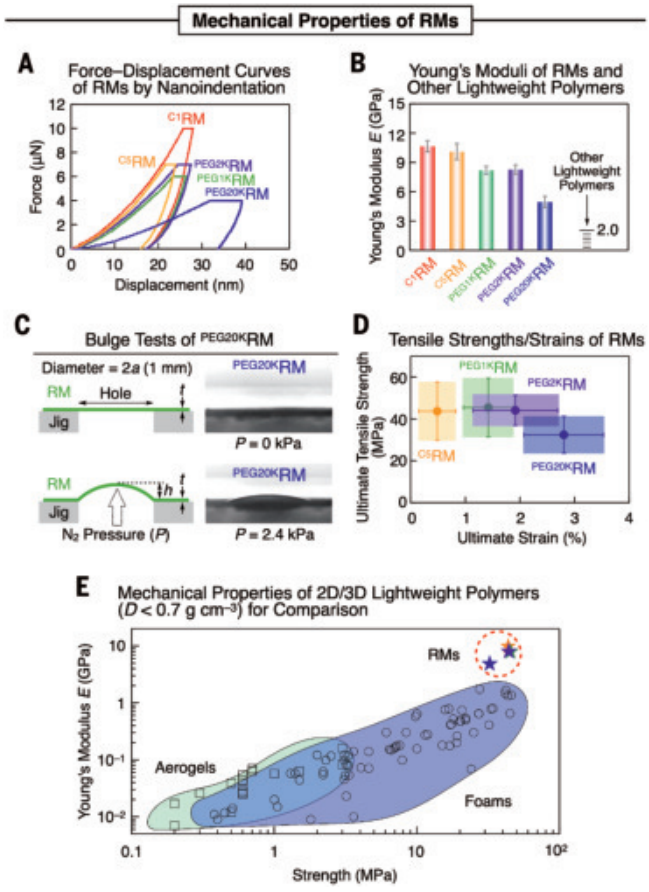

Fig. 3. Mechanical properties of RMs. (**A**) Force-displacement curves of the nanoindentation for ^{C1}RM, ^{C5}RM, ^{PEG1K}RM, ^{PEG2K}RM, and ^{PEG20K}RM. (**B**) Young's moduli (E) of RMs obtained by nanoindentation. (**C**) Bulge-test setup and photographs of the deformation of ^{PEG20K}RM during a test under an applied pressure of 2.4 kPa. (**D**) Plots of the ultimate tensile strengths and ultimate strains of RMs obtained from the bulge test. (**E**) Ashby plots of Young's moduli versus tensile strengths of RMs (stars), together with those of lightweight 2D and 3D reticular polymers (density D < 0.7 g cm^{-3}) processed as foams (circles) and aerogels (squares) (*11*).

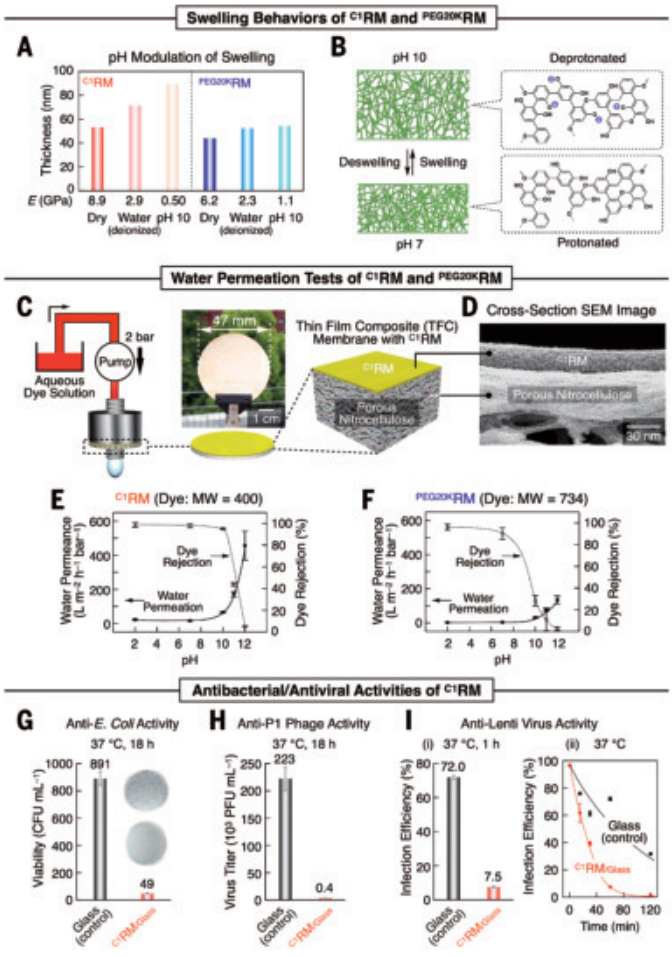

Fig. 4. Swelling, water permeation and antibacterial/viral activities of RMs. (**A**) Changes in thickness and Young's modulus (E) of RMs upon immersion in deionized and alkaline (pH 10) waters. (**B**) RMs swell by electrostatic repulsion of the deprotonated phenolic –OH groups. (**C**) Illustration of the dead-end filtration setup with a photograph of 47-mm-diameter ^{C1}RM. (**D**) Cross-section SEM image of a thin-film composite (TFC) membrane of ^{C1}RM with nitrocellulose. The sample was sputterd with platinum. (**E** and **F**) pH-dependent water permeation and dye rejection properties of ^{C1}RM (acid red 88, molecular weight = 400.38, 10 ppm) (E) and ^{PEG20K}RM (acid violet 49, molecular weight = 733.87, 10 ppm) (F). Dyes were chosen based on their molecular weight–dependent rejection profiles (tables S6 and S7). (**G**) Antibacterial activity of ^{C1}RM against *E. coli* after 18-hour incubation. (**H**) Antibacterial virus activity of ^{C1}RM against P1 phage bacterial virus after 18-hour incubation. (**I**) Antihuman virus activity of ^{C1}RM against lentivirus after 1-hour incubation (i) and its virus infection efficiency at different incubation times (ii).

(Fig. 4A and table S4). Conversely, ^{PEG20K}RM was less swellable than ^{C1}RM (Fig. 4A, fig. S39, and table S5), likely owing to dehydrative aggregation of its PEG chains by electrolyte-induced salting out (*34*, *35*).

The pH-dependent swelling behavior of ^{C1}RM considerably impacted its water permeability (Fig. 4C) (*36*). A thin-film composite (TFC) with a diameter of 13 mm [surface area (S) = 1.3 cm^2; Fig. 4, C and D], prepared by transferring ^{C1}RM onto a nitrocellulose membrane, showed a water permeance of 26.9 ± 1.4 liter m^{-2} hour^{-1} bar^{-1} under a pressure of 2 bar. Notably, when the pH value for testing ^{C1}RM-TFC was >10, its water permeance and anionic dye (acid red 88, molecular weight = 400, 10 ppm) rejection rate increased and decreased nonlinearly with pH, respectively (Fig. 4E). By contrast, the permeation behaviors of ^{PEG20K}RM (Fig. 4F) were less dependent on the applied pH change. These results are consistent with the pH-dependent swelling behaviors of these membranes (Fig. 4A). Lastly, we tested the specially prepared TFC with a larger diameter of 47 mm (S = 17.3 cm^2; Fig. 4C) and confirmed that it showed a similar water permeance of 23.7 ± 3.5 liter m^{-2} hour^{-1} bar^{-1} to that observed for the commonly used TFC with a diameter of 13 mm, indicating that ^{C1}RM is applicable to large-scale permeation devices without failure or leakage.

These reticular membranes bear a polyphenolic structure (Fig. 2C). Phenol and its derivatives, such as catechin and lignin, are known for their antibacterial and antiviral activities (*4*, *37*, *38*). We investigated whether our synthetic membranes with a polyphenolic structure possess such an antibacterial effect by using *Escherichia coli*, a Gram-negative bacterium. As shown in Fig. 4G, the viability of *E. coli* exposed to ^{C1}RM on a glass plate at 37°C for 18 hours was only 5% compared with a reference experiment performed on a glass plate without ^{C1}RM (fig. S43 and table S8). When P1 bacteriophage was exposed to ^{C1}RM on a glass plate at 37°C for 18 hours, its viral activity was reduced to only 0.2% compared with a reference experiment on a glass plate without ^{C1}RM (Fig. 4H, fig. S44, and table S9).

Lentivirus is known to feature a spike protein protruding from its glycoprotein membrane similar to that of severe acute respiratory syndrome coronavirus 2 (SARS-CoV-2). We investigated the antiviral activity of ^{C1}RM against lentivirus by using flow cytometry to monitor the fluorescence from a green fluorescent protein expressed in the infected cells (HeLa). As shown in Fig. 4I, lentivirus on ^{C1}RM exhibited a rapid reduction in its infection efficiency by 60 and 92% within 0.5 hours and 1 hour, respectively.

Conversion to carbon membranes

Thin carbon membranes are desirable for many applications; in particular, they play an important role in advanced electronics such as wearable devices, biosensors, and supercapacitors that take advantage of their potentially high flexibility, low-energy permeability, and high electronic conductivity (*39*). We used our membranes as precursors for nanoporous, ultrathin carbon membranes. By heating on a silicon wafer substrate under vacuum at 1020°C, we found that 60-nm-thick ^{C1}RM was successfully carbonized (fig. S28) into the low-density, nanoporous carbon membrane ^{C1}RM$_{CNZ}$, without any lateral dimensional change (Fig. 5A) (*11*). In this carbonization process, the precursor membrane faded in color as a possible consequence of its thickness decrease from 60 to 22 nm, as determined by AFM (Fig. 5, G and H). ^{C1}RM$_{CNZ}$ thus obtained exhibited a surface resistivity of 3.0 ± 0.2 kΩ/sq, which is comparable to that of ordinary carbon membranes (*39*), and did not possess any obvious structural defect, while maintaining a smooth surface just as ^{C1}RM did (Fig. 5, C, D, and G, and fig. S31).

The density of ^{C1}RM$_{CNZ}$ was determined by XRR as 0.6 g cm^{-3} (fig. S14), which is the lowest among those reported for porous carbon membranes thinner than 100 nm (*40*–*42*). Electron tomography (Fig. 5, E and F, and movie S3) unveiled that ^{C1}RM$_{CNZ}$ was highly porous, with a pore diameter <0.5 nm (fig. S33). We evaluated the intrinsic mechanical strength of ^{C1}RM$_{CNZ}$ by nanoindentation and found that its Young's modulus was 13 GPa (Fig. 5I and fig. S14). By means of cyclic voltammetry (*43*), ^{C1}RM$_{CNZ}$ in 1.0 M H_2SO_4 aq was shown to have a gravimetric double-layer capacitance of 42 F g^{-1} (Fig. 5B and fig. S41), which is comparable to those reported for conventional activated carbons with larger dimensions (*43*). Thus, ^{C1}RM$_{CNZ}$ likely contains a large number of electrolyte-accessible pores and could be used in an ultrathin capacitor device (*44*, *45*).

Discussion

Lignin-based reticular structures are abundant in nature and attractive as lightweight materials for resource conservation. However, lignin is difficult to process as well as purify because it is heavily cross-linked and subject to oxidation, making its practical application difficult (*4*). By contrast, our method of using a negatively charged EDL as a special medium for reacting resorcinol with an aldehyde can spontaneously

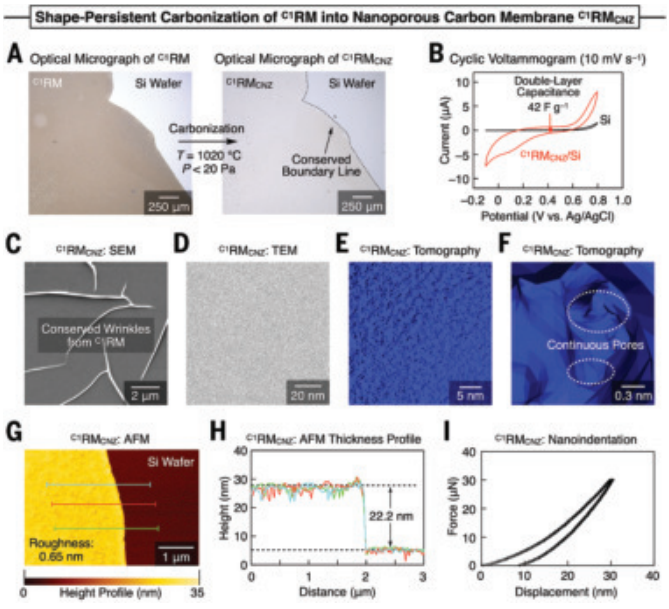

Fig. 5. Shape-persistent carbonization of ^{C1}RM into nanoporous carbon membrane ^{C1}RM$_{CNZ}$. (**A**) Carbonization of ^{C1}RM on a silicon wafer substrate. The initial shape of the membrane remains unchanged upon carbonization at 1020°C at <20 Pa. (**B**) Cyclic voltammogram of a ^{C1}RM$_{CNZ}$ on a silicon wafer electrode at a scan rate of 10 mV s^{-1} in 1.0 M H_2SO_4 aq, and that of a silicon wafer electrode alone. (**C** and **D**) SEM (C) and TEM (D) micrographs of ^{C1}RM$_{CNZ}$. (**E** and **F**) Electron tomographic images of the surface (E) and pore interior (F) of ^{C1}RM$_{CNZ}$. (**G** and **H**) AFM image of ^{C1}RM$_{CNZ}$ (G) and its thickness profile (H). (**I**) Force-displacement curve of ^{C1}RM$_{CNZ}$ upon nanoindentation.

process an ultrathin reticular membrane with a lignin-like cross-linked structure. This process avoids densification, terminates at the thin layer, and affords spontaneous release from the electrode substrate. This luffa spongelike, lightweight, ultrathin membrane has a wide range of applications, as partly described in this paper. The idea of using EDLs constructed by electrostatic accumulation of ionic species in deionized water as a reaction media brought traditional electropolymerization back into the spotlight as a methodology for manufacturing sustainable polymers. The potential-induced delamination suggests a possible extension of our EDL-mediated polymerization to a roll-to-roll continuous process using a cylindrical electrode for both organic and carbon membranes.

REFERENCES AND NOTES

1. M. MacLeod, H. P. H. Arp, M. B. Tekman, A. Jahnke, *Science* **373**, 61–65 (2021).
2. C. P. Ward, C. M. Reddy, B. Edwards, S. T. Perri, *Nature* **625**, 658–662 (2024).
3. T. A. Schaedler, W. B. Carter, *Annu. Rev. Mater. Res.* **46**, 187–210 (2016).
4. X. J. Loh, D. Kai, Z. Li, Eds., *Functional Materials from Lignin: Methods and Advances*, vol. 3 of *Sustainable Chemistry Series*, N. Gathergood, Ed. (World Scientific Publishing Europe, 2018).
5. C. A. Adeyanju, S. Ogunniyi, J. O. Ighalo, A. G. Adeniyi, S. A. Abdulkareem, *J. Mater. Sci.* **56**, 2797–2813 (2021).
6. V. G. Parale *et al.*, *Adv. Mater.* **36**, 2307772 (2023).
7. C. Okolieocha, D. Raps, K. Subramaniam, V. Altstädt, *Eur. Polym. J.* **73**, 500–519 (2015).
8. D. Wu *et al.*, *Chem. Rev.* **112**, 3959–4015 (2012).
9. Z.-L. Yu *et al.*, *Sci. Adv.* **4**, eaat7223 (2018).
10. X. Zheng *et al.*, *Science* **344**, 1373–1377 (2014).
11. Materials and methods are available as supplementary materials.
12. P. Brüesch, T. Christen, *J. Appl. Phys.* **95**, 2846–2856 (2004).
13. R. Morrow, D. R. McKenzie, *Proc. R. Soc. London Ser. A* **468**, 18–34 (2012).
14. H.-J. Butt, K. Graf, M. Kappl, *Physics and Chemistry of Interfaces* (John Wiley & Sons, 2023).
15. S. Chen *et al.*, *Science* **348**, 555–559 (2015).
16. S. Cosnier, A. Karyakin, Eds. *Electropolymerization: Concepts, Materials and Applications* (Wiley-VCH, 2010).
17. R. J. Waltman, J. Bargon, *Can. J. Chem.* **64**, 76–95 (1986).
18. A. Palma-Cando, U. Scherf, *Macromol. Chem. Phys.* **217**, 827–841 (2016).
19. Q. Zhang, H. Dong, W. Hu, *J. Mater. Chem.* **6**, 10672–10686 (2018).
20. G. Mengoli, M. M. Musiani, *J. Electrochem. Soc.* **134**, 643C–652C (1987).
21. L. Pilato, Ed. *Phenolic Resins: A Century of Progress* (Springer Berlin Heidelberg, 2010).
22. A. Awadallah-F, S. Al-Muhtaseb, *Int. J. Energy Res.* **44**, 12259–12268 (2020).
23. E. Steckhan, Ed., *Electrochemistry I* (Springer, 1987).
24. M. F. Ashby, H. Shercliff, D. Cebon, *Materials: Engineering, Science, Processing and Design* (Butterworth-Heinemann, 2018).
25. M. Ferreira, H. Varela, R. M. Torresi, G. Tremiliosi-Filho, *Electrochim. Acta* **52**, 434–442 (2006).
26. M. Balakshin, E. Capanema, *J. Wood Chem. Technol.* **35**, 220–237 (2015).
27. J. C. Salamone, *Polymeric Materials Encyclopedia* (CRC Press LLC, 1996).
28. I. Ichinose, in *Nanomaterials for the Life Sciences*, C. S. S. R. Kumar, Ed. (Wiley-VCH, 2010), 277–302.
29. K. Tang *et al.*, *ACS Appl. Polym. Mater.* **4**, 8303–8314 (2022).
30. R. Vendamme, S.-Y. Onoue, A. Nakao, T. Kunitake, *Nat. Mater.* **5**, 494–501 (2006).
31. K. Kojio *et al.*, *Soft Matter* **14**, 1659–1664 (2018).
32. M. Ariyoshi, S. Fujikawa, T. Kunitake, *ACS Appl. Mater. Interfaces* **13**, 61189–61195 (2021).
33. M. A. C. Stuart *et al.*, *Nat. Mater.* **9**, 101–113 (2010).
34. S. Kraus, L. B. Rogers, *J. Chromatogr. A* **257**, 237–245 (1983).
35. R. Sadeghi, F. Jahani, *J. Phys. Chem. B* **116**, 5234–5241 (2012).
36. Z. Liu, W. Wang, R. Xie, X. J. Ju, L. Y. Chu, *Chem. Soc. Rev.* **45**, 460–475 (2016).
37. T. P. T. Cushnie, A. J. Lamb, *Int. J. Antimicrob. Agents* **38**, 99–107 (2011).
38. A. Boarino *et al.*, *ACS Sustain. Chem.& Eng.* **10**, 14001–14010 (2022).
39. I.-S. Kim *et al.*, *Adv. Mater.* **35**, e2204912 (2023).
40. A. Vasin *et al.*, *J. Phys. D Appl. Phys.* **56**, 275302 (2023).
41. A. C. Ferrari *et al.*, *Phys. Rev. B Condens. Matter* **62**, 11089–11103 (2000).
42. O. M. Slobodian *et al.*, *Appl. Surf. Sci.* **496**, 143735 (2019).
43. H. Nishihara *et al.*, *Chem. Mater.* **23**, 3144–3151 (2011).
44. F. Bu *et al.*, *NPJ Flex. Electron.* **4**, 31 (2020).
45. M. Yu, X. Feng, *Joule* **3**, 338–360 (2019).

ACKNOWLEDGMENTS

We thank M. Shibayama and K. Akutsu from the Comprehensive Research Organization for Science and Society (CROSS) and K. Mayumi from the University of Tokyo for valuable discussions about the internal structures of the membrane. We also thank T.-A. Yamagishi from Kanazawa University, T. Ogoshi from Kyoto University, and M. Kasuya from Komatsu University for their valuable discussions. The authors are grateful to T. Suzuki, K. Yonesato, and K. Yamaguchi from the University of Tokyo for Raman spectroscopy and to K. Takahashi and K. Nozaki from the University of Tokyo for NMR measurement. This work used the computational resources of the supercomputer Fugaku provided by the RIKEN Center for Computational Science through the HPCI System Research Project (project ID: hp230309). A part of this work was supported by the Advanced Research Infrastructure for Materials and Nanotechnology in Japan of the Ministry of Education, Culture, Sports, Science and Technology (MEXT), grant no. JPMXP1223UT1099; and the measurements were conducted in the Takeda Cleanroom with the help of the Nanofabrication Platform Center of the School of Engineering of the University of Tokyo. T.A. thanks the Kao Corporation for their generous support. **Funding:** This work was financially supported by Japan Science and Technology Agency (JST) PRESTO grant JPMJPR21Q1 on "Materials synthesis under electrically perturbated non-equilibrium reaction field" and by a Japan Society for the Promotion of Science (JSPS) Grant-in-Aid for Scientific Research (B) (21H01903) on "Unusual mass transport through nanochannels enabled by inner wall chemical modification" awarded to Y.I. T.A. is grateful for a JSPS Grant-in-Aid for Specially Promoted Research (23H05408) on "Solid-state materials science of supramolecular polymers and their applications." H.J. is grateful for JST CREST grant JPMJCR1993 on "Elucidation of adhesion/fracture mechanism of soft/hard interface by atomic resolution electron microscopy" and grant JPMJCR24S3 on "Development of interface toughening technology for polyolefin recycling society." T.S. is supported by JST-ERATO (JPMJER2002). **Author contributions:** T.A. and Y.I. designed the experiments. Y.I., T.F., P.-L.C., Y.Y., K.N., and J.F. performed the experiments. Y.I., T.F., P.-L.C., Y.Y., and K.N. analyzed the data. T.A. and Y.I. wrote the manuscript. Y.-L.H. and Y.N. performed solid-state NMR measurements. H.-F.W., A.K., and H.J. performed TEM and electron tomography. H.W. helped with bulge testing. T.S.-S. performed AFM measurements. A.N. and T.S. investigated antibacterial/viral properties. Y.S. helped carbonization experiments. K.W. and T.Y. performed capacitance and conductivity measurements of the carbonized membrane. A.T. and K.H. performed MD simulations. **Competing interests:** Y.I., T.F., P.-L.C., A.N., T.S., and T.A. are inventors on a patent related to this work ["Ultra-thin film of thermosetting resin," patent no. 7473993 (JP), application no. 17/999838 (US); date of application: 27 May 2021, priority date: 27 May 2020; publication no. WO2021/241680]. Y.I., Y.Y., K.N., and T.A. are inventors on a patent related to this work ["Resin manufacturing methods, resins, thin films, and composite thin films," application no. 2024-075608 (JP); date of application: 8 May 2024]. The authors declare no other competing interests. **Data and materials availability:** All data are available in the manuscript or in the supplementary materials.

SUPPLEMENTARY MATERIALS

science.org/doi/10.1126/science.adq0782
Materials and Methods; Figs. S1 to S47; Tables S1 to S9; References (*46*–*86*); Supplementary Movies S1 to S3

Submitted 25 April 2024; resubmitted 14 March 2025; accepted 6 May 2025

10.1126/science.adq0782

PALEOANTHROPOLOGY

300,000-year-old wooden tools from Gantangqing, southwest China

Jian-Hui Liu[1], Qi-Jun Ruan[1], Jun-Yi Ge[2,3], Yong-Jiang Huang[4], Xiao-Ling Zhang[2], Jia Liu[5], Shu-Feng Li[6], Hui Shen[2], Yuan Wang[2], Thomas A. Stidham[2], Cheng-Long Deng[7], Sheng-Hua Li[8], Fei Han[9], Ying-Shuai Jin[2], Kieran O'Gorman[10], Bo Li[10,11,12]*, Robin Dennell[13], Xing Gao[2,3]*

Evidence of Early and Middle Pleistocene wooden implements is exceptionally rare, and existing evidence has been found only in Africa and western Eurasia. We report an assemblage of 35 wooden implements from the site of Gantangqing in southwestern China, which was found associated with stone tools, antler billets (soft hammers), and cut-marked bones and is dated from ~361,000 to ~250,000 years at a 95% confidence interval. The wooden implements include digging sticks and small, complete, hand-held pointed tools. The sophistication of many of these tools offsets the seemingly "primitive" aspects of stone tool assemblages in the East Asian Early Paleolithic. This discovery suggests that wooden implements might have played an important role in hominin survival and adaptation in Middle Pleistocene East Asia.

Introduction

Evidence of woodworking can be traced back as early as 1.5 million years ago (*1*) but confirmed Early and Middle Pleistocene wooden tools have been found only sporadically in Africa and western Eurasia. Evidence of early use of wooden tools for foraging and hunting includes spears and throwing sticks from Schöningen, Germany, dated from ~300 to 330 thousand years (kyr) ago (*2*–*4*), and Clacton, UK (~400 kyr) (*5*). Structural use of wood was evidenced from two interlocking logs uncovered from waterlogged deposits at Kalambo Falls, Zambia (approximately >476 ±23 kyr) (*6*). Other evidence of early use of wooden tools include a wooden plank from Gesher Benot Ya'aqov, Israel (approximately >780 kyr) (*7*, *8*) and digging sticks from Poggetti Vecchi, Italy (~171 kyr) (*9*). Although the Bamboo Hypothesis—which posits that the abundance of bamboo in East and Southeast Asia allowed early humans to use it as effective tools—has prevailed for a long time (*10*, *11*), direct evidence for Paleolithic organic-based tools is almost totally absent in this region. The wood pieces uncovered from the site of Gantangqing in southwestern China provide insight into early use of wooden tools in Middle Pleistocene East Asia.

The Gantangqing site (24°18′26.76″N, 102°50′48.20″E, ~1836 meters above sea level) is situated on the southern margin of the Lake Fuxian (Fig. 1), which is a fault-depression basin formed by the uplift of the central Yunnan plateau (*12*–*14*). The site was discovered in 1984 and first excavated in 1989, when numerous lithic materials and faunal remains were found (*15*, *16*). Four trenches (T1 to T4) (Fig. 1C) were newly excavated in 2014 and 2015 (T1 and T2) and in 2018 and 2019 (T3 and T4), respectively, which exposed an area of 64 m^2 with depths from 3.5 to 7 meters (Fig. 2A and figs. S1 and S4). Stone artifacts, wooden implements, and faunal and floral remains were recovered from all trenches (figs. S2 and S3). All materials discussed in this paper came from T1 to T4.

Site setting and stratigraphy

The sedimentary sequence at the site is the result of lake-shore lacustrine/fluvial deposition associated with the ancient Fuxian Lake (*14*). The wooden implement–bearing layers are characterized by grayish-brown and clayey sediments that are rich in organic matter (figs. S1 and S4). Such a reducing or anoxic environment facilitated the preservation of wooden pieces at the site. The sedimentary sequence underneath modern plough soil can be divided into three major units (I, II, and III) that are unconformably bedded from top to bottom (Fig. 2A). Unit I comprises red soils at the top and grayish-yellow clay interbedded with yellowish sand at the bottom. Grain size analysis suggests a lacustrine-fluvial origin of the sediments from Unit I (fig. S5). Unit II consists primarily of blueish-gray lacustrine deposits. Unit III, at the base of the section, is Cambrian sandy shale. Artifacts were uncovered from Unit I only. New excavations revealed the middle and lower parts of Unit I and the upper part of Unit II in all trenches (Fig. 2A). The sedimentary features and stratigraphic sequence are generally similar across trenches (table S1 and fig. S4). Given lateral variations and discontinuities in the layers, different numbers of layers were identified in different trenches (table S1); T1 and T2 have a complete sequence of 20 layers (layers 1 to 20), while T3 and T4 have 16 and 11 layers, respectively.

The wooden implements (Figs. 3 and 4 and figs. S14 to S17), together with numerous stone artifacts and faunal and floral remains, were recovered from layers 10 to 18 of Unit I (Fig. 2B). Organic preservation was exceptional in layers 14 to 17; most fossils and artifacts are fresh, with very little or no indications of weathering. Wooden artifacts were usually intact when found (fig. S1, E to H). No obvious orientation was observed and all materials appear to have been buried rapidly but under gentle conditions of deposition. The vertically banded distribution of stone artifacts, wooden pieces, and fossils indicates an overall stratigraphic integrity of the deposit (fig. S2).

Chronological framework

We established a robust chronologic framework for the site based on the faunal assemblage, palaeomagnetism, optical dating, and electron spin resonance (ESR) dating (*14*). Palaeomagnetic analysis and faunal evidence indicated that Unit I is the Brunhes Normal Chron. The layers of Unit I were dated using coupled U-series and ESR dating of dental fragments from a fossil tooth recovered from layer 13 in T4, as well as single-grain optical dating of potassium-rich feldspar (K-feldspar) from 23 sediment samples from different layers of T1, T3, and T4 (fig. S4). The optical and ESR/U-series dating results range from ~200 to ~400 kyr [at a 95% confidential interval (CI)], which are broadly consistent with each other and stratigraphically coherent (Figs. 2, B and C). The age estimates were combined with stratigraphic information to develop a Bayesian age model for layers 7 to

[1]Yunnan Institute of Cultural Relics and Archaeology, Kunming, China. [2]Institute of Vertebrate Paleontology and Paleoanthropology under Chinese Academy of Sciences and Key Research Base on Paleolithic Human Evolution and Paleogenetics (IVPP) under the State Administration of Cultural Heritage of China, Beijing, China. [3]University of Chinese Academy of Sciences, Beijing, China. [4]Key Laboratory for Plant Diversity and Biogeography of East Asia, Kunming Institute of Botany, Chinese Academy of Sciences, Kunming, China. [5]MNR Key Laboratory of Deep-time Geography and Environment Reconstruction and Applications, Institute of Sedimentary Geology, Chengdu University of Technology, Chengdu, China. [6]CAS Key Laboratory of Tropical Forest Ecology, Xishuangbanna Tropical Botanical Garden, Chinese Academy of Sciences, Mengla, Yunnan, China. [7]State Key Laboratory of Lithospheric Evolution, Institute of Geology and Geophysics, Chinese Academy of Sciences, Beijing, China. [8]Department of Earth Sciences, University of Hong Kong, Pokfulam Road, Hong Kong, China. [9]Yunnan Key Laboratory of Earth System Science, Yunnan University, Kunming, Yunnan, China. [10]School of Science, University of Wollongong, Wollongong, New South Wales, Australia. [11]Environmental Futures Research Centre, School of Science, University of Wollongong, Wollongong, New South Wales, Australia. [12]Australian Research Council (ARC) Centre of Excellence for Australian Biodiversity and Heritage, University of Wollongong, Wollongong, New South Wales, Australia. [13]Department of Archaeology, University of Exeter, Exeter, UK. ***Corresponding author. Email: gaoxing@ivpp.ac.cn (X.G.); bli@uow.edu.au (B.L.)**

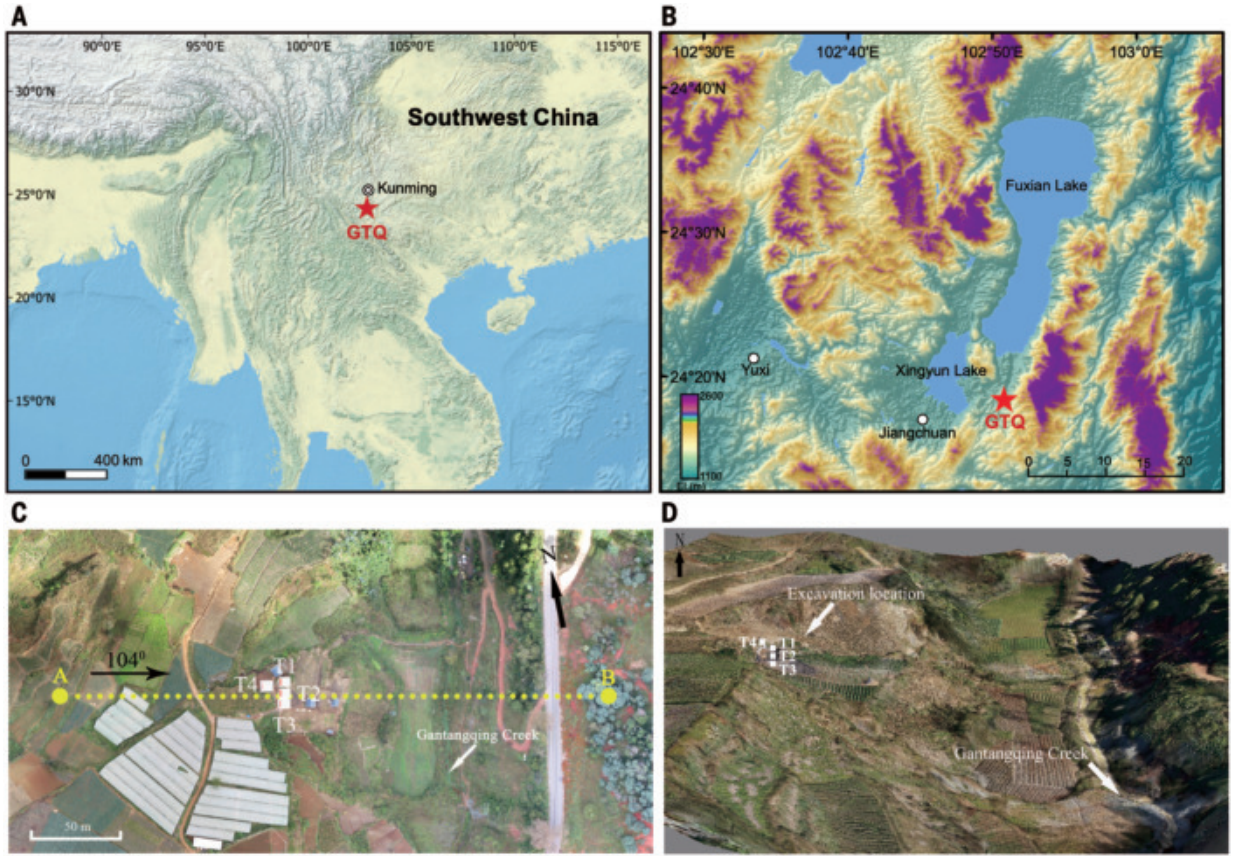

Fig. 1. Location of the Gantangqing (GTQ) site in Yunnan province, China. (**A**) Regional map of southeast Asia showing the location of the site and the provincial capital city Kunming. (**B**) Digital elevation map indicating the Gantangqing site, Fuxian Lake, the cities of Yuxi and Jiangchuan, and the surrounding area. (**C**) Aerial photograph showing the area surrounding the site and the location of excavation trenches (T1 to T4). Lines A and B in this panel refers to the depositional section shown in the Fig. 2A. (**D**) Three-dimensional (3D) model showing the landscape of the site and the locations of T1 to T4.

20 (Fig. 2C and table S12). The age model suggests that Unit I started to accumulate from 374 to 299 kyr ago (here and below, we give modeled age estimates and total uncertainties at 95.4% CI), corresponding to the earliest evidence of hominin occupation at the site (layer 19). The layers containing stone artifacts and wooden implements were dated from 361 to 298 kyr (layer 18) to 286 to 250 kyr (layer 10). The topmost layer dated (layer 7) has a modeled age of 270 to 220 kyr.

Wooden artifacts

The Gantangqing site has preserved a wealth of organic materials. There were nearly 1000 wood remains unearthed from T1 to T4, in addition to numerous lithic artifacts (Fig. 5A), mammalian fossils, and four antler billets (soft hammers) [Fig. 5A (f) and fig. S30]. A few bones exhibit anthropogenic cut marks [Fig. 5A (g and h)]. Charcoal debris was also frequently recovered from the strata, which could indicate the use of wooden materials as fuel on the site. However, these may also be the product of wildfires, given the lack of evidence of hearth or burnt layers. None of the wooden artifacts was charred or fire-shaped, as at Poggetti Vecchi (*9*, *17*).

Although most of the wooden pieces uncovered are fragmented and formless (fig. S12), we successfully identified 35 wood products showing obvious traces of intentional shaping and use (Figs. 3 and 4 and figs. S14 to S17). Most were made from pine (a soft wood for working) but a few were made from harder wood (table S13). Details of each wooden artifact are given in the Supplementary Materials (*14*). Based on morphology and use-wear patterns, we divide these implements into four categories (grades I to IV) according to the presence and absence of five attributes: (i) intentional selection of wood with suitable edges/handles; (ii) shaping marks; (iii) smoothing on surface; (iv) evidence of utilization (i.e., signs of use-wear or residues); and (v) polish or striations (table S14) (*14*). All the implements bear three or more of these attributes, including 12 pieces bearing all five attributes (grade IV), 15 with four attributes (grade III), and 8 with three attributes (grade II). All the Gantangqing implements have tips, edges, or handles suitable for tool-using purposes (attribute 1).

Most of the Gantangqing implements ($n = 32$) were shaped on their tips, edges, or bottom, and only one piece (T1-259) retains some bark (fig. S15E). They are either rounded (T2-1677, fig. S15A), or chisel-like with a thin, flat blade (T1-1901, Fig. 4); or shaped with a ridge toward the point (T2-1672, fig. S15B). Most items are complete in having both ends preserved, unlike the fragmented examples from sites such as Clacton (*18*) (UK), Florisbad (*19*) (South Africa), Kalambo Falls (Zambia) (*20*), Ohalo (Israel) (*21*), Abric Romani (*22*), and Aranbaltzar (Spain) (*23*). Two are large digging sticks (T1-1901 and T3-73) that would probably require both hands when used (Fig. 4 and fig. S27) and are similar to ones found at the ~171-kyr-old site of Poggetti Vecchi, Italy (*9*). Other large items (e.g., T3-486, T1-1902, T2-1679; fig. S15, I, J, and L, respectively), are probably types of digging implements not seen on other sites. The other implements are smaller and likely to have been used in one hand (e.g., T2-1670, T2-1667, T2-1677; figs. S15F, S16B, and S15A, respectively). Four pieces form a distinct subgroup: these are hook-like and appear to have been shaped from the base of a trunk and the top of a root; the root part was then shaped to a sharp,

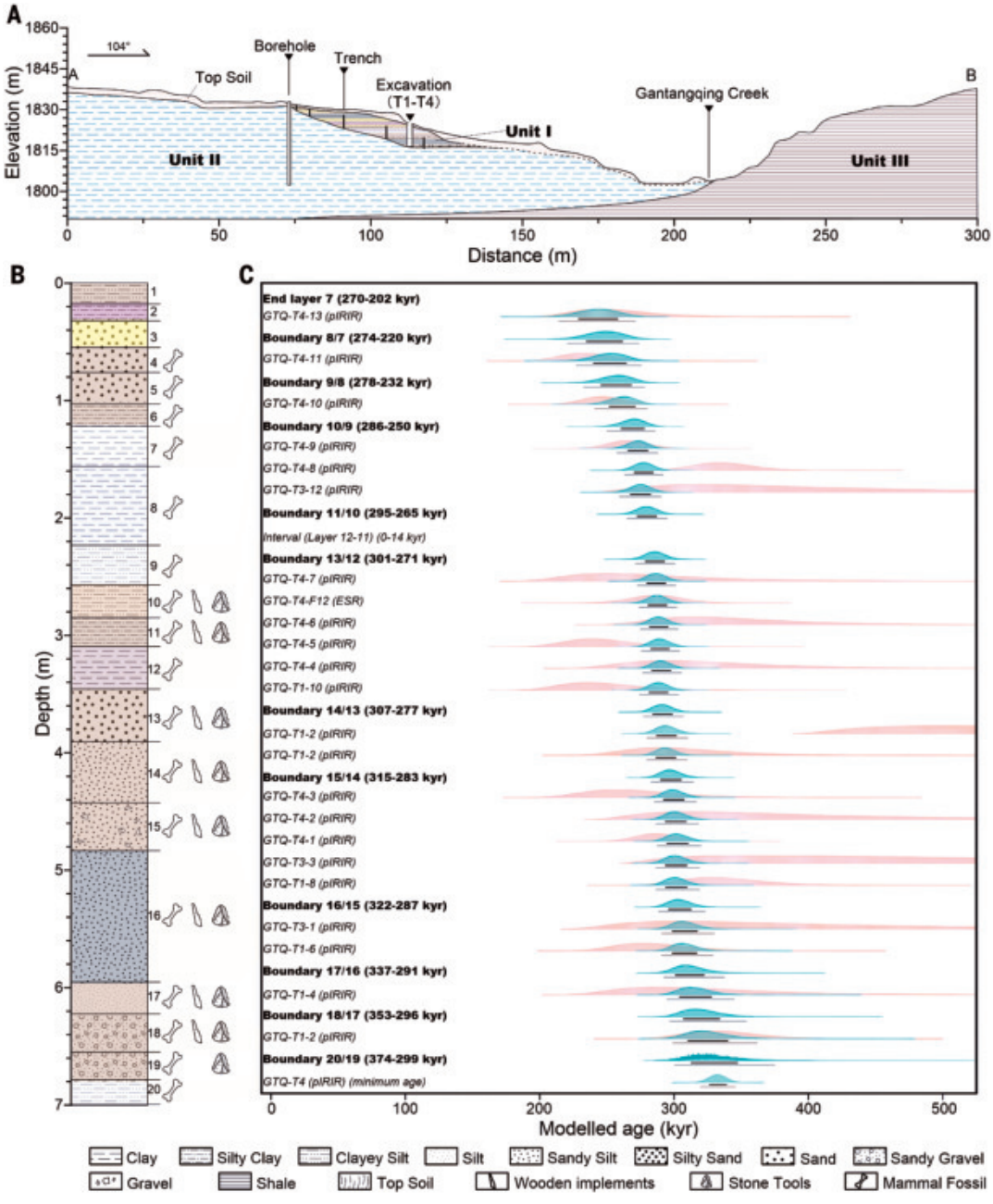

Fig. 2. Stratigraphy and chronology of the Gantangqing site. (**A**) Schematic model of the stratigraphic cross-section between points A and B in Fig. 1C. (**B**) Stratigraphic layers, depth, and archaeological contents. (**C**) Bayesian age modeling of optical and ESR dates. Orange probability distributions represent the unmodeled ages (likelihoods) and green distributions represent the modeled ages (posterior probabilities). The narrow and wide bars beneath each distribution represent the 68.2 and 95.4% probability ranges of the modeled ages, respectively. Modeled ages for each layer boundary and duration for interval are given in parentheses (95.4% probability).

round edge that shows wear through use and could have been used for slicing through roots (T2-1674, T2-1666, T1-1898, and T2-1671; fig. S17, A to D). Two pieces (T2-555 and T4-193; figs. S16G and S26, respectively), are difficult to interpret. They were finely carved into symmetrical lozenge shapes and both tips appear worn, but with a length of only a few centimeters (5.1 and 7.8 cm, respectively) they are too small to use effectively for digging. These pieces might have been used as awls or for separating root tangles, but their precise function remains unknown.

More than half ($n = 19$) of the implements have visible whittling marks/wear associated with tool shaping or use-wear (figs. S22 and S23). Although the preservation of marks/wear varies greatly, we identified intentional shaping through the presence of consistent, overlapping whittling marks or wear. About half of the specimens ($n = 17$) exhibited evidence of intentional smoothing on the surface of the knots of removed branches or twigs (fig. S21). The surfaces are nearly flat, with localized striations and polish distributed in or outside the knot. Of the specimens, sixteen do not exhibit remains of branches, such as T1-1897, which is made on a split segment (fig. S20). An intensive utilization of the tools was indicated by a series of evidence, such as broken tips with soil residues (fig. S23C), rounded breakage, or fractures (fig. S24), flat surfaces (fig. S22), and polish and striations on the edges (fig. S25). These tool-making marks and use-wear patterns

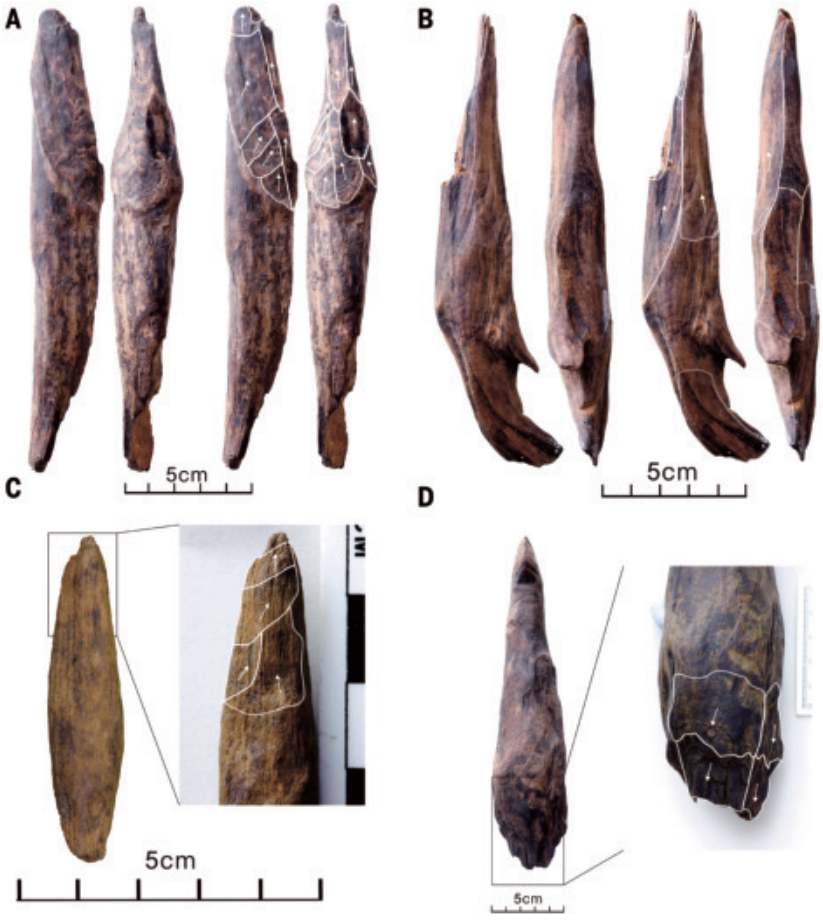

Fig. 3. Schematic diagram of shaping of wooden tools. (**A**) T2-1670. (**B**) T1-1898. (**C**) T4-193. (**D**) T2-1674. Arrow indicates whittling direction; locations outlined by dotted lines represent whittling scars without clear boundaries due to abrasion caused by utilization or poor preservation.

suggest that intentional shaping and smoothing processes are very common. Therefore, we conclude that these Gantangqing wooden pieces should be classified as artifacts made by hominins. This conclusion is further supported by replicative experiments (*14*), which have demonstrated that the key attributes observed on the Gantangqing wooden tools—including shaping wear (whittling facets and striations), rounding, breakage, fractures, and residues—can be successfully replicated (figs. S28 and S29).

Compared with the wooden artifacts found at other sites such as Schöningen (*4*, *24* to *26*), Lehringen (*27*), Cannstat (*28*), Bilzingsleben (*29*), Clacton (*5*), Poggetti Vecchi (*9*), and Border Cave (*30*), Gantangqing has a wider range of implements (particularly of small tools), implying considerable foresight by hominins in the selection of suitable wood for tool-making and the intentional manufacture of tips, edges, or handles suitable for tool-using purposes. The "household tools" from Schöningen are the only medium-sized wooden tools contemporary with Gantangqing wooden implements. The main differences between the Schöningen and Gantangqing wooden artifacts lie in their type: The Schöningen assemblage is dominated by hunting equipment whereas Gantangqing is dominated by digging equipment.

Stone artifacts and billets (soft hammers)

Stone artifacts were uncovered from the same layers as the wooden tools (fig. S2) and comprise cores, flakes, and a small number of retouched flake tools. The stone tools are mostly small scrapers and retouch is extremely fine, with up to five detachments along an edge <10 mm long (Fig. 5A) (*14*). Lithic artifacts were mostly fabricated on small chert pebbles. The source materials cannot be found within 5 km of the site, implying that they were brought to the site, either ready-made or as cores

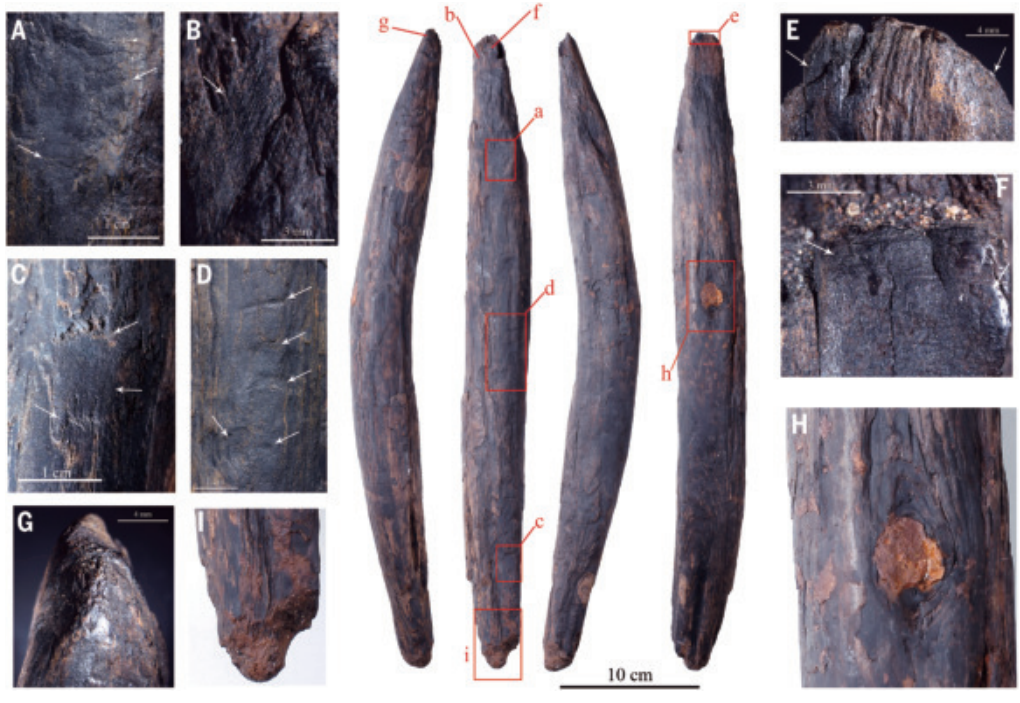

Fig. 4. Modified wooden tool T1-1901 and shaping, use-wear marks on the object. (**A**) The shaping facet with marks (perhaps chatter marks). (**B**) Striation clusters. (**C**) Shaping facet (right middle arrow) and stop mark (right up arrow and left arrow). (**D**) Abraded surface with planning and drawing marks, forming surface facets and stop marks (right arrow), a wide shallow notch damaged the abraded surface (left arrow). (**E**) Tip damage (left arrow) and abraded shaping facet (right arrow). (**F**) Oblique facet with cut marks (left arrow) and polishing (right arrow). (**G**) Rounding and polishing on the tip edge. (**H**) Branch was removed and the knot hole was left and filled with sediments, while the branch collar was shaped and abraded. (**I**) The rounded tip retained some sediment.

from which other tools could be made. The presence of wood-working debris implies that stone tools were used to modify some of the wooden artifacts, but the larger ones were probably made elsewhere and brought to where they used. Overall, the stone tool assemblage of the Gantangqing site exhibits typical characteristics of the so-called simple core-flake industry of the East Asian Earlier Paleolithic (*11*). The scarcity of usable and large lithic raw materials might be the reason for the presence of small expedient stone tools at the site and the dependency on wooden implements in plant food exploitation by the occupants of the site. An alternative possibility is that those who visited Gantangqing anticipated that large (and heavy) stone tools were not needed.

Four billets (soft hammers) were also found (fig. S30) (*14*), and these are the earliest known in East Asia. One is an antler segment with percussion damage at both ends [Fig. 5A (f)]; the other three are pieces of shed antler, with part of the pedicel damaged where it would have touched stone. The sophisticated wooden tools and the application of soft-hammer flaking at the site imply that hominins in Middle Pleistocene East Asia had advanced tool technology and cognitive and adaptive capabilities that are comparable to their western counterparts. However, they might have taken a different trajectory from those of Europe and Western Asia (*31*), and hence the probability that bamboo and other organic materials were used for tools in Pleistocene East Asia deserves further consideration.

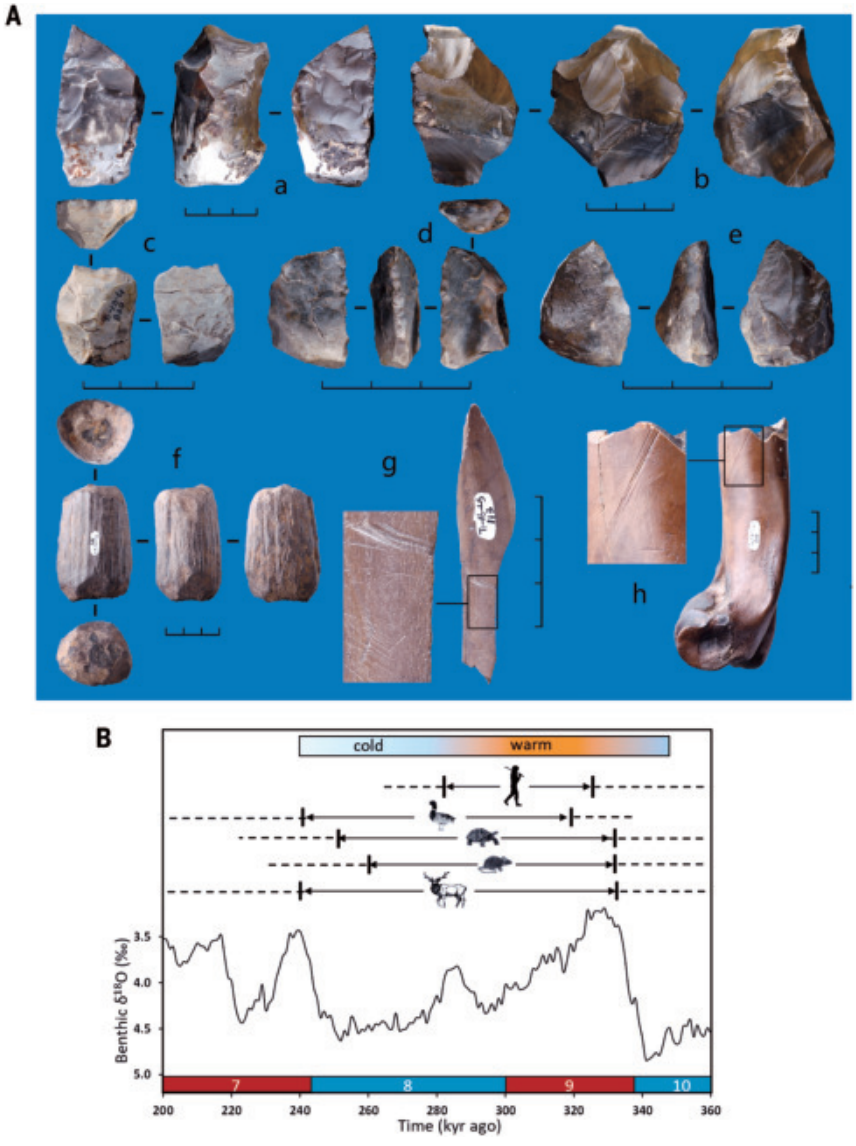

Fig. 5. Stone artifacts and modified bones and climatic context of the Gantangqing site. (**A**) Hard hammer–percussed core (a) and (b), scrapers (c to e), antler soft hammers (f), and broken bones with cutting marks (g and h). Each subdivision on the scale is 1 cm. (**B**) Conceptual model showing the climatic and environmental context of the site. The oxygen isotopic record is the LR04 benthic stack $\delta^{18}O$ record (*31*). The numbers (7 to 10) shown in the red and blue bars on the x-axis represent the corresponding marine isotopic stages. The "cold-warm" bar on the top is based on the pollen record shown in fig. S31. The horizontal lines show the time spans of major fauna identified at the site, which are based on the Bayesian model age estimate (Fig. 2C); both ends of the full and dashed lines represent the highest probability density and the 95% probability ranges, respectively.

Environmental context

The hominin occupation of Gantangqing most likely spans Marine Isotope Stage (MIS) 9 and part of MIS 8 (Fig. 5B). The global oxygen isotope record shows generally warm and wet conditions during MIS 9 and early MIS 8 (*32*) (Fig. 5B), which is consistent with the faunal and floral evidence from the site (*14*). The pollen data shows 40 plant families indicative of a warm and humid subtropical climate; these include several types of aquatic vegetation. A marked decrease in *Quercus* and *Ulmus* and an increase in *Pinus* after layer 15 (315 to 283 kyr) was observed (fig. S31), which probably resulted from an expansion of pine forest at higher elevations as a response to global cooling during the MIS 9/8 transition. The macrofossil records also indicate a subtropical to tropical vegetation that includes several types of trees, lianas, shrubs, and grasses (*14*). Abundant aquatic or hygrophilous taxa such as Cyperaceae, Gramineae, *Alisma*, and most of the ferns indicate that the area around Gantangqing was a swamp or lake. The large mammal fauna was dominated by cervids (*14*). The presence of *Stegodon*, *Megatapirus*, and *Rhinoceros* in layers 18 to 15 (dated to MIS 9)—which were widely distributed in southern China during the Middle and Late Pleistocene—is consistent with a subtropical and tropical environment. Numerous types of small mammals are present (*14*), suggesting open grassland, shrub, woodland, and thick forest. These small mammals may have been taken by avian raptors or by small mammalian carnivores. Nonmammalian fauna includes turtles and several types of birds, notably several types of duck, two types of pheasant, and two types of raptor (table S24). The presence of *Netta* sp. (a diving duck) indicates that the nearby lake was at least 2 to 3 m deep (*33*, *34*) for most of the time that hominins utilized the lake margins.

Many of the plants represented by macro remains are potential plant food resources for hominins (tables S25 and S27). For example, pine nut (*Pinus*), hazel nut (*Corylus*), kiwi fruit (*Actinidia*), redberry and blackberry (*Rubus*), and grape (*Vitis*) are nutritiously valuable. As pine nut and hazel nuts can be kept longer, they could be particularly important in winter when plant food sources were probably rare. The leaves or stems of some herbs such as Amaranthaceae, Phytolaccaceae, and Cucubitaceae and the leaves of some ferns are also edible. Because many of these families contain several thousand species, it is not possible to establish precisely which plants might have been used. However, many

species of aquatic plants in the Cyperaceae and Gramineae families and *Alisma* have edible leaves, seeds, or stems, especially subsoil corms and rhizomes. These could have been extracted from the shallow waters and muddy deposits of the lake shore by digging sticks and grubbing tools. Residue extraction was attempted and some plant starch granules were recovered from the tips of some implements. However, our analysis could not conclusively identify the species of these granules, given the difficulties of preserving organic residues over hundreds of thousands of years.

Our results suggest that hominins at Gantangqing made strategic utilization of lakeshore food resources. They made planned visits to the lakeshore and brought with them fabricated tools of selected wood for exploiting underground tubers, rhizomes, or corms. This scenario implies considerable foresight by hominins in making and using suitable wooden and stone tools for anticipated purpose and a detailed understanding of where, when, and which plants, and which parts of plants, were edible. As such, the Gantangqing assemblage shows the likely use of underground storage organs and the importance of plant foods in early hominin diets in a subtropical environment.

Conclusions

The Gantangqing wooden implements provide the earliest evidence of digging sticks and the exploitation of underground storage organs from the Oriental biogeographic realm and thus document the use of wooden artifacts in a completely different type of environment from Europe or Africa. This site presents a previously unknown range of digging tools and small, complete, hand-held pointed wooden tools, and considerably widens our knowledge of early wooden technology. Gantangqing presents a scenario of early hominin subsistence in subtropical and tropical environments that is plant-orientated, in contrast to northern temperate environments such as Schöningen where the hunting of large mammals is clearly dominant (*3*, *4*). Finally, the evidence from Gantangqing shows the importance of Paleolithic artifacts made from organic materials, and the skill demonstrated in their manufacture offers a clear counterpoint to the apparent "primitive" nature of the stone tools found in East and Southeast Asia (*35*).

REFERENCES AND NOTES

1. M. Dominguez- Rodrigo, J. Serrallonga, J. Juan-Tresserras, L. Alcala, L. Luque, *J. Hum. Evol.* **40**, 289–299 (2001).
2. N. J. Conard *et al.*, *J. Hum. Evol.* **89**, 1–17 (2015).
3. H. Thieme, *Nature* **385**, 807–810 (1997).
4. D. Leder *et al.*, *Proc. Natl. Acad. Sci. U.S.A.* **121**, e2320484121 (2024).
5. L. Allington-Jones, *Archaeol. J.* **172**, 273–296 (2015).
6. L. Barham *et al.*, *Nature* **622**, 107–111 (2023).
7. S. Belitzky, N. Goren-Inbar, E. Werker, *J. Hum. Evol.* **20**, 349–353 (1991).
8. N. Goren-Inbar, E. Werker, C. S. Feibel, *The Acheulian site of Gesher Benot Ya'aqov, Israel: The Wood Assemblage* (Oxbow, 2002).
9. B. Aranguren *et al.*, *Proc. Natl. Acad. Sci. U.S.A.* **115**, 2054–2059 (2018).
10. J. A. West, J. Louys, *J. Archaeol. Sci.* **34**, 512–518 (2007).
11. R. S. Corruccini, R. L. Ciochon, in *Integrative Paths to the Past*. K. D. Schick, ed. (Prentice-Hall, 1994); pp. 569–596
12. L. F. Yang, *Haiyang Huzhao Tongbao* **1**, 34–39 (1984).
13. S.-Y. Cheng, Y.-j. Li, *J. Geomech.* **16**, 383–392 (2010).
14. Materials and methods are available as supplementary materials.
15. X. Y. Zhang, F. Gao, B. Ma, L. P. Hou, *Thinking* **4**, 51–55 (1989).
16. J.-H. Liu, L. Zheng, F. Gao, X.-P. Ji, in *Collected works for "The 40th Anniversary of Yuanmou Man Discovery and the International Conference on Palaeoanthropological Studies"* (Yunnan Science Press, Kuming, 2006), pp. 130–145.
17. A. Revedin, S. Grimaldi, S. Florindi, F. Santaniello, B. Aranguren, *J. Paleolit. Archaeol.* **3**, 525–536 (2020).
18. K. P. Oakley, P. Andrews, L. H. Keeley, J. D. Clark, *Proc. Prehist. Soc.* **43**, 13–30 (1977).
19. M. K. Bamford, Z. L. Henderson, *J. Archaeol. Sci.* **30**, 637–650 (2003).
20. J. D. Clark, J. Cormack, S. Chin, *Kalambo Falls Prehistoric Site: Volume 3, The Earlier Cultures: Middle and Earlier Stone Age*. (Cambridge Univ. Press, 1969), vol. 3, pp. 481–491.
21. D. Nadel, U. Grinberg, E. Boaretto, E. Werker, *J. Hum. Evol.* **50**, 644–662 (2006).
22. E. Carbonell, Z. Castro-Curel, *J. Archaeol. Sci.* **19**, 707–719 (1992).
23. J. Rios-Garaizar *et al.*, *PLOS ONE* **13**, e0195044 (2018).
24. W. H. Schoch, G. Bigga, U. Böhner, P. Richter, T. Terberger, *J. Hum. Evol.* **89**, 214–225 (2015).
25. A. Milks *et al.*, *PLOS ONE* **18**, e0287719 (2023).
26. A. Milks, *Nat. Ecol. Evol.* **2**, 1057–1058 (2018).
27. H. Thieme, S. Veil, W. Meyer, J. Moller, H. Plisson, *Die Kunde* **36**, 11–58 (1985).
28. E. Wagner, Cannstatt. I: Grosswildjäger im Travertingebiet. Forschungen und Berichte zur Vor- und Frühgeschichte in Baden-Württemberg 61. Unpublished PhD thesis, University of Stuttgart (1995).
29. D. Mania, U. Mania, *Praehistoria Thuringica* **2**, 32–72 (1998).
30. F. d'Errico *et al.*, *Proc. Natl. Acad. Sci. U.S.A.* **109**, 13214–13219 (2012).
31. O. Bar-Yosef, *Anthropologie* **53**, 77–92 (2015).
32. L. E. Lisiecki, M. E. Raymo, *Paleoceanography* **20**, PA1003 (2005).
33. A. Salvador, J. A. Amat, I. K. Özgencil, "Red-crested Pochard (*Netta rufina*)" Cornell Lab of Ornithology, 2022).
34. C. Carboneras, G. M. Kirwan, C. J. Sharpe, "Common Pochard (*Aythya ferina*)" (Cornell Lab of Ornithology, 2020).
35. X. Gao, *Curr. Anthropol.* **54**, S358–S370 (2013).

ACKNOWLEDGMENTS

We thank T. Lachlan, Y. Jafari, Y.-J. Guo, and X. Rui for assistance with OSL sample preparation, R.-P. Tang for assistance with field and laboratory work, G. Tong for assistance with references, X. Liu for supporting and coordinating the project, and the members from the local cultural relic authority and other workers taking part in the excavations. **Funding:** This project was funded by the Special Subsidy Fund from National Cultural Heritage Administration of China (2014, 2018, and 2019) to J.-H.L; the Discovery Project from the Australian Research Council to B.L. (DP210100717); the CAS Strategic Priority Research Program (XDB26000000) to X.G., J.-Y.G., Y.W., and H.S.; the Research Grants Council of Hong Kong to S.-H.L. (17307117); the NSFC grants to F.H. (41772174); J.-Y.G. and C.-L.D. (41977380 and 42488201); to Y.-J.H. (42272026); and to H.S. (42002202). **Author contributions:** J.-H.L. organized the overall project and conducted the analysis on the large mammalian fossils. X.G. and J.-H.L. coordinated the research. J.-H.L., R.D., and X.G. conducted the wooden implements analysis and R.D. analyzed the antler soft hammers. X.-L.Z. and Y.-S.J. conducted the use-wear and experimental analysis on the wooden tools. H.S. conducted the wood type identification**.** J.-H.L. and J.-Y.G. conducted the regional geology and stratigraphic analysis. Q.-J.R. and X.G. conducted the lithic analysis. J.-Y.G. and C.-L.D. conducted the analysis on palaeomagnetism and sedimentology. Y.-J.H. conducted the fossil carpological study. J.L. and S.-F.L. conducted the pollen analysis. Y.W. conducted the analysis on rodent fossils. T.S. conducted the nonmammalian fauna analysis. B.L., K.O., and S.-H.L. conducted the optical dating; F.H. and S.-H.L. conducted the ESR/U-series dating. R.D., B.L., J.-H.L., and X.G. wrote the main text with contributions from all coauthors. **Competing interests:** The authors declare no competing interests. **Data and materials availability:** All data needed to evaluate the conclusions in this paper are present in the paper or the supplementary materials. All archaeological remains examined in this study are housed in the Yunnan Institute of Cultural Relics and Archaeology, Kunming, China. Access to the specimens is available upon request. Mailing address of the institute: 4069 Jihong Road, Guandu District, Kunming City, Yunnan Province, China. Postal code: 650206; Telephone number: +86 0871 68250676; Fax: +86 0871 68250730.

SUPPLEMENTARY MATERIALS

science.org/doi/10.1126/science.adr8540
Figs. S1 to S31; Tables S1 to S28; References (*36*–*106*); MDAR Reproducibility Checklist

Submitted 28 November 2024; accepted 25 April 2025

10.1126/science.adr8540

IMMUNE SIGNALING

Membrane topology inversion of GGCX mediates cytoplasmic carboxylation for antiviral defense

Tomohiko Okazaki[1,2,3]*, Keiji Nozaki[2], Nao Morimoto[1], Yuta Otobe[4], Riho Saito[2], Shuntaro Abe[1], Miyuki Okajima[2], Hikari Yoshitane[3,4,5], Tomohisa Hatta[6], Shun-ichiro Iemura[7], Tohru Natsume[8], Hidetaka Kosako[9], Miwako Yamasaki[10], Satoshi Inoue[11,12], Takashi Kondo[13], Haruhiko Koseki[13], Yukiko Gotoh[2,14]

Mitochondrial antiviral signaling protein (MAVS) is an adaptor involved in antiviral immunity, but its regulation is not fully understood. We identified carboxylation of MAVS by vitamin K (VK)–dependent γ-glutamyl carboxylase (GGCX), which was unexpected owing to the reported membrane topology of GGCX. We found that GGCX could undergo topology inversion to carboxylate MAVS within the cytoplasm. This carboxylation enhanced the ability of MAVS to induce type I interferons while suppressing the induction of apoptosis. Genetic knockout of GGCX, a VK-free diet, or depletion of VK by inhibiting VK epoxide reductase 1 with warfarin increased viral susceptibility in mice. Thus, we identified a MAVS regulatory mechanism—the existence of cytoplasmic protein carboxylation and topological inversion of GGCX—and demonstrated how modulating VK levels may influence antiviral defense.

Innate immune responses of mammalian cells to viral infection include the production of interferons (IFNs) and the execution of apoptosis (*1*–*3*). Type I IFNs, such as IFN-α and IFN-β, induce the expression of hundreds of IFN-stimulated genes (ISGs) that play a major role in restricting viral replication within infected cells, whereas apoptosis eliminates infected cells to prevent further viral spread (*2*, *3*). These IFN-mediated and apoptotic responses appear to be differentially regulated in a context-dependent manner upon viral infection, with clearance of infected cells by apoptosis considered beneficial in tissues with a high regenerative capacity (such as skin and lung tissue) (*4*) but detrimental in those in which regeneration rarely occurs (such as brain tissue). Recognition of viral RNA within the host cell by pattern recognition receptors—including retinoic acid–inducible gene I (RIG-I)–like receptors (RLRs), such as RIG-I and melanoma differentiation–associated protein 5 (MDA5) (*5*, *6*)—results in the activation of mitochondrial antiviral signaling protein (MAVS) (*7*–*10*), a transmembrane protein that localizes to mitochondria and peroxisomes and plays an essential role in mediating both IFN and apoptosis responses (*11*, *12*). However, the molecular mechanisms that control the switch between these two arms of the MAVS-mediated antiviral defense system remain unclear.

Results

MAVS is carboxylated in its cytoplasmic domain by GGCX

To explore the molecular mechanisms that underlie discrimination between MAVS-mediated antiviral responses, we investigated posttranslational modification (PTM) of MAVS by performing mass spectrometric analysis of a decahistidine (His_{10})– and Flag epitope–tagged NH_2-terminal fragment (ΔC) of human MAVS (hMAVS) expressed in human embryonic kidney–293T (HEK293T) cells. Because detecting PTMs of endogenous MAVS was challenging owing to its low abundance, we overexpressed MAVS for facilitating identification of its PTMs. Recombinant MAVS protein was isolated from cell lysates under denaturing conditions to prevent artifactual PTMs (fig. S1, A and B). We identified carboxylation at residues Asp^{53}, Glu^{70}, Glu^{80}, and Asp^{83} of hMAVS, all of which are located in the cytoplasmic domain of the protein (Fig. 1A and figs. S1C and S2A). In addition, the His_{10}-Flag–tagged full-length hMAVS protein expressed in HEK293T cells was recognized by a commercially available pan-Gla antibody, which detects γ-carboxyglutamate (Gla) residues in proteins irrespective of species specificity, in immunoblot analysis (Fig. 1B).

In addition, we generated a rabbit polyclonal antibody to recognize the Glu^{80}-carboxylated (Gla^{80}) form of mouse MAVS (mMAVS), which detected His_{10}-Flag–mMAVS in HEK293T cells (Fig. 1C and fig. S3A). A mutant of mMAVS in which Glu^{80} was replaced with alanine [mMAVS(E80A)] as well as a double mutant in which both Glu^{70} and Glu^{80} were replaced with alanine [mMAVS(2EA)] were not detected by the anti-Gla^{80} antibodies (Fig. 1C and fig. S3B). Knockdown of γ-glutamyl carboxylase (GGCX), which adds a carboxyl group to glutamate or aspartate residues (*13*–*15*), reduced MAVS carboxylation detected by anti-Gla^{80} antibodies (Fig. 1C). We also found that carboxylation of mMAVS at Gla^{80} gradually increased following vesicular stomatitis virus (VSV) infection of HEK293T cells (Fig. 1D and fig. S4, A to C). Furthermore, we generated knock-in (KI) mice, where the sequence encoding His_{10} tag was inserted so that it would be expressed at the N terminus of the endogenous MAVS protein to facilitate isolation of endogenous mMAVS from primary mouse tissues (fig. S5). Using lysates from the liver of these KI mice, we found that endogenous mMAVS was indeed recognized by pan-Gla antibodies (Fig. 1E).

Detection of cytoplasmic carboxylation using a reporter

GGCX is a transmembrane protein that resides on membranes of the endoplasmic reticulum (ER), and its activity is dependent on vitamin K (VK), an essential dietary nutrient. VK can be depleted by warfarin, which inhibits vitamin K epoxide reductase 1. Approximately 20 protein substrates of GGCX have been identified (*16*–*18*), and all are exclusively extracellular or reside within the ER lumen. This is consistent with the catalytic domain of GGCX being reported to face the luminal side of ER and unable to access cytoplasmic targets (*19*). In general, membrane proteins have a fixed orientation, and misoriented membrane proteins are destined to be corrected as an error (*20*–*24*). Therefore, GGCX was not thought to carboxylate proteins in the cytoplasm, given its membrane topology. Our finding that cytoplasmic carboxylation of MAVS was dependent on GGCX was, thus, unexpected (Fig. 1C). The N-terminal domains of MAVS (MAVS ΔC) and full-length MAVS overexpressed in HEK293T cells as well as endogenous His_{10}-tag–KI MAVS in mouse embryonic fibroblasts (MEFs) were localized to either the cytosolic or the extraorganellar space of the organelle fraction, indicating that they were not mistargeted to the ER lumen (fig. S6, A to D).

We examined whether GGCX was able to carboxylate cytoplasmic substrates by generating a cytoplasmic Gla reporter (cytoGla) consisting of tandemly repeated Gla domains and a conserved recognition sequence for GGCX as well as a nuclear export signal (fig. S7A). Carboxylation of cytoGla was detected in HEK293T cells in the presence but not the

[1]Institute for Genetic Medicine, Graduate School of Life Science, Hokkaido University, Sapporo, Japan. [2]Graduate School of Pharmaceutical Sciences, University of Tokyo, Tokyo, Japan. [3]Japan Science and Technology Agency (JST) Fusion Oriented Research for Disruptive Science and Technology (FOREST) Program, Kawaguchi, Japan. [4]Circadian Clock Project, Tokyo Metropolitan Institute of Medical Science, Tokyo, Japan. [5]Department of Biological Sciences, School of Science, The University of Tokyo, Tokyo, Japan. [6]Robotic Biology Institute, Inc., Tokyo, Japan. [7]Translational Research Center, Fukushima Medical University, Fukushima, Japan. [8]Molecular Profiling Research Center for Drug Discovery, National Institute of Advanced Industrial Science and Technology, Tokyo, Japan. [9]Institute of Advanced Medical Sciences, Tokushima University, Tokushima, Japan. [10]Department of Anatomy, Faculty of Medicine, Hokkaido University, Sapporo, Japan. [11]Department of Systems Aging Science and Medicine, Tokyo Metropolitan Institute of Gerontology, Itabashi, Tokyo, Japan. [12]Research Center for Genomic Medicine, Saitama Medical University, Hidaka, Saitama, Japan. [13]Laboratory for Developmental Genetics, RIKEN Center for Integrative Medical Sciences (RIKEN-IMS), Yokohama, Japan. [14]International Research Center for Neurointelligence (WPI-IRCN), University of Tokyo, Tokyo, Japan. ***Corresponding author. Email: okazaki@igm.hokudai.ac.jp**

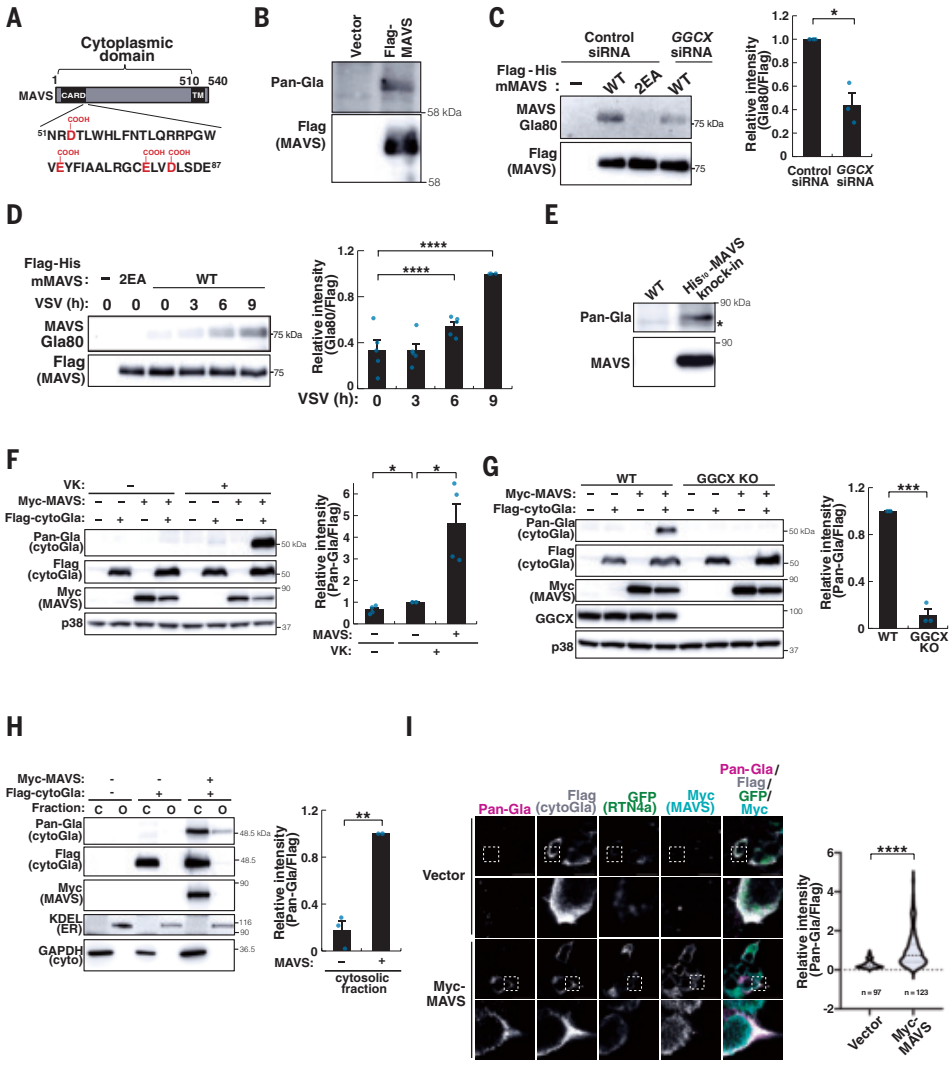

Fig. 1. MAVS is carboxylated in cells. (**A**) Domain structure of hMAVS. Carboxylation sites (Asp^{53}, Glu^{70}, Glu^{80}, and Asp^{83}) in the cytoplasmic domain are colored red. CARD, caspase activation and recruitment domain; TM, transmembrane. (**B**) His_{10}-Flag–tagged hMAVS was isolated from HEK293T cells using Co^{2+} resin and analyzed by immunoblot using antibodies against Flag and pancarboxylated glutamate (pan-Gla). (**C**) His_{10}-Flag–tagged mMAVS or mMAVS(2EA) was isolated from HEK293T cells transfected with GGCX or control small interfering RNAs (siRNAs) for 4 days in the presence of 20 μM vitamin K1 (VK1) using Co^{2+} resin and analyzed by immunoblot using antibodies against Flag and the Glu^{80}-carboxylated (Gla^{80}) form of mMAVS. The signal intensity for Gla^{80} relative to that for Flag were quantified and plotted (normalized to lane 2). Note that Glu^{70}Ala/Glu^{80}Ala/Asp^{83}Ala (3A) mutant of mMAVS expressed in HEK293T cells was still recognized by pan-Gla antibodies, suggesting that MAVS is carboxylated also at sites other than these residues in the CARD domain (fig. S3C). (**D**) His_{10}-Flag–tagged mMAVS was isolated from HEK293T cells infected with 0.3 multiplicity of infection (MOI) of VSV for the indicated times in the presence of 20 μM VK1 using Co^{2+} resin and analyzed by immunoblot using antibodies against Flag and Gla^{80}. The signal intensity for Gla^{80} relative to that for Flag were quantified and plotted (normalized to lane 6). (**E**) His_{10}-tagged protein was isolated from liver extracts derived from WT or heterozygous His_{10}-MAVS KI mice using Co^{2+} resin and analyzed by immunoblot using antibodies against pan-Gla and mMAVS. The asterisk indicates a nonspecific band. (**F**) HEK293T cells maintained in the presence or absence of VK1 were transiently transfected with expression vectors for Flag-tagged cytoGla and Myc epitope–tagged hMAVS for 20 hours, lysed, and analyzed by immunoblot using antibodies against pan-Gla, Flag, Myc, and p38 MAPK (loading control). The signal intensity for pan-Gla relative to that for Flag were quantified and plotted (normalized to lane 6). (**G**) WT or GGCX-KO HEK293T cells maintained in the presence of VK1 were transiently transfected with expression vectors for Flag-cytoGla and Myc-hMAVS for 20 hours, lysed, and analyzed by immunoblot using antibodies against pan-Gla, Flag, Myc, GGCX, and p38 MAPK. The signal intensity for Pan-Gla relative to that for Flag were quantified and plotted (normalized to lane 4). (**H**) HEK293T cells maintained in the presence of VK1 were transiently transfected with expression vectors for Flag-cytoGla and Myc-hMAVS for 20 hours, lysed, and subjected to subcellular fractionation into cytosol (C) and organelle-bound (O) fractions followed by immunoblot using antibodies against pan-Gla, Flag, Myc, KDEL (ER marker), and glyceraldehyde-3-phosphate dehydrogenase (GAPDH, cytosolic marker). The signal intensity for Pan-Gla relative to that for Flag were quantified and plotted (normalized to lane 5). (**I**) HEK293T cells maintained in the presence of VK1 were transiently transfected with expression vectors for Flag-cytoGla, Myc-hMAVS (or the corresponding empty vector), and green fluorescent protein (GFP)–tagged RTN4a (ER marker) for 20 hours. Cells were fixed and subjected to immunofluorescence staining with antibodies against pan-Gla, Flag, and Myc. The boxed regions in the upper panels of each set are shown at higher magnification in the corresponding lower panels. Data in (B), (C) to (E), and (H) are representative from three independent experiments, that in (F) is from four independent experiments, and that in (D) is from five independent experiments. Individual datapoints show results for independent experiments, and the bars show mean ± SEM. Data in (I) are representative images (scale bars, 50 μm) shown together with a violin plot for the relative Pan-Gla/Flag fluorescence intensity ratio determined for the indicated numbers of cells pooled together from three independent experiments (three fields per experiment). Statistical analyses in (D) were performed using Dunnett's multiple comparison test (****$P < 0.001$); in (C), (F), (G), and (H), using a one-sample *t* test (*$P < 0.05$; **$P < 0.01$; ***$P < 0.005$); and, in (I), using an unpaired two-tailed Mann-Whitney *U* test (****$P < 0.001$). Single-letter abbreviations for the amino acid residues referenced throughout the figures are as follows: D, Asp; E, Glu; A, Ala; N, Asn; R, Arg; T, Thr; L, Leu; W, Trp; F, Phe; Q, Gln; P, Pro; G, Gly; V, Val; Y, Tyr; I, Ile; C, Cys; S, Ser.

absence of VK, a cofactor for GGCX (Fig. 1F). Carboxylation of cytoGla was lost in cells where endogenous GGCX had been depleted (Fig. 1G). Moreover, carboxylation of cytoGla was only detected when MAVS or a constitutively active form of RIG-I or MDA5 was overexpressed (Fig. 1F and fig. S8A). Subcellular fractionation and immunostaining confirmed that MAVS overexpression increased cytoGla carboxylation in the cytoplasm (Fig. 1, H and I).

These results suggested that cytoplasmic proteins were potential targets of carboxylation by GGCX and that the RLR-MAVS pathway promoted such cytoplasmic carboxylation.

Topology inversion of GGCX

We considered that one potential mechanism of cytoplasmic carboxylation may be inversion of GGCX topology. GGCX is described as a type II integral membrane protein with multiple N-linked glycosylation sites in its C-terminal region (*25*). If the topology of GGCX were to be inverted, the C-terminal domain would be localized in the cytoplasm, which would be expected to result in loss of glycosylation (Fig. 2A). We expressed Myc-tagged GGCX in HEK293T cells and analyzed its apparent molecular weight by SDS–polyacrylamide gel electrophoresis and immunoblotting. We observed a slower-migrating band (fig. S9A), designated GGCX(A), in addition to a band migrating according to the expected molecular weight (88 kDa), designated GGCX(B). The faster migration of GGCX(B) appeared to be due to the lack of glycosylation in its C-terminal region, given that GGCX(A) but not GGCX(B) was bound by the lectin concanavalin A (ConA) and that treatment with endoglycosidase H (EndoH) reduced the apparent molecular size of only GGCX(A), resulting in the merging of both bands into one migrating at the position of GGCX(B) (Fig. 2B).

MAVS expression did not overtly affect the overall level or localization of GGCX (fig. S9, B and C). The relative abundance of GGCX(B) was greatly increased by forced expression of MAVS or a constitutively active form of RIG-I or MDA5 (Fig. 2B and fig. S8B)

We explored whether loss of glycosylation of GGCX(B) corresponded to a change of its topology. We performed a split mNeonGreen2 (mNG2) assay in which the mNG2 protein is divided into two nonfluorescent fragments, $mNG2_{1–10}$ and $mNG2_{11}$. Fluorescence is only detected when these fragments are brought into proximity and reconstituted in the same subcellular compartment (Fig. 2C and fig. S9D). A low level of mNG2 fluorescence was detected when KDEL-tagged (ER-localized) $mNG2_{1–10}$ and N-terminally $mNG2_{11}$-tagged GGCX were coexpressed in HEK293T cells (Fig. 2D), indicating that a small fraction of GGCX existed with type III topology. The intensity of this signal increased by overexpression of MAVS (Fig. 2D).

We investigated other proteins inserted into the ER membrane, transmembrane 4 six family member 20 (TM4SF20) and cluster of differentiation 38 (CD38), and did not detect their topology changed upon MAVS expression (fig. S10, A to C). In addition, we did not detect elevation of ER stress markers, such as spliced X-box binding protein 1 (XBP1) and heat shock protein family A member 5 (HSPA5), suggesting that MAVS overexpression did not cause ER malfunction (fig. S10, D to G).

Stress-activated mitogen-activated protein kinase (MAPK) pathways, which are crucial for type I IFN induction, are known to be activated downstream of MAVS (*26*). We found that GGCX(B) was increased upon expression of active forms of MAPK kinase kinase (MAPKKK) apoptosis signal-regulating kinase 1 (ASK1) and MAPK kinase 6 (MKK6), both of which activate p38 MAPK (fig. S11A). Furthermore, the increase in GGCX(B) by MAVS expression was blocked in cells expressing a dominant-negative p38 MAPK mutant (p38 AGF) (fig. S11B). These findings suggest that p38 MAPK may mediate MAVS-induced topology inversion of GGCX. Additionally, coimmunoprecipitation assays suggested that MAVS preferentially interacted with GGCX(B) rather than GGCX(A). Therefore, MAVS might stabilize inverted GGCX through interactions in the cytoplasm (fig. S12A).

Mutation of MAVS carboxylation sites suppresses IFN production and promotes caspase activation

We examined whether carboxylation affected MAVS-induced production of type I IFN and activation of caspases. We generated alanine substitution mutants for each carboxylation site (Asp^{53}Ala, Glu^{70}Ala, Glu^{80}Ala, and Asp^{83}Ala) of hMAVS. Overexpression of wild-type (WT) hMAVS in HEK293T cells was sufficient to activate the mouse IFN-β gene (Ifnb1) promoter in a reporter assay; induce phosphorylation of IFN regulatory factor 3 (IRF3), a critical step for IFN induction; and trigger caspase activation, as evidenced by the cleavage of both poly[adenosine diphosphate (ADP)–ribose] polymerase (PARP) and MAVS itself (Fig. 3, A and B, and fig. S13, A and B). By contrast, expression of the Asp^{53}Ala mutant or the Glu^{70}Ala / Glu^{80}Ala / Asp^{83}Ala (3A) triple mutant failed to induce IRF3 phosphorylation and subsequent IFN-β promoter activation but strongly enhanced caspase activation, as assessed by immunoblot analysis of the cleavage of both PARP and MAVS itself (Fig. 3B and fig. S13B). Treatment with the pan-caspase inhibitor zVAD did not rescue IRF3 phosphorylation by these carboxylation-deficient MAVS mutants (fig. S14A), suggesting that suppression of *Ifnb1* expression was not a secondary effect of enhanced cell death. We concluded that mutation of the carboxylation sites of MAVS did not inhibit overall protein function but rather induced a switch in regulation from type I IFN induction to caspase activation.

To determine the role of MAVS carboxylation in immune defense, we used MEFs derived from MAVS–knockout (KO) mice and expressed either WT or 3A mutant forms of mMAVS. We then examined the responses to polyinosinic-polycytidylic acid poly(I:C) double-stranded RNA (as a model of RNA virus infection) and infection with VSV. Poly(I:C) and VSV infection increased the levels of *Ifnb1* mRNA and IRF3 phosphorylation in MEFs expressing WT mMAVS but not in those expressing the 3A mutant (Fig. 3, C and D, and fig. S15, A and B). By contrast, the extent of VSV-induced PARP cleavage was greater in cells expressing the 3A mutant of mMAVS than in those expressing the WT protein (fig. S15B). The titer of VSV in culture supernatants at 24 hours after infection was higher for MEFs expressing the 3A mutant than for those expressing WT mMAVS (Fig. 3E). The effects of the MAVS 3A mutation on *Ifnb1* expression and viral replication were observed even in the presence of zVAD (fig. S16, A to C). Together, these results indicated that carboxylation of MAVS played a role in the induction of IFN-β in response to viral RNA and the suppression of viral expansion.

GGCX promotes type I IFN production and inhibits caspase activation

Because mutation of MAVS carboxylation sites altered its function, we investigated how GGCX influenced antiviral responses. Depletion of GGCX in HeLa S3 cells attenuated the increase in *IFNB1* mRNA and IRF3 phosphorylation as well as in enhancement of PARP cleavage induced by poly(I:C) treatment (Fig. 3, F and G). Depletion of GGCX in the neuronal cell line N2a attenuated IFN-inducing signaling but enhanced caspase activation in response to VSV infection (fig. S17A). The effect of GGCX RNAi on *IFNB1* induction in HeLa S3 cells was observed even in the presence of zVAD (fig. S18, A and B). Overexpression of mGGCX in HEK293T cells promoted hMAVS-induced *IFNB1* expression without affecting the abundance of *MAVS* mRNA (Fig. 3H and fig. S19A) and inhibited hMAVS-induced caspase-3 cleavage (Fig. 3I). However, these effects of mGGCX were not observed with the MAVS 4A mutant (fig. S20, A to C). Furthermore, mGGCX overexpression did not affect *IFNB1* expression (fig. S19B) or caspase-3 activation (Fig. 3I) induced by TBK1, suggesting that GGCX regulated the switch from caspase activation to type I IFN induction through MAVS rather than its downstream mediator TBK1.

We treated HeLa S3 cells with warfarin to deplete VK and found that it inhibited poly(I:C)-mediated induction of *IFNB1* mRNA (fig. S21A). In addition, warfarin enhanced PARP cleavage induced by poly(I:C) transfection in these cells (fig. S21B). These results supported the conclusion that VK-dependent carboxylation of MAVS by GGCX promoted the type I IFN response and, in parallel, suppresses the apoptotic response to viral infection.

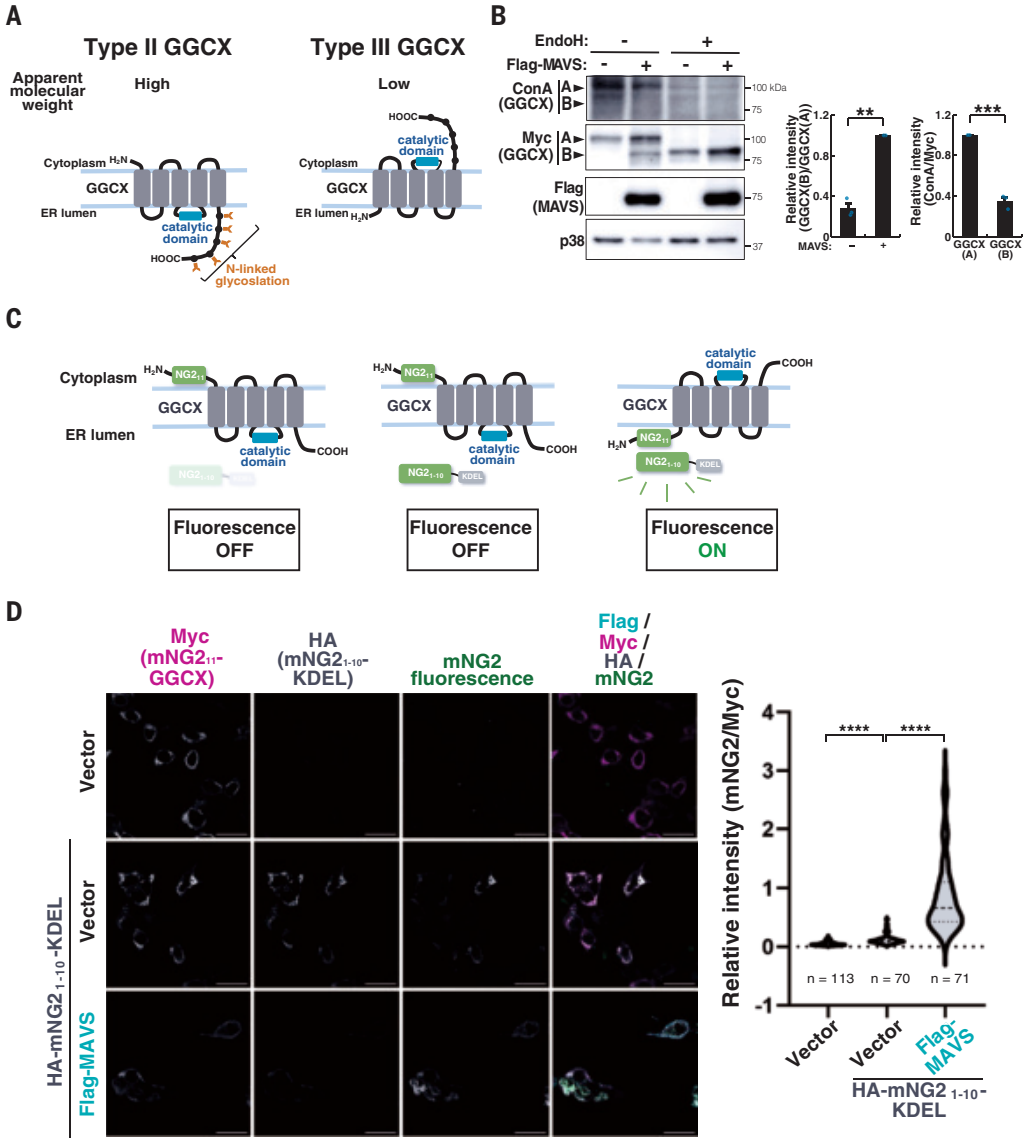

Fig. 2. Topology inversion of GGCX. (**A**) Schematic model for the membrane topology inversion of GGCX from type II to type III—where, in the type II orientation, the N terminus is positioned in the cytoplasm and the C terminus in the ER lumen, whereas, in the type III orientation, the N terminus is localized to the ER lumen, and the C terminus, to the cytoplasm—as well as its effect on N-linked glycosylation. (**B**) HEK293T cells maintained in the presence of VK1 were transiently transfected with expression vectors for Myc-mGGCX and Flag-hMAVS for 20 hours, lysed, and subjected to EndoH treatment for 5 hours followed by immunoblot with antibodies against Myc, Flag, and p38 MAPK or lectin blot analysis with horseradish peroxidase–conjugated concanavalin A lectin (ConA). Note that two bands of GGCX, corresponding to apparent high molecular weight (A) and low molecular weight (B) forms, were detected in the presence of MAVS overexpression. The signal intensity for GGCX (B) relative to those for GGCX (A) (normalized to lane 2) and ConA relative to Myc were quantified and plotted [normalized to GGCX (A) in lane 2]. (**C**) Schematic model of the split mNG2 reporter system for monitoring the membrane topology of GGCX. (**D**) HEK293T cells were transfected with expression vectors for Flag-hMAVS, Myc– mNG2$_{11}$-mGGCX, and hemagglutinin epitope (HA)–tagged mNG2$_{1–10}$-KDEL for 20 hours. Cells were fixed and subjected to immunofluorescence staining with antibodies against Flag, Myc, and HA. Data in (B) is representative from three independent experiments, shown as individual points, and the bars show mean ± SEM. In (D), representative images (scale bars, 20 μm) are shown together with a violin plot for the relative mNG2/Myc fluorescence intensity ratio determined for the indicated numbers of cells pooled together from three independent experiments. Statistical analyses in (B) were performed using a one-sample *t* test (**$P < 0.01$; ***$P < 0.005$), and, in (D), using a Kruskal-Wallis test followed by Dunn's multiple comparison test (****$P < 0.001$).

Proteomic identification of MAVS carboxylation site–associated proteins

We hypothesized that proteins that specifically associated with either carboxylated or noncarboxylated MAVS may account for the functional switch between IFN induction and caspase activation. We used mass spectrometry (MS) to identify proteins differentially bound by Flag-tagged WT hMAVS or a carboxylation-deficient form (4A, with the substitutions Asp^{53}Ala, Glu^{70}Ala, Glu^{80}Ala, and Asp^{83}Ala) isolated from HEK293T cells.

Among the differentially associated proteins, we found that the TOMM subunit TOMM40 associated preferentially with the 4A mutant form of MAVS relative to the WT protein (Fig. 4A and data S1). This preferential association was confirmed by coimmunoprecipitation (Fig. 4B). We also found that overexpression of human TOMM40 (hTOMM40) enhanced MAVS-mediated caspase activation but not IRF3 phosphorylation and attenuated MAVS-mediated IFN-β induction in HEK293T cells (Fig. 4, C and D). Conversely, knockdown of TOMM40 inhibited MAVS-mediated caspase activation but had little

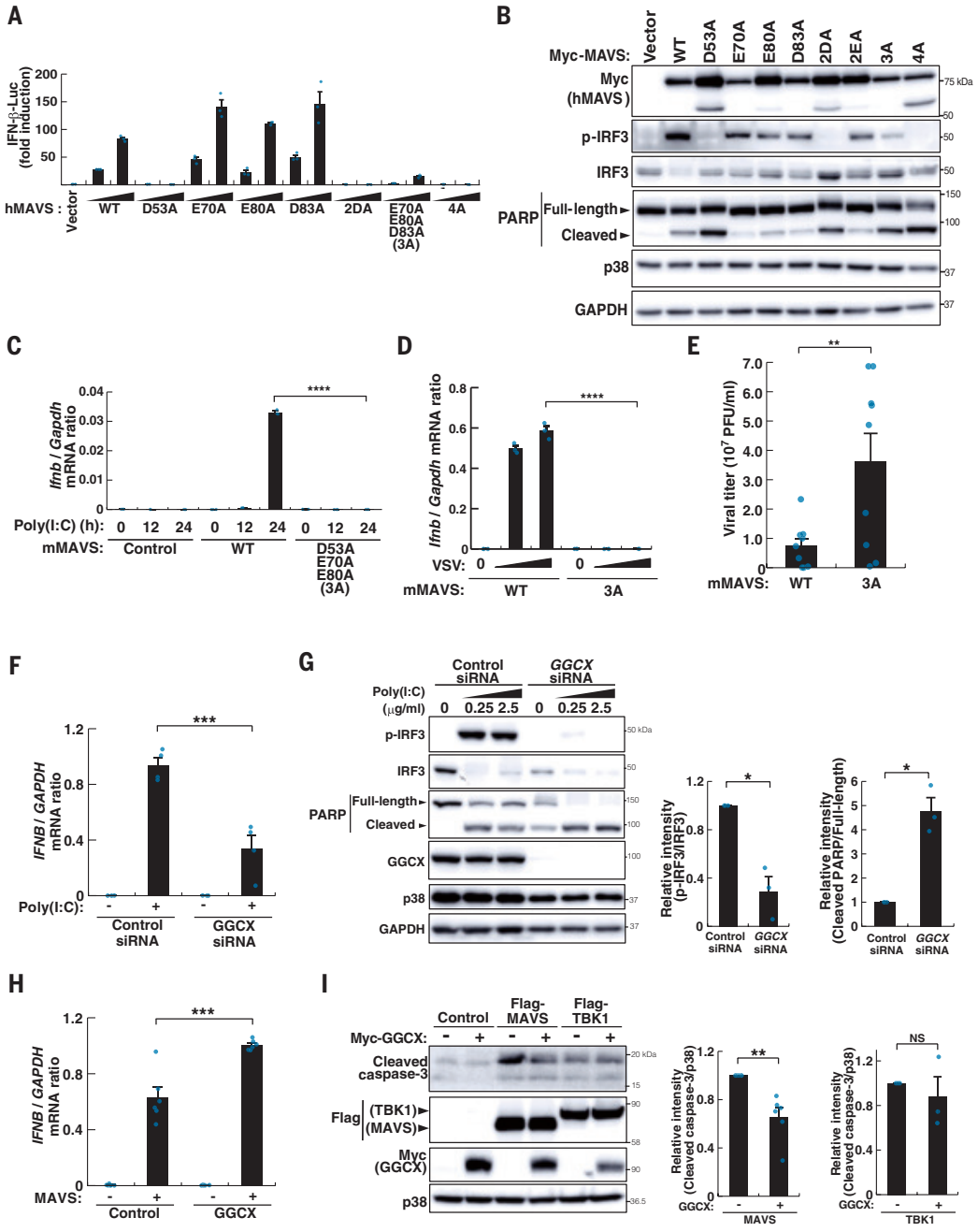

Fig. 3. GGCX-mediated carboxylation of MAVS promotes IFN production and inhibits caspase activation. (**A**) HEK293T cells were transfected for 24 hours with expression plasmids for WT or the indicated mutant forms of hMAVS (100 or 500 ng), a reporter plasmid encoding *Renilla* luciferase (Luc) under the control of the mouse *Ifnb1* promoter, and the pGL3-control vector encoding firefly Luc as an internal control. Cells were lysed for measurement of Luc activity, and activity of *Renilla* Luc was normalized against that of firefly Luc. (**B**) HEK293T cells transiently transfected for 20 hours with expression plasmids for Myc-tagged WT or mutant forms of hMAVS were lysed and analyzed by immunoblot using antibodies against Myc, phosphorylated IRF3 (p-IRF3), IRF3, PARP, p38 MAPK, and GAPDH. (**C** and **D**) MEFs isolated from MAVS-KO mice were infected with retroviruses encoding either WT or 3A ($Asp^{53}Ala$, $Glu^{70}Ala$, and $Glu^{80}Ala$) mutant forms of mMAVS, transfected with 0.25-μg/ml poly(I:C) for the indicated times (C) or infected with VSV for 12 hours (D), and assayed for *Ifnb1* mRNA by reverse transcription quantitative polymerase chain reaction (RT-qPCR). (**E**) MAVS-KO MEFs expressing WT or 3A mutant forms of mMAVS were infected for 24 hours with VSV at an MOI of 0.3, washed, and incubated for 24 hours in fresh medium, which was then collected for assay of VSV titer measuring plaque-forming units (PFUs) by standard plaque assay. (**F** and **G**) HeLa S3 cells were transfected first with GGCX or control siRNAs for 4 days then with poly(I:C) at 2.5 μg/ml (F) or 0.25 or 2.5 μg/ml (G) for 6 hours. They were then subjected to RT-qPCR analysis of *IFNB1* mRNA (F) or to immunoblot using antibodies against p-IRF3, IRF3, PARP, GGCX, p38, and GAPDH (G). The signal intensities for p-IRF3 relative to IRF3 as well as for cleaved PARP relative to full-length PARP were quantified and plotted (normalized to lane 3). (**H** and **I**) HEK293T cells were transfected for 20 hours with expression vectors for Myc-mGGCX and Flag-hMAVS (or Flag-mTBK1) then subjected to RT-qPCR analysis of *IFNB1* mRNA (H) or immunoblot using antibodies against cleaved caspase-3, Flag, Myc, and p38 MAPK (I). The signal intensities for cleaved caspase-3 relative to p38 were quantified and plotted (normalized to lane 3 for MAVS and normalized to lane 5 for TBK1, respectively). Data in (A), (C), and (D) are mean ± SD of triplicates from an experiment repeated three times with similar results. Data in (B) and (G) are from three independent experiments, data in (I) is from six independent experiments, data in (F) is from three independent experiments, data in (H) is from six independent experiments, and data in (E) is from nine independent experiments. The bars show mean ± SEM. Statistical analyses in (C), (D), (E), (F), and (H) were performed using an unpaired Student's *t* test (**$P < 0.01$; ***$P < 0.005$; ****$P < 0.001$), and, in (G) and (I), using a one-sample *t* test (*$P < 0.05$; **$P < 0.01$; NS, not significant).

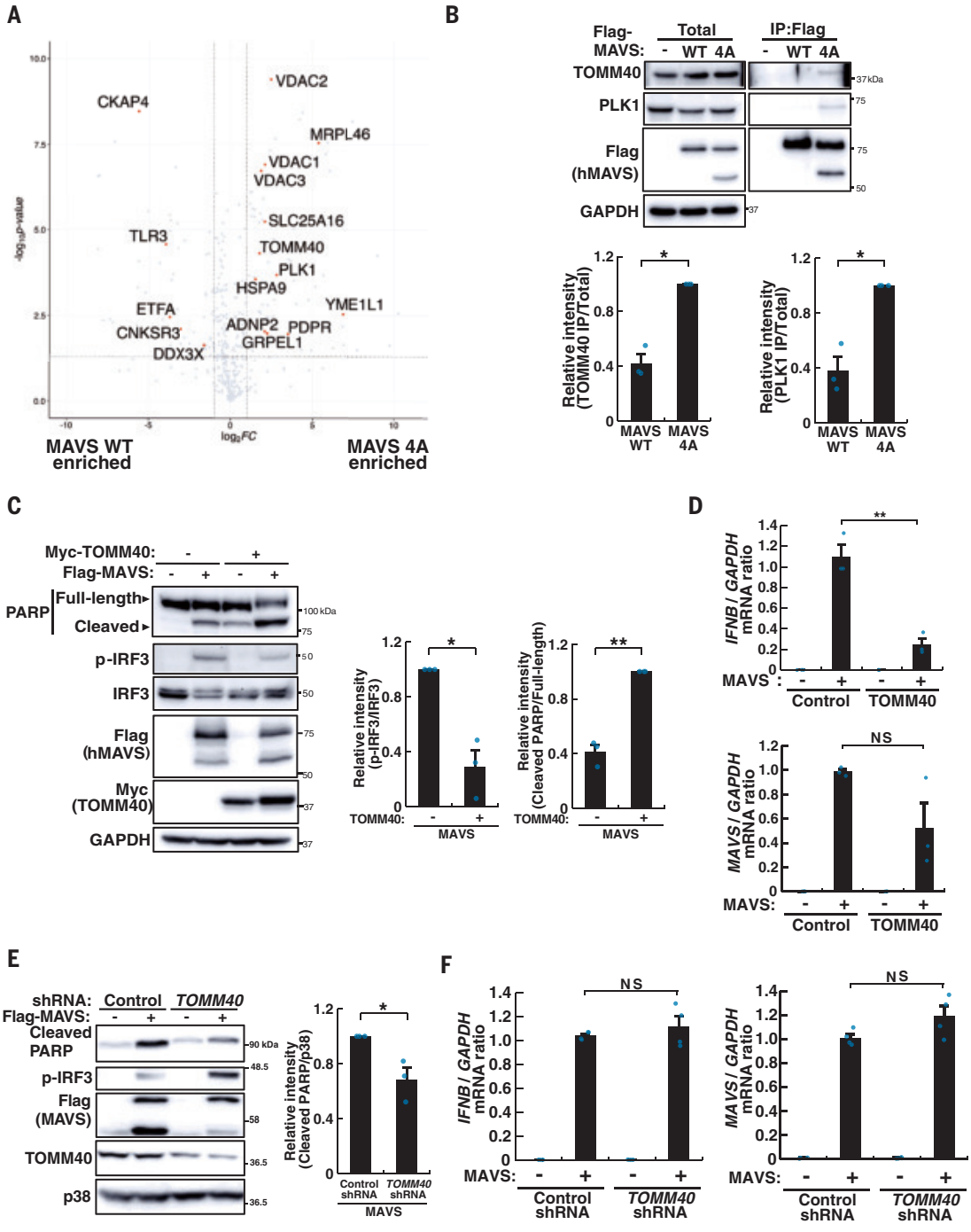

Fig. 4. Proteomic identification of MAVS carboxylation site–associated proteins. (**A**) Volcano plot obtained from immunoprecipitation (IP)–MS analysis of WT versus 4A mutant forms of hMAVS in HEK293T cells. Red points indicate mitochondria-localized proteins and known MAVS interactors with fold change (FC) > 2 and $P < 0.05$. PLK1 and TOMM40 are differentially associated proteins of WT and 4A mutant forms of hMAVS in HEK293T cells. (**B**) HEK293T cells transiently transfected for 20 hours with expression vectors for Flag-tagged WT or 4A mutant forms of hMAVS were subjected to IP with antibodies against Flag, and the resulting precipitates and original cell lysates (Total) were analyzed by immunoblot using antibodies against TOMM40, PLK1, Flag, and GAPDH. The signal intensities for coimmunoprecipatated TOMM40 and PLK1 relative to the total were quantified and plotted (normalized to lane 6). (**C** and **D**) HEK293T cells transiently transfected with expression vectors for Myc-hTOMM40 and Flag-hMAVS for 20 hours were either analyzed by immunoblot using antibodies against p-IRF3, IRF3, PARP, Flag, Myc, and GAPDH (C) or assayed for *IFNB1* and *MAVS* mRNAs by RT-qPCR (D). The signal intensities for p-IRF3 relative to IRF3 (normalized to lane 2) and for cleaved PARP relative to full-length were quantified and plotted (normalized to lane 4). (**E** and **F**) HeLa S3 cells were transiently transfected first with expression vectors for TOMM40 or GFP (control) short hairpin RNAs (shRNAs) for 4 days then with an expression vector for Flag-hMAVS for 20 hours. Cell lysates were then either analyzed by immunoblot using antibodies against cleaved PARP, p-IRF3, Flag, TOMM40, and p38 MAPK (E) or assayed for *IFNB1* and *MAVS* mRNAs by RT-qPCR (F). The signal intensities for cleaved PARP relative to that for p38 were quantified and plotted (normalized to lane 2). Data in (B), (C), and (E) are from three independent experiments, data in (D) is from three independent experiments, and data in (F) is from four independent experiments. Individual data points show data from independent experiments, and bars show mean ± SEM. Statistical analyses in (D) and (F) were performed using an unpaired Student's *t* test (**$P < 0.01$; NS, not significant), and, in (B), (C), and (E), using a one-sample *t* test (*$P < 0.05$; **$P < 0.01$).

effect on MAVS-mediated IRF3 phosphorylation and IFN-β induction in HeLa S3 cells (Fig. 4, E and F). These results indicated that TOMM40, which associated preferentially with MAVS 4A rather than MAVS WT, selectively promoted MAVS-mediated caspase activation.

We searched for a potential mediator of the effect of MAVS carboxylation on type I IFN induction. Our proteomics analysis revealed that Polo-like kinase 1 (PLK1), known to inhibit MAVS-mediated IRF3 activation (*27*), was also preferentially associated with the 4A mutant of MAVS compared with the WT protein (Fig. 4A). We confirmed the specificity of the interaction by coimmunoprecipitation (Fig. 4B). We concluded that carboxylation site–dependent effectors of MAVS, such as TOMM40 and PLK1, may mediate its carboxylation-dependent functional switch.

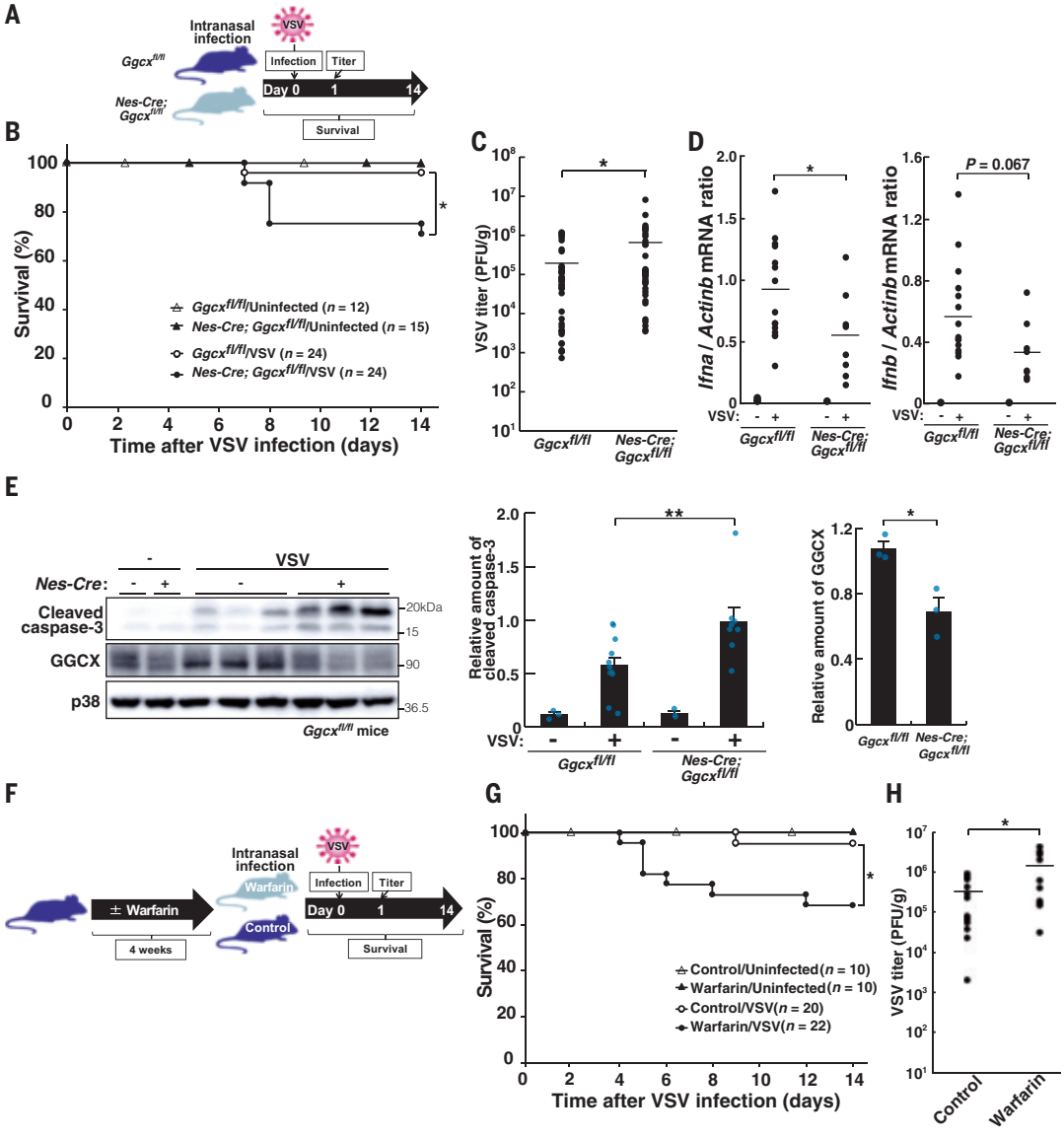

Fig. 5. VK-dependent GGCX activity protects against viral infection in vivo. (**A** to **C**) Age- and sex-matched mice with neural cell lineage–specific ablation of GGCX (*Nes-Cre;Ggcx*$^{fl/fl}$) and control (*Ggcx*$^{fl/fl}$) mice were infected intranasally with VSV (1×10^7 PFU) (A) and monitored daily for survival for 14 days (B). The viral titer in the brain (PFU per gram wet weight) was also determined by standard plaque assay at 1 day after VSV infection (5×10^6 PFU) (C). (**D**) RT-qPCR analysis of *Ifna1*, *Ifnb1*, and *Actb* mRNAs in the brain of *Nes-Cre;Ggcx*$^{fl/fl}$ and *Ggcx*$^{fl/fl}$ mice at 1 day after VSV infection (5×10^6 PFU). Results for three control mice and GGCX-deficient mice not infected with VSV are also shown. (**E**) Olfactory bulbs of mice at 3 days after VSV infection were analyzed by immunoblot using antibodies against cleaved caspase-3, GGCX, and p38 MAPK. A representative blot with each lane corresponding to one mouse as well as quantitative data for the band intensity are shown. Note that the incomplete reduction of GGCX levels in Nestin-Cre–KO mice is likely due to the remaining expression of GGCX in Nestin-negative cell populations. (**F** to **H**) Age- and sex-matched WT mice were treated with warfarin (0.96 mg/l) or vehicle (ethanol) in drinking water for 4 weeks then infected intranasally with VSV (1×10^7 PFU) (F). Mice were monitored daily for survival for 14 days (G). The viral titer in the brain was also determined at 1 day after VSV infection (5×10^6 PFU) (H). Data in (B) are shown for the indicated numbers of animals pooled together from five independent experiments, data in (C) are for 36 *Nes-Cre;Ggcx*$^{fl/fl}$ and 35 *Ggcx*$^{fl/fl}$ mice from eight independent experiments, and data in (D) are for 8 and 15 mice, respectively, from three independent experiments. Data in (E) are shown for 8 and 12 mice for caspase-3 quantification and 3 mice for GGCX quantification from three independent experiments. Data in (G) are shown for the indicated numbers of animals pooled together from two independent experiments, and data in (H) are for 13 mice per group from three independent experiments. Individual data points represent data from a single animal; bars in (C), (D), and (H) indicate the mean; and the bars in (E) represent mean SEM. Statistical analyses in (C), (D), (E), and (H) were performed using an unpaired Student's *t* test (*$P < 0.05$; **$P < 0.01$), and, in (B) and (G), using a log-rank test (*$P < 0.05$).

GGCX and VK protect against viral infection in vivo

Given the relatively high level of GGCX activity in the brain (*28*), we investigated its role in defense against intranasal VSV infection of mouse brain (*29*). Tissue immune responses often involve resident cells as well as infiltrating immune cells, such as myeloid cells. To assess the role of GGCX in these distinct cell populations, we selectively deleted *Ggcx* in neural and myeloid cells using the mouse Nestin gene (*Nes*) or LysM gene (*Lyz2*) promoters, respectively, to drive the expression of Cre recombinase in mice homozygous for a floxed allele of *Ggcx* (*Ggcx*$^{fl/fl}$ mice). Ablation of GGCX in neural or myeloid cells of these mice did not appear to affect the overall development or survival rate of mice in the absence of infection (Fig. 5, A and B, and fig. S22, A and B). However, loss of GGCX in neural but not myeloid cells attenuated mouse survival after intranasal VSV infection (Fig. 5, A and B, and fig. S22, A and B). Deletion of *Ggcx* in neural but not myeloid cells increased the titer of VSV in brain homogenates, which reflect overall immune responses in the brain (Fig. 5C and fig. S22C). Moreover, the extent of VSV-induced expression of IFN-α and IFN-β genes in the brain was lower in mice lacking GGCX in neural cells than in control animals (Fig. 5D). The extent of VSV-induced caspase-3 cleavage in the brain was increased by ablation of GGCX in neural cells (Fig. 5E).

We concluded that GGCX in neural cells protects the central nervous system against viral infection and skews antiviral responses away from apoptosis and toward type I IFN induction in vivo.

Because the activity of GGCX is dependent on VK, we examined how modulating VK availability in mice impacted antiviral responses. We fed a cohort of WT mice a VK-free diet for 4 weeks and administered the antibiotic cefotiam hydrochloride to both VK-free and control diets to deplete VK-producing bacteria in the gut. The bodyweight of mice fed the VK-free diet did not differ from that of mice fed the control diet (fig. S23, A and B). However, the VK-free diet exacerbated loss of bodyweight and increased the viral titer in the brain after intranasal VSV infection (fig. S23, C and D). We examined whether warfarin treatment, which suppressed VK-dependent protein carboxylation, attenuated antiviral defense in vivo. WT mice were treated with warfarin or vehicle for 4 weeks then infected intranasally with VSV (Fig. 5F). Although warfarin treatment alone did not affect mouse survival, it decreased the survival rate after VSV infection (Fig. 5G). Furthermore, the viral titer in brain homogenates was higher for warfarin-treated mice than control mice (Fig. 5H). A warfarin-induced increase in susceptibility to VSV infection was not evident in MAVS-KO mice under conditions in which warfarin effectively inhibited coagulation (fig. S24, A to C). These results indicated that loss of VK ability impairs immune responses in the brains of mice in part through modulation of MAVS.

Discussion

We identified the existence of cytoplasmic protein carboxylation and its relevance to antiviral defense, demonstrating topology inversion of GGCX as a mechanism enabling this modification. Although a few cases of topology inversion of transmembrane proteins have been reported in mammalian cells (*30*, *31*), none have been shown to transition from type II to type III in a signal-dependent manner. Our findings suggested that the RLR-MAVS-ASK1-MKK6-p38 axis may play a role in this process, although the substrates of p38 required for this inversion remain unknown.

Furthermore, given that p38 MAPK signaling is activated not only by cytoplasmic viral RNA but also by various cellular stresses, including cytoplasmic viral DNA (*32*, *33*), cytoplasmic protein carboxylation through topologically inverted GGCX may occur in response to infection by a wide range of viruses. Moreover, carboxylation of cytoplasmic proteins other than MAVS may be induced by GGCX topology inversion and modulate cellular functions in response to viral infection or other cellular stresses.

Carboxylation of MAVS by GGCX functions to switch MAVS activity from apoptosis induction to type I IFN induction by altering its binding partners. Although the precise mechanism remains unclear, carboxylation may affect the structure or association partners of MAVS, leading to alterations in its functions or subcellular localization.

REFERENCES AND NOTES

1. D. B. Stetson, R. Medzhitov, *Immunity* **25**, 373–381 (2006).
2. R. J. Clem, L. K. Miller, *J. Virol.* **67**, 3730–3738 (1993).
3. J. Tschopp, M. Thome, K. Hofmann, E. Meinl, *Curr. Opin. Genet. Dev.* **8**, 82–87 (1998).
4. S. Chattopadhyay, T. Kuzmanovic, Y. Zhang, J. L. Wetzel, G. C. Sen, *Immunity* **44**, 1151–1161 (2016).
5. M. Yoneyama *et al.*, *Nat. Immunol.* **5**, 730–737 (2004).
6. L. Gitlin *et al.*, *Proc. Natl. Acad. Sci. U.S.A.* **103**, 8459–8464 (2006).
7. T. Kawai *et al.*, *Nat. Immunol.* **6**, 981–988 (2005).
8. R. B. Seth, L. Sun, C. K. Ea, Z. J. Chen, *Cell* **122**, 669–682 (2005).
9. E. Meylan *et al.*, *Nature* **437**, 1167–1172 (2005).
10. L. G. Xu *et al.*, *Mol. Cell* **19**, 727–740 (2005).
11. J. Rintahaka, D. Wiik, P. E. Kovanen, H. Alenius, S. Matikainen, *J. Immunol.* **180**, 1749–1757 (2008).
12. R. Besch *et al.*, *J. Clin. Invest.* **119**, 2399–2411 (2009).
13. B. Furie, B. A. Bouchard, B. C. Furie, *Blood* **93**, 1798–1808 (1999).
14. S. E. Hamilton, D. Tesch, B. Zerner, *Biochem. Biophys. Res. Commun.* **107**, 246–249 (1982).
15. J. J. McTigue, M. K. Dhaon, D. H. Rich, J. W. Suttie, *J. Biol. Chem.* **259**, 4272–4278 (1984).
16. A. Zhu *et al.*, *Blood* **109**, 5270–5275 (2007).
17. M. Ferron, J. Lacombe, A. Germain, F. Oury, G. Karsenty, *J. Cell Biol.* **208**, 761–776 (2015).
18. K. Azuma *et al.*, *PLOS ONE* **9**, e88643 (2014).
19. K. L. Berkner, *Annu. Rev. Nutr.* **25**, 127–149 (2005).
20. R. S. Hegde, R. J. Keenan, *Nat. Rev. Mol. Cell Biol.* **23**, 107–124 (2022).
21. M. L. Wohlever, A. Mateja, P. T. McGilvray, K. J. Day, R. J. Keenan, *Mol. Cell* **67**, 194–202.e6 (2017).
22. P. J. Chitwood, S. Juszkiewicz, A. Guna, S. Shao, R. S. Hegde, *Cell* **175**, 1507-1519.e1516 (2018).
23. S. Matsumoto *et al.*, *Mol. Cell* **76**, 191–205.e10 (2019).
24. M. J. McKenna *et al.*, *Science* **369**, eabc5809 (2020).
25. J. K. Tie, M. Y. Zheng, R. M. Pope, D. L. Straight, D. W. Stafford, *Biochemistry* **45**, 14755–14763 (2006).
26. T. Okazaki *et al.*, *Sci. Signal.* **8**, ra78 (2015).
27. D. Vitour *et al.*, *J. Biol. Chem.* **284**, 21797–21809 (2009).
28. E. E. Romero, L. J. Velazquez-Estades, R. Deo, B. Schapiro, D. A. Roth, *Exp. Cell Res.* **243**, 334–346 (1998).
29. U. Kalinke, I. Bechmann, C. N. Detje, *Virulence* **2**, 367–370 (2011).
30. Q. Chen *et al.*, *Mol. Cell* **63**, 567–578 (2016).
31. B. Denard, S. Han, J. Kim, E. M. Ross, J. Ye, *eLife* **8**, e40234 (2019).
32. K. R. Balka, D. De Nardo, *FEBS J.* **288**, 5504–5529 (2021).
33. T. Abe, G. N. Barber, *J. Virol.* **88**, 5328–5341 (2014).

ACKNOWLEDGMENTS

We thank S. Fujiyama, A. Yokoyama, K. Nishino, A. Abe, F. Yamamoto, and N. Kato for technical assistance; T. Mizuno, H. Kusuhara, and members of the Gotoh laboratory for discussion; T. Taniguchi for providing VSV; and T. Taniguchi, J. A. Cooper, and C. Yokoyama for comments on the manuscript. We also acknowledge the use of ChatGPT-4o (OpenAI) to assist with suggesting improvements to the text for conciseness and clarity. **Funding:** Ministry of Education, Culture, Sports, Science, and Technology of Japan (MEXT) JP16K19149 (T.O.); MEXT JP18K07168 (T.O.); MEXT JP21K07064 (T.O.); MEXT JP24K02172 (T.O.); MEXT JP24K22007 (T.O.); MEXT JP15H05773 (Y.G.); MEXT JP16H06481 (Y.G.); MEXT JP16H06479 (Y.G.); MEXT JP16H06279 (Y.G.); MEXT JP22H00431 (Y.G.); MEXT JP22H04925(PAGS) (Y.G.); MEXT JP24H02322 (Y.G.); MEXT JP18 g0610013 (Y.G.); MEXT JP24 g1310004 (Y.G.); MEXT JP24H02299 (H.Y.); MEXT JP24H02302 (H.Y.); JSPS KAKENHI JP22H04926 (M.Y.); FOREST program of the Japan Science and Technology Agency JPMJFR204Q (T.O.); FOREST program of the Japan Science and Technology Agency JPMJFR2150 (H.Y.); Takano Life Science Research Foundation (T.O.); Chemo-Sero-Therapeutic Research Institute (T.O.); Mitsubishi Foundation (T.O.); Naito Foundation (T.O.); Secom Foundation (T.O.); Astellas Foundation for Research on Metabolic Disorders (T.O.); Promotion Project for Young Investigators in Hokkaido University (T.O.); Nagase Science and Technology Foundation (Y.G.). **Author contributions:** Conceptualization: T.O., Y.G.; Methodology: T.O., T.H., T.N., S.-i.I., S.I., H.Ko., M.Y., TK., Ha.K.; Investigation: T.O., K.N., M.O., N.M., Y.O., R.S., S.A., H.Y.; Visualization: T.O., K.N.; Funding acquisition: T.O., H.Y., Y.G.; Project administration: T.O., Y.G.; Supervision: T.O., Y.G.; Writing – original draft: T.O., Y.G.; Writing – review & editing: T.O., K.N., R.S., Y.G. **Competing interests:** The authors declare that they have no competing interests. **Data and materials availability:** All data needed to evaluate the manuscript are available in the main text or supplementary materials. MS raw files and identifications were deposited at the ProteomeXChange JPOST database with the following dataset identifiers: JPST003494 (PXD058403), proteomic identification of proteins associated with the MAVS carboxylation site; JPST003495 (PXD058405), proteomic identification of PTMs in MAVS (residues 1 to 200) (this dataset corresponds to fig. S1); JPST003699 (PXD061814), proteomic identification of PTMs in MAVS (residues 1 to 200) (this dataset corresponds to fig. S2).

SUPPLEMENTARY MATERIALS

science.org/doi/10.1126/science.adk9967
Materials and Methods; Figs. S1 to S67; References (*34*–*52*); MDAR Reproducibility Checklist; Data S1

Submitted 22 September 2023; resubmitted 3 December 2024; accepted 2 May 2025
10.1126/science.adk9967

QUANTUM INFORMATION

Random unitaries in extremely low depth

Thomas Schuster[1,2,3]*, Jonas Haferkamp[4,5]*, Hsin-Yuan Huang[3,2,6]*

Random unitaries are central to quantum technologies and the study of complex quantum many-body physics. However, existing protocols for generating random unitaries require long evolution times and deep circuits. In this work, we prove that local quantum circuits can form random unitaries in extremely low depth on any geometry. These shallow circuits have low complexity and create only short-range correlations, yet are indistinguishable from random unitaries with exponential complexity. This finding contrasts sharply with classical systems, in which a long evolution time is required to appear random. Our results have widespread applications across quantum science, from device benchmarking to quantum advantages. Moreover, they reveal that fundamental physical properties—including evolution time, causal structure, and phases of matter—are provably hard to learn.

Random processes are fundamental to both technology (*1*–*5*) and our understanding of nature (*6*–*8*). In quantum systems, the analog of a random process is a Haar-random unitary operation. Random unitaries form the backbone of numerous components of quantum technologies, including quantum device benchmarking (*9*–*11*), efficient measurement protocols (*12*–*14*), quantum advantage demonstrations (*15*–*18*), and quantum cryptography (*19*–*21*). They also serve as essential models for understanding quantum chaos (*22*–*24*), quantum machine learning (*25*–*27*), and quantum gravity (*28*, *29*).

A central open question concerns the minimal time, or circuit depth, needed for a local quantum circuit to behave like a Haar-random unitary. This determines both the resources required to implement such unitaries on a quantum device and their relevance as models of physical systems. Although a true Haar-random unitary requires exponential time to generate, two important approximations have emerged: approximate unitary k-designs (*30*–*33*), which mimic a Haar-random unitary U in any experiments using U up to k times, and pseudorandom unitaries (*19*, *34*, *35*), which mimic a Haar-random unitary in any efficient quantum experiments (Fig. 1). Enormous effort has gone into constructing these random unitaries in as low a depth as possible (*19*, *34*–*45*). Despite extensive research, all known constructions require circuit depths that grow polynomially with the qubit count n.

In this work, we show that local quantum circuits can form random unitaries in exponentially lower depths on any circuit geometry, including a one-dimensional (1D) line. Our construction glues together small random unitaries on local patches of $\log n$ or $\mathrm{poly}(\log n)$ qubits to create approximate designs or pseudorandom unitaries on n qubits (Fig. 2). By instantiating the small random unitaries with existing constructions (*34*, *35*, *43*, *45*), we achieve three main results: approximate unitary designs in $\log n$ depth on any circuit geometry, and pseudorandom unitaries in $\mathrm{poly}(\log n)$ depth on any geometry, and $\mathrm{poly}(\log\log n)$ depth in all-to-all-connected circuits. In all three cases, we prove that our achieved scaling in the system size n is optimal.

Our results reveal a sharp contrast with classical systems, in which a time/depth linear in the system size n is necessary to mimic truly random classical dynamics. The fact that quantum dynamics can become indistinguishable from random in exponentially shorter time than classical dynamics is surprising in many regards. Indeed, several extremely basic properties of physical systems, such as their causal structure and entanglement entropy, require at least linear depth to approach their truly random behaviors. If these properties were efficiently observable, they could be used to distinguish our constructed short-time random unitaries from exponential-time Haar-random unitaries. The resolution to this seeming contradiction is that our results prove that these basic physical properties are in fact not efficiently observable in any quantum experiment that can access the unitary U many times (*46*).

These discoveries have wide-ranging implications across quantum science. In classical shadow tomography (*12*, *47*–*49*), our approximate unitary designs enable estimation of highly nonlocal observables using log-depth instead of linear-depth circuits. This substantially reduces the experimental resources needed for classical shadows, making near-term implementations feasible for larger qubit counts. In many-body physics, our pseudorandom construction rigorously establishes that identifying topological order (*50*) is super-polynomially hard for any quantum experiment. Additional applications include quantum advantages for learning low-complexity dynamics and improved hardness results for random circuit sampling (*15*).

Low-depth random unitary designs

We now introduce our random circuit construction (Fig. 2) and present our main results. For simplicity, we begin with the simplest possible circuit geometry: a 1D line. We organize the n qubits of the 1D line into m local patches of $\xi = n/m$ qubits each. Our random unitary ensemble $\mathcal{E}$ corresponds to a two-layer circuit, in which small random unitaries act on pairs of neighboring patches in a brickwork fashion between the two layers. When these small random unitaries have depth d in terms of two-qubit gates, our proposed construction has total circuit depth $2d$.

We first show how our construction yields low-depth unitary designs. An ensemble $\mathcal{E}$ forms an ε-approximate unitary k-design if it approximates the Haar ensemble H up to error ε in any quantum experiment querying U up to k times. The gold standard for quantifying this approximation (*38*) is

$$(1-\varepsilon)\ \Phi_H \ \leq\ \Phi_{\mathcal{E}} \ \leq\ (1+\varepsilon)\ \Phi_H \tag{1}$$

where $\Phi_{\mathcal{E}}(\cdot) = \mathbb{E}_{U\sim\mathcal{E}}\left[U^{\otimes k}\cdot U^{\dagger,\otimes k}\right]$, and similarly for Φ_H. Here, $\Phi \leq \Phi'$ denotes that $\Phi' - \Phi$ is completely positive. Physically, this inequality guarantees that the output state of any experiment involving U sampled from $\mathcal{E}$ up to k times is 2ε-close in trace distance to the output state when U is sampled from the Haar ensemble H.

Let us assume that each small random unitary in the two-layer brickwork ensemble $\mathcal{E}$ is drawn independently from an ε/n-approximate unitary k-design on 2ξ qubits. Our main result shows that the resulting ensemble $\mathcal{E}$ forms an ε-approximate unitary k-design whenever the number ξ of qubits in each local patch is at least logarithmic in n, k, and ε^{-1}.

Theorem 1 (Gluing small random unitary designs) For any approximation error $\varepsilon \leq 1$, suppose each small random unitary in the two-layer brickwork ensemble $\mathcal{E}$ is drawn from an ε/n-approximate unitary k-design on 2ξ qubits with circuit depth d. Then $\mathcal{E}$ forms an ε-approximate unitary k-design on n qubits with depth $2d$, whenever the local patch size satisfies $\xi \geq \log_2\left(nk^2/\varepsilon\right)$.

[1]Walter Burke Institute for Theoretical Physics, California Institute of Technology, Pasadena, CA, USA. [2]Institute for Quantum Information and Matter, California Institute of Technology, Pasadena, CA, USA. [3]Google Quantum AI, Los Angeles, CA, USA. [4]Harvard John A. Paulson School Of Engineering And Applied Sciences, Cambridge, MA, USA. [5]Department of Mathematics, Saarland University, Saarbruecken, Germany. [6]Center for Theoretical Physics, Massachusetts Institute of Technology, Cambridge, MA, USA. ***Corresponding author. Email: schuster@caltech.edu (T.S.); jhaferkamp42@gmail.com (J.H.); hsinyuan@caltech.edu (H.-Y.H.)**

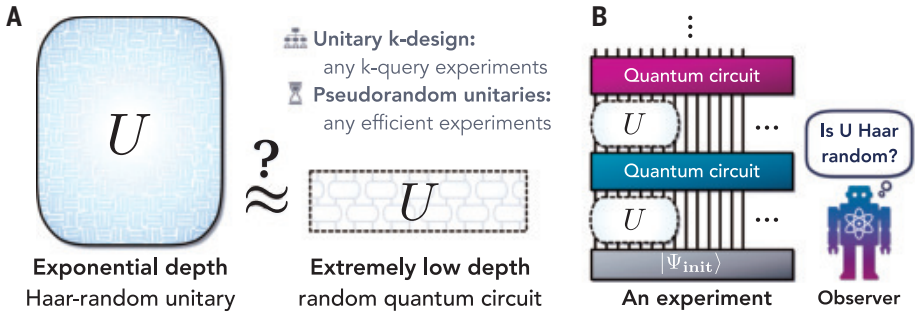

Fig. 1. Random unitaries and quantum experiments. The central question we seek to answer is: How shallow can a quantum circuit be while replicating the behavior of a Haar-random unitary? (**A**) A Haar-random unitary over n qubits requires a circuit depth that grows exponentially in n. Approximate unitary k-designs replicate the behavior of Haar-random unitaries within any quantum experiment that queries the unitary k times. Pseudorandom unitaries replicate the behavior of Haar-random unitaries within any efficient quantum experiment. (**B**) Any quantum experiment can be represented as follows: An observer prepares an initial state $|\Psi_{\text{init}}\rangle$, applies the unitary U many times, interleaved with many quantum circuits for quantum information processing, and concludes by performing a measurement (not shown).

The main ideas and technical lemmas behind the theorem are described in the materials and methods (*51*). Proof details are provided in the supplementary text section 3.3.

By using existing constructions of random unitary designs for the small random unitaries, Theorem 1 immediately yields designs in very low depth.

Corollary 1 (Low-depth random unitary designs) Random quantum circuits over n qubits can form ε-approximate unitary k-designs in circuit depth: $d = \mathcal{O}(\log(n/\varepsilon)\cdot k\,\mathrm{poly}(\log k))$, for 1D circuits without ancilla qubits and $k \le \Theta\left(2^{2n/5}\right)$, and $d = \mathcal{O}(\log\log(n/\varepsilon))$, for all-to-all circuits with $\mathcal{O}(n\log(n/\varepsilon))$ ancilla qubits and $k \le 3$.

For general k, we take each small unitary to be a 1D local random circuit on 2ξ qubits, which forms an ε/n-approximate k-design in depth $d = \mathcal{O}((k\xi + \log(n/\varepsilon))\,\mathrm{poly}(\log k))$ for $k \le \Theta\left(2^{2(2\xi)/5}\right)$ (*45*, *52*). For $k \le 3$, we use random Clifford unitaries (*53*), implementable in depth $d = \mathcal{O}(\log\xi)$ using ancilla qubits and nonlocal two-qubit gates (*54*). In both cases, our result exponentially improves the system size n dependence over all known constructions.

Finally, we prove that the system size n dependence of our approximate unitary designs is optimal for both 1D circuits and general all-to-all circuit architectures.

Proposition 1 (Depth lower bound for unitary designs) Consider any $k \ge 2$. A quantum circuit ensemble over n qubits that forms an approximate unitary k-design requires circuit depth: $d = \Omega(\log n)$, for 1D circuits with any number of ancilla qubits, and $d = \Omega(\log\log n)$, for all-to-all circuits with any number of ancilla qubits.

The proposition follows by analyzing the output distribution when a state $U|0^n\rangle$ is measured in a random product basis. When U is too shallow, the output distribution features large fluctuations in its low-weight marginals that differ from those of a Haar-random unitary (*51*). A lower bound proving the optimality of our ε dependence is in the supplementary text section 3.6.

Low-depth pseudorandom unitaries

We now show how our construction (Fig. 2) also yields low-depth pseudorandom unitaries (PRUs). PRUs are random unitary ensembles that are indistinguishable from the Haar ensemble by any efficient quantum algorithm that can query U many times (*19*, *42*, *43*). Specifically, an n-qubit PRU is secure against a $t(n)$-time adversary if it is indistinguishable from a Haar unitary by any $t(n)$-time quantum algorithm. An introduction to PRUs is in supplementary text section 4.

Although several PRU constructions have been proposed (*19*, *34*, *35*, *42*, *43*), all known constructions require circuit depth poly(n). To construct PRUs in exponentially lower depths, we draw each small random unitary in our two-layer brickwork ensemble $\mathcal{E}$ from a PRU ensemble on 2ξ qubits, setting $\xi = \omega(\log n)$. We assume that each small unitary is secure against poly(n)-time quantum adversaries. Because $\xi = \omega(\log n)$, a poly(n)-time adversary is an $\exp(o(\xi))$-time adversary, which is automatically satisfied by using any PRU ensemble with subexponential security (*34*). Our main finding is that the resulting ensemble $\mathcal{E}$ forms an n-qubit PRU (*51*).

Theorem 2 (Gluing small pseudorandom unitaries) Suppose each small random unitary in the two-layer brickwork ensemble $\mathcal{E}$ is a 2ξ-qubit pseudorandom unitary secure against poly(n)-time adversaries for $\xi = \omega(\log n)$. Then $\mathcal{E}$ forms an n-qubit pseudorandom unitary secure against poly(n)-time adversaries.

Using existing PRU constructions (*34*, *35*, *43*) to instantiate each small random unitary, which rely on the widely accepted conjecture regarding the quantum hardness of learning with errors (LWE) (*55*), we obtain n-qubit pseudorandom unitaries in the following low circuit depths.

Corollary 2 (Low-depth pseudorandom unitaries) Under the conjecture that no subexponential-time quantum algorithm can solve LWE, random quantum circuits over n qubits can form pseudorandom unitaries secure against any polynomial-time quantum adversary in circuit depth: $d = \mathrm{poly}(\log n)$, for 1D circuits, and $d = \mathrm{poly}(\log\log n)$, for all-to-all circuits.

Our depth improves exponentially over all known proposals (*19*, *34*, *35*, *42*, *43*), which require poly(n) depth for 1D circuits and poly(log n) depth for all-to-all circuits. Moreover, our scaling is optimal: Recent work shows that any 1D circuit of depth $\mathcal{O}(\log n)$ and any general circuit of depth $\mathcal{O}(\log\log n)$ can be learned in polynomial time (*56*), implying that 1D circuits require $\omega(\log n)$ depth and general circuits require $\omega(\log\log n)$ depth to form PRUs. These shallow quantum circuits have extremely low complexity and generate only short-range entanglement, yet they are indistinguishable from unitaries with exponential complexity. This result shows that the evolution time of a quantum system is not physically observable, even when considering the two extremes of poly(log n) and exp(n) time scales.

Comparison between quantum and classical circuits

It is instructive to contrast our results with random classical circuits. A simple light-cone argument (Fig. 3) shows that it easy to distinguish short-time from long-time classical dynamics, and hence classical circuits require depth $d = \Omega(n)$ in 1D and $d = \Omega(\log n)$ in all-to-all geometries to be indistinguishable from exponentially complex truly random dynamics. By contrast, quantum dynamics become indistinguishable from truly random dynamics in exponentially shorter time.

This exponential reduction is made possible by a fundamental feature of quantum mechanics: the abundance of noncommuting observables. To distinguish any circuit (classical or quantum) from a truly random one, an observer must eventually measure the system in some chosen basis. Noncommuting observables allow quantum circuits to locally hide information in observables unlikely to commute with any fixed basis. This causes measurement outcomes to be nearly independent of the random unitary's details, enabling it to appear exponentially complex at very low depths. We formalize this intuition in our

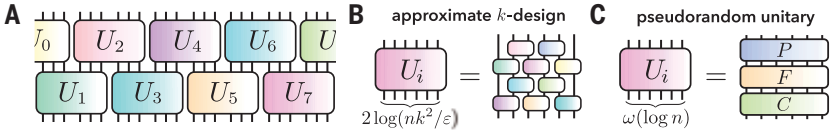

Fig. 2. Low-depth random unitary construction. (**A**) We consider a two-layer brickwork circuit, in which each small unitary acts on 2ξ qubits in each layer. (**B**) To generate ε-approximate unitary k-designs in $\log n$ depth, we draw each small unitary from an approximate unitary k-design on $2\xi = 2\log_2(nk^2/\varepsilon)$ qubits. (**C**) To generate pseudorandom unitaries in $\text{poly}(\log n)$ depth, we draw each small unitary from a pseudorandom unitary ensemble, such as the *PFC* ensemble (*34*,*35*,*43*), on $2\xi = \omega(\log n)$ qubits.

proof of the lower bound on unitary designs in the materials and methods (*51*).

Creating random unitaries on any geometry

We provide two methods to extend our construction from 1D circuits to any circuit geometry. Our first method shows that any depth-d quantum circuit on a 1D line can be implemented on any geometry in depth $\mathcal{O}(d)$. The key is to efficiently construct a path on the geometry that visits every qubit exactly once. Although such paths do not always exist and are generally hard to find, we prove that allowing jumps to constant-distance neighbors guarantees the existence of an efficiently constructible path (Fig. 3B). Two-qubit gates between constant-distance neighbors can then be implemented using a carefully designed swap network. Our second method extends Theorem 1 directly to general two-layer brickwork circuits. This enables gluing together small random unitaries on various geometries of interest, such as a 2D circuit consisting of overlapping squares (fig. S1C). Both methods apply to both our constructions of low-depth unitary designs and low-depth PRUs. Details are in supplementary text section 5.

Applications

We now present key applications of our results (Fig. 4), with full details in supplementary text section 6.

Provably efficient shallow classical shadows

Classical shadows use random measurements to estimate many non-commuting observables (*12*). Standard shadow protocols require random Clifford unitaries, with linear circuit depth. We prove these can be replaced by $\log n$-depth Clifford circuits from our construction while maintaining the same sample complexity guarantees, confirming conjectures in (*47*, *48*). A key motivation for these shallow shadow protocols is to address experimental limitations on circuit depths due to noise in quantum devices. Given any linear-depth circuit compilation of random Clifford circuits, our construction can achieve a provable 2 to 3 times reduction in circuit depth for $n = 100$ qubits and a 100 times depth reduction for $n = 6000$ qubits.

Quantum hardness of recognizing topological order

The detection of topologically ordered phases of matter has remained a notoriously difficult challenge across both materials and atomic, molecular, and optical experiments (*50*, *57*, *58*). A defining feature of topological order is its invariance under low-depth local unitary circuits (*50*). Using Corollary 2, we prove:

Corollary 3 (Hardness of recognizing topological order) For any definition of topological order where (i) the product state has trivial order and the toric code state has nontrivial order, and (ii) this order is preserved under any depth-ℓ geometrically local circuit, recognizing topological order is quantum computationally hard for any $\ell = \Omega(\text{polylog } n)$.

The criteria in the corollary apply to nearly all existing definitions of topological order (*59*).

Quantum advantage for learning low-complexity quantum systems

Several well-known quantum learning advantages (*60*–*63*) have so far applied only to highly complex systems. For instance, distinguishing a random unitary from a depolarizing channel requires superpolynomial time for classical observers but is easy for quantum observers (*62*, *63*). Until now, this advantage was only known for Haar-random unitaries, which require $\exp(\mathcal{O}(n))$ time to generate and are thus poor models for physical processes. Our results show that this superpolynomial advantage holds for dynamics of double-exponentially shorter time, $\text{poly}(\log n)$. We also establish similar quantum-classical separations for learning entanglement structure in short-range entangled states.

The power of time-reversal for learning causal structures

Leveraging interaction engineering techniques, some modern quantum experiments have the ability to time-reverse their dynamics (*64*–*66*). A surprising consequence of our results is that such experiments can learn properties of quantum dynamics exponentially more efficiently than standard experiments lacking time reversal (*67*, *68*). This advantage is particularly pronounced for uncovering the causal structure of the dynamics. For example, our results show that detecting whether a shallow circuit contains only local interactions versus a mix of local and long-range couplings is hard without time reversal, but becomes easy with it; see supplementary text section 6.4. This separation is fundamentally quantum mechanical, following light-cone arguments similar to those in Fig. 3A.

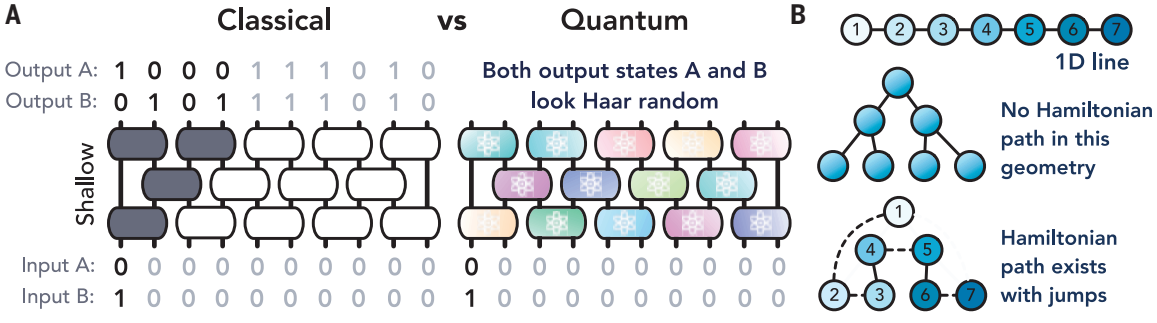

Fig. 3. Comparison with classical circuits, and extension to any circuit geometry. (**A**) Shallow random classical circuits cannot look uniformly random. By contrast, our results show that shallow random quantum circuits can already look Haar-random. (**B**) To create random unitaries on any circuit geometry, we implement a 1D random circuit along a Hamiltonian path of the geometry. Although Hamiltonian paths do not exist in any geometry, when jumping to constant-distance neighbor is allowed, they always exist and are efficient to construct.

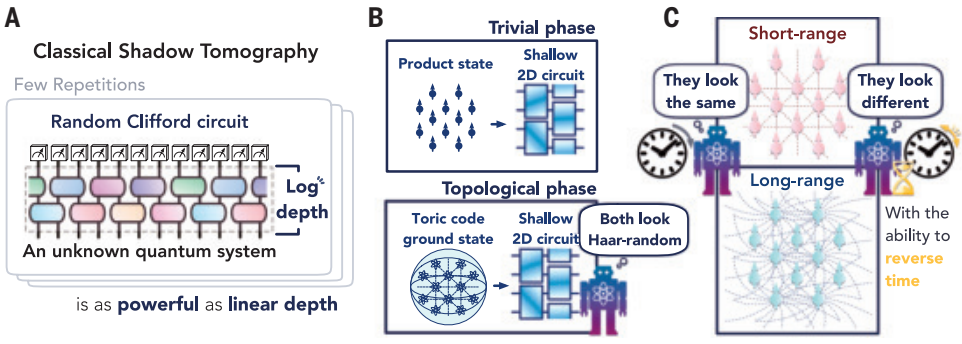

Fig. 4. Applications of low-depth random unitaries. (**A**) Log-depth classical shadows: Our shallow unitary 3-designs enable provably efficient classical shadow tomography using log(n)-depth random Clifford circuits instead of linear depth. (**B**) Quantum hardness of recognizing topological order: By applying our shallow pseudorandom unitaries to product and toric code states, we generate pseudorandom states with trivial and topological order, respectively. This demonstrates that recognizing topological order in an unknown state is quantumly hard. (**C**) Power of time-reversal in learning: We establish that quantum experiments capable of reversing time evolution can exhibit superpolynomial advantages over conventional experiments. We prove this in a simple example where one wishes to detect whether long-range couplings are present in a strongly interacting dynamical quantum system.

Output distributions of random quantum circuits

Random circuit sampling (RCS) is a leading candidate for quantum computational advantage (*15*). Proofs of its hardness require both worst-case hardness and anti-concentration (*16*, *17*)—requirements previously met only in 2D circuits of depth $\Omega(\sqrt{n})$ (*40*). Our approximate unitary 2-designs achieve both properties in depth $\log n$. Furthermore, using higher-k designs, we prove that at depth $\Omega(\log n)$, the output distributions of random circuits are far from uniform with probability close to one, and at depth $\mathrm{poly}(\log n)$, they become computationally indistinguishable from uniform while remaining far from it.

Barren plateaus in variational quantum algorithms

Variational quantum algorithms represent a promising approach for quantum computing applications (*27*). However, these algorithms encounter optimization challenges known as barren plateaus, which arise when the parameterized quantum circuits approach unitary 2-designs under random initialization, leading to vanishingly small loss function variances (*25*). As an ε-approximate unitary 2-design yields a loss function variance of $\mathcal{O}\left(\varepsilon+\frac{1}{2^n}\right)$, our results imply that barren plateaus with loss function variance ϵ emerge at circuit depths of only $\mathcal{O}(\log(n/\epsilon))$ for both local and global observables. This scaling reveals that circuits with depth slightly higher than logarithmic, e.g., $d=\Omega\left(\log(n)^2\right)$, inevitably produce barren plateaus with variance smaller than any $1/\mathrm{poly}(n)$, creating insurmountable optimization barriers even for shallow quantum circuits with local cost functions (*69*). These results underscore the need for structured, problem-specific ansätze for practical applications.

Discussion

We have shown that random unitaries can be naturally generated in extremely low circuit depths. Our results reveal a surprising and profound property of quantum circuits that differs fundamentally from those of classical systems. Our construction of random unitaries is both exceptionally simple and highly versatile, offering benefits from both experimental and theoretical perspectives.

These discoveries open numerous avenues for future research. The applications that we have explored likely represent only a fraction of the potential impact, given that random unitaries are ubiquitous tools in quantum technology and in understanding complex quantum processes. In quantum benchmarking, efficient learning using random unitaries extends to fermionic, bosonic, and Hamiltonian systems (*13*, *24*, *70*–*72*). Can one show that the formation of random unitaries in extremely short times applies to these systems as well? In quantum gravity, a widespread conjecture states that black holes are the fastest scramblers in nature (*28*). If we consider scrambling to be the formation of random unitary designs, could our discovery of surprisingly fast design formation on any geometry provide new insight into quantum black holes and the holographic correspondence (*73*, *74*)?

Perhaps most intriguingly, the ability to generate random unitaries in extremely low depth reveals fundamental limits on what is physically observable. Our results show that several fundamental physical properties—evolution time, phases of matter, and causal structure—are provably hard to learn through conventional quantum experiments. This raises profound questions about the nature of physical observation itself: What other fundamental physical properties might be intrinsically hard to measure? What are the implications of these properties being imperceptible? Should physical theories contain quantities that are fundamentally hard to see, or does this suggest a deeper principle about the nature of physical reality?

REFERENCES AND NOTES

1. M. Blum, S. Micali, *SIAM J. Comput.* **13**, 850–864 (1984).
2. L. Blum, M. Blum, M. Shub, *SIAM J. Comput.* **15**, 364–383 (1986).
3. Reuven Y Rubinstein and Dirk P Kroese, *Simulation and the Monte Carlo method* (John Wiley & Sons, 2016).
4. M. Santha, U. V. Vazirani, *J. Comput. Syst. Sci.* **33**, 75–87 (1986).
5. J. Håstad, R. Impagliazzo, L. A. LevinM. Luby, *SIAM J. Comput.* **28**, 1364–1396 (1999).
6. A. Einstein, *Ann. Phys.* **322**, 549–560 (1905).
7. J. S. Linda, *Allen. An Introduction to Stochastic Processes with Applications to Biology* (CRC Press, 2010).
8. E. P. Wigner, *SIAM Rev.* **9**, 1–23 (1967).
9. J. Emerson, R. Alicki, K. Życzkowski, *J. Opt. B Quantum Semiclassical Opt.* **7**, S347–S352 (2005).
10. E. Knill *et al.*, *Phys. Rev. A* **77**, 012307 (2008).
11. A. Elben *et al.*, *Phys. Rev. Lett.* **125**, 200501 (2020).
12. H.-Y. Huang, R. Kueng, J. Preskill, *Nat. Phys.* **16**, 1050–1057 (2020).
13. A. Zhao, N. C. Rubin, A. Miyake, *Phys. Rev. Lett.* **127**, 110504 (2021).
14. A. Elben *et al.*, *Nat. Rev. Phys.* **5**, 9–24 (2023).
15. F. Arute *et al.*, *Nature* **574**, 505–510 (2019).
16. R. Movassagh, *Nat. Phys.* **19**, 1719–1724 (2023).
17. A. Bouland, B. Fefferman, C. Nirkhe, U. Vazirani, *Nat. Phys.* **15**, 159–163 (2019).
18. A. Morvan *et al.*, Phase transition in random circuit sampling. arXiv:2304.11119 [quant-ph] (2023).
19. Z. Ji, Y.-K. Liu, F. Song, Pseudorandom quantum states, in *Advances in Cryptology–CRYPTO 2018: 38th Annual International Cryptology Conference, Santa Barbara, CA, USA, August 19–23, 2018, Proceedings, Part III* (Springer, 2018), pp. 126–152.
20. P. Ananth, L. Qian, H. Yuen, Cryptography from pseudorandom quantum states, in *Annual International Cryptology Conference* (Springer, 2022), pp. 208–236.
21. W. Kretschmer, L. Qian, M. Sinha, A. Tal, Quantum cryptography in algorithmica" in *Proceedings of the 55th Annual ACM Symposium on Theory of Computing* (2023), pp. 1589–1602.
22. A. Nahum, J. Ruhman, S. Vijay, J. Haah, *Phys. Rev. X* **7**, 031016 (2017).
23. A. Nahum, S. Vijay, J. Haah, *Phys. Rev. X* **8**, 021014 (2018).
24. J. Choi *et al.*, *Nature* **613**, 468–473 (2023).
25. J. R. McClean, S. Boixo, V. N. Smelyanskiy, R. Babbush, H. Neven, *Nat. Commun.* **9**, 4812 (2018).
26. E. R. Anschuetz, B. T. Kiani, *Nat. Commun.* **13**, 7760 (2022).
27. M. Larocca *et al.*, arXiv:2405.00781 [quant-ph] (2024).
28. Y. Sekino,L. Susskind, *J. High Energy Phys.* **2008**, 065 (2008).
29. P. Hayden, J. Preskill, *J. High Energy Phys.* **2007**, 120 (2007).
30. J. Emerson, Y. S. Weinstein, M. Saraceno, S. Lloyd, D. G. Cory, *Science* **302**, 2098–2100 (2003).

31. D. Gross, K. Audenaert, J. Eisert, *J. Math. Phys.* **48**, 052104 (2007).
32. C. Dankert, arXiv:quant-ph/0512217 [quant-ph] (2005).
33. C. Dankert, R. Cleve, J. Emerson, E. Livine, *Phys. Rev. A* **80**, 012304 (2009).
34. F. Ma, H.-Y. Huang, arXiv:2410.10116 [quant-ph] (2024).
35. A preliminary note for constructing n-qubit polylog(n)-depth pseudorandom unitaries secure against $exp(o(n))$-time adversary can be found at https://hsinyuan-huang.github.io/assets/img/FermiMa_HsinYuanHuang_PolyLogDepthPRUs_against_SubExpAdv.pdf.
36. J. Emerson, E. Livine, S. Lloyd, *Phys. Rev. A* **72**, 060302 (2005).
37. A. W. Harrow, R. A. Low; Aram W Harrow and Richard A Low, *Commun. Math. Phys.* **291**, 257–302 (2009).
38. G. S. L. Fernando, Horodecki. Local random quantum circuits are approximate polynomial-designs. *Commun. Math. Phys.* **346**, 397–434 (2016).
39. J. Haferkamp, *Quantum* **6**, 795 (2022).
40. A. W. Harrow, S. Mehraban, *Commun. Math. Phys.* **401**, 1531–1626 (2023).
41. S.-K. Jian, G. Bentsen, B. Swingle, *J. High Energy Phys.* **2023**, 190 (2023).
42. C.-F. Chen, A. Bouland, F. G. S. L. Brandão, J. Docter, P. Hayden, M. Xu, Efficient unitary designs and pseudorandom unitaries from permutations. arXiv:2404.16751 [quant-ph] (2024).
43. T. Metger, A. Poremba, M. Sinha, H. Yuen, arXiv:2404.12647 [quant-ph] (2024). https://doi.org/10.1109/FOCS61266.2024.00038
44. J. Haah, Y. Liu, X. Tan, arXiv:2402.05239 [quant-ph] (2024). https://doi.org/10.1109/FOCS61266.2024.00036
45. C.-F. Chen *et al.*, arXiv:2406.07478 [quant-ph] (2024).
46. Intriguingly, this essential point does not carry over to experiments that query both the unitary U and its inverse, $U^{\dagger}$ (*67*, *68*). See the applications section and Appendix 6.4 for further discussions.
47. C. Bertoni *et al.*, arXiv:2209.12924 [quant-ph] (2022).
48. M. Ippoliti, Y. Li, T. Rakovszky, V. Khemani, *Phys. Rev. Lett.* **130**, 230403 (2023).
49. H.-Y. Hu, S. Choi, Y.-Z. You, *Phys. Rev. Res.* **5**, 023027 (2023).
50. X.-G. Wen, *Rev. Mod. Phys.* **89**, 041004 (2017).
51. Materials and methods are available as supplementary materials.
52. This k dependence is optimal up to poly(log k) factors (*45*). Hence, our k dependence is similarly optimal.
53. Z. Webb, arXiv:1510.02769 [quant-ph] (2015).
54. J. Jiang *et al.*, Optimal space-depth trade-off of cnot circuits in quantum logic synthesis" in *Proceedings of the Fourteenth Annual ACM-SIAM Symposium on Discrete Algorithms* (SIAM, 2020), pp. 213–229.
55. O. Regev, *J. Assoc. Comput. Mach.* **56**, 1–40 (2009) (JACM).
56. H.-Y. Huang *et al.*, Jarrod R McClean, "Learning shallow quantum circuitsin *Proceedings of the 56th Annual ACM Symposium on Theory of Computing* (2024), pp. 1343–1351.
57. G. Semeghini *et al.*, *Science* **374**, 1242–1247 (2021).
58. J. Léonard *et al.*, *Nature* **619**, 495–499 (2023).
59. Definitions of topological order are often stated colloquially in terms of constant-depth circuits, i.e., $= \mathcal{O}(1)$. However, more precise definitions are nearly always robust up to any depth that is subextensive in the system diameter, e.g., $= o\left(\sqrt{n}\right)$ in 2D. We refer to Appendix 6.2 for a detailed discussion.
60. D. Aharonov, J. Cotler, X.-L. Qi, *Nat. Commun.* **13**, 887 (2022).
61. H.-Y. Huang, R. Kueng, J. Preskill, *Phys. Rev. Lett.* **126**, 190505 (2021).
62. H.-Y. Huang *et al.*, *Science* **376**, 1182–1186 (2022).
63. S. Chen, J. Cotler, H.-Y. Huang, J. Li, "Exponential separations between learning with and without quantum memory" in *2021 IEEE 62nd Annual Symposium on Foundations of Computer Science (FOCS)* (IEEE, 2022), pp. 574–585.
64. J. Baum, M. Munowitz, A. N. Garroway, A. Pines, *J. Chem. Phys.* **83**, 2015–2025 (1985).
65. S. Choi, N. Y. Yao, M. D. Lukin, *Phys. Rev. Lett.* **119**, 183603 (2017).
66. M. Gärttner *et al.*, *Nat. Phys.* **13**, 781–786 (2017).
67. J. Cotler, T. Schuster, M. Mohseni, *Phys. Rev. A* **108**, 062608 (2023).
68. T. Schuster *et al.*, *Phys. Rev. Res.* **5**, 043284 (2023).
69. M. Cerezo, A. Sone, T. Volkoff, L. Cincio, P. J. Coles, *Nat. Commun.* **12**, 1791 (2021).
70. K. Wan, W. J. Huggins, J. Lee, R. Babbush*Commun. Math. Phys.* **404**, 629–700 (2023).
71. S. Gandhari, V. V. Albert, T. Gerrits, J. M. Taylor, M. J. Gullans, *PRX Quantum* **5**, 010346 (2024).
72. S. Becker, N. Datta, L. Lami, C. Rouzé, *IEEE Trans. Inf. Theory* **70**, 3427–3452 (2024).
73. J. Maldacena, *Int. J. Theor. Phys.* **38**, 1113–1133 (1999).
74. A. Bouland, B. Fefferman, U. Vazirani, arXiv:1910.14646 [quant-ph] (2019).

ACKNOWLEDGMENTS

We are grateful to E. Anschuetz, R. Babbush, C. Bertoni, A. Bouland, S. Boixo, F. Brandão, X. Chen, S. Choi, J. Cotler, J. Eisert, B. Fefferman, D. Gosset, S. Goush, P. Hayden, N. Hunter-Jones, M. Ioannou, M. Ippoliti, V. Khemani, I. Kim, W. Kretschmer, D. Kufel, D. Liang, F. Ma, J. R. McClean, T. Metger, R. Movassagh, Q. Nguyen, M. Soleimanifar, N. Tantivasadakarn, M. Tomamichel, U. Vazirani, and N. Yao for valuable discussions and insights. We thank S. Choi for introducing T.S. and J.H. to each other, which was vital for this work. **Funding:** T.S. acknowledges support from the Walter Burke Institute for Theoretical Physics at Caltech. J.H. acknowledges funding from the Harvard Quantum Initiative. H.H. acknowledges the visiting associate position at the Massachusetts Institute of Technology. T.S. and H.H. acknowledges support from the US Department of Energy, Office of Science, National Quantum Information Science Research Centers, Quantum Systems Accelerator. The Institute for Quantum Information and Matter, with which T.S. and H.H. are affiliated, is an NSF Physics Frontiers Center (NSF grant PHY-2317110). This work was conducted while J.H. and H.H. were at the Simons Institute for the Theory of Computing, supported by DOE QSA grant FP00010905. **Author contributions:** T.S. and J.H. independently conceived of the low-depth construction of unitary designs. T.S. and H.H. conceived of the low-depth construction of pseudorandom unitaries. All authors contributed to the theoretical development, proofs, applications, writing, and presentation of the work. **Competing interests:** There are no competing interests to declare. **Data and materials availability:** All data needed to evaluate the conclusions in the paper are present in the paper or the supplementary materials.

SUPPLEMENTARY MATERIALS

science.org/doi/10.1126/science.adv8590
Materials and Methods; Supplementary Text; Figs. S1 to S3; References (*75*–*157*)
Submitted 9 January 2025; accepted 13 May 2025
10.1126/science.adv8590

What's Your Next Career Move?

From networking to mentoring to evaluating your skills, find answers to your career questions on *Science* Careers

To view the complete collection, visit **ScienceCareers.org/booklets**

ScienceCareers
FROM THE JOURNAL SCIENCE AAAS

My Ph.D. pregnancy

Blessing Okosun

I was in my first year of grad school, preparing to present my research plans to my thesis committee and department for approval. I kept brushing away the feelings of sickness. I could not afford to be sick with an 18-month-old to take care of and my presentation looming. But after a few days, at the encouragement of my supervisor, I went to the student clinic—only to be told I was pregnant. It felt as though the floor had been pulled out from under my feet. I had fought to carve out a space for myself in science as a hard-working Black mom. An unplanned pregnancy seemed like certain professional doom.

Juggling parenthood and my studies was already challenging, but I was determined to follow my dream. I had gotten married and had my first child while pursuing the second bachelor's degree I needed after having finally found my professional direction. In 2020, I was ready to apply for grad school—not an easy feat during a global pandemic, let alone as a parent. For one virtual interview, I was not able to secure child care. The professor—who would go on to become my Ph.D. supervisor—graciously allowed the interview to continue with an infant bouncing in my arms. But I knew then and there that to succeed in graduate school, I should wait before having more children. Once I entered graduate school I had no doubt about that choice. I quickly realized I would have to commit to my work as never before to succeed as I hoped, flawlessly checking every academic box.

After going to the clinic, I didn't return to the lab. Instead I went home, quietly panicking. Two days later, my supervisor called to check on me, having noticed my absence. I told her everything. She listened kindly and offered me a key piece of advice: Don't panic. I realized she was right, and instead of retreating from others and spiraling into silence, what I really needed was community.

I called my best friend, mom of two teenage boys, to cry and vent. I barely knew how to process everything I was feeling—shame, fear, grief, frustration about being pregnant in a foreign land far from my family—but naming those feelings helped. Over the following weeks, I began to understand that surviving graduate school as a pregnant student would take a village, made up not of blood relatives, but of fellow graduate student parents. They helped babysit my toddler when my husband was away so I could battle morning sickness or take a nap. We drafted schedules to coordinate day care pickup and babysitting when one of us had a long experiment, a conference to attend, or an emergency. Sometimes we just met up to talk about life and the challenges and joys of being parents in graduate school.

It wasn't all rosy. I often had to call my supervisor for help to complete experiments because pregnancy symptoms left me too dizzy. I missed deadlines because of intense nausea and conferences because of anemia and low blood pressure. Peers questioned my commitment, whispering comments when I had to leave early for appointments or showed signs of morning sickness. One attributed my few successes during that period solely to my supervisor, making me feel inadequate as a student and scientist. Still, the steadfast support of my village and my supervisor, and my own determination to achieve my professional goals, saw me through. I persisted, at home and in the lab, and my definition of success expanded to include resilience.

My younger child is now almost 3 years old, and I expect to graduate next year. I now know that my unexpected pregnancy didn't make me less of a scientist. Redefining what success means to me was liberating, allowing me to become a scholar shaped by motherhood rather than diminished by it. Now, I pride myself not just on academic and research successes, but also on celebrating my kids' milestones, showing up for playdates, being present for tantrums and bedtime stories. I am grateful to my supervisor, who reminded me: "You belong here. Even like this. Especially like this." □

Blessing Okosun is a Ph.D. student at the University of North Dakota.
Send your career story to SciCareerEditor@aaas.org.

ILLUSTRATION: ROBERT NEUBECKER

Science AAAS

CHEN INSTITUTE TIANQIAO & CHRISSY

CO-HOST ETH zürich

AI & MENTAL HEALTH

SEPTEMBER 8–9, 2025 | ZURICH

Mental health is a vast and growing worldwide problem. In addition to the suffering experienced by individuals and their affected family members it also has an enormous economic impact. Because it can affect people at a young age they will often need treatment for many years and during that period they will not be able to participate to their full potential in society.

REGISTER TODAY!

FROM GUT SCIENCE TO REAL-WORLD FULL HEALTH

Noster Inc. in Kyoto advancing personalized, preventive care through postbiotics research and in-house omics analytics with clinicians in Japan and global partners

CONTACT US TO LEARN MORE

NOSTER®

info@noster.inc www.noster.inc/